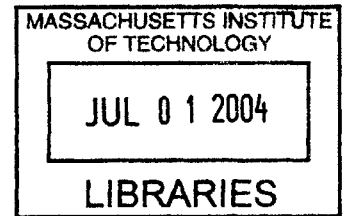


Dynamics of Multi-Body Space Interferometers Including Reaction Wheel Gyroscopic Stiffening Effects: Structurally Connected and Electromagnetic Formation Flying Architectures

by

Laila Mireille Elias



B.S., Aeronautics and Astronautics
University of Washington, 1998

S.M., Aeronautics and Astronautics
Massachusetts Institute of Technology, 2001

SUBMITTED TO THE DEPARTMENT OF AERONAUTICS AND ASTRONAUTICS **AERO**
IN PARTIAL FULFILLMENT OF THE DEGREE OF

DOCTORATE OF PHILOSOPHY IN AERONAUTICS AND ASTRONAUTICS

at the

MASSACHUSETTS INSTITUTE OF TECHNOLOGY

June 2004

© 2004 Massachusetts Institute of Technology. All rights reserved.

Signature of Author
Department of Aeronautics and Astronautics
March 12, 2004

Certified by Associate Professor David W. Miller
Thesis Committee Chairman

Certified by Dr. Raymond Sedwick
Thesis Committee Member

Certified by Dr. Marthinus Van Schoor
Thesis Committee Member

**Dynamics of Multi-Body Space Interferometers
Including Reaction Wheel Gyroscopic Stiffening Effects:
Structurally Connected and Electromagnetic Formation Flying Architectures**

by

LAILA MIREILLE ELIAS

Submitted to the Department of Aeronautics and Astronautics
on March 12, 2004 in Partial Fulfillment of the
Requirements for the Degree of Doctorate of Philosophy
at the Massachusetts Institute of Technology

ABSTRACT

Space telescopes have the potential to revolutionize astronomy and our search for life-supporting planets beyond our Solar System. Free of atmospheric distortions, they are able to provide a much “clearer” view of the universe than ground-based telescopes. A developing technology that appears promising is space-based interferometry, which uses multiple apertures separated at great distances to act as a large virtual aperture. In this way, interferometers will achieve angular resolutions far greater than those achievable by monolithic telescopes. In this thesis, we investigate the dynamics and control of two proposed architectures for spaceborne interferometers: structurally connected interferometers and electromagnetic formation flying interferometers.

For structurally connected interferometers, we develop a coupled disturbance analysis method that accurately predicts a space telescope’s optical performance in the presence of reaction wheel vibrational disturbances. This method “couples” a reaction wheel to a structure using estimates of the accelerances (or mobilities) of both bodies. This coupled analysis method is validated on the Micro-Precision Interferometer testbed at NASA’s Jet Propulsion Laboratory. The predictions show great improvement over a simplified “decoupled” analysis method when compared to experimental data.

For formation flying interferometers, we consider the use of electromagnets as relative position actuators. A high fidelity, nonlinear dynamic model of a deep-space electromagnetic formation flight (EMFF) array is derived from first principles. The nonlinear dynamics are linearized for a two-vehicle array about a nominal trajectory, and the linearized model is shown to be unstable, but controllable, and therefore stabilizable. A linear optimal controller is designed for the system and implemented to form the closed-loop dynamics. Time simulations of the closed-loop nonlinear dynamics demonstrate that EMFF using linear control proves very effective, despite the nonlinearities of the system’s dynamics and the electromagnetic actuators.

Thesis Supervisor: David W. Miller
Associate Professor of Aeronautics and Astronautics

ACKNOWLEDGMENTS

This work was performed partially under contract with NASA's Jet Propulsion Laboratory at the California Institute of Technology, partially under contract NRO-000-02-C0387-CLIN0001 with the National Reconnaissance Office and Lt. Col. John Comtois as technical scientific officer, and partially under contract 07600-097 with the NASA Institute for Advanced Concepts and Dr. Robert A. Cassanova as technical monitor. The author gratefully thanks the sponsors for their generous support that enabled this research. The author also thanks Zonta International for the honor and the emotional and financial support offered by the Amelia Earhart Fellowship.

The author also wishes to thank Professor David Miller for supporting this research, for inspiring new ideas, and for having enough faith in his students to allow them to perform independent research. Dr. Ray Sedwick and Dr. Martinus Van Schoor both offered valuable advice and feedback and greatly influenced this work. Their willingness to spend time discussing the work and to make thought-provoking suggestions inspired a great deal of this research.

The departmental readers of this thesis, Professor Jonathan How and Professor Charles Coleman, spent a great deal of their personal time critiquing this thesis, and that effort is greatly appreciated.

Ipek Basdogan, Lisa Sievers, and Frank Dekens were wonderful to work with at JPL and taught me a great deal. I look forward to rejoining their team.

SharonLeah Brown deserves special thanks not only for her incredible job as fiscal officer, but also for being a friend and big sister to me. Her support and concern carried me through the preparation of this thesis, even when the task seemed impossible. Marilyn Good was also there, not only to help with scheduling meetings and travel arrangements, but to offer a smiling face and a gentle manner when they were most lacking.

The technical and personal support from my friends and colleagues in the lab has been amazing, and I want to thank Sam Schweighart, Dan Kwon, Edmund Kong, Matthew Neave, Alvar Saenz-Otero, Scott Uebelhart, Rebecca Masterson, Jeremy Yung, Tim Glenn (for this thesis template!), and everyone else who helped shape my experience at MIT. I learned an immense amount from each of you and have been truly humbled by your abilities. Thank you for inspiring me.

My family and their support have been without parallel. There is no way to express my appreciation to my parents, Ziad and Ralda, my sister and brother, Maria and Paul, and my second family, Phil, Barb, Nat, Theresa, and Andrew for the amazing and unfailing support they have given me. They remind me that, despite being surrounded by amazing people, I, too, can accomplish this task if I keep trying. I could not have done so without their support.

Finally, my husband, David Cutler, has been my backbone throughout the last six years at MIT. His unconditional faith in me both surprises me and drives me to accomplish my goals. His love and support are superhuman, and for that I thank him.

TABLE OF CONTENTS

Abstract	iii
Acknowledgments	v
Table of Contents	vii
List of Figures	xi
List of Tables	xv
Nomenclature	xvii
Chapter 1. Introduction	1
1.1 Motivation	1
1.2 Research Objectives and Approach	3
1.2.1 Structurally Connected Interferometer	4
1.2.2 Formation Flying Interferometer	6
1.3 Literature Review	8
1.3.1 Review of Flexible Body Coupling Literature	8
1.3.2 Review of Formation Flight Literature	9
1.4 Thesis Overview	11
Chapter 2. Structural Dynamic Coupling Theory	13
2.1 Introduction	13
2.2 Decoupled Disturbance Analysis Method	14
2.3 Coupled Disturbance Analysis Method	16
2.3.1 Motivation for Coupled Analysis Method	16
2.3.2 The Load Filter	17
2.3.3 Coupled Analysis Method	20
2.4 Summary and Conclusions	23
Chapter 3. Structural Dynamic Coupling Experiments	25
3.1 MPI Testbed	26
3.1.1 MPI Testbed Description	26
3.1.2 MPI Testbed Transfer Functions	26

3.2	Intermediate Results	28
3.2.1	Hardmounted Reaction Wheel Disturbance Spectra	28
3.2.2	On-MPI Reaction Wheel Disturbance Spectra	30
3.2.3	MPI Accelerances	30
3.2.4	Reaction Wheel Accelerances	32
3.2.5	Performance Measurements	40
3.3	Performance Predictions	41
3.3.1	Decoupled Analysis	41
3.3.2	Coupled Analysis Using “rigid-RW, model3-MPI” Filters	42
3.3.3	Coupled Analysis Using “rigid-RW, model6-MPI” Filters	43
3.3.4	Coupled Analysis Using “rigid-gyro-RW, model6-MPI” Filters	45
3.3.5	Decoupled Analysis Using Cross-Spectral Density Terms	49
3.4	Summary and Conclusions	50
Chapter 4. Review of Kane’s Method		53
4.1	Introduction	53
4.2	Definitions	54
4.2.1	Generalized Coordinates and Configuration Constraints	54
4.2.2	Generalized Speeds and Motion Constraints (Holonomic vs. Nonholonomic Systems)	54
4.2.3	Partial Velocities and Partial Angular Velocities	56
4.2.4	Generalized Active Forces	57
4.2.5	Generalized Inertia Forces	60
4.3	Kane’s Equations of Motion	64
4.4	Example Using Kane’s Equations	65
4.5	Applicability of Kane’s Equations to EMFF Systems	69
4.6	Summary and Conclusions	70
Chapter 5. Electromagnetic Formation Flight Dynamics		73
5.1	Introduction	73
5.2	System Description	74
5.2.1	Vehicle Description	75
5.2.2	Coordinate Frames	76
5.2.3	Degrees of Freedom	78
5.2.4	Rotation Matrices	80
5.2.5	Velocity Vectors	81
5.2.6	Actuator Description	88

5.3	Electromagnetic Forces and Torques	92
5.3.1	Magnetic Moment Vectors Expressed in Global Coordinates	92
5.3.2	Calculation of Electromagnetic Forces and Torques	93
5.4	Nonlinear Equations of Motion	95
5.4.1	Generalized Coordinates and Generalized Speeds	96
5.4.2	Partial Velocities and Partial Angular Velocities	97
5.4.3	Generalized Forces	99
5.4.4	Nonlinear Equations of Motion	113
5.4.5	Nonlinear Equations of Motion with Infinite Spring Stiffness	118
5.5	Summary and Conclusions	120
Chapter 6. Electromagnetic Formation Flight Dynamics Analysis		123
6.1	System Description	124
6.2	Linearized Equations of Motion	134
6.2.1	Nominal Trajectory	134
6.2.2	Nominal Control	137
6.2.3	Conservation of Angular Momentum	141
6.2.4	Linearization of Equations	142
6.3	Stability Analysis of Linearized Dynamics	151
6.3.1	System Eigenvalues	151
6.3.2	System Mode Shapes	154
6.4	Controllability Analysis of Linearized Dynamics	155
6.4.1	Full Degree-of-Freedom, Full Actuator System	155
6.4.2	Full Degree-of-Freedom, Reduced Actuator System	156
6.4.3	Reduced Degree-of-Freedom, Reduced Actuator System	158
6.5	Optimal Control Design Using Linearized Dynamics	159
6.6	Summary and Conclusions	162
Chapter 7. Electromagnetic Formation Flight Control Simulations		165
7.1	Introduction	165
7.2	Dynamics Simulation Method	165
7.2.1	Simulation Tools	165
7.2.2	Simulation Approach	166
7.3	Simulation Results	167
7.4	Summary and Conclusions	170
Chapter 8. Conclusions and Recommendations		175

8.1 Thesis Summary	175
8.2 Thesis Contributions	176
8.3 Recommendations for Future Work	178
8.4 Concluding Remarks	179
References	181
Appendix A. Empirical Force Filters	185
Appendix B. Two-Vehicle EMFF Symbolic Eigenvalues	189
Appendix C. Two-Vehicle EMFF Optimal Gains	213
Appendix D. EMFF Control Experiments	221
D.1 Linear Airtrack	222
D.1.1 Airtrack Description	222
D.1.2 Airtrack Dynamics and Control	224
D.1.3 Discussion of System Poles	231
D.1.4 Airtrack Experimental Results	232
D.2 Planar Testbed	234
D.2.1 Testbed Description	235
D.2.2 Testbed Dynamics and Control	236
D.2.3 Testbed Preliminary Experimental Results	237
D.2.4 Testbed Proposed Experiments	237
D.3 Summary	238
Appendix E. EMFF Spin-Up Dynamics	241

LIST OF FIGURES

Figure 1.1	NASA's Future Space Interferometry Mission (SIM)	3
Figure 1.2	NASA's Future Terrestrial Planet Finder (TPF) Mission	4
Figure 1.3	Research Approach	6
Figure 1.4	Thesis Overview	11
Figure 3.1	The Micro-Precision Interferometer (MPI) Testbed at NASA's Jet Propulsion Laboratory.	27
Figure 3.2	RW on the MPI Base Plate.	27
Figure 3.3	Voice Coil Shakers on the MPI Base.	28
Figure 3.4	MPI FRF: x-Force-to-OPD.	29
Figure 3.5	Magellan RW: Blocked Disturbance Amplitude Spectra	31
Figure 3.6	Magellan RW: Coupled Disturbance Amplitude Spectra	31
Figure 3.7	MPI FEM-Predicted Translational Accelerances.	33
Figure 3.8	MPI FEM-Predicted Rotational Accelerances.	33
Figure 3.9	RW Rigid-Body-Model Translational Accelerances.	35
Figure 3.10	Shapes Used to Estimate the Magellan RW's Mass Moments of Inertia: (a) Cylinder and (b) Cone.	36
Figure 3.11	RW Rigid-Body-Model Rotational Accelerances.	37
Figure 3.12	Rigid Flywheel Model.	38
Figure 3.13	Measured Versus Predicted OPD Using Blocked RW Disturbances.	41
Figure 3.14	Measured Versus Predicted OPD Using Coupled RW Disturbances.	42
Figure 3.15	Translational "rigid-RW, model3-MPI" Force Filters.	44
Figure 3.16	Measured Versus Predicted OPD Using Blocked RW Disturbances and "rigid-RW, model3-MPI" Filters.	44
Figure 3.17	Rotational "rigid-RW, model6-MPI" Moment Filters.	46
Figure 3.18	Measured Versus Predicted OPD Using Blocked RW Disturbances and "rigid-RW, model6-MPI" Force and Moment Filters.	46
Figure 3.19	"Rigid-gyro-RW, model6-MPI" Moment Filters: (a) M_x Filter and (b) M_y Filter.	48
Figure 3.20	Measured Versus Predicted OPD Using Blocked RW Disturbances and the "rigid-gyro-RW, model6-MPI" Force and Moment Filters.	48

Figure 3.21	Measured Versus Predicted OPD Using Blocked RW Disturbance PSDs and CSDs (Without Force and Moment Filters)	50
Figure 4.1	Sample System: Pendulum Tube with Ball	65
Figure 5.1	Representative Model of One Spacecraft in an EMFF Array	75
Figure 5.2	Global Reference Frame, G, for Multiple-Spacecraft EMFF Array	78
Figure 5.3	Typical Electromagnetic Coil Consisting of Multiple Windings of Conducting Wire	90
Figure 5.4	Schematic of the Electromagnetic Actuator Configuration in an EMFF Array	91
Figure 6.1	Geometry of Two-Spacecraft EMFF Array	126
Figure 6.2	Local Curvilinear Coordinate Frame at Spacecraft A	126
Figure 6.3	Pole-Zero Map for Two-Spacecraft EMFF Array, Using Geometric Values in Table 6.1.	153
Figure 6.4	Open-Loop and Closed-Loop Eigenvalues of the Linearized Design Model	163
Figure 7.1	Dynamic Simulation with Very Small Initial Conditions: State Responses .	168
Figure 7.2	Dynamic Simulation with 10% Initial Condition on Dr: State Responses .	169
Figure 7.3	Dynamic Simulation with 10% Initial Condition on Dr: Actuator Signals .	169
Figure 7.4	Dynamic Simulation with 35% Initial Condition on Dr: State Responses .	171
Figure 7.5	Dynamic Simulation with 35% Initial Condition on Dr: Actuator Signals .	171
Figure 7.6	Dynamic Simulation with 40% Initial Condition on Dr: State Responses .	172
Figure 7.7	Dynamic Simulation with 40% Initial Condition on Dr: Actuator Signals .	172
Figure A.1	F_x Empirical Force Filter	186
Figure A.2	M_x Empirical Moment Filter.	186
Figure D.1	Linear Airtrack Used to Demonstrate Simplified Electromagnetic Formation Control	223
Figure D.2	dSPACE Virtual Control Panel Created for Airtrack System	224
Figure D.3	Schematic of the Stable Airtrack Configuration	227

Figure D.4	Stable Airtrack Pole-Zero Map	227
Figure D.5	Schematic of the Unstable Airtrack Configuration	230
Figure D.6	Unstable Airtrack Pole-Zero Map	230
Figure D.7	Open- and Closed-Loop Step Responses of Stable Airtrack	233
Figure D.8	Open- and Closed-Loop Responses of Unstable Airtrack.	234
Figure D.9	EMFF Testbed Vehicle	236
Figure D.10	Angle-Tracking Results Using One Vehicle on the Planar Testbed . . .	238
Figure E.1	Two Spacecraft Spinning Up About the Array Centerpoint	242
Figure E.2	Translation-Dependent Shear Force on Two Vehicles with Perpendicular Magnetic Dipoles	244
Figure E.3	Phase-Plane Portrait of the Perpendicular Magnet Geometry	245

LIST OF TABLES

TABLE 2.1	Generalized Input-Output Relationships Between a Load and Displacement, Velocity, and Acceleration.	21
TABLE 3.1	Estimated Mass Moments of Inertia [kgm^2] for the Magellan RW.	36
TABLE 5.1	Summary of the Coordinates Defined for Spacecraft A and its Reaction Wheel (RW-3)	80
TABLE 5.2	Components of the Angular Velocity Vectors in Terms of Euler Angles	86
TABLE 5.3	Generalized Coordinates for Spacecraft A and RW-3	96
TABLE 5.4	Generalized Speeds for Spacecraft A and RW-3	97
TABLE 6.1	Physical Parameters Used to Plot the Eigenvalues in Figure 6.3.	153
TABLE 6.2	State Penalties for LQR Control Design	161
TABLE 6.3	Actuator Penalties for LQR Control Design	162

NOMENCLATURE

A, A_S	Coil Cross-Sectional Area [m^2]
$\hat{a}_1, \hat{a}_2, \hat{a}_3$	Body-Fixed Coordinate Axes on Spacecraft A
$\hat{b}_1, \hat{b}_2, \hat{b}_3$	Body-Fixed Coordinate Axes on Spacecraft B
\vec{B}_i	Magnetic Field due to Magnetic Moment of i^{th} Spacecraft [T]
CSD	Cross Spectral Density [N^2/Hz]
DAQ	Data Acquisition System
DOF	Degree(s) of Freedom
EM	Electromagnet, Electromagnetic
EMFF	Electromagnetic Formation Flight/Flying
$\hat{e}_r, \hat{e}_\phi, \hat{e}_\psi$	Spherical Coordinate Axes
$\hat{e}_x, \hat{e}_y, \hat{e}_z$	Global Coordinate Axes
FEM	Finite Element Model/Method
FRF	Frequency Response Function
F_r, F_ϕ, F_ψ	Forces on Spacecraft, Resolved on Spherical Frame [N]
F_x, F_y, F_z	Forces on Spacecraft, Resolved on Global Cartesian Frame [N]
F_1, F_2, F_3	Forces on Spacecraft, Resolved on Body-Fixed Frame [N]
i	Current Running Through Electromagnetic Coil [A]
I_1^A	Mass-Moment of Inertia of Spacecraft A about Radial Axes [$\text{kg}\cdot\text{m}^2$]
I_3^A	Mass-Moment of Inertia of Spacecraft A about Spin Axis [$\text{kg}\cdot\text{m}^2$]
I_1^D, I_{rr}	Reaction Wheel Mass-Moment of Inertia about Radial Axes [$\text{kg}\cdot\text{m}^2$]
I_3^D, I_{zz}	Reaction Wheel Mass-Moment of Inertia about Spin Axis [$\text{kg}\cdot\text{m}^2$]
JPL	Jet Propulsion Laboratory
m_A	Spacecraft Mass [kg]
m_C	Reaction Wheel Mass [kg]
MIT	Massachusetts Institute of Technology
MPI	Micro-Precision Interferometer
n	Number of States of the System
n, n_S	Number of Conductor Wraps around Electromagnet
OPD	Optical Pathlength Difference
PSD	Power Spectral Density [N^2/Hz]
\vec{r}_{AG}	Position Vector of Spacecraft A [m]
r, ϕ, ψ	Spherical Coordinates of the Position of Spacecraft A
RMS	Root Mean Square
RPM	Revolutions per Minute
RW	Reaction Wheel
RWA	Reaction Wheel Assembly
SIM	Space Interferometry Mission
SSL	Space Systems Laboratory
TPF	Terrestrial Planet Finder
T_m	Motor Torque on Reaction Wheel [Nm]
T_r, T_ϕ, T_ψ	Torques on Spacecraft, Resolved on Spherical Frame [Nm]

T_x, T_y, T_z	Torques on Spacecraft, Resolved on Global Cartesian Frame [Nm]
u	Control Vector
x	State Vector
x_{AG}, y_{AG}, z_{AG}	Global Cartesian Coordinates of Spacecraft A
x_{BG}, y_{BG}, z_{BG}	Global Cartesian Coordinates of Spacecraft B
x_{CA}, y_{CA}, z_{CA}	Position Coordinates of RW-3 with Respect to Spacecraft A
α_i	i^{th} Euler Angle of Spacecraft A [rad]
β_i	i^{th} Euler Angle of Spacecraft B [rad]
γ_i	i^{th} Euler Angle of RW-3 on Spacecraft A [rad]
δ_3	Rotation angle of RW-3 on Spacecraft A [rad]
$\dot{\delta}_3$	Spin Rate of RW-3 on Spacecraft A [rad]
μ	Magnetic Moment of Coil [A·m ²]
μ_0	Permeability of Free Space [T·m/A]
$\dot{\phi}_0$	Nominal Spin Rate of Array [rad/s]
Ω	Spin Rate of RW [rad/s]

Chapter 1

INTRODUCTION

1.1 Motivation

Space-based telescopes are an enabling technology that will allow us to observe solar systems around neighboring stars, and will ultimately aid in the search for life beyond Earth. Telescopes in space avoid the atmospheric distortions that ground-based telescopes are subject to, and therefore allow us to see farther into space and gain better images of extra-solar planets. As space telescope technology continues to improve, we will answer more and more questions about the universe.

However, there are several design challenges associated with space-based telescopes. For instance, there is a trade between the angular resolution of a space telescope and its cost. A larger aperture provides improved angular resolution, but at the expense of an increased mass and volume. Hence the ideal telescope has as large an aperture as possible, within the limits of the given launch vehicle.

Space-based interferometry is a technology that has been proposed to provide the desired angular resolution, while maintaining a vehicle (or set of vehicles) that can be launched into space. An optical interferometer uses several separated apertures to collect light for scientific observation. The light from each aperture is then passed to a combiner, where an image is formed by interfering the light from the collectors. A set of separated apertures thus act as one large *virtual* aperture. Just as a monolithic telescope's angular resolu-

tion improves with an increased *aperture size*, an interferometer's resolution improves with increased *spacing between the separated apertures*. Hence the ideal space interferometer will be composed of multiple apertures separated by large distances.

Two main architectures have been proposed for implementing space-based interferometry: a structurally connected platform, and a free-flying (formation flying) array of spacecraft. The former concept is shown in Figure 1.1, which depicts NASA's forthcoming Space Interferometry Mission (SIM) [1]. SIM uses a 10-meter flexible truss platform to support the multiple apertures that compose the interferometer. There are both benefits and limitations of this architecture:

- The main *benefit* of this architecture is that the relative distances between the apertures are fixed, to within the vibrational tolerances of the flexible boom. Hence there is no need for very coarse (on the order of meters) control of the relative spacing between apertures. Finer-level control may be implemented using optical delay lines, voice coils, and fast-steering mirrors [2, 3].
- The main *limitation* of this architecture is the relatively small (and fixed) baseline distance between the apertures; the aperture spacing is limited by the length of the boom, which is in turn limited by the volume of the launch vehicle fairing. Hence the angular resolution of this system is less than that of a system with a larger baseline.
- The main *challenge* of this architecture is the fine control of the distances between the apertures. Because the light from the collectors must be interfered to form an image, the optical pathlength of the light from each aperture must be controlled to within a fraction of the wavelength of the light. This nanometer-level precision must be maintained in the presence of on-board dynamic disturbances, such as imperfectly balanced, spinning reaction wheels, which cause vibrations of the support structure. For this reason, strict tolerances are placed on the magnitudes of vibration of such spacecraft, and detailed disturbance analyses and control design are required to ensure that deflections and vibrations are limited to acceptable levels for scientific data collection.

The free-flying concept for space-based interferometry is shown in Figure 1.2, which depicts a potential architecture for NASA's forthcoming Terrestrial Planet Finder (TPF) mission [4]. TPF is considering this formation flying interferometer architecture, as well as a structurally connected interferometer and a monolithic coronagraph. In the formation



Figure 1.1 NASA's Future Space Interferometry Mission (SIM)

flight architecture, four spacecraft act as collectors of light, and the fifth spacecraft acts as a combiner. Like the structurally connected interferometer concept, there are both benefits and limitations to this architecture:

- The main *benefit* of this architecture is the increased and variable baseline distance between the vehicles. TPF proposes a baseline between 75 meters and 1 kilometer, distances that are far greater than those possible with a structurally connected interferometer [5]. Further, the baseline is variable, and may be set to an optimal length for a given data collection mode.
- The main *challenge* of this architecture is the coarse level of control (on the order of meters and centimeters) needed to maintain the relative separation distances between the free-flying vehicles. Coarse control using thrusters raises several concerns, including the thermal and optical contamination due to the thruster plumes, as well as a mission lifetime limited by a finite thruster fuel supply.

1.2 Research Objectives and Approach

In this thesis, we address some of the dynamics and control challenges of both the structurally connected and formation flying interferometer concepts described above. We now discuss the research objectives and approach for each architecture.

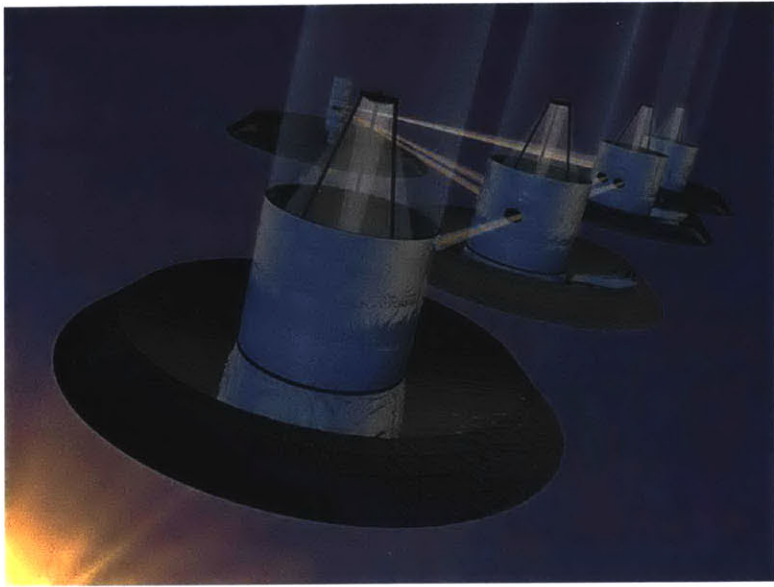


Figure 1.2 NASA’s Future Terrestrial Planet Finder (TPF) Mission

1.2.1 Structurally Connected Interferometer

In Chapters 2 and 3, we consider the dynamics of a structurally connected interferometer. The primary challenge of such a system was described above. Namely, we are concerned with the vibrational tolerances of the support structure, and the resulting tolerances of the optical instruments. The goal is to maintain the optical pathlength difference (OPD) of the multiple arms of the interferometer to the nanometer level, with either passive damping or active control. We focus here on the dynamic analysis, rather than the control of this structure. Specifically, we develop an analysis method for determining the *optical performance* of the system, even in the presence of on-board vibrational disturbance sources. The result will be a toolbox that, given a set of dynamic disturbances and a model of the structural-optical system, predicts the resulting performance. The performance will then be assessed to determine whether the structure achieves the required jitter tolerances, and therefore whether the optical interferometer achieves sufficient dynamic stability to operate successfully.

As discussed in detail in references [6, 7], the primary disturbance source anticipated for missions such as SIM is the on-board reaction wheel, used for attitude control. In [6], a

dynamic disturbance analysis method is developed that dynamically couples the reaction wheel to the spacecraft in order to predict the resulting system performance. The motivation lies in the fact that reaction wheel disturbances are typically measured with the reaction wheel assembly “hardmounted” to a rigid surface, so that the interface loads are measured by load transducers while the flywheel spins. The problem with this measurement technique is that the boundary conditions of the hardmounted reaction wheel are not representative of the conditions when the wheel is fixed to the spacecraft. Hence the hard-mounted *disturbances* that are measured do not accurately represent the “coupled” disturbances that occur when the wheel is fixed to the spacecraft.

To account for this, the coupled disturbance analysis method uses the hardmounted disturbances as the input disturbance source to the structural-optical model, but first “corrects” them so that they represent the *coupled* disturbance loads that would occur if the reaction wheel were mounted to the spacecraft. As will be described in Chapter 2, this correction of the disturbance loads relies on estimates of the driving-point *mobilities* or *accelerances* of the spacecraft and the reaction wheel at their common interface points.

In this thesis, we build upon the disturbance analysis method developed in [6]. First, we increase the fidelity of the analysis method by accounting for the nonlinear gyroscopic stiffening dynamics of the spinning flywheel in the reaction wheel’s accelerance model. Any improvement in results will allow us to assess the degree of gyroscopic stiffening of the wheel, as well as its influence on the system performance. Further, we validate the analysis methodology on representative hardware, the Micro-Precision Interferometer (MPI) testbed at NASA’s Jet Propulsion Laboratory (JPL). As this testbed is a scale model of SIM, validating the analysis method on MPI will prove very useful.

Our approach is shown on the left-hand side of Figure 1.3. First, the coupled disturbance analysis method is reviewed. Then the gyroscopic accelerance model of the reaction wheel is developed and implemented. Finally, the method is validated on the MPI testbed,

and we use the results to assess both the success of the analysis method and the importance of reaction wheel gyroscopic stiffening on the system performance.

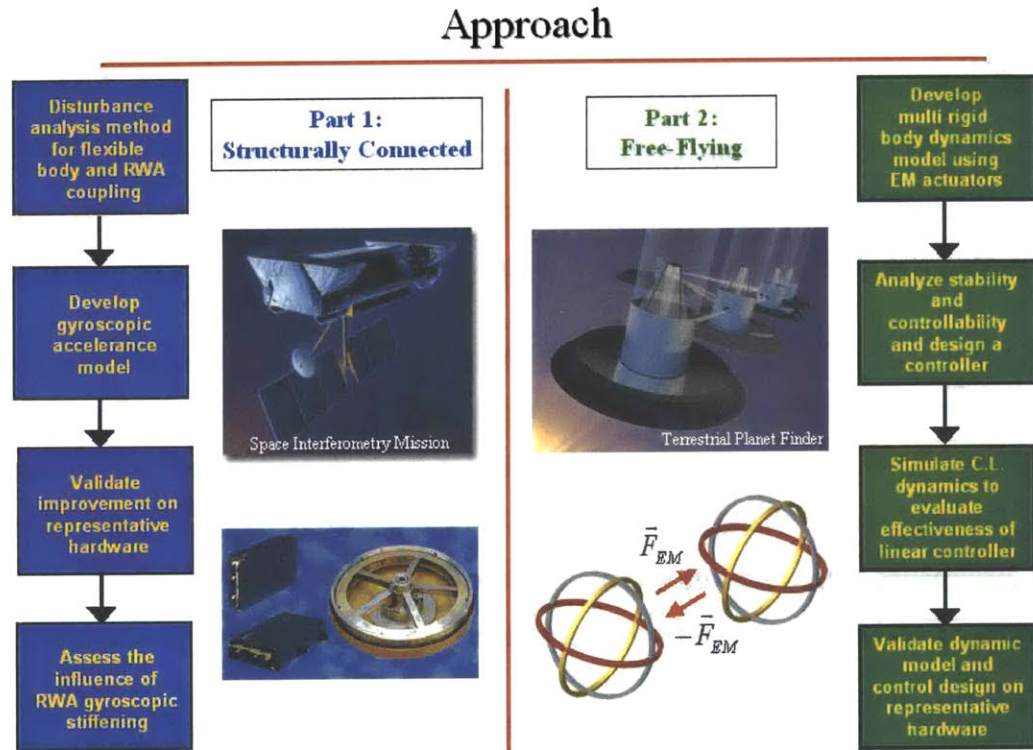


Figure 1.3 Research Approach

1.2.2 Formation Flying Interferometer

In Chapters 4-7, we consider the dynamics and control of a formation flying interferometer. The primary challenge of such a system was described above. Namely, we seek a method for the coarse control of the relative distances and the attitudes of the spacecraft in an array, and we would like to achieve this without the use of thrusters (in order to eliminate the contamination they cause and to extend the lifetime of the mission). We propose the use of electromagnetic actuators, whereby each spacecraft is equipped with a set of electromagnets, and the relative distances between the vehicles are controlled using the

interaction forces of the magnetic fields of the vehicles. We refer to this concept as electromagnetic formation flight (EMFF).

The EMFF concept is promising for many reasons. First, it eliminates thermal and optical contamination issues associated with thruster plumes. Second, it has the potential to greatly increase the mission lifetime, since it relies on a renewable energy source (electrical power from solar arrays), rather than a finite fuel supply. Further, if superconducting wires are used to form the electromagnets, the system will sustain very small resistive losses, and therefore will require only a very small amount of power. Finally, EMFF controls the relative separation distances between vehicles, which is the metric of importance in space interferometry applications. Hence valuable effort is not spent controlling the absolute degrees of freedom of each vehicle, as with thrusters.

While EMFF has many benefits, it also has many challenges. First, the electromagnetic forces are spatially nonlinear. The forces between any two electromagnets (EMs) are inversely proportional to the fourth power of the separation distance. Hence EMs may produce very strong forces when they are near each other, and very weak forces when they are farther apart. Also, the control is coupled. Every powered EM affects every other powered EM in the array, so a systematic method should be used to derive the control law.

As EMFF is a newly proposed technology, we focus on demonstrating the feasibility of the dynamics and controls of an EMFF system. Our approach is shown on the right-hand side of Figure 1.3. First, we develop from first principles a high-fidelity *model* of the system. In addition to modeling the nonlinear actuator terms, we model the nonlinear dynamics of each vehicle in the array, as well as the nonlinear gyroscopic stiffening dynamics of its spinning reaction wheel. Next we linearize the dynamics about a nominal trajectory, and the resulting linearized equations of motion serve as a *design model*. We analyze the linearized dynamics to determine whether the system is stable, and whether it is controllable. The controllability of the system is a key factor to determining the practicability of EMFF. Next we design a linear, optimal controller for the system using the design model,

and we implement the controller with the nonlinear equations of motion (the *evaluation model*) to form the closed-loop nonlinear dynamics. Finally, we simulate the closed-loop dynamics in order to assess the effectiveness of the EMFF concept. Initial hardware demonstrations are also presented in Appendix D, and recommendations will be made for higher fidelity hardware demonstrations.

1.3 Literature Review

1.3.1 Review of Flexible Body Coupling Literature

The derivation of the coupled disturbance analysis method in this thesis was motivated by the fact that the SIM integrated modeling team at NASA's JPL has relied on a decoupled disturbance analysis method that generally overpredicts their coupled measurements. References [8] and [9] describe the decoupled method used at JPL.

In an attempt to correct the overprediction by the decoupled method, Ploen [10] developed a “force filter,” which modifies the hardmounted forces so that they resemble the coupled forces. Although this was the first attempt within the SIM integrated modeling group to account for dynamic coupling between a structurally connected interferometer and its reaction wheel disturbance source, this method is very limited and invokes several approximations. For instance, it modifies only the hardmounted disturbance *forces*, and not the torques. Also, the force filters derived by Ploen assume that the accelerance matrix of a body is purely diagonal, and therefore that cross-accelerance terms do not exist. In reality, this holds true only in a very limited number of cases, and it is an approximation for most bodies. Reference [10] does provide a very clear, systematic derivation for the coupling theory, and provides a nice nomenclature (the “force filter” terminology) that we will adopt here.

Simultaneous with the work of Ploen, Elias [6] developed a full matrix coupling method, where the *matrix accelerances* of each body are taken into account (including cross-

accelerance terms). This results in a 6×6 *load filter matrix*, which is used to transform the hardmounted loads (forces and torques) into the equivalent coupled loads.

The work in this thesis will expand upon [6] by including the nonlinear, gyroscopic stiffening dynamics of the reaction wheel in the wheel's accelerance model. We use the "filter" notation from [10], and expand upon this concept to include full matrix load filters. Finally, we validate this method on representative hardware and draw conclusions about which terms are influential, and which may be neglected without significantly altering the results of the analysis.

1.3.2 Review of Formation Flight Literature

Formation flight has recently become a key research interest among the aerospace community because of its many applications, including space interferometry, earth observation, and synthetic aperture radar.

A great deal of research has been done in the MIT Space Systems Laboratory to demonstrate formation flight on a hardware testbed. The SPHERES project [11] has evolved from a two-dimensional, ground-based laboratory experiment to one being tested in a zero-gravity, three-dimensional environment, both on NASA's KC-135 aircraft and in the future on the International Space Station (ISS). This testbed has demonstrated successful formation flight maneuvers, including leader-follower tracking and docking. The SPHERES Guest Scientist Program will allow engineers from around the world to upload algorithms to the vehicles while they are on the ISS. This will add a great deal to our current understanding of formation flight control algorithms.

Similar hardware-based demonstrations have been performed at JPL, UCLA, Stanford, and the NASA Goddard Space Flight Center. All of these testbeds assume the use of thrusters to control the relative positions of the spacecraft. Open areas of research include the use of microthrusters, Micro-Electro-Mechanical Systems (MEMS), pulse plasma thrusters (PPTs), and colloid microthrusters [12].

In addition to hardware demonstrations, much theoretical work has been done in the area of formation flight dynamics and control for spacecraft in deep space. Wang et. al. [13] present a formulation for the rigid-body dynamics of a multi-spacecraft spinning array, modeling each vehicle as a lumped mass and inertia. A similar approach was taken by Smith et. al. [14], who investigate various control topologies and their associated stability properties.

While all the above references assume a traditional actuation method, such as thrusters, for control of the relative spacecraft separation distances, Kong et. al. [2, 15] investigate the use of electromagnets for relative position control. In [15], several trade studies are presented, demonstrating that the required mass and power of EMFF systems are comparable to or more attractive than traditional propulsion methods. Reference [2] also investigates the controllability of *non-rotating* EMFF arrays and draws conclusions about the necessary electromagnetic topologies for such systems to be controllable.

Like Kong et. al., we extend the previous work by focusing on the use of electromagnets as the relative position actuators of the array. As described above, eliminating the use of thrusters offers several benefits, and we attempt to demonstrate the feasibility of this novel actuation method from a dynamics and controls perspective. Specifically, we extend the research in references [2, 15] by developing a higher fidelity, nonlinear dynamic model of an EMFF system. We model the spacecraft-reaction wheel system as a system of *two* rigid bodies that can rotate relative to one another about the reaction wheel's spin axis. Modeling the dynamics in this way allows us to capture the nonlinear gyroscopic dynamics associated with the reaction wheel's spinning. As we will find in Chapter 5, the reaction wheels of a rotating array may store a significant amount of angular momentum, and therefore their nonlinear dynamics should be considered. Further, we analyze the system's dynamics in its mode of scientific observation (rotation of the entire array about its center point), and we assess the control possibilities for such a system via analysis and simulation.

1.4 Thesis Overview

As shown in Figure 1.4, this thesis is divided into two parts. Chapters 2 and 3 discuss the dynamics of a *structurally connected* space interferometer, while Chapters 4-7 discuss the dynamics and control of an *electromagnetic formation flying* space interferometer.

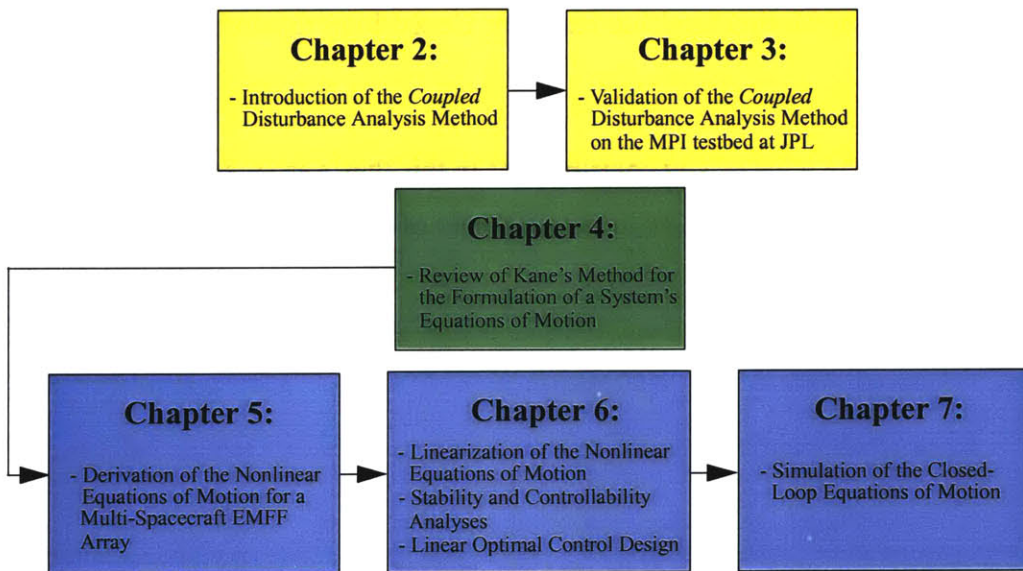


Figure 1.4 Thesis Overview

In Chapter 2, the theory for a disturbance analysis method that *accounts for the structural dynamic coupling between a flexible body and its disturbance source* is introduced. In Chapter 3, the hardware and experimental configurations used to validate the coupled disturbance analysis method are described in detail. The experimental results are then presented for comparison with the predictions, so that the effectiveness of the analysis method may be assessed.

In Chapter 4, Kane's method for the derivation of a system's equations of motion is reviewed in detail. Kane's method is then applied in Chapter 5 to derive the nonlinear equations of motion for an electromagnetic formation flying array with an arbitrary number of spacecraft. Expressions are given for the electromagnetic forces and torques applied to one spacecraft by another. Also, the nonlinear gyroscopic dynamics associated

with the spinning reaction wheels are captured in the model, along with their effect on the attitude dynamics of the spacecraft.

In Chapter 6, the nonlinear equations of motion are linearized for a two-spacecraft system about a nominal trajectory. The linearized equations are analyzed for stability and controllability, and a linear optimal controller is designed. The controller is implemented into the nonlinear equations of motion, and the resulting closed-loop dynamics are simulated in Chapter 7.

Finally, a summary and a list of key contributions in this thesis are presented in Chapter 8, along with recommendations for further development of this work.

Chapter 2

STRUCTURAL DYNAMIC COUPLING THEORY

2.1 Introduction

NASA's future Space Interferometry Mission (SIM), depicted in Figure 1.1, will be the first space-based optical interferometer. With optics mounted to its flexible truss structure, SIM must achieve nanometer-level stability requirements in the presence of on-board disturbances. The primary disturbance source anticipated for SIM is the reaction wheel (RW), a spinning flywheel assembly used for attitude control. In order to ensure mission success, a disturbance analysis method must be developed to predict SIM's on-orbit performance in the presence of RW disturbances.

RW disturbances are typically measured in a “blocked” or “infinite-impedance” configuration, in which the RW is hardmounted to a rigid surface and its interface is constrained to have zero motion. The RW is spun, and a load transducer is used to measure the resulting disturbance loads at the interface. While this method provides well-defined and repeatable boundary conditions, they are not an accurate representation of the coupled boundary conditions that occur when the RW is mounted to a structure. In other words, the *blocked* RW disturbances differ from the *coupled* disturbances that would actually exist at the spacecraft-RW interface if the two bodies were coupled together.

In this chapter, we present a modeling methodology to predict the dynamic performance of a flexible structure in the presence of on-board RW vibrational disturbances. Two *distur-*

bance analysis methods are presented: a *decoupled* method and a *coupled* method. In the *decoupled* method, the blocked RW disturbances are propagated through a spacecraft frequency response function (FRF) to predict the resulting spacecraft performance. In the *coupled* method, “load filters” are used to correct the blocked disturbances for the artificial boundary conditions imposed on the RW during disturbance testing. The filters, which rely on estimates of the RW and spacecraft interface *accelerances*, are used to “transform” the blocked RW disturbances into the corresponding coupled disturbances. The coupled disturbances are then propagated, in place of the blocked disturbances, through a spacecraft FRF to predict the coupled performance.

The decoupled and coupled methodologies will be presented in this chapter. First, the decoupled method is presented in Section 2.2. In Section 2.3, motivation is provided for the derivation of the coupled disturbance analysis method, and the coupled analysis method is described in detail. Finally, a summary and conclusions are presented in Section 2.4. In the following chapter, both methods will be validated by experimental data from the Micro-Precision Interferometer (MPI) testbed at NASA’s Jet Propulsion Laboratory (JPL).

2.2 Decoupled Disturbance Analysis Method

The *decoupled disturbance analysis method* is based on a simple frequency-domain input-output principle. The performance metric, Z , of a flexible structure is related to the input disturbance source, F , as:

$$Z(\omega, \Omega) = G_{ZF}(\omega)F(\omega, \Omega) \quad (2.1)$$

where G_{ZF} is the FRF of the structure, ω represents frequency (in units of radians per second), and Ω represents the reaction wheel spin rate (in units of radians per second). Notice that the disturbance, F , is a function of both frequency and reaction wheel spin rate, and hence the performance metric, Z , is also a function of frequency and wheel spin rate. For a structural-optical system, such as a structurally connected interferometer, Z may be

defined either as a mechanical performance metric, such as the relative displacement of two points, or as an *optical* performance metric, such as the optical pathlength difference (OPD) between various light paths within the interferometer.

If we are considering a number, p , of performance metrics, then Z is the $p \times 1$ *predicted performance* vector. Since the disturbance source is a reaction wheel producing three disturbance forces and three disturbance moments, F is a 6×1 disturbance load vector. Finally, G_{ZF} is the $p \times 6$ FRF of the structure, relating the six disturbance loads at the RW-mounting location on the structure to the structure's p performance metrics.

Post-multiplying each side of Equation 2.1 by its complex-conjugate transpose and taking the expectation allows us to write the analysis equation in terms of spectral density matrices, which are a useful form for implementing experimental data. This yields:

$$\Phi_{ZZ}(\omega, \Omega) = G_{ZF}(\omega)\Phi_{FF}(\omega, \Omega)G_{ZF}^{*T}(\omega) \quad (2.2)$$

where $[\cdot]^{*T}$ denotes a complex-conjugate transpose operation, Φ_{ZZ} is the $p \times p$ predicted performance spectral density matrix, and Φ_{FF} is the 6×6 RW disturbance spectral density matrix, with disturbance power spectra as diagonal components and cross-spectra as off-diagonal components.

If we have a single performance metric of interest, so that $p = 1$ and Z is a scalar, the root mean square (RMS) of the performance metric can then be calculated for a given reaction wheel spin rate, Ω , as:

$$\sigma_z(\Omega) = \sqrt{\int_{-\omega_{max}}^{\omega_{max}} \Phi_{ZZ}(\omega, \Omega) d\omega} \quad (2.3)$$

When Z is a vector containing more than one performance metric, σ_z is a matrix whose diagonal components are the scalar RMS functions of the performance metrics contained in Z .

In the case that the diagonal terms of Φ_{FF} , or power spectral densities (PSDs), dominate the off-diagonal terms, or cross spectral densities (CSDs):

$$\Phi_{F_i F_i} \gg |\Phi_{F_i F_j}| , \quad i \neq j \quad (2.4)$$

then Φ_{FF} may be approximated as a diagonal matrix, and Equation 2.2 reduces from a fully populated *matrix equation* to a simple *summation of diagonal terms*:

$$\Phi_{ZZ}(\omega, \Omega) \approx \sum_{j=1}^6 \Phi_{F_i F_i}(\omega, \Omega) |G_{ZF_i}(\omega)|^2 \quad (2.5)$$

It is important to note that Equation 2.2 represents a *decoupled* disturbance analysis method, since the disturbance loads are usually measured in a blocked configuration (denoted $\Phi_{FF,b}$) and are then substituted for the disturbance loads (Φ_{FF}) in Equation 2.2. Clearly $\Phi_{FF,b}$ differs from the loads that occur when the RW is mounted to the spacecraft (denoted $\Phi_{FF,c}$). We will account for this discrepancy in the following section by deriving a relationship between the blocked and coupled loads.

2.3 Coupled Disturbance Analysis Method

2.3.1 Motivation for Coupled Analysis Method

The remainder of this chapter is motivated by the fact that there is often a discrepancy between measured performances and those predicted by the decoupled analysis method presented above. For instance, performance predictions for the MPI testbed at JPL have been found to consistently overbound experimental measurements when calculated using Equation 2.5 [16]. The degree of discrepancy is not acceptable, since accurate performance predictions will be required to ensure the success of future NASA missions, such as the Space Interferometry Mission, prior to assembly and launch.

The discrepancy has been, up to now, attributed to two primary factors:

- the decoupled nature of the disturbance analysis method described in Equation 2.5.
- the approximation made by Equation 2.4, yielding Equation 2.5 as a simplified representation of Equation 2.2.

The first concern is addressed in this chapter, and the latter is addressed in Chapter 3, where we will use experimental data to investigate the validity of the approximation in Equation 2.4.

In the remainder of this chapter, we propose a *coupled* disturbance analysis method to improve upon the decoupled method presented in Section 2.2. In propagating *blocked* RW disturbances through a structural FRF, *the decoupled method neglects the structural dynamic coupling between the flexible structure and the RW*. Our goal is thus to correct the mismatch in RW disturbance-testing boundary conditions by applying a coupling theory to the performance predictions. Reconciling the measured and predicted performances will affirm our ability to predict a spacecraft’s on-orbit dynamic behavior prior to flight.

2.3.2 The Load Filter

In order to correct the mismatch of boundary conditions that occurs in blocked RW disturbance testing, a *load filter matrix*, G_f , may be used to relate the measured *blocked* RW disturbances, F_b , with the “true” *coupled* disturbances, F_c , [16, 6]:

$$F_c(\omega, \Omega) = G_f(\omega, \Omega)F_b(\omega, \Omega) \quad (2.6)$$

where ω represents frequency, and Ω represents the reaction wheel spin rate (in units of radians per second). Recall the loads, F_b and F_c , are 6×1 matrices, each consisting of the three disturbance forces and three disturbance moments imparted by the RW with the given boundary conditions (blocked or coupled, respectively). Therefore the load filter, G_f , is a 6×6 matrix.

By post-multiplying each side of Equation 2.6 by its complex-conjugate transpose and manipulating slightly, we can express Equation 2.6 in terms of spectral density matrices:

$$\Phi_{FF,c}(\omega, \Omega) = G_f(\omega, \Omega)\Phi_{FF,b}(\omega, \Omega)G_f^{*T}(\omega, \Omega) \quad (2.7)$$

where the $[\cdot]^T$ operation was defined in Section 2.2.

The goal is to now define the load filter, G_f , which provides a relationship between the blocked and coupled loads. Once that relationship is defined, we will have the ability to “filter” any set of blocked loads into the corresponding coupled loads for use in a coupled disturbance analysis.

By studying the derivation in references [6, 17] and adopting the notation used in [10], we can define the load filter matrix as:

$$G_f(\omega, \Omega) \equiv [I + A_{RW}^{-1}(\omega, \Omega)A_S(\omega)]^{-1} \quad (2.8)$$

where I is the 6×6 identity matrix, A_{RW} is the 6×6 driving-point acceleration matrix of the RW at its interface point with the structure, and A_S is the 6×6 driving-point acceleration matrix of the flexible structure at its interface point with the RW.¹ Notice that the RW’s acceleration matrix is dependent upon the wheel’s spin rate, since the spinning of the wheel causes a nonlinear, gyroscopic stiffening effect and thereby influences the wheel’s acceleration. *Therefore the load filter matrix, G_f , is also dependent upon the RW’s spin rate.*

1. The driving-point acceleration is a complex, frequency-dependent ratio of co-located acceleration and force at the interface, or “driving point” of a body. It is the inverse of the driving-point apparent mass. For more information, see reference [18].

A simplified version of the load filter matrix in Equation 2.8 was introduced in reference [10]. A scalar *force filter* was defined to relate the measured *blocked* RW forces with the “true” *coupled* forces:

$$\tilde{G}_{f,ii}(\omega) \equiv \frac{F_{c,i}(\omega)}{F_{b,i}(\omega)} = \frac{1}{1 + \frac{A_{S,ii}(\omega)}{A_{RW,ii}(\omega)}} , \quad i = 1, 2, 3 \quad (2.9)$$

where $i = 1, 2, 3$ refers to the x , y , and z axes, respectively, $\tilde{G}_{f,ii}$ is a “force filter” along the i^{th} axis, $F_{c,i}$ is the Fourier transform of the coupled interface force along the i^{th} axis, $F_{b,i}$ is the Fourier transform of the measured blocked force along the i^{th} axis, $A_{S,ii}$ is the spacecraft’s driving-point accelerance along the i^{th} axis, and $A_{RW,ii}$ is the RW’s driving-point accelerance along the i^{th} axis. Note that this force filter is an approximation of the load filter in Equation 2.8 in two ways:

1. The force filter is not dependent on the wheel’s spin rate, Ω , and therefore does not capture the effect of the wheel’s gyroscopic stiffening on its accelerance. (In other words, $A_{RW}(\omega, \Omega)$ is approximated as $A_{RW}(\omega)$, so that $\tilde{G}_{f,ii}$ is independent of the RW’s spin rate.) While this may be a fair approximation at low wheel speeds, it may not hold true for higher wheel speeds.
2. The force filter assumes that the accelerances of the RW and spacecraft are diagonal matrices (with negligible off-diagonal components), and therefore that the product $A_{RW}A_S$ in the load filter (Equation 2.8) can be approximated as a diagonal matrix with components $A_{S,ii}/A_{RW,ii}$. In reality, this holds true only for a limited number of geometries.

The concept of the scalar force filter was expanded in [16] to include a similar “moment filter,” which may be expressed as:

$$\tilde{G}_{f,ii}(\omega) \equiv \frac{M_{c,i}(\omega)}{M_{b,i}(\omega)} = \frac{1}{1 + \frac{A_{S,ii}(\omega)}{A_{RW,ii}(\omega)}} , \quad i = 4, 5, 6 \quad (2.10)$$

where $i = 4, 5, 6$ refers to *rotations about* the x , y , and z axes, respectively, $M_{c,i}$ is the Fourier transform of the coupled interface *moment* along the i^{th} axis, $M_{b,i}$ is the Fourier

transform of the measured blocked *moment* along the i^{th} axis, $A_{S,ii}$ is the spacecraft's driving-point *rotational* accelerance about the i^{th} axis, and $A_{RW,ii}$ is the RW's driving-point *rotational* accelerance about the i^{th} axis.

Table 2.1 lists the generalized input-output relationships between a load, F , imparted on a body and its resulting position, velocity, and acceleration: Q , \dot{Q} , and \ddot{Q} , respectively [18]. (Where there is more than one acceptable term, the more common term is shown in bold.) From this table, it is clear that accelerance, A , is simply a derivative of mobility, Y [6]:

$$A(\omega) = \frac{Q(\omega)}{F(\omega)} = \frac{j\omega Q(\omega)}{F(\omega)} = j\omega Y(\omega) \quad (2.11)$$

and thus that the ratio of two bodies' *accelerances* is equivalent to the ratio of their *mobil-
ities*:

$$\frac{A_{S,ii}}{A_{RW,ii}} = \frac{j\omega Y_{S,ii}}{j\omega Y_{RW,ii}} = \frac{Y_{S,ii}}{Y_{RW,ii}} \quad (2.12)$$

Hence the scalar force and moment filters in Equations 2.9 and 2.10, respectively, can be formed using the ratio of spacecraft and RW *accelerances or mobilities*:

$$\tilde{G}_{f,ii}(\omega) \equiv \frac{F_{c,i}(\omega)}{F_{b,i}(\omega)} = \frac{1}{1 + \frac{A_{S,ii}(\omega)}{A_{RW,ii}(\omega)}} = \frac{1}{1 + \frac{Y_{S,ii}(\omega)}{Y_{RW,ii}(\omega)}} , \quad i = 1, 2, 3 \quad (2.13)$$

$$\tilde{G}_{f,ii}(\omega) \equiv \frac{M_{c,i}(\omega)}{M_{b,i}(\omega)} = \frac{1}{1 + \frac{A_{S,ii}(\omega)}{A_{RW,ii}(\omega)}} = \frac{1}{1 + \frac{Y_{S,ii}(\omega)}{Y_{RW,ii}(\omega)}} , \quad i = 4, 5, 6 \quad (2.14)$$

2.3.3 Coupled Analysis Method

Recall from Equation 2.2 the input-output relationship used as the basis for the decoupled disturbance analysis method, where blocked disturbance PSDs, $\Phi_{FF,b}(\omega, \Omega)$, are used to

TABLE 2.1 Generalized Input-Output Relationships Between a Load and Displacement, Velocity, and Acceleration.

Response/Load Ratios		Load/Response Ratios	
$\alpha(\omega) = \frac{Q(\omega)}{F(\omega)}$	Receptance, Admittance, Dynamic Compliance, Dynamic Flexibility	$\frac{1}{\alpha(\omega)} = \frac{F(\omega)}{Q(\omega)}$	Dynamic Stiffness
$Y(\omega) = \frac{\dot{Q}(\omega)}{F(\omega)}$	Mobility	$Z(\omega) = \frac{F(\omega)}{\dot{Q}(\omega)}$	Mechanical Impedance
$A(\omega) = \frac{\ddot{Q}(\omega)}{F(\omega)}$	Accelerance, Inertance	$\frac{1}{A(\omega)} = \frac{F(\omega)}{\ddot{Q}(\omega)}$	Apparent Mass, Dynamic Mass

represent the disturbance PSDs, $\Phi_{FF}(\omega, \Omega)$, that are applied to a spacecraft. If instead, we use the coupled disturbance PSDs, $\Phi_{FF,c}(\omega, \Omega)$, as expressed in Equation 2.7, to represent the disturbance PSDs applied to the spacecraft, we will obtain a *coupled disturbance analysis equation* analogous to the decoupled Equation 2.2:

$$\Phi_{zz}(\omega, \Omega) = G_{ZF}(\omega)G_f(\omega, \Omega)\Phi_{FF,b}(\omega, \Omega)G_f^{*T}(\omega, \Omega)G_{ZF}^*(\omega) \quad (2.15)$$

Comparing Equations 2.2 and 2.15, we see that the load filter, G_f , effectively “filters” the loads measured in the blocked configuration ($\Phi_{FF,b}$) to represent the loads that would occur at the coupled spacecraft-RW interface ($\Phi_{FF,c}$). For this reason, the name “force filter” was originally coined [10], although it is replaced by “load filter” here, to represent the matrix, G_f , that filters both forces and moments.

Also recall the assumption in Equation 2.4 that the disturbance PSDs dominate the CSDs, allowing us to approximate Equation 2.2 as Equation 2.5. Following this same assumption, the coupled disturbance analysis method in Equation 2.15 can be approximated as:

$$\Phi_{zz}(\omega, \Omega) \approx \sum_{j=1}^6 \Phi_{F_i F_j b}(\omega, \Omega) |G_{f,ii}(\omega)|^2 |G_{ZF,i}(\omega)|^2 \quad (2.16)$$

where $G_{f,ii}$ are the diagonal components of the load filter matrix in 2.8. Analogous to Equation 2.7, the terms $\Phi_{F_i F_b, b}(\omega, \Omega) |G_{f,ii}(\omega)|^2$ represent the *filtered* or *coupled* disturbance PSDs, $\Phi_{F_i F_b, c}(\omega, \Omega)$. Hence using Equation 2.16 in place of Equation 2.5 effectively transforms the experimentally-measured blocked RW disturbances into the disturbances that would occur at the coupled spacecraft-RW interface.

Further, if only scalar accelerances are available and matrix accelerances are not, Equation 2.16 may be further simplified as:

$$\Phi_{zz}(\omega, \Omega) \approx \sum_{j=1}^6 \Phi_{F_i F_b, b}(\omega, \Omega) |\tilde{G}_{f,ii}(\omega)|^2 |G_{ZF_i}(\omega)|^2 \quad (2.17)$$

where $\tilde{G}_{f,ii}$ represents the scalar force and moment filters in Equations 2.13 and 2.14, respectively. As explained above, $G_{f,ii}$ and $\tilde{G}_{f,ii}$ are equivalent only if the acceleration matrices of the spacecraft and RW are diagonal (with off-diagonal components equal to zero). Otherwise, $\tilde{G}_{f,ii}$ is an approximation of $G_{f,ii}$.

One final simplifying assumption may be made. Since translational accelerances are simpler to measure experimentally (using accelerometers) than rotational accelerances, there may be cases in which force filters are available, but moment filters are not. In this case, Equation 2.17 is further approximated by:

$$\begin{aligned} \Phi_{zz}(\omega, \Omega) &\approx \sum_{j=1}^3 \Phi_{F_i F_b, b}(\omega, \Omega) |\tilde{G}_{f,ii}(\omega)|^2 |G_{ZF_i}(\omega)|^2 \\ &+ \sum_{j=4}^6 \Phi_{F_i F_b, b}(\omega, \Omega) |G_{ZF_i}(\omega)|^2 \end{aligned} \quad (2.18)$$

where the moment filters have been set to unity. This equation represents a compromise between the decoupled and coupled methods, since it is coupled in the translational degrees of freedom (forces), but decoupled in the rotational degrees of freedom

(moments). With only translational accelerances (and therefore force filters) available, this approximation may still yield an improvement over the decoupled analysis method.

2.4 Summary and Conclusions

In this chapter, we have:

- provided the motivation for a disturbance analysis method to predict the dynamic performance of a flexible space structure in the presence of reaction wheel vibrational disturbances.
- presented a decoupled disturbance analysis method.
- provided the motivation for a coupled disturbance analysis method.
- derived a coupled disturbance analysis method and highlighted the differences from the decoupled method.

The primary contribution has been the derivation of a new, coupled disturbance analysis method. This method will improve our prediction capability for precision space missions, such as NASA's forthcoming Space Interferometry Mission (SIM), which has very strict tolerances on its optical performance metrics. With this new, high-fidelity method of predicting SIM's optical on-orbit performance prior to launch, we will be able to accurately assess SIM's behavior and to ensure the success of the mission and its ability to achieve scientific goals. The coupled disturbance analysis method has been adopted by the SIM integrated modeling team and may prove to be an invaluable analysis tool in future precision-space-telescope missions.

In the following chapter, we will demonstrate and validate both the decoupled and coupled disturbance analysis methods using representative hardware.

Chapter 3

STRUCTURAL DYNAMIC COUPLING EXPERIMENTS

In Chapter 2, two disturbance analysis methods were presented for predicting the performance of a precision space structure in the presence of reaction wheel (RW) vibrational disturbances. In this chapter, we demonstrate and validate both of these methods using representative hardware. Since these methods were developed to support NASA's forthcoming Space Interferometry Mission (SIM), we will validate the methods using a representative testbed, the Micro-Precision Interferometer (MPI), that was developed specifically to validate technologies for SIM.

In Section 3.1, the MPI testbed is described in detail. Then in Section 3.2, we discuss how some of the values necessary for the disturbance analyses are obtained experimentally or from models. These include all the terms that make up the decoupled and coupled analysis equations (2.2 and 2.15, respectively, or the simplified versions, 2.5 and 2.17-2.18), including the spacecraft and RW accelerances. In Section 3.3, we present the results of the decoupled and coupled disturbance analyses, along with experimentally measured performance metrics for comparison. Finally, in Section 3.4, we present a summary and conclusions for this chapter.

3.1 MPI Testbed

3.1.1 MPI Testbed Description

The Micro-Precision Interferometer (MPI) testbed, shown in Figure 3.1 in its suspended configuration at NASA’s Jet Propulsion Laboratory (JPL), is a scale model of SIM. Like a space-based interferometer, MPI is a lightweight, flexible truss structure with operation-critical dynamics. Active optics, located on the left arm of the $7 \times 7 \times 6.5$ meter boom assembly, are used to measure MPI’s performance in the presence of vibrational disturbances induced by an on-board reaction wheel (RW) at the base of the three booms [19]. In this study, the performance metric of interest is the optical pathlength difference (OPD) between the two paths of the optical interferometer, usually expressed in nanometers.¹ Hence the number, p , of performance metrics, as introduced in Section 2.2, is $p = 1$.

Since the RW is anticipated to be the largest disturbance source on SIM, the MPI disturbance analysis focuses on the load path from the RW vibrational inputs at the base of the three booms to the interferometer’s OPD. The RW, shown hardmounted directly to the MPI base plate in Figure 3.2, is similar to the one used for attitude control on the NASA’s Magellan mission. Although it is sometimes mounted on an isolator for research purposes, this work focuses on the hardmounted configuration shown in Figure 3.2.

3.1.2 MPI Testbed Transfer Functions

While the RW is used to induce cross-correlated, tonal force and moment disturbances to MPI characteristic of those expected to occur on SIM, voice coil shakers, shown in Figure 3.3, are alternatively used to induce “pure,” decoupled, white-noise forces and moments. The shaker assembly subsequently applies known forces along the x , y , and z axes of MPI, and then applies known moments about the x , y , and z axes, while the corresponding OPD is measured in each case. The data are manipulated to provide the six fre-

1. Another metric for MPI is front-end pointing, expressed in milli-arcseconds and measured by a “position sensitive device.” This metric is not considered in this study.

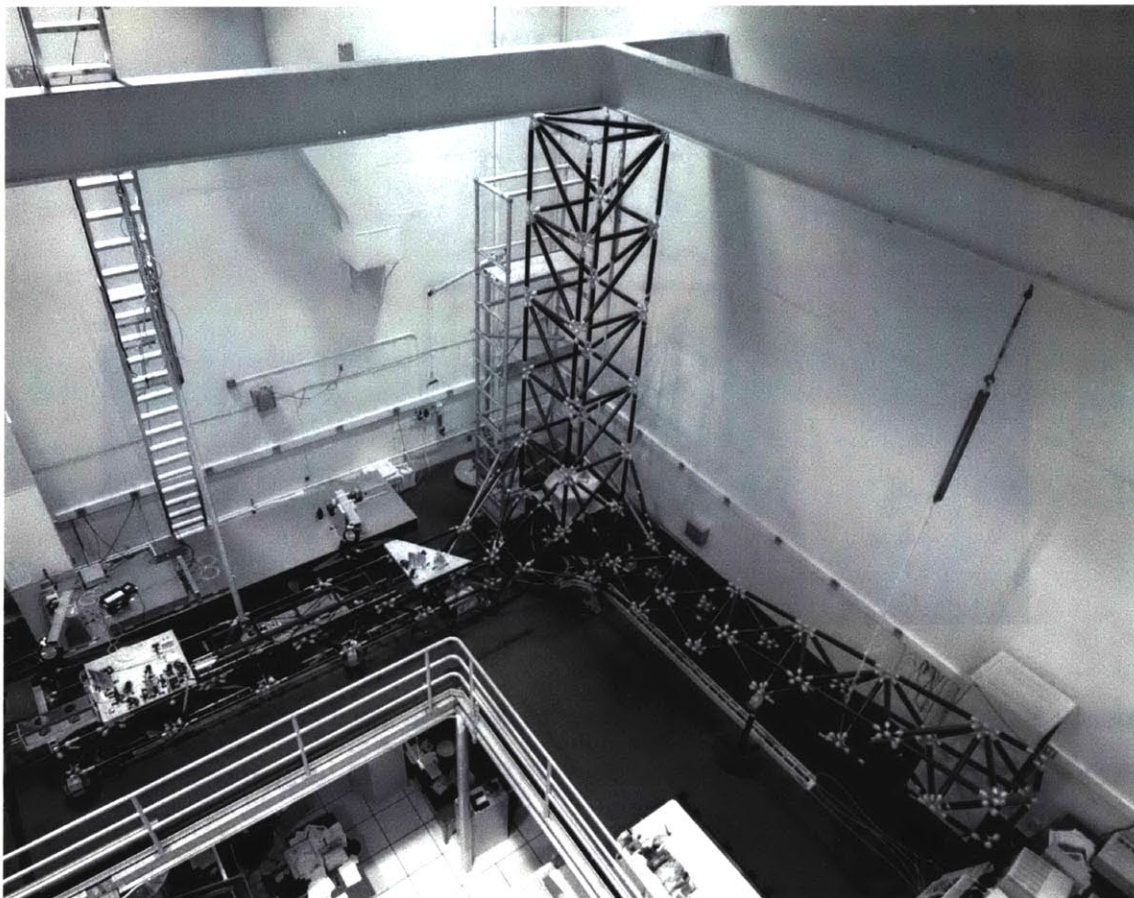


Figure 3.1 The Micro-Precision Interferometer (MPI) Testbed at NASA's Jet Propulsion Laboratory.

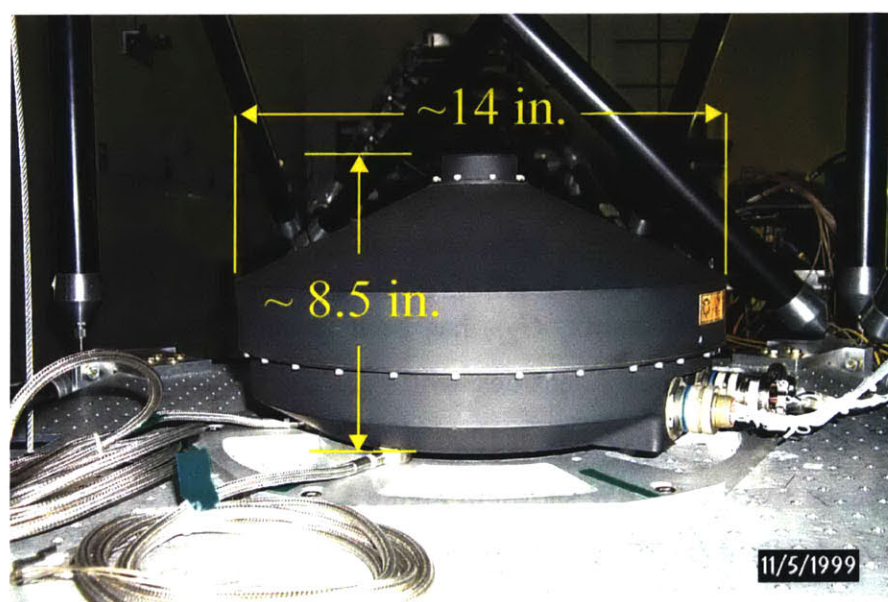


Figure 3.2 RW on the MPI Base Plate.



Figure 3.3 Voice Coil Shakers on the MPI Base.

quency response functions (FRFs) from the six loads to the OPD, respectively. These FRFs make up the six components of the FRF matrix, G_{ZF} , that was introduced in Section 2.2.

The first component of G_{ZF} , the x -force-to-OPD FRF, is shown for MPI in Figure 3.4. Low-frequency suspension modes are visible, along with higher-frequency, modally dense flexible modes of the MPI system.

3.2 Intermediate Results

3.2.1 Hardmounted Reaction Wheel Disturbance Spectra

Once the transfer function matrix, G_{ZF} , has been characterized, we must obtain the blocked RW disturbance spectral densities, which are a necessary component of both the decoupled and coupled analysis methods (Equations 2.2 and 2.15, respectively). To obtain these disturbance spectra, the RW shown in Figure 3.2 is mounted to a rigid “block” and spun, while load cells at the RW-block interface measure the resulting interface forces and moments.

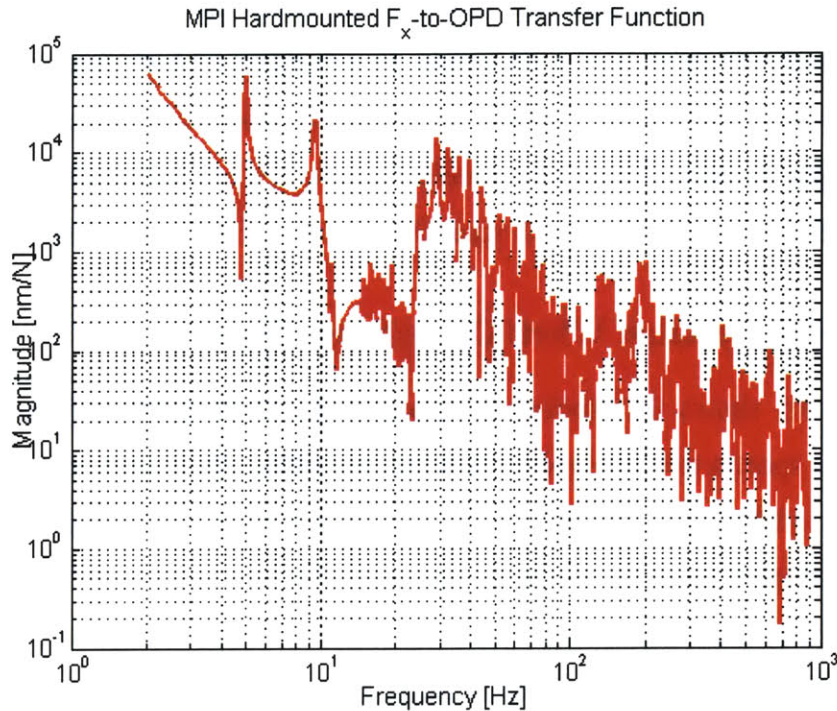


Figure 3.4 MPI FRF: x -Force-to-OPD.

The wheel is “ramped up” from zero rotations-per-minute (RPM) to ~ 4800 RPM at a rate of ~ 2.5 RPM/sec. The resulting force and moment time histories measured by the load cells are then divided into three-second time “slices,” each of which is used to represent a “pseudo-steady” rotation rate of the wheel (taken as the average wheel speed of that time slice).

Next, the disturbance spectral density matrices are calculated in the frequency domain, yielding a frequency-dependent matrix, $\Phi_{FF,b}(\omega)$, for each time slice’s average wheel speed, Ω . This set of matrices forms a discretized approximation of the frequency- and wheel-speed-dependent spectral density matrix, $\Phi_{FF,b}(\omega, \Omega)$, introduced in Chapter 2.

Figure 3.5 shows five of the six diagonal components of the blocked spectral density matrix (the power spectral densities, or PSDs)¹, scaled to represent the actual amplitudes

1. The sixth disturbance, the moment about the reaction wheel’s spin axis, is much smaller in magnitude than these five disturbances, and is therefore not depicted here.

of the disturbances. For instance, the first plot represents the amplitude spectrum of the measured disturbance force along the x -axis, as a function of both frequency and wheel spin-rate. Clearly visible in the disturbance spectra are a primary harmonic disturbance at the wheel's spin frequency, higher harmonic disturbances at non-integer multiples of the wheel's spin frequency, and structural resonances of the wheel at constant frequencies [6].

3.2.2 On-MPI Reaction Wheel Disturbance Spectra

While Figure 3.5 shows the blocked disturbance amplitude spectra, it is interesting to compare these spectra to the *coupled* disturbance spectra, $\Phi_{FF,c}(\omega)$, measured with the RW mounted to MPI. Because MPI is an accessible testbed, we have the luxury of measuring these coupled spectra. We note, however, that this would not be possible for an actual flight program. Hence these measurements will demonstrate the importance of “correcting” the blocked disturbances to yield the coupled disturbances, even when the coupled disturbances cannot be measured directly.

Figure 3.6 shows the corresponding diagonal components (PSDs) of the coupled spectral density matrix, scaled to represent the actual amplitudes of the disturbances. It is not surprising to find that the structural resonances of the RW shift in frequency; it is interesting to find that they shift to *higher* frequencies. Also, the harmonic disturbances have changed in both frequency and magnitude. This supports our claim that the hardmounted boundary conditions imposed on an RW during disturbance testing cause the measured (blocked) disturbances to differ from the true coupled disturbances that occur when the RW is mounted to a structure.

3.2.3 MPI Accelerances

Three different methods were attempted to characterize the accelerances of MPI:

- experimental techniques using impulse tap tests,
- experimental techniques using electromechanical “shaker” tests, and
- modeling techniques using the finite element method.

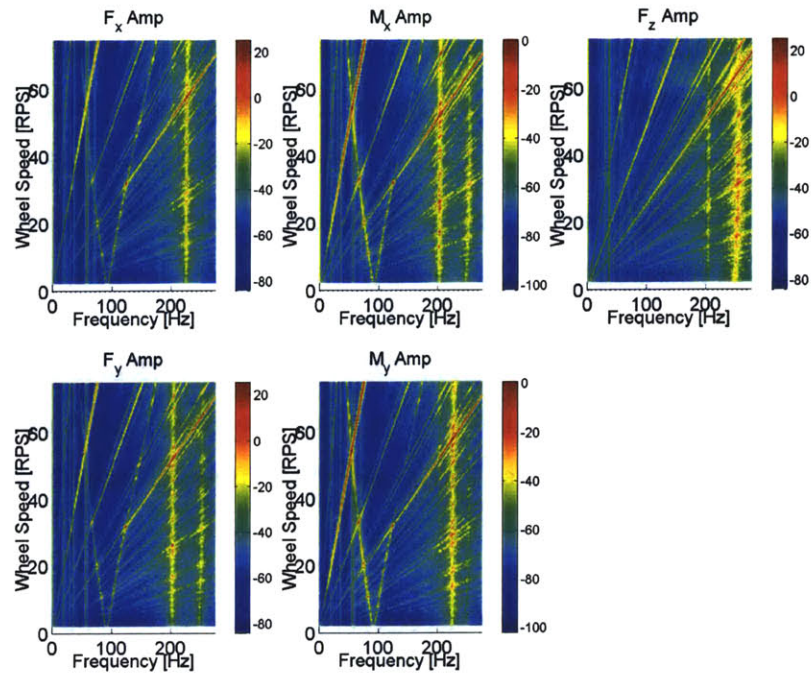


Figure 3.5 Magellan RW: Blocked Disturbance Amplitude Spectra

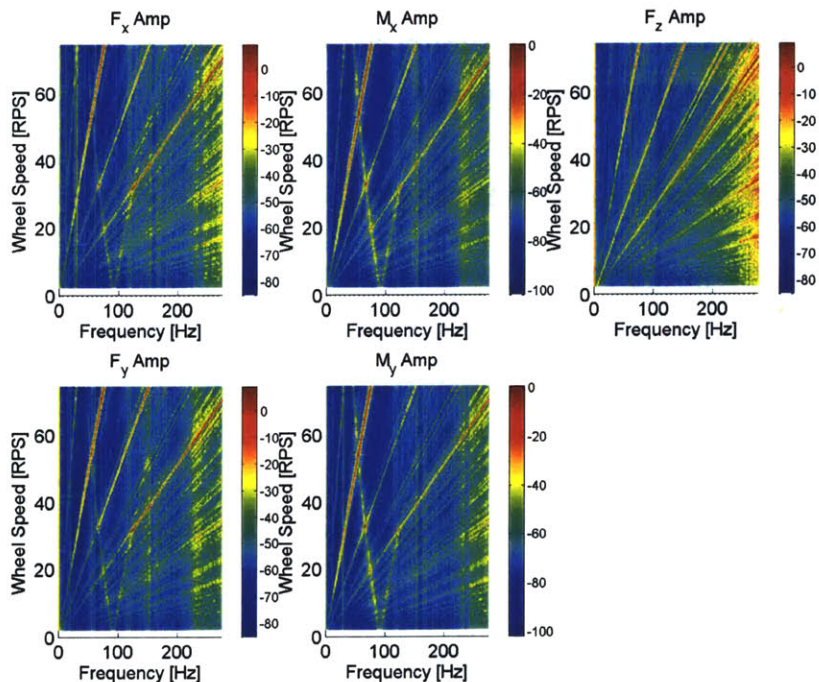


Figure 3.6 Magellan RW: Coupled Disturbance Amplitude Spectra

The experimental techniques involved applying known disturbances to MPI at its interface point with the RW and measuring the resulting acceleration of MPI at the interface. The disturbances were applied first using an impulse hammer, and later using an electromechanical “shaker” device. Because of various issues associated with noise and the corruption of the data, the experimental techniques were abandoned [29], and the finite element modeling technique was adopted.

The MPI translational accelerances, $A_{MPI,ii}$ for $i = 1, 2, 3$, were thus characterized using a finite element model (FEM) of MPI. An existing Integrated Modeling of Optical Systems (IMOS) model of MPI was used to generate the x , y , and z translational accelerances shown in Figure 3.7.

The magnitudes of the FEM-generated accelerances appear reasonable. Treating the MPI as a rigid body at low frequency, we expect its acceleration to tend toward the inverse of its mass. Since the MPI mass is ~ 500 kg, its low-frequency acceleration should tend toward $2 \cdot 10^{-3}$ kg $^{-1}$. The FEM-based accelerances are consistent with this, particularly the x -axis translational acceleration. The MPI rotational accelerances can be generated from the MPI FEM, as well. They are shown in Figure 3.8.

3.2.4 Reaction Wheel Accelerances

As for MPI, both experimental and modeling techniques were attempted to characterize the accelerances of the reaction wheel. For reasons similar to MPI, the measurement techniques for characterizing the RW’s accelerances didn’t prove successful, so modeling techniques were adopted instead.

In the following two subsections, the RW accelerances are characterized in two different ways:

- using a zero-spin rigid-body model, and
- using a spinning-flywheel (gyroscopic) rigid-body model.

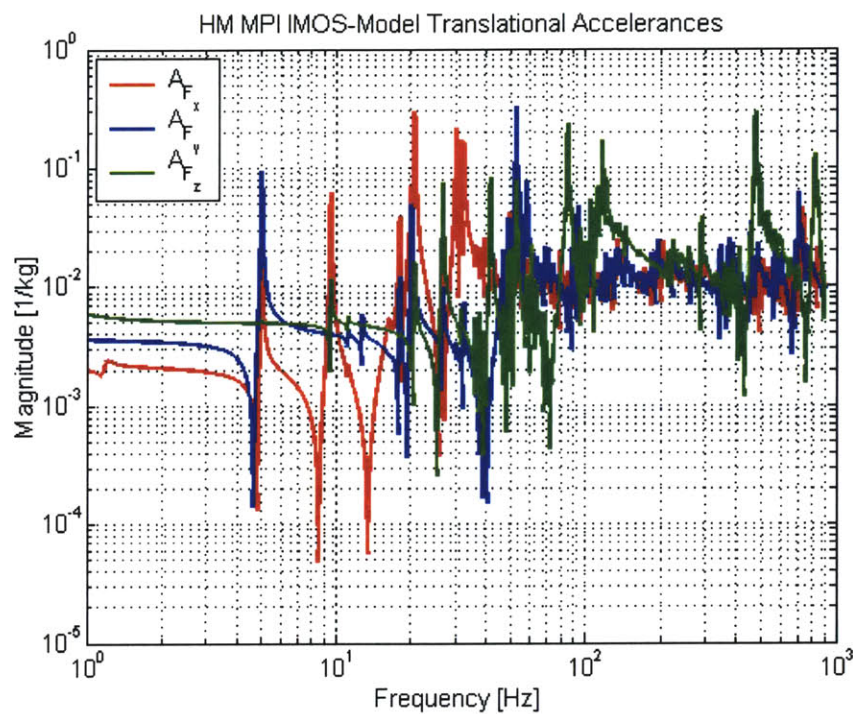


Figure 3.7 MPI FEM-Predicted Translational Accelerances.

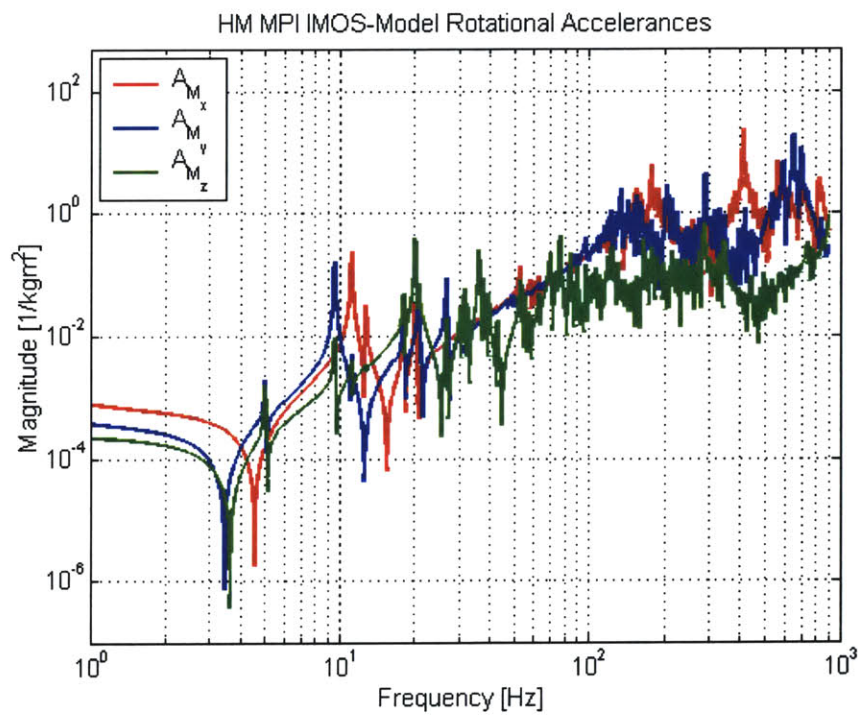


Figure 3.8 MPI FEM-Predicted Rotational Accelerances.

“Zero-Spin” Rigid-Body Model

The RW may be approximated as a rigid body with the equation of motion along each translational axis ($i = 1, 2, 3$):

$$f_i(t) = m_{RW} \ddot{q}_i(t) \quad (3.1)$$

where f_i is the force acting on the RW along its i^{th} axis, m_{RW} is the RW mass, and \ddot{q}_i is the RW acceleration along the i^{th} axis. From Equation 3.1, we find the RW translational accelerances along the x , y , and z axes are:

$$A_{RW,ii}(\omega) = \frac{\ddot{Q}_i(\omega)}{F_i(\omega)} = \frac{1}{m_{RW}} \quad (3.2)$$

where $\ddot{Q}_i(\omega)$ and $F_i(\omega)$ are the Fourier transforms of $\ddot{q}_i(t)$ and $f_i(t)$, respectively.

Substituting the RW accelerances into Equation 2.13 yields the force filters for $i = 1, 2, 3$:

$$\frac{F_{c,i}}{F_{b,i}} = \frac{1}{1 + m_{RW} A_{MPI,ii}} \quad (3.3)$$

The RW translational accelerances, based on Equation 3.2 and the measured RW mass (8.885 kg), are shown in Figure 3.9. Since they are frequency-independent, they have constant magnitudes equal to the inverse of the RW mass.

The RW rotational accelerances can also be generated from a rigid-body model, with the following rotational equation of motion about each axis ($i = 4, 5, 6$):

$$m_i(t) = I_{RW,ii} \ddot{\theta}_i(t) \quad (3.4)$$

where m_i is the moment acting on the RW about its i^{th} axis, $I_{RW,ii}$ is the RW mass moment of inertia about its i^{th} axis, and $\ddot{\theta}_i$ is the RW angular acceleration about its i^{th} axis. From Equation 3.4, we find the RW rotational accelerances about the x , y , and z axes are:

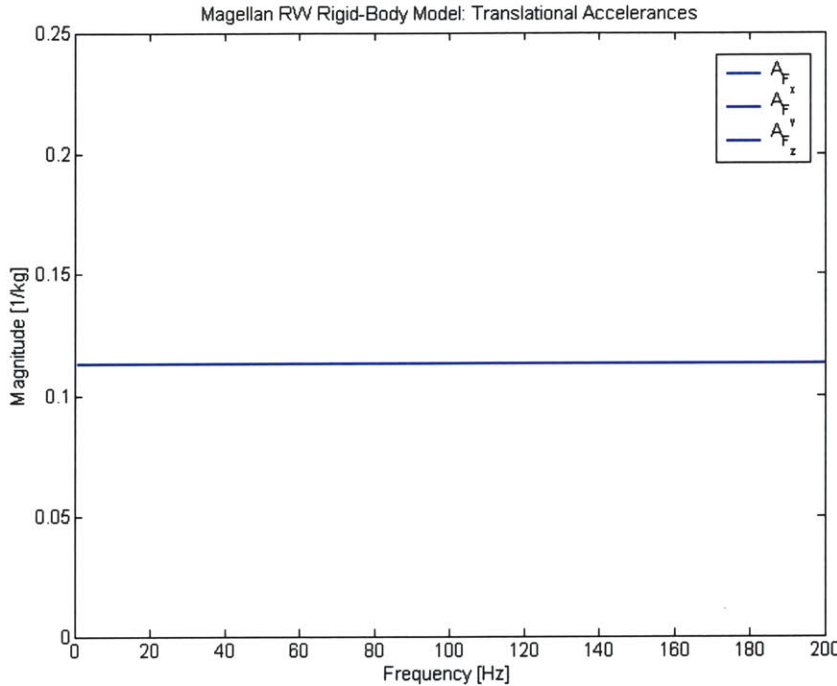


Figure 3.9 RW Rigid-Body-Model Translational Accelerances.

$$A_{RW, ii} = \frac{\ddot{\Theta}_i(\omega)}{M_i(\omega)} = \frac{1}{I_{RW, ii}} , \quad i = 4, 5, 6 \quad (3.5)$$

where $\ddot{\Theta}_i(\omega)$ and $M_i(\omega)$ are the Fourier transforms of $\ddot{\theta}_i(t)$ and $m_i(t)$, respectively.

Thus in order to calculate the RW's *driving-point* rotational accelerances using Equation 3.5, we must determine its moments of inertia, $I_{RW, ii}$, about principal coordinate axes originating at the RW-MPI interface point. Since inertia information is not available from the RW manufacturer, the inertias are estimated from a constant-mass-density model.

From Figure 3.2, we see the Magellan RW lies somewhere between a cylindrical and conical shape. We can thus estimate the RW inertia by averaging the inertias of a cylinder and a cone with similar mass and dimensions to the RW. For the cylinder in Figure 3.10(a), the moments of inertia about axes at the origin are:

$$\begin{aligned}
 I_{xx} &= \frac{m}{12}(3r^2 + 4h^2) \\
 I_{yy} &= \frac{m}{12}(3r^2 + 4h^2) \\
 I_{zz} &= \frac{m}{2}r^2
 \end{aligned} \tag{3.6}$$

and for the cone in Figure 3.10(b),

$$\begin{aligned}
 I_{xx} &= \frac{m}{20}(3r^2 + 2h^2) \\
 I_{yy} &= \frac{m}{20}(3r^2 + 2h^2) \\
 I_{zz} &= \frac{3}{10}mr^2
 \end{aligned} \tag{3.7}$$

Substituting the RW mass (8.885 kg) and dimensions (depicted in Figure 3.2) into 3.6 and 3.7 and averaging the cylindrical and conical values, we obtain the RW inertia estimates listed in Table 3.1. Although these values are approximate, any influence they might have will motivate the measurement of more accurate values or the direct measurement of the RW rotational accelerances.

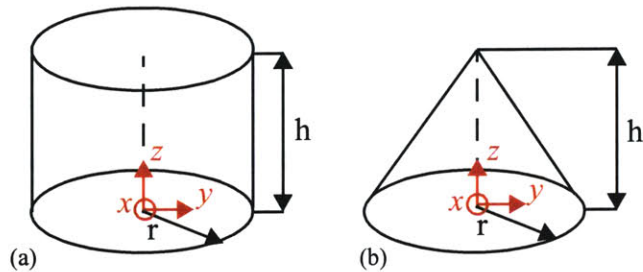


Figure 3.10 Shapes Used to Estimate the Magellan RW's Mass Moments of Inertia: (a) Cylinder and (b) Cone.

TABLE 3.1 Estimated Mass Moments of Inertia [kg·m²] for the Magellan RW.

$I_{RW,44}, I_{RW,55}$	0.1459
$I_{RW,66}$	0.1124

The RW rotational accelerances, based on Equation 3.5 and the inertias in Table 3.1, are shown in Figure 3.11. Since they are frequency-independent, they appear as constant lines, with magnitudes equal to the inverse of the RW inertias.

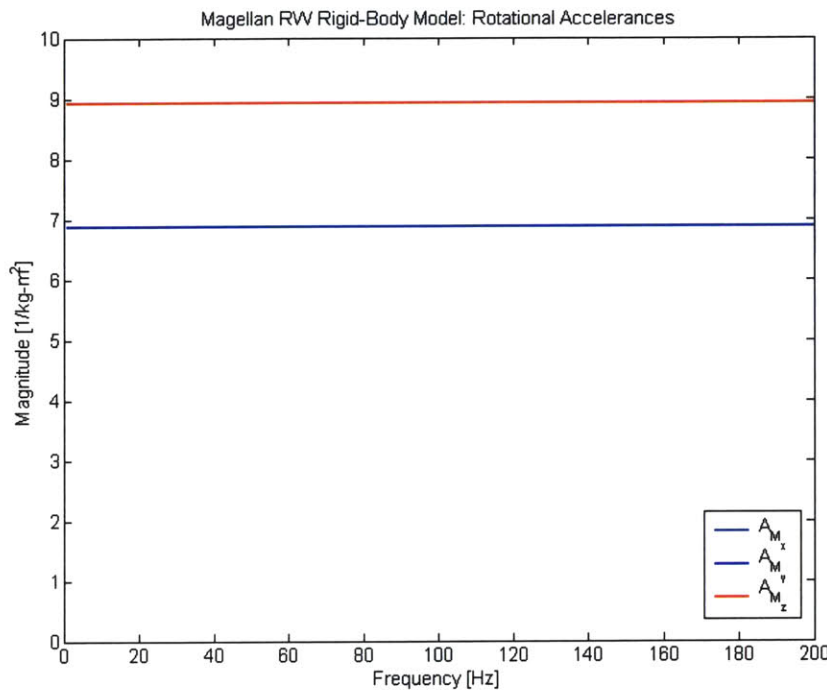


Figure 3.11 RW Rigid-Body-Model Rotational Accelerances.

Spinning-Flywheel (Gyroscopic) Rigid-Body Model

In the “zero-spin,” rigid-body model of the RW above, the RW was modeled as a non-spinning, rigid wheel. In reality, the spinning of the flywheel about its spin axis will introduce nonlinear, gyroscopic dynamics that will influence the RW’s acceleration. In order to capture these dynamics in the load filter, we must first capture them in the RW acceleration model. Hence we create a higher-fidelity model of the RW that includes its nonlinear rotational dynamics.

Consider the symmetric, rigid, spinning flywheel in Figure 3.12. Its rotational equations of motion about the radial axes are:

$$\begin{bmatrix} I_{rr} & 0 \\ 0 & I_{rr} \end{bmatrix} \begin{Bmatrix} \ddot{\theta}_x \\ \ddot{\theta}_y \end{Bmatrix} + \begin{bmatrix} 0 & \Omega(I_{zz} - I_{rr}) \\ -\Omega(I_{zz} - I_{rr}) & 0 \end{bmatrix} \begin{Bmatrix} \dot{\theta}_x \\ \dot{\theta}_y \end{Bmatrix} = \begin{Bmatrix} m_x \\ m_y \end{Bmatrix} \quad (3.8)$$

where I_{rr} is the mass moment of inertia about the radial axes, I_{zz} is the mass moment of inertia about the spin axis, θ_x and θ_y are the angular rotations about the x and y axes, respectively, Ω is the flywheel spin-rate about the spin axis, and m_x and m_y are external moments applied about the x and y axes, respectively. Notice the skew-symmetric damping matrix with two off-diagonal, wheel-speed-dependent terms, $\pm\Omega(I_{zz} - I_{rr})$. These are the gyroscopic terms of interest.

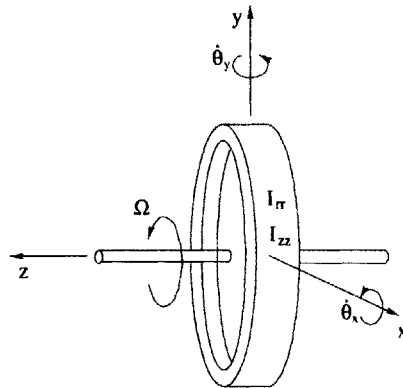


Figure 3.12 Rigid Flywheel Model.

Taking the Fourier Transform of 3.8, using 2.11 to write velocities in terms of accelerations, and collecting terms,

$$\begin{bmatrix} I_{rr} & \frac{\Omega(I_{zz} - I_{rr})}{j\omega} \\ \frac{-\Omega(I_{zz} - I_{rr})}{j\omega} & I_{rr} \end{bmatrix} \begin{Bmatrix} \ddot{\theta}_x \\ \ddot{\theta}_y \end{Bmatrix} = \begin{Bmatrix} M_x \\ M_y \end{Bmatrix} \quad (3.9)$$

Equation 3.9 can now be solved to yield the flywheel's rotational accelerations in terms of the moments:

$$\begin{Bmatrix} \ddot{\Theta}_x \\ \ddot{\Theta}_y \end{Bmatrix} = \begin{bmatrix} I_{rr} & \frac{\Omega(I_{zz} - I_{rr})}{j\omega} \\ \frac{-\Omega(I_{zz} - I_{rr})}{j\omega} & I_{rr} \end{bmatrix}^{-1} \begin{Bmatrix} M_x \\ M_y \end{Bmatrix} \quad (3.10)$$

so that the coupled *rotational accelerance* of the wheel about its x - and y -axes is:

$$\begin{bmatrix} I_{rr} & \frac{\Omega(I_{zz} - I_{rr})}{j\omega} \\ \frac{-\Omega(I_{zz} - I_{rr})}{j\omega} & I_{rr} \end{bmatrix}^{-1} = \frac{1}{I_{rr}^2 - \left[\left(\frac{\Omega}{\omega} \right) (I_{zz} - I_{rr}) \right]^2} \begin{bmatrix} I_{rr} & \frac{-\Omega(I_{zz} - I_{rr})}{j\omega} \\ \frac{\Omega(I_{zz} - I_{rr})}{j\omega} & I_{rr} \end{bmatrix} \quad (3.11)$$

We would like to substitute this accelerance in place of the expression in Equation 3.5 (for $i = 4, 5$), which does *not* include gyroscopic effects. However, the accelerances in Equation 3.5 are scalar approximations of the diagonals of the accelerance matrix (for $i = 4, 5$). Hence we approximate the RW accelerance in Equation 3.11 as having only its diagonal terms.¹ We recognize that these diagonal terms are an improvement over the RW rotational accelerances in Equation 3.5, since they now depend on RW wheel-speed.

From Equations 3.10 and 3.11, if only M_x is applied, the rotational accelerance about the x -axis is:

$$\boxed{\frac{\ddot{\Theta}_x}{M_x} = \frac{I_{rr}}{I_{rr}^2 - \left[\left(\frac{\Omega}{\omega} \right) (I_{zz} - I_{rr}) \right]^2}} \quad (3.12)$$

and if only M_y is applied, the rotational accelerance about the y -axis is:

$$\boxed{\frac{\ddot{\Theta}_y}{M_y} = \frac{I_{rr}}{I_{rr}^2 - \left[\left(\frac{\Omega}{\omega} \right) (I_{zz} - I_{rr}) \right]^2}} \quad (3.13)$$

1. A separate study confirmed that the off-diagonal terms are not highly influential here.

These “gyroscopic” rotational accelerances depend on both frequency and wheel speed, as expected. When the wheel is at rest ($\Omega = 0$), it is easily shown that Equations 3.12 and 3.13 reduce to Equation 3.5 (for $i = 4, 5$), the RW rotational accelerances *without* gyroscopic effects. It is also interesting to note that when $I_{zz} \approx I_{rr}$, the same phenomenon occurs.

3.2.5 Performance Measurements

Finally, we seek to experimentally measure the performance of the structure, yielding a metric by which to assess the decoupled and coupled disturbance analysis predictions. The RW is simply mounted in its location on MPI, as shown in Figure 3.2, and spun at various wheel speeds, as is done for the blocked and coupled disturbance measurements.¹ The OPD is measured while the RW “ramps up” from 0 to ~ 4800 RPM at a rate of ~ 2.5 RPM/sec. The OPD time history is then divided into three-second time slices and its power spectral density, $\Phi_{zz}(\omega)$, is calculated for each “pseudo-steady” RW spin rate, Ω . Analogous to the RW disturbance spectral density matrix, this yields a discretized approximation to the OPD spectral density, $\Phi_{zz}(\omega, \Omega)$, that is both frequency- and wheel spin-rate-dependent.

Finally, Equation 2.3 is used to calculate the resulting root-mean-square (RMS), $\sigma_z(\Omega)$, of the OPD as a function of the wheel’s spin rate. This result will be shown along with the OPD performance predictions in the following section, and will be used to assess the accuracy of both the decoupled and coupled disturbance analysis methods.

1. In fact, the coupled disturbance measurements presented in Section 3.2.2 are acquired simultaneously with these performance measurements.

3.3 Performance Predictions

3.3.1 Decoupled Analysis

For each wheel speed, Ω , the OPD spectrum, Φ_{ZZ} , is predicted using Equation 2.5, and its RMS is calculated using Equation 2.3. Figure 3.13 shows the *predicted* and *measured* OPD RMS, both as functions of wheel speed.

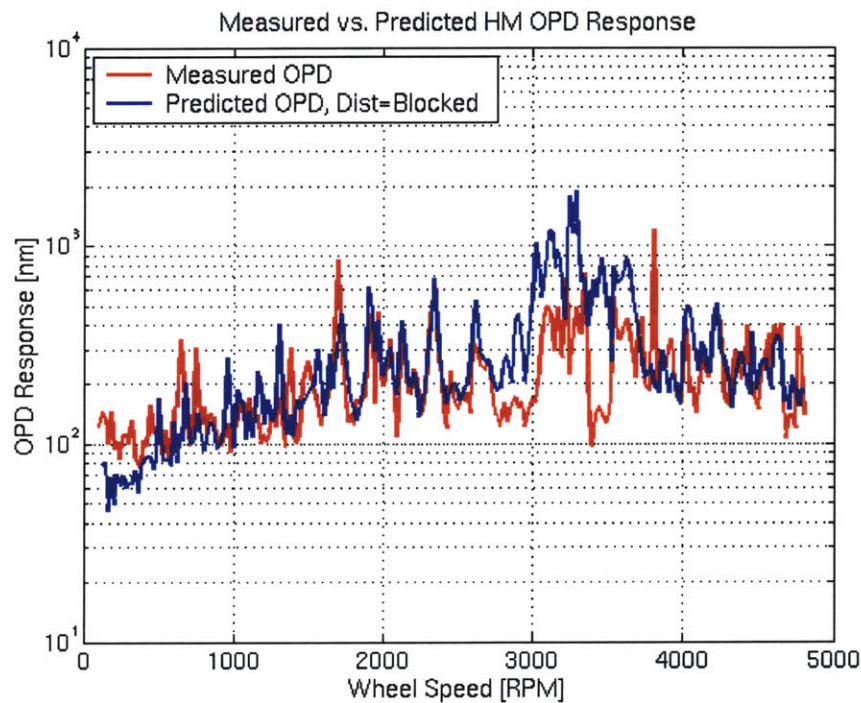


Figure 3.13 Measured Versus Predicted OPD Using Blocked RW Disturbances.

Previous MPI predictions have overbounded measurements by up to a factor of four, significantly more than shown in Figure 3.13. Recent hardware modifications have stiffened the MPI-RW interface, both *decreasing* the amount of overprediction and *confining* it to the range of wheel speeds between 2700 and 3700 revolutions per minute (RPM). This confirms that dynamic coupling may be the critical aspect neglected by the decoupled method, since stiffening the interface effectively decreased the dynamic coupling between the two bodies and improved the prediction. Another indication that coupling is a concern is the fact that the OPD predicted using *coupled* disturbances, measured with the RW

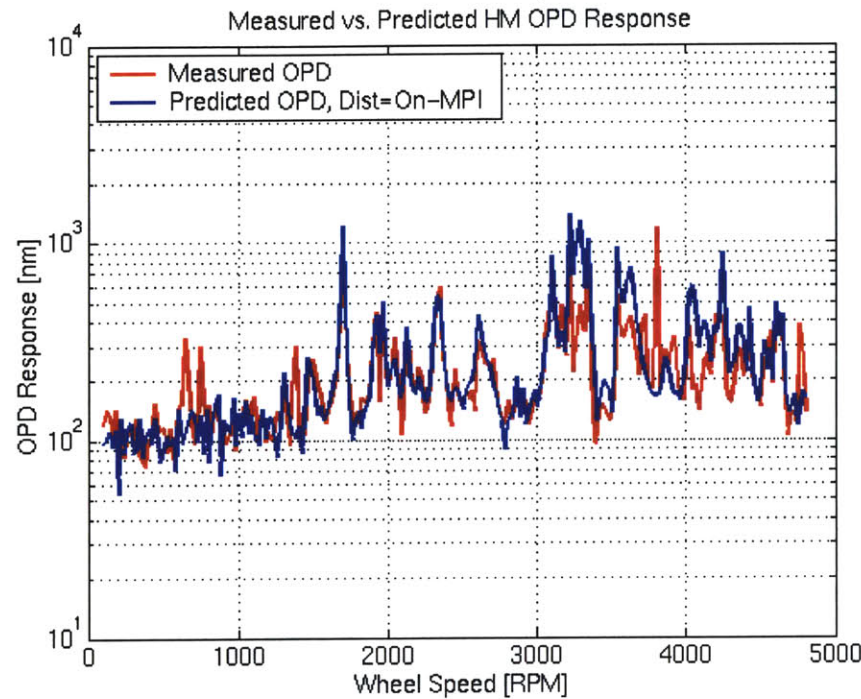


Figure 3.14 Measured Versus Predicted OPD Using Coupled RW Disturbances.

mounted to MPI, in place of *blocked* disturbances yields much better results. Figure 3.14 shows that using the *coupled* disturbances eliminates the overprediction at 2700-3200 and 3400-3500 RPM.

However, since there are still local regions in Figure 3.14 (such as 3200-3400 and 3500-3700 RPM) where the analysis overpredicts the measurement, we consider other potential error sources. Aside from neglecting coupling, the disturbance analysis method in Equation 2.5 makes other mathematical and physical approximations, such as neglecting the off-diagonal disturbance CSD terms in Equation 2.2. Additionally, Equation 2.5 fails to account for the gyroscopic stiffening dynamics of the spinning RW.

3.3.2 Coupled Analysis Using “rigid-RW, model3-MPI” Filters

In order to test the coupled analysis theory, Equations 2.13 and 2.18 were implemented on MPI. The RW translational accelerances were modeled as those of a non-spinning rigid-

body, and the MPI translational accelerances were modeling using a finite element model of MPI. The rotational accelerances were neglected in this analysis.

The RW and MPI translational accelerances are substituted into Equation 3.3 to yield the three translational force filters shown in Figure 3.15. Because the filters are defined as ratios of coupled to blocked disturbances, their magnitudes are less than unity where the blocked loads *overpredict* the coupled ones, and greater than unity where the blocked loads *underpredict* the coupled ones. These filters are called the “rigid-RW, model3-MPI” filters because they are based on the zero-spin, rigid-body model of the RW accelerances and the FEM-based model of the MPI accelerances. (The “3” in the filter name refers to the fact that we are filtering the three forces, but not the moments. Hence this analysis is coupled in the translational degrees of freedom (DOF) only, using Equation 2.18 as an approximation to Equation 2.17.)

The “rigid-RW, model3-MPI” filters are now used to perform a coupled disturbance analysis for MPI. The resulting coupled OPD prediction is shown in Figure 3.16, along with the decoupled prediction from Section 3.3.1 and the measured OPD from Section 3.2.5.

Recall from Section 3.3.1 that the region of concern (where the decoupled analysis over-predicts the measurements) is 2700-3700 RPM. Figure 3.16 demonstrates that the coupled prediction makes significant improvements to the decoupled prediction between 3050 and 3200 RPM, as well as between 3380 and 3520 RPM.

3.3.3 Coupled Analysis Using “rigid-RW, model6-MPI” Filters

We now investigate whether including the rotational “moment” filters (using Equation 2.17 instead of Equation 2.18) yields an additional improvement to the performance prediction. Recall from Equation 2.14 that moment filters are formed from the ratio of RW-to-MPI rotational accelerances. We will calculate the moment filters using the zero-spin rigid-body model of the RW rotational accelerances, and the FEM-based model of the MPI rotational accelerances.

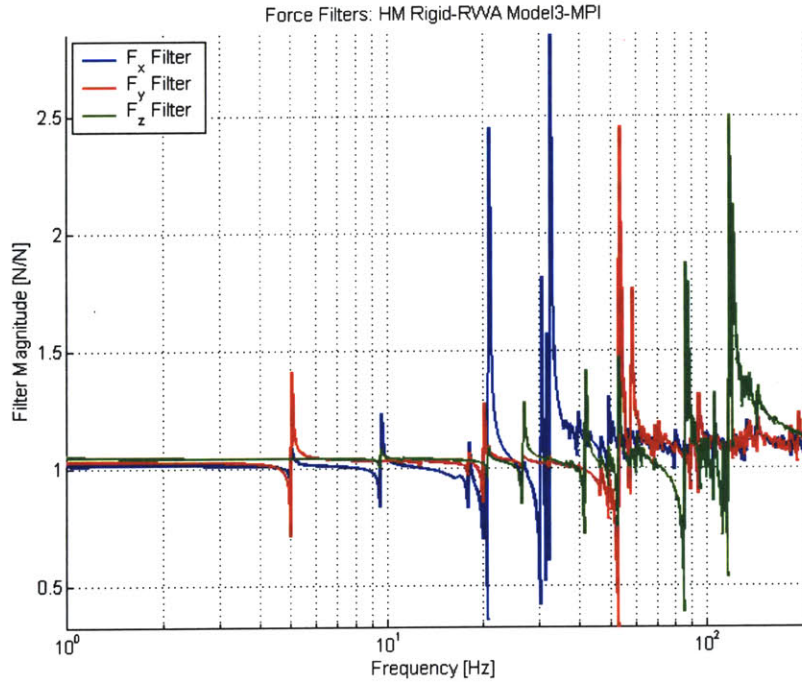


Figure 3.15 Translational “rigid-RW, model3-MPI” Force Filters.

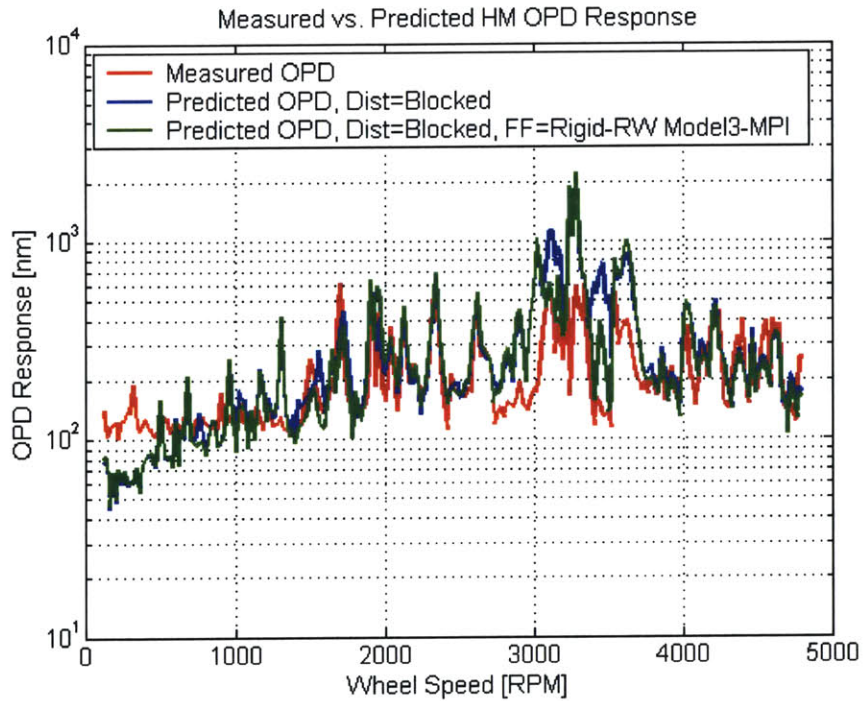


Figure 3.16 Measured Versus Predicted OPD Using Blocked RW Disturbances and “rigid-RW, model3-MPI” Filters.

The resulting moment filters, based on the rigid-body-model RW accelerance and FEM-based MPI accelerance, are shown in Figure 3.17, and are referred to as “rigid-RW, model6-MPI” filters. (The “6” in the filter name refers to the fact that we are filtering all six degrees of freedom: moments, as well as forces.)

Figure 3.18 shows the resulting coupled OPD prediction, using both the “rigid-RW, model3-MPI” *force* filters and the “rigid-RW, model6-MPI” *moment* filters. This prediction is compared to both the decoupled prediction from Section 3.3.1 and the measured OPD from Section 3.2.5. The predictions due to the three-DOF and six-DOF filters in Figures 3.16 and 3.18, respectively, appear virtually indistinguishable, *indicating that the use of moment filters, in addition to the force filters, does not yield a significant improvement to the performance prediction when the gyroscopic dynamics of the RW are not included in its accelerance model.*

3.3.4 Coupled Analysis Using “rigid-gyro-RW, model6-MPI” Filters

In Sections 3.3.2 and 3.3.3, we used the non-spinning, rigid-body model of the RW to estimate its accelerance. Therefore both the RW accelerance and the resulting force and moment filters were independent of the spin rate of the RW. We now use the spinning-flywheel (gyroscopic) rigid-body model of the RW to estimate its accelerance. The resulting moment filters will then also be dependent on the RW’s spin rate.

Capturing the gyroscopic dynamics of the spinning RW in the RW accelerance model was motivated by what we call “empirical filters,” in which we calculate the ratio of *measured coupled disturbances* (with the RW mounted on MPI) to *measured blocked disturbances* (with the RW mounted to a rigid surface). (This is equivalent to calculating G_f using Equation 2.6 with measured values of $F_c(\omega, \Omega)$ and $F_b(\omega, \Omega)$.) Using experimental data, these empirical filters represent what we are trying to calculate using Equation 2.8 with accelerance estimates of MPI and the RW. As shown in Appendix A, the resulting moment filters appear to be dependent on the wheel’s spin rate. Hence we attempt to cap-

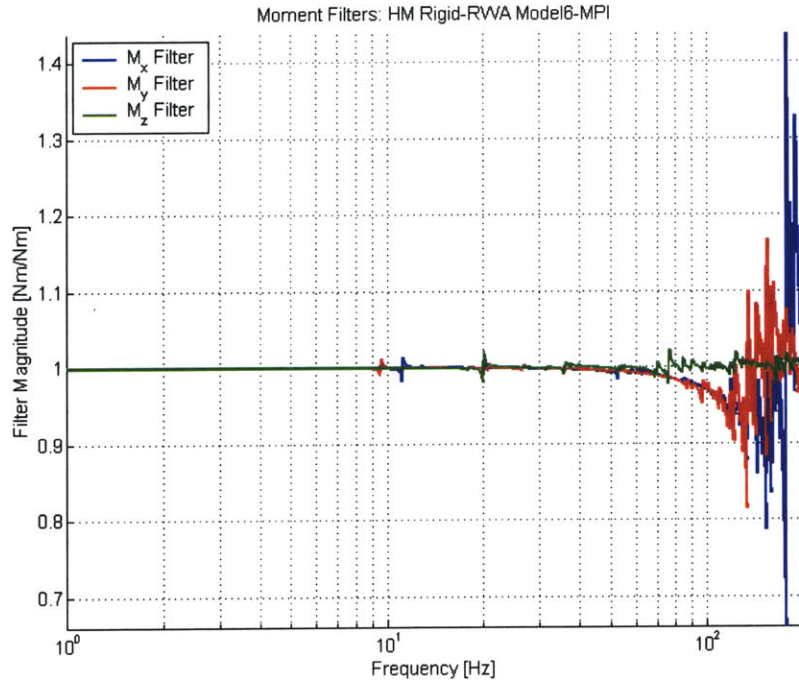


Figure 3.17 Rotational “rigid-RW, model6-MPI” Moment Filters.

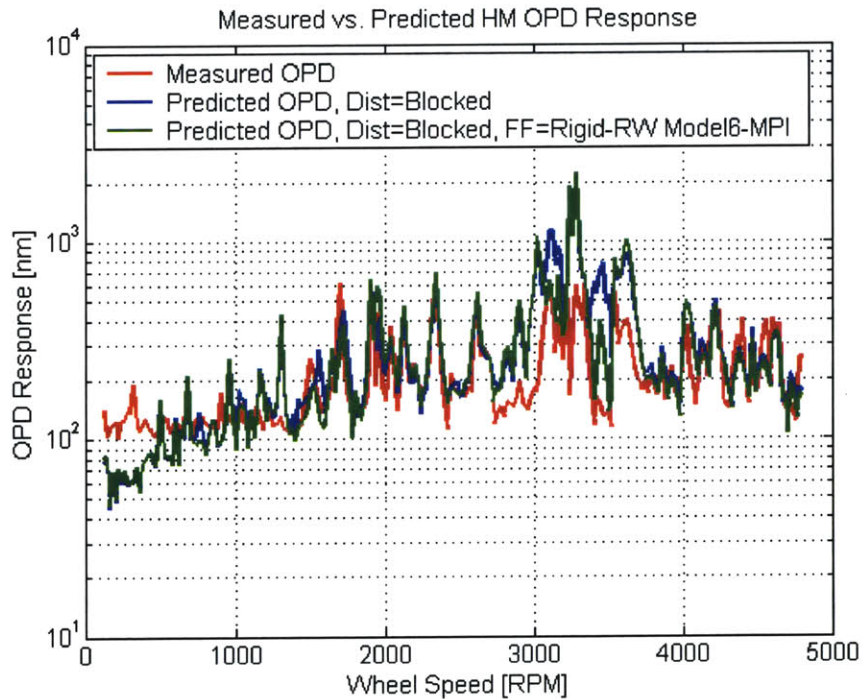


Figure 3.18 Measured Versus Predicted OPD Using Blocked RW Disturbances and “rigid-RW, model6-MPI” Force and Moment Filters.

ture a wheel-spin-rate dependence in the RW acceleration model (as shown in Equations 3.12 and 3.13), and therefore in the moment filters.

Substituting Equations 3.12 and 3.13 into Equation 2.14, along with the MPI FEM-based rotational accelerances, yields the “rigid-gyro-RW, model6-MPI” moment filters that *include the RW’s gyroscopic dynamics* and therefore depend on both frequency and wheel-spin rate, but neglect cross-axis terms. The resulting moment filters are shown in Figure 3.19. Although their dependence on the wheel’s spin rate is visible (especially at low frequencies), the filters are dominated by behavior that is independent of the spin rate. As explained on page 40, this is due in large part to the fact that the radial-axis and spin-axis inertias of this RW are fairly close in magnitude, as shown in Table 3.1. When these values are slightly more distinct, the wheel-speed dependence of the filters becomes very obvious.

Figure 3.20, shows the coupled prediction using both the “rigid-RW, model3-MPI” *force* filters and the “rigid-gyro-RW, model6-MPI” *moment* filters. This coupled prediction is compared to both the decoupled prediction from Section 3.3.1 and the measured OPD from Section 3.2.5. The predictions due to the three-DOF and six-DOF-gyroscopic filters in Figures 3.16 and 3.20, respectively, appear virtually indistinguishable, indicating that, for this system, *the use of moment filters, even those including the RW’s nonlinear, gyroscopic dynamics, does not yield a significant improvement to the performance prediction* when compared to the use of only force filters.

We note that for an RW with a very different ratio of inertias, or for an RW that spins at much faster spin rates than those considered here, the gyroscopic dynamics may become influential. Hence although they may be neglected in the present results, we have developed an analysis method that includes these dynamics in case they are influential in other systems. It would also be useful in the future to develop a non-dimensional parameter (or set of parameters) to characterize the influence of the RW gyroscopic dynamics on a given

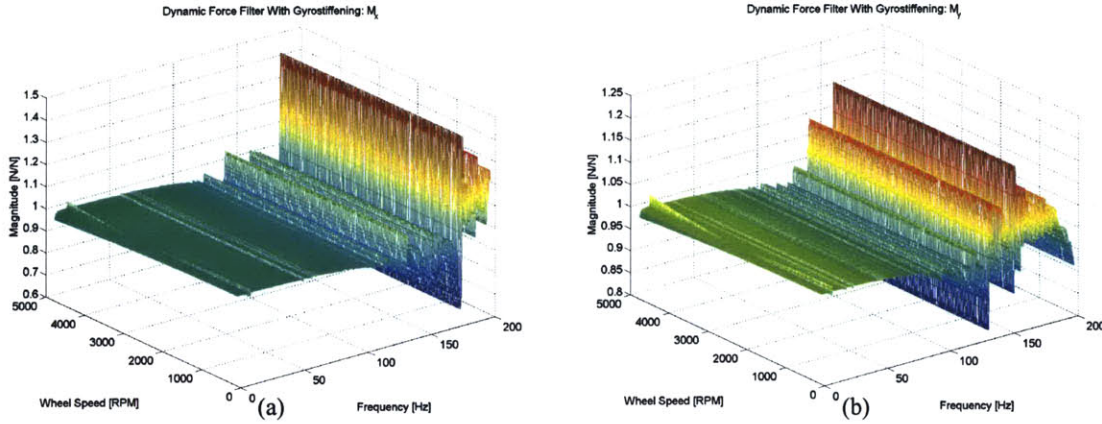


Figure 3.19 “Rigid-gyro-RW, model6-MPI” Moment Filters: (a) M_x Filter and (b) M_y Filter.

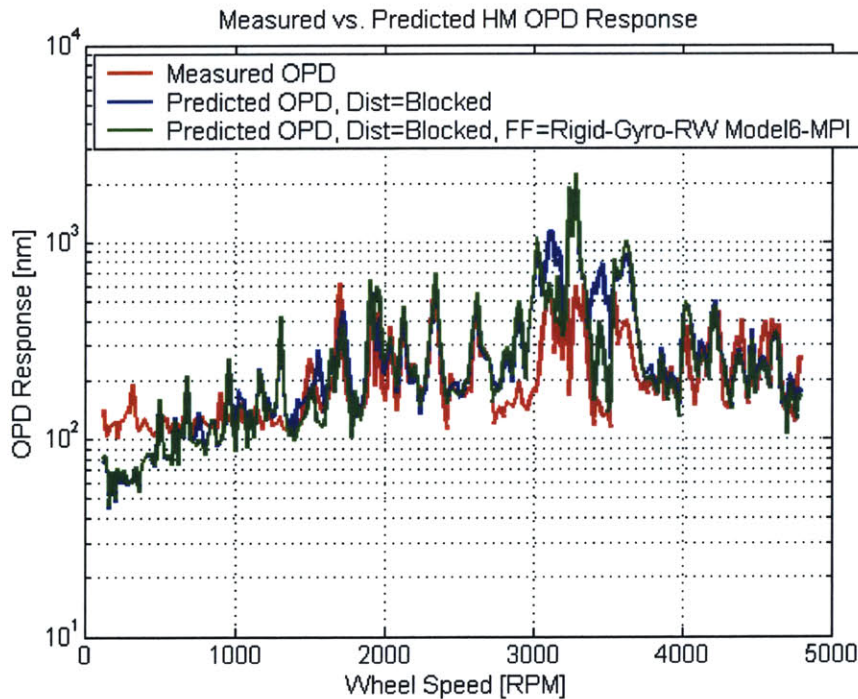


Figure 3.20 Measured Versus Predicted OPD Using Blocked RW Disturbances and the “rigid-gyro-RW, model6-MPI” Force and Moment Filters.

spacecraft-RW system, and therefore to help determine whether these dynamics should be modeled when predicting the coupled performance of a system.

3.3.5 Decoupled Analysis Using Cross-Spectral Density Terms

One final approximation in the disturbance analysis method is now investigated. Recall the simplification from the coupled matrix analysis equation, 2.15, to the scalar equations, 2.16-2.18. The latter equations neglect two types of off-diagonal terms:

- the off-diagonal terms in the RW and MPI acceleration matrices and
- the off-diagonal terms in the RW disturbance spectral density matrix (the CSDs).

Accounting for the first set of terms would be difficult, since measuring a body's 6×6 acceleration matrix is not trivial and may require considerable resources. Even if MPI's acceleration matrix were generated from a FEM, it would still be necessary to measure the RW acceleration matrix. We focus instead on the latter terms, the RW disturbance CSDs.

We can isolate the effect of these CSD terms by returning to the decoupled disturbance analysis equations, and investigating the difference between the matrix analysis equation, Equation 2.2, and its scalar approximation without CSD terms, Equation 2.5. The resulting decoupled prediction that includes CSDs (using Equation 2.2) is shown in Figure 3.21, along with the original decoupled prediction from Section 3.3.1 that uses only PSDs (Equation 2.5) and the measured OPD from Section 3.2.5.

Figure 3.21 demonstrates that including the disturbance CSDs improves the decoupled OPD prediction in some regions (particularly near 3450-3550 RPM), yet degrades the prediction in other regions, such as near 2600 RPM.¹ Since this is a decoupled prediction, and the improvement *is due simply to the addition of disturbance CSDs*, it is recommended in future analyses, whether decoupled or coupled, to include RW disturbance CSDs in the analysis equations.

1. A similar study, however, has shown that CSD terms cause a *significant* improvement for the isolated-RW configuration on MPI.

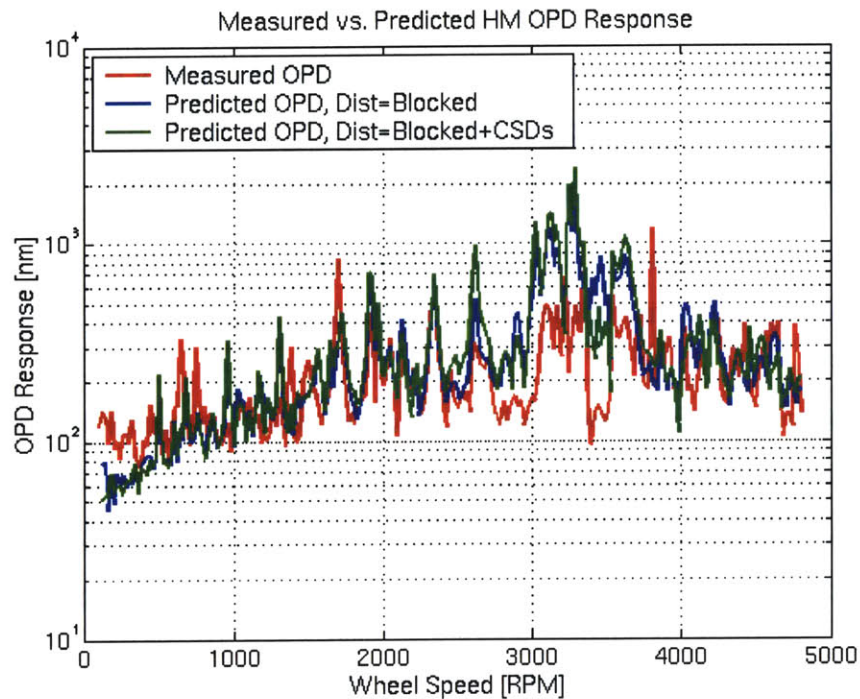


Figure 3.21 Measured Versus Predicted OPD Using Blocked RW Disturbance PSDs and CSDs (Without Force and Moment Filters).

3.4 Summary and Conclusions

Experimental validation on the MPI testbed indicates that both the *decoupled* and *coupled* disturbance analysis methods have the potential to predict the optical performance of a structurally connected interferometer. However, the coupled analysis method yields great improvements compared to the decoupled method in certain ranges of the wheel's spin rate. The improvements in this study were greater than a factor of two in some ranges, when compared to the decoupled predictions and the measured performance results.

After using several increasingly complex force and moment filter representations, we conclude that the first representation (the simplest) provides the largest amount of improved accuracy when compared to the decoupled method. This simple filter involves only three force filters (and no moment filters), and therefore relies on RW accelerances estimated from a non-spinning, rigid-body model.

The two more complex filters investigated here include moment filters in addition to the force filters (with a non-spinning RW acceleration model), and a set of moment filters that include the gyroscopic dynamics of the spinning RW. We discovered in Sections 3.3.3 and 3.3.4 that these increasing levels of complexity in the acceleration models (and therefore in the filters) do not yield any visible improvement in the coupled analysis results when compared to the measured performance. Hence a recommendation is made to avoid the unnecessary complexity associated with these acceleration models, and instead to implement a simplified version of the coupling method that accounts only for force filters (using translational accelerances), and not moment filters (using rotational accelerances).

Additionally, the RW disturbance cross spectral density terms were found to be influential. The inclusion of RW disturbance CSDs in Section 3.3.5 improves the OPD prediction significantly in certain regions, despite adversely affecting the prediction in other localized regions. Because of their influence, a recommendation is made that RW disturbance CSDs should be retained in future disturbance analyses.

The key contribution of this chapter is that we have experimentally validated the coupled disturbance analysis method presented in Chapter 2. With this validation, the method will be transferred to the SIM integrated modeling team at JPL for use in performance predictions for SIM. Further, we make the following recommendations:

- The use of *force filters* in the coupled analysis method yields sufficient accuracy, and the use of moment filters (with or without a gyroscopic model of the RW) is not necessary for systems similar to the one considered here.
- RW disturbance CSD terms are influential in the performance predictions and should be retained in future analyses.

Chapter 4

REVIEW OF KANE'S METHOD

4.1 Introduction

In this chapter, we review Kane's equations, a method of formulating the dynamic equations of motion of a system. Kane's method was originally presented by Kane et. al. in *Dynamics: Theory and Applications* [20]. The method is outlined in this chapter, so that it may be used to derive the equations of motion for an electromagnetic formation flying (EMFF) array in Chapter 5.

Kane's equations may be applied to systems composed of any finite number of rigid bodies and particles (point masses). The degrees of freedom of the system will be characterized by a set of generalized coordinates and generalized speeds. Although Kane's equations are similar to Lagrange's equations and to equations based on the Principle of Virtual Work, they are actually a generalization of these two methods because of the manner in which the generalized speeds are defined and used. As we will find, Kane's equations allow a simpler derivation of the attitude dynamics of a system, since generalized speeds may be defined as components of the angular velocity vectors, rather than as rates of Euler angles.

We proceed as follows. In Section 4.2, we define several important terms and a set of notation that may be used for formulating Kane's equations. In Section 4.3, we present the formulation of Kane's Equations, and in Section 4.4, we apply this method to derive

the equations of motion for a sample two-body system. Finally, in Section 4.5, we discuss the applicability of Kane's equations to EMFF systems, so that in Chapter 5, we can use this method to derive the equations of motion of a two-spacecraft EMFF array.

4.2 Definitions

4.2.1 Generalized Coordinates and Configuration Constraints

We begin by defining the *generalized coordinates of a system*. Similar to a Lagrange formulation, the generalized coordinates of a system are a set of n variables, $\{q_1(t), \dots, q_n(t)\}$, that completely characterize the configuration of the system at any time t . Generalized coordinates are non-unique; for many systems, there is more than one logical way to assign the coordinates that characterize the system. As in a Lagrange formulation, generalized coordinates typically include displacements of points, angles of rotation of bodies about certain axes, or combinations of these values. However, we assume n to be the smallest number of coordinates that will uniquely specify the system configuration at any time.

Configuration constraints are restrictions placed on the generalized coordinates of a system, so as to limit the possible configurations of the system at any time.

4.2.2 Generalized Speeds and Motion Constraints (Holonomic vs. Nonholonomic Systems)

Generalized speeds are a generalization of the “generalized velocities” in a Lagrange formulation. In Lagrange's equations, the n generalized velocities are necessarily the time-derivatives of the n generalized coordinates:

$$\dot{u}_r^L = \dot{q}_r \quad (r = 1, \dots, n) \tag{4.1}$$

In Kane's formulation, however, the generalized speeds are a generalization of the generalized velocities defined in 4.1. In fact, each generalized speed is a linear combination of the generalized velocities:

$$u_r \equiv \sum_{s=1}^n Y_{rs} \dot{q}_r + Z_r \quad (r = 1, \dots, n) \quad (4.2)$$

where Y_{rs} and Z_r are functions of the generalized coordinates, q_r ($r = 1, \dots, n$), and time, t . It is important to note that Y_{rs} and Z_r must be chosen so that the set of equations in 4.2 is invertible; that is, given all the generalized speeds, u_r ($r = 1, \dots, n$), we can uniquely determine the generalized velocities, \dot{q}_r .

Notice that if Y_{rs} and Z_r are chosen such that $Y_{rr} = 1$, $Y_{rs} = 0$ ($r \neq s$) and $Z_r = 0$ for $r = 1, \dots, n$, then the generalized speeds in 4.2 are identical to the generalized velocities in 4.1. However, for any other values of Y_{rr} , Y_{rs} ($r \neq s$) and Z_r , the generalized speeds are composed of a linear combination of the generalized velocities. *This is an important detail and defines a fundamental difference between Kane's equations and Lagrange's equations.*

There is a special case when *motion constraints* are applied to a system. In this case, the generalized speeds are not independent of each other, and we express the $n - p$ dependent generalized speeds in terms of the p independent generalized speeds as:

$$u_r \equiv \sum_{s=1}^p A_{rs} u_s + B_r \quad (r = p + 1, \dots, n) \quad (4.3)$$

where A_{rs} and B_r are functions of the generalized coordinates, q_r ($r = 1, \dots, n$), and time, t .

When motion constraints of the form 4.3 exist, a system is said to be *nonholonomic*; hence 4.3 is called a *nonholonomic constraint equation*. When the generalized speeds are all

independent ($p = n$), the system is said to be *holonomic*. These definitions will play a role in the manner in which we formulate Kane's equations of motion.

4.2.3 Partial Velocities and Partial Angular Velocities

If the velocity vector of a particle in a holonomic or nonholonomic system is \mathbf{v} , and the angular velocity vector of a rigid body in this system is $\boldsymbol{\omega}$, then the velocity and angular velocity vectors may be expressed uniquely as:

$$\mathbf{v} = \sum_{r=1}^n \mathbf{v}_r u_r + \mathbf{v}_t \quad (4.4)$$

$$\boldsymbol{\omega} = \sum_{r=1}^n \boldsymbol{\omega}_r u_r + \boldsymbol{\omega}_t \quad (4.5)$$

The vectors \mathbf{v}_r and $\boldsymbol{\omega}_r$ are called the *holonomic partial velocities* and *holonomic partial angular velocities*, respectively, of \mathbf{v} and $\boldsymbol{\omega}$.

For a nonholonomic system with p independent generalized speeds, the velocity and angular velocity may also be expressed uniquely as:

$$\mathbf{v} = \sum_{r=1}^p \tilde{\mathbf{v}}_r u_r + \tilde{\mathbf{v}}_t \quad (4.6)$$

$$\boldsymbol{\omega} = \sum_{r=1}^p \tilde{\boldsymbol{\omega}}_r u_r + \tilde{\boldsymbol{\omega}}_t \quad (4.7)$$

Although the n partial velocities and n partial angular velocities in 4.4 and 4.5 are unique, for a nonholonomic system they may be replaced by p *nonholonomic partial velocities*, $\tilde{\mathbf{v}}_r$ ($r = 1, \dots, p$), and p *nonholonomic partial angular velocities*, $\tilde{\boldsymbol{\omega}}_r$ ($r = 1, \dots, p$), as defined in 4.6 and 4.7, respectively.

The definitions in Equations 4.4-4.7 are sufficient to proceed toward the presentation of Kane's formulation, but for completeness, we show the relationships between the holonomic and nonholonomic partial velocities:

$$\tilde{\mathbf{v}}_r \equiv \mathbf{v}_r + \sum_{s=p+1}^n \mathbf{v}_s A_{sr} \quad (r = 1, \dots, p) \quad (4.8)$$

and

$$\tilde{\mathbf{v}}_t \equiv \mathbf{v}_t + \sum_{r=p+1}^n \mathbf{v}_r B_r \quad (4.9)$$

where A_{sr} and B_r are defined by the nonholonomic constraint equation, 4.3. Similarly, the holonomic and nonholonomic partial angular velocities are related as:

$$\tilde{\omega}_r \equiv \omega_r + \sum_{s=p+1}^n \omega_s A_{sr} \quad (r = 1, \dots, p) \quad (4.10)$$

and

$$\tilde{\omega}_t \equiv \omega_t + \sum_{r=p+1}^n \omega_r B_r \quad (4.11)$$

Notice that in a holonomic system, for which $p = n$, Equations 4.6-4.7 reduce to Equations 4.4-4.5, as expected.

4.2.4 Generalized Active Forces

We now define the *generalized active forces* for a system of particles, a rigid body, and a system of particles *and* rigid bodies.

System of Particles

The n *holonomic generalized active forces* for a system of v_p particles, P_i ($i = 1, \dots, v_p$), are:

$$(F_r)_P \equiv \sum_{i=1}^{v_p} \mathbf{v}_r^{P_i} \cdot \mathbf{R}^{P_i} \quad (r = 1, \dots, n) \quad (4.12)$$

where $\mathbf{v}_r^{P_i}$ is the r^{th} holonomic partial velocity of particle P_i , and \mathbf{R}^{P_i} is the resultant of all external forces acting on particle P_i . The external forces may include contact forces, such as friction, or distance forces, such as gravity or magnetic forces.

Similarly, the p *nonholonomic generalized active forces* for a system of v_p particles are:

$$(\tilde{F}_r)_P \equiv \sum_{i=1}^{v_p} \tilde{\mathbf{v}}_r^{P_i} \cdot \mathbf{R}^{P_i} \quad (r = 1, \dots, p) \quad (4.13)$$

where $\tilde{\mathbf{v}}_r^{P_i}$ is the r^{th} nonholonomic partial velocity of particle P_i .

The holonomic and nonholonomic generalized active forces for a system of particles are related as:

$$(\tilde{F}_r)_P = (F_r)_P + \sum_{s=p+1}^n F_s A_{sr} \quad (r = 1, \dots, p) \quad (4.14)$$

where A_{sr} ($s = 1, \dots, p$, $r = p+1, \dots, n$) was introduced in Equation 4.3. For $p = n$, Equation 4.14 becomes trivial, and 4.13 reduces to 4.12.

Rigid Body

The n *holonomic generalized active forces for a rigid body*, B , are:

$$(F_r)_B \equiv \mathbf{v}_r^Q \cdot \mathbf{R} + \boldsymbol{\omega}_r \cdot \mathbf{T} \quad (r = 1, \dots, n) \quad (4.15)$$

where \mathbf{R} is the resultant of all external (contact or distance) forces acting on B , Q is a point in B through which the line of action of \mathbf{R} passes, \mathbf{v}_r^Q is the r^{th} holonomic partial velocity of Q , ω_r is the r^{th} holonomic partial angular velocity of B , as defined in Equation 4.5, and \mathbf{T} is the resultant external torque acting on B .

Note that it is often convenient to replace \mathbf{R} with an equivalent force whose line of action passes through the mass center of B , along with the coupling torque that would result from applying \mathbf{R} at the point Q instead of the mass center. In this case, \mathbf{v}_r^Q is replaced with \mathbf{v}_r^* , the r^{th} holonomic partial velocity at the mass center.

The p nonholonomic generalized active forces for a rigid body, B , are:

$$(\tilde{F}_r)_B \equiv \tilde{\mathbf{v}}_r^Q \cdot \mathbf{R} + \omega_r \cdot \mathbf{T} \quad (r = 1, \dots, p) \quad (4.16)$$

where $\tilde{\mathbf{v}}_r^Q$ is the r^{th} nonholonomic partial velocity of Q , and ω_r is the r^{th} nonholonomic partial angular velocity of B , as defined in Equation 4.7. Again, \mathbf{R} can be replaced with an equivalent force acting through the mass center, along with the appropriate coupling torque, in which case $\tilde{\mathbf{v}}_r^Q$ is replaced with $\tilde{\mathbf{v}}_r^*$, the r^{th} nonholonomic partial velocity at the mass center.

System of Particles and Rigid Bodies

The n holonomic generalized active forces for a system, S , of v_p particles and v rigid bodies are:

$$(F_r)_S \equiv \sum_{i=1}^v (\mathbf{v}_r^{B_i Q_i} \cdot \mathbf{R}^{B_i} + \omega_r^{B_i} \cdot \mathbf{T}^{B_i}) + (F_r)_P \quad (r = 1, \dots, n) \quad (4.17)$$

where \mathbf{R}^{B_i} is the resultant of all external (contact or distance) forces acting on body B_i , Q_i is a point in B_i through which the line of action of \mathbf{R}^{B_i} passes, $\mathbf{v}_r^{B_i Q_i}$ is the r^{th} holonomic partial velocity of Q_i in body B_i , $\omega_r^{B_i}$ is the r^{th} holonomic partial angular velocity of body B_i , as defined in Equation 4.5, and \mathbf{T}^{B_i} is the resultant external torque acting on body B_i .

$(F_r)_P$ is the r^{th} holonomic generalized active force for the system of particles, as defined in Equation 4.12.

The p nonholonomic generalized active forces for a system, S , of v_P particles and v rigid bodies are:

$$(\tilde{F}_r)_S \equiv \sum_{i=1}^v (\tilde{v}_r^{B_i Q_i} \cdot \mathbf{R}^{B_i} + \tilde{\omega}_r^{B_i} \cdot \mathbf{T}^{B_i}) + (\tilde{F}_r)_P \quad (r = 1, \dots, p) \quad (4.18)$$

where $\tilde{v}_r^{B_i Q_i}$ is the r^{th} nonholonomic partial velocity of Q_i in body B_i , and $\tilde{\omega}_r^{B_i}$ is the r^{th} nonholonomic partial angular velocity of body B_i , as defined in Equation 4.7. $(\tilde{F}_r)_P$ is the r^{th} nonholonomic generalized active force for the system of particles, as defined in Equation 4.13.

Again, for any rigid body, B_i , \mathbf{R}^{B_i} can be replaced with an equivalent force acting through the mass center of the body, along with the appropriate coupling torque. In this case, $\tilde{v}_r^{B_i Q_i}$ in Equation 4.17 is replaced with $v_r^{B_i*}$, the r^{th} holonomic partial velocity of B_i at its mass center, and $\tilde{v}_r^{B_i Q_i}$ in Equation 4.18 is replaced with $\tilde{v}_r^{B_i*}$, the r^{th} nonholonomic partial velocity of B_i at its mass center.

4.2.5 Generalized Inertia Forces

We now define the *generalized inertia forces* for a system of particles, a rigid body, and a system of particles and rigid bodies.

System of Particles

The n holonomic generalized inertia forces for a system of v_P particles, P_i ($i = 1, \dots, v_P$), are:

$$(F_r^*)_P \equiv \sum_{i=1}^{v_P} \mathbf{v}_r^{P_i} \cdot \mathbf{R}^{P_i*} \quad (r = 1, \dots, n) \quad (4.19)$$

where $\mathbf{v}_r^{P_i}$ is the r^{th} holonomic partial velocity of particle P_i , and \mathbf{R}^{P_i*} is the *inertia force* acting on particle P_i :

$$\mathbf{R}^{P_i*} \equiv -m_i \mathbf{a}_i \quad (i = 1, \dots, v_p) \quad (4.20)$$

where m_i is the mass of particle P_i , and \mathbf{a}_i is its acceleration.

The p nonholonomic generalized inertia forces for a system of v_p particles are:

$$(\tilde{F}_r^*)_p \equiv \sum_{i=1}^{v_p} \tilde{\mathbf{v}}_r^{P_i} \cdot \mathbf{R}^{P_i*} \quad (r = 1, \dots, p) \quad (4.21)$$

where $\tilde{\mathbf{v}}_r^{P_i}$ is the r^{th} nonholonomic partial velocity of particle P_i .

The holonomic and nonholonomic generalized inertia forces for a system of particles are related to one another as:

$$(\tilde{F}_r^*)_p = (F_r^*)_p + \sum_{s=p+1}^n (F_s^*)_p A_{sr} \quad (r = 1, \dots, p) \quad (4.22)$$

where A_{sr} ($s = 1, \dots, p$, $r = p+1, \dots, n$) was introduced in Equation 4.3. For $p = n$, Equation 4.22 becomes trivial, and 4.21 reduces to 4.19.

Rigid Body

The n holonomic generalized inertia forces for a rigid body, B, are:

$$(F_r^*)_B \equiv \mathbf{v}_r^* \cdot \mathbf{R}^* + \boldsymbol{\omega}_r \cdot \mathbf{T}^* \quad (r = 1, \dots, n) \quad (4.23)$$

\mathbf{v}_r^* is the r^{th} holonomic partial velocity of the mass center of B, and $\boldsymbol{\omega}_r$ is the r^{th} holonomic partial angular velocity of B, as defined in Equation 4.5. \mathbf{R}^* is the *inertia force* acting on B, and \mathbf{T}^* is the *inertia torque* acting on B, defined respectively as:

$$\mathbf{R}^* \equiv -M \mathbf{a}^* \quad (4.24)$$

$$\mathbf{T}^* \equiv -\boldsymbol{\alpha} \cdot \mathbf{I} - \boldsymbol{\omega} \times (\mathbf{I} \cdot \boldsymbol{\omega}) \quad (4.25)$$

where M is the mass of B, \mathbf{a}^* is the acceleration of the mass center of B, $\boldsymbol{\alpha}$ is the angular acceleration vector of B, $\boldsymbol{\omega}$ is the angular velocity vector of B, and \mathbf{I} is the central inertia dyadic of B.

In the special case that a set of orthogonal unit vectors, $\{\mathbf{e}_1, \mathbf{e}_2, \mathbf{e}_3\}$, is aligned with the principal axes of B (but not necessarily fixed in B), we can associate coordinates with the dyadic notation in 4.25 and express \mathbf{T}^* as:

$$\begin{aligned} \mathbf{T}^* &\equiv -[\alpha_1 I_1 - \omega_2 \omega_3 (I_2 - I_3)] \mathbf{e}_1 \\ &\quad -[\alpha_2 I_2 - \omega_3 \omega_1 (I_3 - I_1)] \mathbf{e}_2 \\ &\quad -[\alpha_3 I_3 - \omega_1 \omega_2 (I_1 - I_2)] \mathbf{e}_3 \end{aligned} \quad (4.26)$$

where:

$$\alpha_i \equiv \boldsymbol{\alpha} \cdot \mathbf{e}_i \quad \omega_i \equiv \boldsymbol{\omega} \cdot \mathbf{e}_i \quad I_i \equiv \mathbf{e}_i \cdot \mathbf{I} \cdot \mathbf{e}_i \quad i = 1, 2, 3 \quad (4.27)$$

The p nonholonomic generalized inertia forces for a rigid body, B, are:

$$(\tilde{F}_r^*)_B \equiv \tilde{\mathbf{v}}_r^* \cdot \mathbf{R}^* + \tilde{\boldsymbol{\omega}}_r \cdot \mathbf{T}^* \quad (r = 1, \dots, p) \quad (4.28)$$

where $\tilde{\mathbf{v}}_r^*$ is the r^{th} nonholonomic partial velocity of the mass center of B, and $\tilde{\boldsymbol{\omega}}_r$ is the r^{th} nonholonomic partial angular velocity of B, as defined in Equation 4.7.

System of Particles and Rigid Bodies

The n holonomic generalized inertia forces for a system, S, of v_p particles and v rigid bodies are:

$$(F_r^*)_S \equiv \sum_{i=1}^v \left(\mathbf{v}_r^{B_i*} \cdot \mathbf{R}^{B_i*} + \boldsymbol{\omega}_r^{B_i} \cdot \mathbf{T}^{B_i*} \right) + (F_r^*)_P \quad (r = 1, \dots, n) \quad (4.29)$$

where $\mathbf{v}_r^{B_i*}$ is the r^{th} holonomic partial velocity of the mass center of body B_i , and $\omega_r^{B_i}$ is the r^{th} holonomic partial angular velocity of B_i , as defined in Equation 4.5. \mathbf{R}^{B_i*} is the *inertia force* acting on B_i , and \mathbf{T}^{B_i*} is the *inertia torque* acting on B_i , defined by Equations 4.24 and 4.25, respectively. $(F_r^*)_P$ is the r^{th} holonomic generalized inertia force for the system of particles, as defined in Equation 4.19.

The p nonholonomic generalized inertia forces for a system, S , of v_p particles and v rigid bodies are:

$$(\tilde{F}_r^*)_S \equiv \sum_{i=1}^v \left(\tilde{\mathbf{v}}_r^{B_i*} \cdot \mathbf{R}^{B_i*} + \tilde{\omega}_r^{B_i} \cdot \mathbf{T}^{B_i*} \right) + (\tilde{F}_r^*)_P \quad (r = 1, \dots, p) \quad (4.30)$$

where $\tilde{\mathbf{v}}_r^{B_i*}$ is the r^{th} nonholonomic partial velocity of the mass center of body B_i , and $\tilde{\omega}_r^{B_i}$ is the r^{th} nonholonomic partial angular velocity of B_i , as defined in Equation 4.7. $(\tilde{F}_r^*)_P$ is the r^{th} nonholonomic generalized inertia force for the system of particles, as defined in Equation 4.21.

4.3 Kane's Equations of Motion

With all of the definitions presented in Section 4.2, we now write *Kane's dynamical equations for a holonomic system* as:

$$F_r + F_r^* = 0 \quad (r = 1, \dots, n) \quad (4.31)$$

where F_r is the r^{th} *holonomic generalized active force*, defined by:

- Equation 4.12 for a system of particles
- Equation 4.15 for a rigid body
- Equation 4.17 for a system of particles and rigid bodies

and F_r^* is the r^{th} *holonomic generalized inertia force*, defined by:

- Equation 4.19 for a system of particles.
- Equation 4.23 for a rigid body.
- Equation 4.29 for a system of particles and rigid bodies.

For a nonholonomic system, Kane's dynamical equations may be written:

$$\tilde{F}_r + \tilde{F}_r^* = 0 \quad (r = 1, \dots, n) \quad (4.32)$$

where \tilde{F}_r is the r^{th} *nonholonomic generalized active force*, defined by:

- Equation 4.13 for a system of particles
- Equation 4.16 for a rigid body
- Equation 4.18 for a system of particles and rigid bodies

and \tilde{F}_r^* is the r^{th} *nonholonomic generalized inertia force*, defined by:

- Equation 4.21 for a system of particles.
- Equation 4.28 for a rigid body.
- Equation 4.30 for a system of particles and rigid bodies.

4.4 Example Using Kane's Equations

We now define a sample system and derive its equations of motion using Kane's method. Consider the system shown in Figure 4.1, in which a long, hollow tube of mass m_1 and length $2L$ is pinned at its top end to a fixed support and allowed to rotate without friction through angle q_1 relative to the vertical. Inside the tube is a small ball of mass m_2 that is

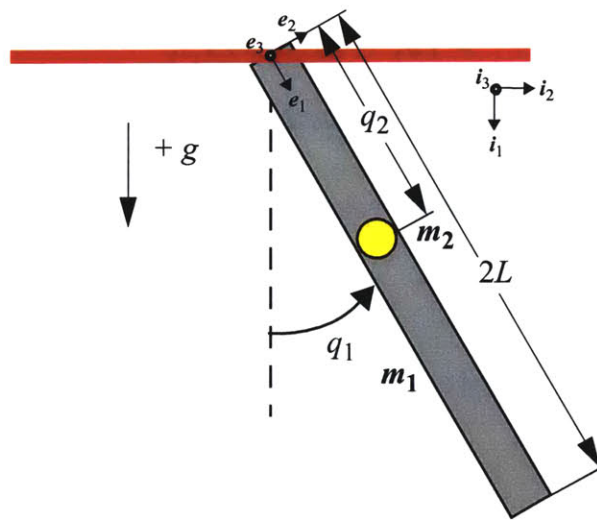


Figure 4.1 Sample System: Pendulum Tube with Ball

allowed to move without friction through the tube. The only external force on the system is that due to gravity. A global coordinate frame (i_1, i_2, i_3) is fixed inertially, while a “local” coordinate frame (e_1, e_2, e_3) rotates with the tube and ball through angle q_1 .

We define the generalized speeds simply as the time-derivatives of the generalized coordinates:

$$u_1 = \dot{q}_1 \quad u_2 = \dot{q}_2 \quad (4.33)$$

Because this system does not have any motion constraints of the form in Equation 4.3, *this system is holonomic*, and all the terms considered below will be holonomic.

We now consider the kinematics of the system. The two coordinate frames are related as:

$$\begin{aligned}\mathbf{e}_1 &= c_1 \mathbf{i}_1 + s_1 \mathbf{i}_2 \\ \mathbf{e}_2 &= -s_1 \mathbf{i}_1 + c_1 \mathbf{i}_2\end{aligned}\quad (4.34)$$

where s_1 and c_1 denote the sine and cosine of the angle q_1 , respectively.

We recognize this as a system composed of one rigid body, B_1 (the tube), and one particle, P_1 (the ball). The position vectors of the tube's mass center and the ball, respectively, are:

$$\begin{aligned}\mathbf{r}^{B_1*} &= L\mathbf{e}_1 = Lc_1 \mathbf{i}_1 + Ls_1 \mathbf{i}_2 \\ \mathbf{r}^{P_1} &= q_2 \mathbf{e}_1 = q_2 c_1 \mathbf{i}_1 + q_2 s_1 \mathbf{i}_2\end{aligned}\quad (4.35)$$

From 4.33 and 4.35, the corresponding velocities are:

$$\begin{aligned}\mathbf{v}^{B_1*} &= \dot{\mathbf{r}}^{B_1*} = Lu_1[-s_1 \mathbf{i}_1 + c_1 \mathbf{i}_2] \\ \mathbf{v}^{P_1} &= \dot{\mathbf{r}}^{P_1} = u_2[c_1 \mathbf{i}_1 + s_1 \mathbf{i}_2] + q_2 u_1[-s_1 \mathbf{i}_1 + c_1 \mathbf{i}_2]\end{aligned}\quad (4.36)$$

and the accelerations are:

$$\begin{aligned}\mathbf{a}^{B_1*} &= \ddot{\mathbf{v}}^{B_1*} = L\dot{u}_1[-s_1 \mathbf{i}_1 + c_1 \mathbf{i}_2] + Lu_1^2[-c_1 \mathbf{i}_1 - s_1 \mathbf{i}_2] \\ \mathbf{a}^{P_1} &= \ddot{\mathbf{v}}^{P_1} = (\dot{u}_2 - q_2 u_1^2)[c_1 \mathbf{i}_1 + s_1 \mathbf{i}_2] + (q_2 \dot{u}_1 + 2u_1 u_2)[-s_1 \mathbf{i}_1 + c_1 \mathbf{i}_2]\end{aligned}\quad (4.37)$$

The angular velocity of the tube is:

$$\boldsymbol{\omega}^{B_1} = \dot{q}_1 \mathbf{i}_3 = u_1 \mathbf{i}_3 \quad (4.38)$$

We now write the partial velocities and partial angular velocities by inspection from Equations 4.36 and 4.38. The partial velocities of the tube's mass center are:

$$\begin{aligned}\mathbf{v}_1^{B_1*} &= \frac{\partial \mathbf{v}^{B_1*}}{\partial u_1} = L(-s_1 \mathbf{i}_1 + c_1 \mathbf{i}_2) \\ \mathbf{v}_2^{B_1*} &= \frac{\partial \mathbf{v}^{B_1*}}{\partial u_2} = 0\end{aligned}\quad (4.39)$$

The partial velocities of the ball are:

$$\begin{aligned}\mathbf{v}_1^{P_1} &= \frac{\partial \mathbf{v}^{P_1}}{\partial u_1} = q_2(-s_1\mathbf{i}_1 + c_1\mathbf{i}_2) \\ \mathbf{v}_2^{P_1} &= \frac{\partial \mathbf{v}^{P_1}}{\partial u_2} = (c_1\mathbf{i}_1 + s_1\mathbf{i}_2)\end{aligned}\quad (4.40)$$

Similarly, the partial angular velocities of the tube are:

$$\begin{aligned}\boldsymbol{\omega}_1^{B_1} &= \frac{\partial \boldsymbol{\omega}^{B_1}}{\partial u_1} = \mathbf{i}_3 \\ \boldsymbol{\omega}_2^{B_1} &= \frac{\partial \boldsymbol{\omega}^{B_1}}{\partial u_2} = 0\end{aligned}\quad (4.41)$$

Next we define the generalized active forces. Since the only external force on the system is that due to gravity, the resultant external forces on the tube's mass center and the ball, respectively, are:

$$\mathbf{R}^{B_1} = m_1 g \mathbf{i}_1 \quad \mathbf{R}^{P_1} = m_2 g \mathbf{i}_1 \quad (4.42)$$

and since there is no external torque on the tube,

$$\mathbf{T}^{B_1} = 0 \quad (4.43)$$

Substituting Equations 4.39-4.43 into 4.17, we find the generalized active forces of the system to be:

$$\begin{aligned}F_1 &= -g s_1 (m_1 L + m_2 q_2) \\ F_2 &= g c_1 m_2\end{aligned}\quad (4.44)$$

To determine the generalized inertia forces, we first consider the resultant inertia force on each body:

$$\mathbf{R}^{B_1*} = -m_1 \mathbf{a}^{B_1*} \quad \mathbf{R}^{P_1*} = -m_2 \mathbf{a}^{P_1} \quad (4.45)$$

where \mathbf{a}^{B_1*} and \mathbf{a}^{P_1} are defined in Equation 4.37. The resultant inertia torque on the tube is found easily in this case, using the expression in Equation 4.26:

$$\mathbf{T}^{B_1*} = -\dot{u}_1 I_1 \mathbf{e}_3 = -\dot{u}_1 I_1 \mathbf{i}_3 \quad (4.46)$$

where I_1 is the central inertia¹ of the tube about an axis perpendicular to the plane of motion.

Substituting Equations 4.39-4.41 and 4.45-4.46 into 4.29, we find the generalized inertia forces of the system to be:

$$\begin{aligned} F_1^* &= -(m_1 L^2 + I_1 + m_2 q_2^2) \ddot{q}_1 - m_2 q_2 (2\dot{q}_1 \dot{q}_2) \\ F_2^* &= -m_2 \ddot{q}_2 + m_2 q_2 \dot{q}_1^2 \end{aligned} \quad (4.47)$$

Finally, substituting Equations 4.44 and 4.47 into 4.31, we write the equations of motion for the system:

$$\begin{aligned} (m_1 L^2 + m_2 q_2^2 + I_1) \ddot{q}_1 + 2m_2 q_2 \dot{q}_1 \dot{q}_2 &= -g \sin q_1 (m_1 L + m_2 q_2) \\ \ddot{q}_2 - q_2 \dot{q}_1^2 &= g \cos q_1 \end{aligned} \quad (4.48)$$

This result is a pair of coupled, second-order, nonlinear differential equations.

We recognize the first equation as a sort of modified pendulum equation. The first term is a product of the angular acceleration with the sum of inertias in the system. The second term represents the torque associated with the coriolis acceleration of the ball, and results from the ball's ability to slide freely within the rotating tube. Finally, the third term represents the sum of "gravitational torques" on the two bodies.

1. Central inertias are those defined about axes passing through a body's center of mass.

In fact, if the mass, m_1 , of the tube approaches zero, and the ball is fixed at a constant radial distance $q_2 = 2L = \tilde{L}$ from the pivot point of the pendulum, then the first equation reduces to the well-known “pendulum equation” for a massless rod with tip-mass:

$$\tilde{L}\ddot{q}_1 = -g \sin q_1 \quad (4.49)$$

It is also interesting to note that neither the tube’s mass, m_1 , nor the ball’s mass, m_2 , appears in the second equation! In this case, the first term represents the ball’s radial acceleration relative to the tube, the second term represents the carrying centripetal acceleration of the tube, and the third term represents the component of gravitational acceleration along the direction of q_2 .

4.5 Applicability of Kane's Equations to EMFF Systems

We now discuss how Kane’s equations may be useful in the field of research involving electromagnetic formation flight (EMFF) of multiple spacecraft.

The concept of formation flight in this context refers to an array of multiple spacecraft flying in close formation and contributing to a common mission, acting essentially as a large virtual spacecraft in applications such as space-based interferometry. In such situations, it is critical that the relative displacements and orientations of all the spacecraft be carefully controlled. In the EMFF concept, electromagnetic coils are placed on each spacecraft, current is run through these coils to create an electromagnetic dipole moment on each spacecraft, and the interactions of the dipoles are used to apply forces and torques to the spacecraft, thus controlling their relative displacements and orientations.

One of the inherent difficulties in this field of research is that the dynamics of such systems are quite complicated. The systems are composed of multiple bodies with multiple (often rotating) reference frames. Once we consider adding reaction wheels (RWs) as additional actuators to control the rotational degrees of freedom of the bodies, the system becomes even more complicated. Rather than simple bodies flying in formation, the sys-

tem is composed of multiple “subsystems,” each of which contains multiple bodies constrained to move in certain ways relative to one another. For example, most spacecraft use three orthogonal RWs to control rotation about three orthogonal axes, and often use a fourth RW (not parallel to any of the other three) in case of failure of a primary RW. Hence each spacecraft is composed of multiple bodies, rotating relative to one another about various axes. Further, in EMFF systems, we often encounter both nonlinear system dynamics and nonlinear actuator dynamics. Although we often linearize these dynamics to assess the system using linear analysis tools, first determining the fully nonlinear dynamics is a challenging task, even for an experienced dynamicist.

What we have learned about Kane’s formulation in this chapter -- that it is a systematic method of deriving the dynamical equations of motion for complex systems composed of multiple bodies with multiple coordinate frames -- suggests that Kane’s equations might be very useful in deriving the nonlinear equations of motion for EMFF systems. Further, because the generalized speeds can be defined as components of the angular velocity vectors, rather than the rates of Euler angles (the former being a linear combination of the latter), the equations may be derived in a much simpler form.

The following chapters focus specifically on formulating and analyzing the dynamics of a two-vehicle EMFF system. In Chapter 5, Kane’s method will be used to systematically derive the equations of motion for such a system.

4.6 Summary and Conclusions

In this chapter, we have reviewed Kane’s method for the formulation of a system’s dynamic equations of motion. This includes a geometric description of the system, a kinematic description, a definition of the generalized coordinates and generalized speeds, a definition of the partial velocities and partial angular velocities, and finally the identification of the generalized active and inertia forces. By following the systematic method outlined in this chapter, one can formulate the equations of motion for even very complex systems.

We have also identified Kane's method as a useful technique to derive the equations of motion for an electromagnetic formation flight (EMFF) array. We will derive such a set of equations in Chapter 5 for an EMFF array containing an arbitrary number of spacecraft.

Chapter 5

ELECTROMAGNETIC FORMATION FLIGHT DYNAMICS

5.1 Introduction

Chapter 4 provided a review of Kane's method for formulating the dynamic equations of motion for a system. In this chapter, we apply Kane's method to derive the nonlinear equations of motion for a multi-spacecraft electromagnetic formation flight (EMFF) array. Each spacecraft will be modeled as a core spacecraft "bus," along with multiple reaction wheels (RWs) that rotate relative to the spacecraft bus. Hence Kane's method will yield a set of coupled, nonlinear equations of motion for each spacecraft-RW system.

Also captured in these nonlinear equations will be the electromagnetic forces and torques generated by the interaction of the electromagnets on the various spacecraft. Since these electromagnetic loads will depend on variables such as the separation distance between the spacecraft, the resulting set of equations for each spacecraft will also be coupled with the equations of all the other spacecraft.

While the full set of coupled, nonlinear equations will be derived in this chapter for the multi-spacecraft EMFF array, the equations will be simplified in Chapter 6 to represent a two-vehicle system, and will then be linearized about a nominal operating trajectory. The nominal trajectory is a steady-state spin maneuver, which is useful for scientific observation in deep-space separated-spacecraft interferometry applications, such as NASA's forthcoming Terrestrial Planet Finder, depicted in Figure 1.2 [4]. If one RW on each vehi-

cle is nominally aligned with the spin axis of the entire array, that RW will need to store the angular momentum of the array as it “spins up” from a static system to a rotating one. Since one RW on each vehicle thus has the potential to store a great deal of angular momentum, we are naturally concerned about the nonlinear gyrostiffening effect of this rapidly spinning body. This is the primary motivation for modeling the dynamics of this RW on each vehicle as a body spinning relative to the spacecraft bus. Hence even in the derivation of the nonlinear equations (before linearization) in this chapter, we seek to capture the gyrostiffening effect of the RWs in the array’s equations of motion.

In Chapter 6, the equations for a two-spacecraft EMFF array are linearized and analyzed. First, we investigate the stability of the linearized dynamics, and then we design an optimal controller for the system. For this reason, we refer to the linearized system of equations as a *design model*. Then in Chapter 7, the original *nonlinear* equations will serve as an *evaluation model* for simulating the closed-loop behavior of the nonlinear system. As the dynamics of the nominal trajectory will prove to be unstable, as well as nonlinear, demonstrating a closed-loop, stable simulation using simple linear control techniques will be very enabling.

Chapter 5 is organized as follows. In Section 5.2, we define the geometry of the system being considered. In Section 5.3, expressions are presented for the electromagnetic forces and torques acting between the spacecraft. In Section 5.4, the nonlinear equations of motion are derived using Kane’s method. Finally, in Section 5.5, the results and contributions are summarized.

5.2 System Description

We now consider a detailed description of the EMFF system. First we describe each vehicle in the array (Section 5.2.1), as well as some coordinate frames and degrees of freedom that are useful in characterizing the system (Sections 5.2.2 and 5.2.3, respectively). We then introduce rotation matrices that relate the various coordinate frames to one another (Section 5.2.4), present expressions for the velocity vectors of the bodies under consider-

ation (Section 5.2.5), and provide a detailed description of the actuators being used in this system (Section 5.2.6).

5.2.1 Vehicle Description

The system of interest is a formation flying array containing n spacecraft. A typical spacecraft in the array is depicted in Figure 5.1. It consists of a spacecraft bus (the central body) and an orthogonal triad of reaction wheels (RWs), the smaller, disc-like bodies that interface with the spacecraft bus (denoted RW-1, RW-2, and RW-3, respectively). Because RWs are anticipated to be the largest dynamic disturbance source onboard many precision space vehicles, we are interested in characterizing their behavior, in addition to that of the spacecraft bus. The flexibility of reaction wheels has proven influential in previous studies [7], so we will model that flexibility here. Further, we showed in Chapters 2 and 3 that the gyroscopic stiffening effects of spinning RWs may have an impact on the dynamics of the associated spacecraft. Hence we attempt to capture the dynamics of the spinning RWs in the model of each vehicle in the array.

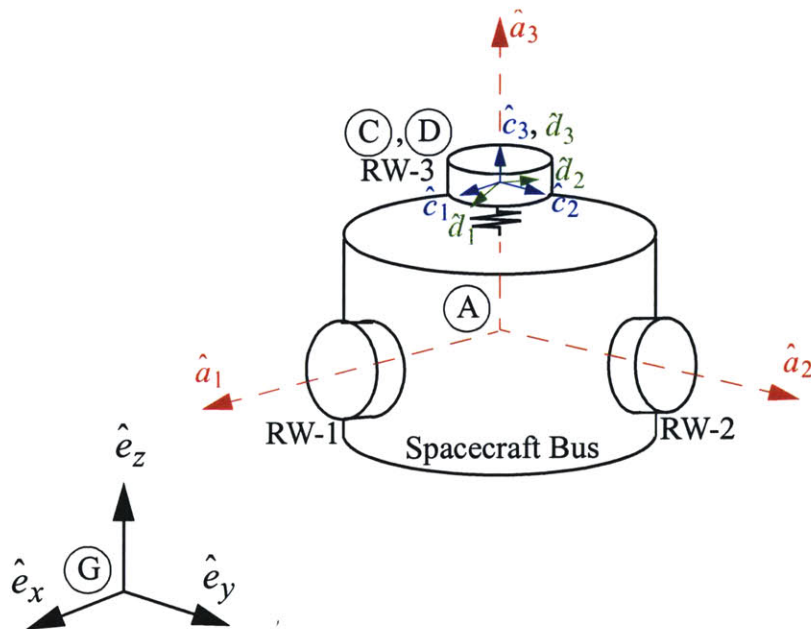


Figure 5.1 Representative Model of One Spacecraft in an EMFF Array

The interface of each RW to its associated spacecraft bus is treated as a five-degree-of-freedom (DOF) spring, allowing relative translation and rotation between the two bodies in all DOF. The spring has stiffness along all three translational DOF, as well as about the two rotational DOF perpendicular to the RW's spin axis. The sixth degree of freedom, rotation of the RW about its designated spin axis, has zero spring stiffness. It is unconstrained so that the RW may spin freely about this axis.

At this point, we make the assumption that each vehicle may be modeled as if it has only one RW. This assumption will greatly simplify the derivation of the equations. To derive the terms for additional RWs, one would follow a similar procedure.

5.2.2 Coordinate Frames

The following set of reference frames will be useful in deriving the equations of motion. A global, inertial reference frame, G, is shown in Figure 5.1. This reference frame consists of an orthonormal triad of unit vectors:

$$\hat{e}_G \equiv \left\{ \begin{array}{c} \hat{e}_x \\ \hat{e}_y \\ \hat{e}_z \end{array} \right\} \quad (5.1)$$

While G represents a global, inertial reference frame, another frame, A, represents a body-fixed frame that is constrained to the spacecraft bus of a given spacecraft, here denoted "spacecraft A." The body-fixed frame, A, is composed of a triad of unit vectors, \hat{a}_1 , \hat{a}_2 , and \hat{a}_3 , as shown in Figure 5.1:

$$\hat{e}_A \equiv \left\{ \begin{array}{c} \hat{a}_1 \\ \hat{a}_2 \\ \hat{a}_3 \end{array} \right\} \quad (5.2)$$

The origin of A is fixed at the center of mass of the spacecraft bus (excluding the RW mass), and the orientation of the triad, \hat{e}_A , is fixed within the body (and thus rotates with the body).

If another spacecraft in the array is denoted “spacecraft B,” we can define a body-fixed frame, B, similar to that on A, but composed of a triad of unit vectors \hat{b}_1 , \hat{b}_2 , and \hat{b}_3 :

$$\hat{e}_B \equiv \begin{Bmatrix} \hat{b}_1 \\ \hat{b}_2 \\ \hat{b}_3 \end{Bmatrix} \quad (5.3)$$

Analogous body-fixed frames can be defined for all remaining spacecraft in the array.

Finally, reference frames C and D, shown in Figure 5.1, are defined such that their origins are collocated and fixed at the RW mass center.¹ Both C and D are composed of triads of unit vectors:

$$\hat{e}_C \equiv \begin{Bmatrix} \hat{c}_1 \\ \hat{c}_2 \\ \hat{c}_3 \end{Bmatrix}, \quad \hat{e}_D \equiv \begin{Bmatrix} \hat{d}_1 \\ \hat{d}_2 \\ \hat{d}_3 \end{Bmatrix} \quad (5.4)$$

These frames differ in that D is body-fixed to the RW in *all* degrees of freedom (translational and rotational), but C is only partially fixed, in that it does not spin with the RW about its spin axis, \hat{c}_3 . In other words, \hat{e}_C “tips” with the RW about axes \hat{c}_1 and \hat{c}_2 , but does not rotate about \hat{c}_3 , while \hat{e}_D tips with the RW about \hat{d}_1 and \hat{d}_2 and “spins” about \hat{d}_3 (or \hat{c}_3) with the RW. Hence \hat{c}_3 and \hat{d}_3 are always parallel, and \hat{d}_1 and \hat{d}_2 “rotate” about \hat{d}_3 within the same plane formed by \hat{c}_1 and \hat{c}_2 .

1. Because the equations of motion will be linearized about a steady-state spin trajectory within the \hat{e}_x, \hat{e}_y plane, we assume that RW-3, whose spin axis is aligned with \hat{a}_3 in Fig 5.1, will store the majority of the system’s angular momentum. Hence we develop the equations of motion using RW-3.

5.2.3 Degrees of Freedom

We now define the degrees of freedom for each spacecraft and its reaction wheel. Each spacecraft bus is characterized by a position and attitude description. The position is defined relative to the global, inertial reference frame, G. For instance, the position vector of spacecraft A may be expressed relative to G as:

$$\hat{r}_{AG} = \begin{bmatrix} x_{AG} & y_{AG} & z_{AG} \end{bmatrix} \begin{Bmatrix} \hat{e}_x \\ \hat{e}_y \\ \hat{e}_z \end{Bmatrix} \quad (5.5)$$

where x_{AG} , y_{AG} , and z_{AG} are the cartesian coordinates of the position vector, \hat{r}_{AG} , resolved on the coordinate axes of the global frame, G, as illustrated in Figure 5.2.

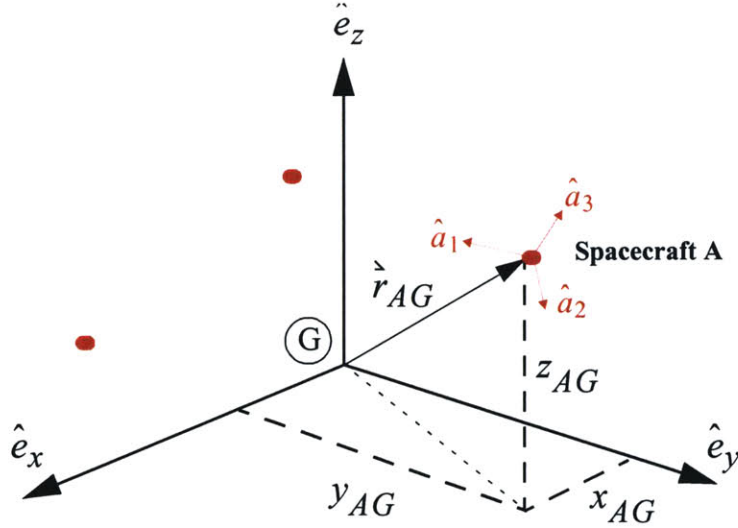


Figure 5.2 Global Reference Frame, G, for Multiple-Spacecraft EMFF Array

To describe the attitude of the spacecraft bus, we introduce three Euler angles, defined as successive rotations about the body-fixed triad, \hat{e}_A :

- first, a rotation α_3 about \hat{a}_3 ,

- then a rotation α_2 about the modified \hat{a}_2 axis, and
- finally, a rotation α_1 about the modified \hat{a}_1 axis.

Euler angle rotations of other spacecraft in the array may be defined analogously. For instance, spacecraft B will rotate first by β_3 about \hat{b}_3 , then by β_2 about the modified \hat{b}_2 axis, and finally by β_1 about the modified \hat{b}_1 axis.

We now consider the position and attitude of the RW. Since the RW can translate relative to the spacecraft bus, we can define its position vector relative to the spacecraft's center of mass as:

$$\vec{r}_{CA} = \begin{bmatrix} x_{CA} & y_{CA} & z_{CA} \end{bmatrix} \left\{ \begin{array}{c} \hat{a}_1 \\ \hat{a}_2 \\ \hat{a}_3 \end{array} \right\} \quad (5.6)$$

where x_{CA} , y_{CA} , and z_{CA} are the cartesian coordinates of the position vector, \vec{r}_{CA} , resolved on the coordinate axes of the spacecraft-fixed frame, A. The position vector of the RW relative to the global frame, G, is then:

$$\vec{r}_{CG} = \vec{r}_{CA} + \vec{r}_{AG} = \begin{bmatrix} x_{CA} & y_{CA} & z_{CA} \end{bmatrix} \left\{ \begin{array}{c} \hat{a}_1 \\ \hat{a}_2 \\ \hat{a}_3 \end{array} \right\} + \begin{bmatrix} x_{AG} & y_{AG} & z_{AG} \end{bmatrix} \left\{ \begin{array}{c} \hat{e}_x \\ \hat{e}_y \\ \hat{e}_z \end{array} \right\} \quad (5.7)$$

To describe the attitude of the RW, we introduce three Euler angles, similar to those of the spacecraft, but defined instead as successive rotations about the RW-fixed triads, \hat{e}_C and \hat{e}_D , relative to \hat{e}_A :

- first, a rotation γ_2 about \hat{c}_2 ,
- then a rotation γ_1 about the modified \hat{c}_1 axis, and
- finally, a rotation δ_3 about the modified \hat{d}_3 axis.

Hence δ_3 is the rotation angle of the RW about its spin axis, \hat{d}_3 , which “tips” with the RW relative to the spacecraft bus.

It should be noted that the Euler angles of the spacecraft are defined such that when $\alpha_i = 0$ ($i = 1, 2, 3$), the coordinate frame \hat{e}_A aligns with the global frame, \hat{e}_G . Similarly, the Euler angles of the RW are defined such that when $\gamma_j = 0$ ($j = 1, 2$), the coordinate frame \hat{e}_C aligns with \hat{e}_A , and when $\delta_3 = 0$, the coordinate frame \hat{e}_D aligns with \hat{e}_C . Hence when all the Euler angles of the spacecraft and the RW are zero, the coordinate frames \hat{e}_A , \hat{e}_C , and \hat{e}_D all align with the global frame, \hat{e}_G . (Analogous statements can be made for each additional spacecraft in the array.)

Also, although the coordinates of spacecraft A and its RW have been defined here, analogous coordinates may be defined for the remaining $n - 1$ spacecraft in the n -spacecraft array. The coordinates defined for spacecraft A and its RW are summarized in Table 5.1.

TABLE 5.1 Summary of the Coordinates Defined for Spacecraft A and its Reaction Wheel (RW-3)

	Position Coordinates	Attitude Coordinates
Spacecraft A	x_{AG}, y_{AG}, z_{AG} (Equation 5.5)	$\alpha_3, \alpha_2, \alpha_1$ (Page 78)
RW-3	x_{CA}, y_{CA}, z_{CA} (Equation 5.6)	$\gamma_2, \gamma_1, \delta_3$ (Page 79)

5.2.4 Rotation Matrices

With the Euler angles defined in Section 5.2.3, we can now express rotation matrices to relate the coordinate frame triads, \hat{e}_G , \hat{e}_A , \hat{e}_C , and \hat{e}_D , to one another. We define the following three rotation matrices as functions of an arbitrary angle, θ :

$$R_1(\theta) \equiv \begin{bmatrix} 1 & 0 & 0 \\ 0 & c\theta & -s\theta \\ 0 & s\theta & c\theta \end{bmatrix} \quad (5.8)$$

$$R_2(\theta) = \begin{bmatrix} c\theta & 0 & s\theta \\ 0 & 1 & 0 \\ -s\theta & 0 & c\theta \end{bmatrix} \quad (5.9)$$

$$R_3(\theta) = \begin{bmatrix} c\theta & -s\theta & 0 \\ s\theta & c\theta & 0 \\ 0 & 0 & 1 \end{bmatrix} \quad (5.10)$$

where $c\theta$ and $s\theta$ denote $\cos(\theta)$ and $\sin(\theta)$, respectively.

Hence the coordinate frames, \hat{e}_G , \hat{e}_A , \hat{e}_C , and \hat{e}_D , are related as:

$$\hat{e}_G = R_3(\alpha_3)R_2(\alpha_2)R_1(\alpha_1)\hat{e}_A \quad (5.11)$$

$$\hat{e}_A = R_2(\gamma_2)R_1(\gamma_1)\hat{e}_C \quad (5.12)$$

$$\hat{e}_C = R_3(\delta_3)\hat{e}_D \quad (5.13)$$

Conversely, since $R_i^{-1}(\theta) = R_i^T(\theta)$ for $i = 1, 2, 3$, Equations 5.8, 5.9, and 5.10 can be expressed as:

$$\hat{e}_A = R_1^T(\alpha_1)R_2^T(\alpha_2)R_3^T(\alpha_3)\hat{e}_G \quad (5.14)$$

$$\hat{e}_C = R_1^T(\gamma_1)R_2^T(\gamma_2)\hat{e}_A \quad (5.15)$$

$$\hat{e}_D = R_3^T(\delta_3)\hat{e}_C \quad (5.16)$$

5.2.5 Velocity Vectors

Angular Velocity Vectors

While the Euler angles that characterize the attitude of a spacecraft and its reaction wheel were defined in Section 5.2.3, we discuss here the *angular velocity vectors* of the space-

craft and reaction wheel, and the relationships between the angular velocity vectors and the Euler angles.

We first introduce some useful notation. In order to describe velocity vectors as relative to some reference frame, we indicate the reference frame by a pre-superscript, and the body under consideration by a post-superscript. For instance, the angular velocity vector of spacecraft A with respect to the global coordinate frame, G, is denoted ${}^G\vec{\omega}^A$, and is called “the angular velocity of A in G.”

With this notation, we proceed to relate the angular velocity vectors of the system to the Euler angles. As described in Section 5.2.3, the attitude of spacecraft A is characterized first by a rotation α_3 about \hat{a}_3 , then a rotation α_2 about \hat{a}_2 , and finally, a rotation α_1 about \hat{a}_1 . Since the Euler angles are defined such that \hat{e}_A and \hat{e}_G are aligned when the angles are zero (and thus \hat{a}_3 and \hat{e}_z are aligned when the angles are zero), the first rotation can equivalently be described as a rotation, α_3 , about \hat{e}_z . Then the second rotation, α_2 , is actually about a *modified* (or intermediate) \hat{a}_2 , which we call $\hat{a}_{2'}$, that represents the \hat{a}_2 axis *after* the rotation α_3 but *before* the rotation α_1 . Finally, the third rotation, α_1 , is indeed about the \hat{a}_1 axis, as it exists after the first two rotations. The *angular velocity vector of A in G* can thus be expressed as:

$${}^G\vec{\omega}^A = \dot{\alpha}_3 \hat{e}_z + \dot{\alpha}_2 \hat{a}_{2'} + \dot{\alpha}_1 \hat{a}_1 \quad (5.17)$$

In order to express the components of ${}^G\vec{\omega}^A$ on axes of the same coordinate frame, we use the rotation matrix definitions in Section 5.2.4 and the coordinate frame definitions in Section 5.2.2. Hence Equation 5.17 may be written as:

$$\begin{aligned} {}^G\vec{\omega}^A &= \dot{\alpha}_3 \begin{bmatrix} 0 & 0 & 1 \end{bmatrix} \hat{e}_G + \dot{\alpha}_2 \begin{bmatrix} 0 & 1 & 0 \end{bmatrix} \hat{e}_A + \dot{\alpha}_1 \begin{bmatrix} 1 & 0 & 0 \end{bmatrix} \hat{e}_A \\ &= \dot{\alpha}_3 \begin{bmatrix} 0 & 0 & 1 \end{bmatrix} R_3(\alpha_3) R_2(\alpha_2) R_1(\alpha_1) \hat{e}_A \\ &\quad + \dot{\alpha}_2 \begin{bmatrix} 0 & 1 & 0 \end{bmatrix} R_2(\alpha_2) R_1(\alpha_1) \hat{e}_A \\ &\quad + \dot{\alpha}_1 \begin{bmatrix} 1 & 0 & 0 \end{bmatrix} \hat{e}_A \end{aligned} \quad (5.18)$$

Finally, since a given body-fixed axis, \hat{a}_i ($i = 1, 2, 3$), remains fixed in direction during an isolated rotation about that axis, we recognize that $\begin{bmatrix} 0 & 0 & 1 \end{bmatrix} R_3 R_2 R_1 \hat{e}_A$ is equivalent to $\begin{bmatrix} 0 & 0 & 1 \end{bmatrix} R_2 R_1 \hat{e}_A$, and similarly, $\begin{bmatrix} 0 & 1 & 0 \end{bmatrix} R_2 R_1 \hat{e}_A$ is equivalent to $\begin{bmatrix} 0 & 1 & 0 \end{bmatrix} R_1 \hat{e}_A$. (This is also evident in a purely mathematical sense, by inspection of the forms of the rotation matrices, R_3 and R_2 .) Hence 5.18 may be expressed as:

$$\begin{aligned} {}^G\vec{\omega}^A &= \dot{\alpha}_3 \begin{bmatrix} 0 & 0 & 1 \end{bmatrix} R_2(\alpha_2) R_1(\alpha_1) \hat{e}_A \\ &\quad + \dot{\alpha}_2 \begin{bmatrix} 0 & 1 & 0 \end{bmatrix} R_1(\alpha_1) \hat{e}_A \\ &\quad + \dot{\alpha}_1 \begin{bmatrix} 1 & 0 & 0 \end{bmatrix} \hat{e}_A \end{aligned} \quad (5.19)$$

Now consider ${}^G\vec{\omega}^D$, the angular velocity vector of the reaction wheel (D) with respect to the global, inertial reference frame (G). ${}^G\vec{\omega}^D$ can be expressed as a sum of *relative* angular velocity vectors [20]:

$${}^G\vec{\omega}^D = {}^C\vec{\omega}^D + {}^A\vec{\omega}^C + {}^G\vec{\omega}^A \quad (5.20)$$

where ${}^C\vec{\omega}^D$ is the angular velocity vector of D with respect to the reference frame C, ${}^A\vec{\omega}^C$ is the angular velocity vector of C with respect to the reference frame A, and ${}^G\vec{\omega}^A$ (defined in 5.19) is the angular velocity of A with respect to the inertial reference frame, G.

Because the reference frame, D, is constrained to rotate only by angle δ_3 about axis \hat{d}_3 relative to C, the expression for ${}^C\vec{\omega}^D$ is simple:

$${}^C\vec{\omega}^D = \dot{\delta}_3 \hat{d}_3 = \dot{\delta}_3 \begin{bmatrix} 0 & 0 & 1 \end{bmatrix} \hat{e}_D \quad (5.21)$$

Recall that the frame C is derived from A as first a rotation γ_2 about \hat{c}_2 (which is initially aligned with \hat{a}_2), then a rotation γ_1 about the \hat{c}_1 axis, as it exists after undergoing the rotation γ_2 . Analogous to the definition of ${}^G\vec{\omega}^A$, we can thus write:

$$\begin{aligned}
{}^A\dot{\omega}^C &= \dot{\gamma}_2 \hat{a}_2 + \dot{\gamma}_1 \hat{c}_1 \\
&= \dot{\gamma}_2 \begin{bmatrix} 0 & 1 & 0 \end{bmatrix} \hat{e}_A + \dot{\gamma}_1 \begin{bmatrix} 1 & 0 & 0 \end{bmatrix} \hat{e}_C \\
&= \dot{\gamma}_2 \begin{bmatrix} 0 & 1 & 0 \end{bmatrix} R_2(\gamma_2) R_1(\gamma_1) R_3(\delta_3) \hat{e}_D + \dot{\gamma}_1 \begin{bmatrix} 1 & 0 & 0 \end{bmatrix} R_3(\delta_3) \hat{e}_D \\
&= \dot{\gamma}_2 \begin{bmatrix} 0 & 1 & 0 \end{bmatrix} R_1(\gamma_1) R_3(\delta_3) \hat{e}_D + \dot{\gamma}_1 \begin{bmatrix} 1 & 0 & 0 \end{bmatrix} R_3(\delta_3) \hat{e}_D
\end{aligned} \tag{5.22}$$

Substituting Equations 5.21, 5.22, and 5.19 into Equation 5.20 yields the angular velocity of the reaction wheel with respect to the global frame:

$$\begin{aligned}
{}^G\dot{\omega}^D &= \dot{\delta}_3 \begin{bmatrix} 0 & 0 & 1 \end{bmatrix} \hat{e}_D \\
&\quad + \dot{\gamma}_2 \begin{bmatrix} 0 & 1 & 0 \end{bmatrix} R_1(\gamma_1) R_3(\delta_3) \hat{e}_D + \dot{\gamma}_1 \begin{bmatrix} 1 & 0 & 0 \end{bmatrix} R_3(\delta_3) \hat{e}_D \\
&\quad + \dot{\alpha}_3 \begin{bmatrix} 0 & 0 & 1 \end{bmatrix} R_2(\alpha_2) R_1(\alpha_1) \hat{e}_A + \dot{\alpha}_2 \begin{bmatrix} 0 & 1 & 0 \end{bmatrix} R_1(\alpha_1) \hat{e}_A + \dot{\alpha}_1 \begin{bmatrix} 1 & 0 & 0 \end{bmatrix} \hat{e}_A
\end{aligned} \tag{5.23}$$

Expressed with components in consistent coordinate frames, ${}^G\dot{\omega}^D$ becomes:

$$\begin{aligned}
{}^G\dot{\omega}^D &= \left\{ \dot{\delta}_3 \begin{bmatrix} 0 & 0 & 1 \end{bmatrix} + \left(\dot{\gamma}_2 \begin{bmatrix} 0 & 1 & 0 \end{bmatrix} R_1(\gamma_1) + \dot{\gamma}_1 \begin{bmatrix} 1 & 0 & 0 \end{bmatrix} \right) R_3(\delta_3) \right. \\
&\quad \left. + \left(\dot{\alpha}_3 \begin{bmatrix} 0 & 0 & 1 \end{bmatrix} R_2(\alpha_2) R_1(\alpha_1) + \dot{\alpha}_2 \begin{bmatrix} 0 & 1 & 0 \end{bmatrix} R_1(\alpha_1) + \dot{\alpha}_1 \begin{bmatrix} 1 & 0 & 0 \end{bmatrix} \right) R_2(\gamma_2) R_1(\gamma_1) R_3(\delta_3) \right\} \hat{e}_D
\end{aligned} \tag{5.24}$$

Using the definitions in 5.19, 5.22, 5.21, and 5.24, we define the components of ${}^G\dot{\omega}^A$, ${}^A\dot{\omega}^C$, ${}^C\dot{\omega}^D$, and ${}^G\dot{\omega}^D$, respectively, as:

$${}^G\dot{\omega}^A \equiv \left[{}^G\omega_1^A \ {}^G\omega_2^A \ {}^G\omega_3^A \right] \left\{ \begin{array}{c} \hat{a}_1 \\ \hat{a}_2 \\ \hat{a}_3 \end{array} \right\} \tag{5.25}$$

$${}^A\vec{\omega}^C \equiv \begin{bmatrix} {}^A\omega_1^C & {}^A\omega_2^C & {}^A\omega_3^C \end{bmatrix} \begin{Bmatrix} \hat{d}_1 \\ \hat{d}_2 \\ \hat{d}_3 \end{Bmatrix} \quad (5.26)$$

$${}^C\vec{\omega}^D \equiv \begin{bmatrix} {}^C\omega_1^D & {}^C\omega_2^D & {}^C\omega_3^D \end{bmatrix} \begin{Bmatrix} \hat{d}_1 \\ \hat{d}_2 \\ \hat{d}_3 \end{Bmatrix} \quad (5.27)$$

$${}^G\vec{\omega}^D \equiv \begin{bmatrix} {}^G\omega_1^D & {}^G\omega_2^D & {}^G\omega_3^D \end{bmatrix} \begin{Bmatrix} \hat{d}_1 \\ \hat{d}_2 \\ \hat{d}_3 \end{Bmatrix} \quad (5.28)$$

Notice the components of ${}^G\vec{\omega}^A$, as defined, are resolved on the \hat{e}_A frame, while the components of the remaining angular velocity vectors, as defined, are resolved on the \hat{e}_D frame. Table 5.2 lists the explicit expressions for the components of ${}^G\vec{\omega}^A$, ${}^A\vec{\omega}^C$, ${}^C\vec{\omega}^D$, and ${}^G\vec{\omega}^D$, from inspection of Equations 5.19, 5.22, 5.21, and 5.24 (consistent with the definitions in Equations 5.25-5.28).

While the expressions in Table 5.2 represent the rotational kinematics of spacecraft A and its reaction wheel, similar expressions will represent the kinematics of spacecraft B and its reaction wheel, as well as all other spacecraft in the array and their associated reaction wheels.

Translational Velocity Vectors

Recall from Equations 5.5 and 5.7 the position vectors, \vec{r}_{AG} and \vec{r}_{CG} , of the centers of mass of spacecraft A and its reaction wheel, respectively, relative to the global, inertial frame, G. The velocity vector of spacecraft A with respect to the inertial frame, G, is then:

TABLE 5.2 Components of the Angular Velocity Vectors in Terms of Euler Angles

Angular Velocity Component	Definition (Function of Euler Angles)
${}^G\omega_1^A$	$-\dot{\alpha}_3 s\alpha_2 + \dot{\alpha}_1$
${}^G\omega_2^A$	$\dot{\alpha}_3 s\alpha_1 c\alpha_2 + \dot{\alpha}_2 c\alpha_1$
${}^G\omega_3^A$	$\dot{\alpha}_3 c\alpha_1 c\alpha_2 - \dot{\alpha}_2 s\alpha_1$
${}^A\omega_1^C$	$\dot{\gamma}_2 c\gamma_1 s\delta_3 + \dot{\gamma}_1 c\delta_3$
${}^A\omega_2^C$	$\dot{\gamma}_2 c\gamma_1 c\delta_3 - \dot{\gamma}_1 s\delta_3$
${}^A\omega_3^C$	$-\dot{\gamma}_2 s\gamma_1$
${}^C\omega_1^D$	0
${}^C\omega_2^D$	0
${}^C\omega_3^D$	$\dot{\delta}_3$
${}^G\omega_1^D$	${}^C\omega_1^D + {}^A\omega_1^C + {}^G\omega_1^A(s\gamma_1 s\gamma_2 s\delta_3 + c\gamma_2 c\delta_3) + {}^G\omega_2^A(c\gamma_1 s\delta_3) + {}^G\omega_3^A(s\gamma_1 c\gamma_2 s\delta_3 - s\gamma_2 c\delta_3)$
${}^G\omega_2^D$	${}^C\omega_2^D + {}^A\omega_2^C + {}^G\omega_1^A(s\gamma_1 s\gamma_2 c\delta_3 - c\gamma_2 s\delta_3) + {}^G\omega_2^A(c\gamma_1 c\delta_3) + {}^G\omega_3^A(s\gamma_1 c\gamma_2 c\delta_3 + s\gamma_2 s\delta_3)$
${}^G\omega_3^D$	${}^C\omega_3^D + {}^A\omega_3^C + {}^G\omega_1^A(c\gamma_1 s\gamma_2) + {}^G\omega_2^A(-s\gamma_1) + {}^G\omega_3^A(c\gamma_1 c\gamma_2)$

$$\overset{G_A}{v} = \dot{\overset{G_A}{r}} = \left[\begin{array}{c} \dot{x}_{AG} \\ \dot{y}_{AG} \\ \dot{z}_{AG} \end{array} \right] \left\{ \begin{array}{l} \hat{e}_x \\ \hat{e}_y \\ \hat{e}_z \end{array} \right\} \quad (5.29)$$

where (\cdot) denotes a derivative with respect to time. Note that because G is an inertial frame, the unit vectors \hat{e}_x , \hat{e}_y , and \hat{e}_z are constant with respect to time, and therefore $\dot{\hat{e}}_x = \dot{\hat{e}}_y = \dot{\hat{e}}_z = 0$.

Similarly, the velocity vector of the reaction wheel on spacecraft A with respect to the inertial frame, G, is:

$$\overset{G}{\dot{r}}_{CA} = \overset{\dot{s}}{r}_{CA} + \overset{\dot{s}}{r}_{AG} \quad (5.30)$$

where:

$$\overset{\dot{s}}{r}_{CA} = \left[\begin{array}{c} \dot{x}_{CA} \ \dot{y}_{CA} \ \dot{z}_{CA} \end{array} \right] \left\{ \begin{array}{c} \hat{a}_1 \\ \hat{a}_2 \\ \hat{a}_3 \end{array} \right\} + \left[\begin{array}{c} x_{CA} \ y_{CA} \ z_{CA} \end{array} \right] \left\{ \begin{array}{c} \dot{\hat{a}}_1 \\ \dot{\hat{a}}_2 \\ \dot{\hat{a}}_3 \end{array} \right\} \quad (5.31)$$

From kinematics, we know that [20]:

$$\dot{\hat{a}}_i = {}^G\vec{\omega}^A \times \hat{a}_i, \quad i = 1, 2, 3 \quad (5.32)$$

where ${}^G\vec{\omega}^A$ is the angular velocity vector of spacecraft A with respect to the global coordinate frame, G, as defined in 5.19. Hence:

$$\left\{ \begin{array}{c} \dot{\hat{a}}_1 \\ \dot{\hat{a}}_2 \\ \dot{\hat{a}}_3 \end{array} \right\} = \left\{ \begin{array}{c} {}^G\vec{\omega}^A \times \hat{a}_1 \\ {}^G\vec{\omega}^A \times \hat{a}_2 \\ {}^G\vec{\omega}^A \times \hat{a}_3 \end{array} \right\} = \left\{ \begin{array}{c} {}^G\omega_3^A \hat{a}_2 - {}^G\omega_2^A \hat{a}_3 \\ {}^G\omega_1^A \hat{a}_3 - {}^G\omega_3^A \hat{a}_1 \\ {}^G\omega_2^A \hat{a}_1 - {}^G\omega_1^A \hat{a}_2 \end{array} \right\} \quad (5.33)$$

so that Equation 5.31 may be expressed as:

$$\begin{aligned} \overset{\dot{s}}{r}_{CA} &= \left[\begin{array}{c} \dot{x}_{CA} \ \dot{y}_{CA} \ \dot{z}_{CA} \end{array} \right] \left\{ \begin{array}{c} \hat{a}_1 \\ \hat{a}_2 \\ \hat{a}_3 \end{array} \right\} + \left[\begin{array}{c} x_{CA} \ y_{CA} \ z_{CA} \end{array} \right] \left\{ \begin{array}{c} {}^G\omega_3^A \hat{a}_2 - {}^G\omega_2^A \hat{a}_3 \\ {}^G\omega_1^A \hat{a}_3 - {}^G\omega_3^A \hat{a}_1 \\ {}^G\omega_2^A \hat{a}_1 - {}^G\omega_1^A \hat{a}_2 \end{array} \right\} \\ &= \left\{ \begin{array}{c} (\dot{x}_{CA} - y_{CA} {}^G\omega_3^A + z_{CA} {}^G\omega_2^A) \\ (\dot{y}_{CA} + x_{CA} {}^G\omega_3^A - z_{CA} {}^G\omega_1^A) \\ (\dot{z}_{CA} - x_{CA} {}^G\omega_2^A + y_{CA} {}^G\omega_1^A) \end{array} \right\}^T \left\{ \begin{array}{c} \hat{a}_1 \\ \hat{a}_2 \\ \hat{a}_3 \end{array} \right\} \end{aligned} \quad (5.34)$$

Substituting Equations 5.34 and 5.29 into Equation 5.30 yields the velocity vector of the reaction wheel on spacecraft A with respect to the inertial frame, G:

$$\overset{G}{v}_{\Delta C} = \left\{ \begin{array}{l} (\dot{x}_{CA} - y_{CA} \overset{G}{\omega}_3^A + z_{CA} \overset{G}{\omega}_2^A) \\ (\dot{y}_{CA} + x_{CA} \overset{G}{\omega}_3^A - z_{CA} \overset{G}{\omega}_1^A) \\ (\dot{z}_{CA} - x_{CA} \overset{G}{\omega}_2^A + y_{CA} \overset{G}{\omega}_1^A) \end{array} \right\}^T \left\{ \begin{array}{l} \hat{a}_1 \\ \hat{a}_2 \\ \hat{a}_3 \end{array} \right\} + \left[\begin{array}{l} \dot{x}_{AG} \dot{y}_{AG} \dot{z}_{AG} \end{array} \right] \left\{ \begin{array}{l} \hat{e}_x \\ \hat{e}_y \\ \hat{e}_z \end{array} \right\} \quad (5.35)$$

5.2.6 Actuator Description

As described in Section 5.2.1, each spacecraft has three reaction wheels (RWs) for attitude control, but to simplify the derivation of the system's equations of motion, we will model only one reaction wheel on each vehicle. (For example, for spacecraft A, we model only the third RW, whose spin axis is aligned with \hat{a}_3 in Figure 5.1.) Since the derivation for the other reaction wheels would be identical, the terms that characterize their behavior may be added by inspection of the nonlinear equations of motion, once they are derived assuming only one RW per vehicle.

Reaction wheels function on the principle of conservation of angular momentum. Consider a single spacecraft-RW pair with a common spin axis. If both bodies are initially at rest, and the RW begins to spin about the common axis, the spacecraft must spin in the opposite direction about that axis to maintain the net angular momentum of the system. A motor is used to apply the torque that causes the RW to spin relative to the spacecraft. Because the motor serves as a mechanical interface between the RW and the spacecraft bus, it applies a torque on the bus that is equal in magnitude and opposite in direction to that applied to the RW. Hence the RW actuator can be represented by a motor at the spacecraft-RW interface point that applies equal and opposite torques to the two bodies. Also, recall from Chapters 2 and 3 that because the RW spins in inertial space, its nonlinear dynamics cause a gyrostiffening effect on the dynamics of the spacecraft-RW system. Hence the nonlinear dynamics of the spinning RW must be captured in the RW model, in addition to the motor torque.

While reaction wheels are used for attitude control, electromagnets (EMs) are used to control the relative positions and attitudes of the spacecraft in the array. Chapter 1 described some of the benefits and limitations of using electromagnetic actuators in place of thrusters. One very important characteristic is the ability of EMs to control relative separation distances of the vehicles, but not their absolute positions. This is due to the fact that EM forces on two given vehicles are generated by the interaction of the magnetic fields of those two vehicles. Hence the forces generated by the EMs on any two vehicles will be equal in magnitude and opposite in direction.¹

Each electromagnet is formed by wrapping a conducting wire multiple times to form a coil, as depicted in Figure 5.3. A power supply is used to run current through the coil, generating a local magnetic field [21, 22]. If we make the assumption that the coils in the EMFF system are small compared to the separation distances between the vehicles in the array, the magnetic fields generated by the coils can be approximated as magnetic dipole moments. The dipole moment, $\hat{\mu}$, of each coil may then be modeled as a vector with a given field strength (magnitude) and direction. The dipole moment vector of a coil, depicted in Figure 5.3, is oriented perpendicular to the enclosed area of the coil, and is therefore parallel to the coil's axis of symmetry, denoted \hat{e}_μ . The dipole moment may be expressed as:

$$\hat{\mu} = \mu \hat{e}_\mu = niA \hat{e}_\mu \quad (5.36)$$

where n is the number of concentric wraps of the wire around the perimeter of the coil, i is the current passing through the wire, and A is the area enclosed by the coil. Thus the *strength* of the dipole moment is proportional to the number of wire wraps, the current running through the wire, and the enclosed area of the coil. Since n and A are constants

1. Although the EMs will be used primarily as relative position actuators, it should be noted that their interactions will also cause resultant torques to be applied to the vehicles. The EM torques, unlike the EM forces, are not necessarily equal and opposite, since a third variable is involved in the conservation of angular momentum: the torque on the entire array, and the resulting angular acceleration of the array about its center point.

fixed by the coil's geometry, the current, i , may be used to actively control the dipole strength.

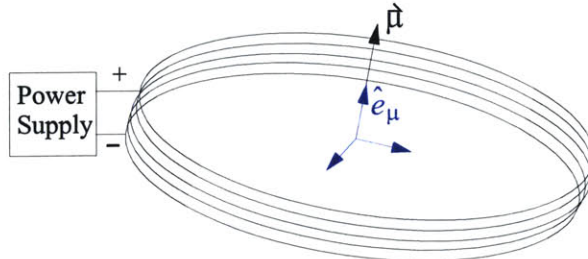


Figure 5.3 Typical Electromagnetic Coil Consisting of Multiple Windings of Conducting Wire

We now assume each spacecraft is equipped with three orthogonal electromagnetic actuators. On spacecraft A, the three EMs are oriented such that their axes of symmetry are aligned with the body-fixed \hat{a}_1 , \hat{a}_2 , and \hat{a}_3 axes, respectively. Similarly, for another spacecraft, B, the three EMs would be oriented such that their axes of symmetry are aligned with the body-fixed \hat{b}_1 , \hat{b}_2 , and \hat{b}_3 axes, and so forth. A schematic of the EM configuration is shown in Figure 5.4.

Assuming that the three electromagnets on each spacecraft are geometrically identical, we define the magnetic dipole moments of the electromagnets on spacecraft A as:

$$\hat{\mu}_{A_1} = \mu_{A_1} \hat{a}_1 = n_A i_{A_1} A_A \hat{a}_1 \quad (5.37)$$

$$\hat{\mu}_{A_2} = \mu_{A_2} \hat{a}_2 = n_A i_{A_2} A_A \hat{a}_2 \quad (5.38)$$

$$\hat{\mu}_{A_3} = \mu_{A_3} \hat{a}_3 = n_A i_{A_3} A_A \hat{a}_3 \quad (5.39)$$

where n_A is the number of conductor wraps for each coil on spacecraft A, A_A is the enclosed area of each coil on spacecraft A, and i_{A_1} , i_{A_2} , and i_{A_3} are the currents running through the three coils on spacecraft A, respectively. The magnitudes (μ_{A_1} , μ_{A_2} , μ_{A_3}) of the magnetic moment vectors represent the electromagnetic dipole strengths of the three

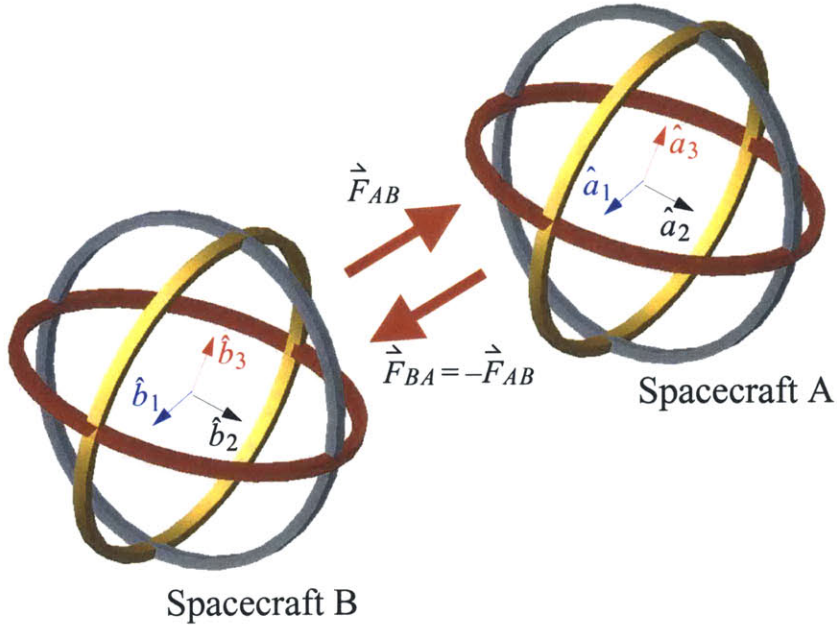


Figure 5.4 Schematic of the Electromagnetic Actuator Configuration in an EMFF Array

EM coils on spacecraft A. Given a fixed coil geometry, they are controlled by varying the respective currents in each coil.

The magnetic moments of the electromagnets on another spacecraft, B, are defined similarly as $\hat{\mu}_{B_1}$, $\hat{\mu}_{B_2}$, and $\hat{\mu}_{B_3}$, and point along the local body-fixed \hat{b}_1 , \hat{b}_2 , and \hat{b}_3 axes, respectively. For this analysis, we assume that all spacecraft contain EM coils of the same geometry, so that:

$$n_A = n_B = n_S, \quad A_A = A_B = A_S \quad (5.40)$$

where n_S and A_S are the number of coil wraps and enclosed area, respectively, of any coil on any spacecraft in the array. Note, however, that the currents (i_{A_1} , i_{A_2} , i_{A_3} , i_{B_1} , and so forth) running through each coil are distinct, and are allowed to vary independently; they are the control variables of the EM actuators.

Finally, with the assumption that each coil may be modeled as an idealized magnetic dipole, a resultant magnetic dipole moment for each spacecraft may be expressed as a superposition of all of its individual dipole moment vectors. For spacecraft A, whose

magnetic dipole “components” are expressed in Equations 5.37-5.39, the resultant magnetic dipole moment may be expressed as:

$$\begin{aligned}\hat{\mu}_A &\equiv \hat{\mu}_{A_1} + \hat{\mu}_{A_2} + \hat{\mu}_{A_3} \\ &= n_S A_S \left[\begin{array}{ccc} i_{A_1} & i_{A_2} & i_{A_3} \end{array} \right] \left\{ \begin{array}{c} \hat{a}_1 \\ \hat{a}_2 \\ \hat{a}_3 \end{array} \right\} \quad (5.41)\end{aligned}$$

Similarly, for another spacecraft, B, in the array, the resultant magnetic dipole moment may be expressed as:

$$\begin{aligned}\hat{\mu}_B &\equiv \hat{\mu}_{B_1} + \hat{\mu}_{B_2} + \hat{\mu}_{B_3} \\ &= n_S A_S \left[\begin{array}{ccc} i_{B_1} & i_{B_2} & i_{B_3} \end{array} \right] \left\{ \begin{array}{c} \hat{b}_1 \\ \hat{b}_2 \\ \hat{b}_3 \end{array} \right\} \quad (5.42)\end{aligned}$$

5.3 Electromagnetic Forces and Torques

We now characterize the electromagnetic forces and torques applied to a spacecraft by the interaction of its magnetic field with that of another spacecraft. In the following subsection, we characterize the magnetic moment created by each vehicle, and in Section 5.3.2, we provide expressions for the resulting electromagnetic forces and torques.

5.3.1 Magnetic Moment Vectors Expressed in Global Coordinates

The dipole moments defined in Equations 5.41 and 5.42 are expressed in components resolved on two different coordinate frames: \hat{e}_A and \hat{e}_B , respectively. Since the dipole moments on various spacecraft will be used to calculate the EM forces and moments acting between the spacecraft, it is useful to express the dipole moments in coordinates resolved on the same coordinate axes.

The relationships between the coordinate frames were defined in terms of Euler angle rotations in Equations 5.14-5.16. Specifically, Equation 5.14 allows \hat{e}_A , the body-fixed frame on spacecraft A, to be expressed in terms of \hat{e}_G , the global, inertial frame, using the Euler angle rotations of A (defined in Section 5.2.3). Substituting this expression for \hat{e}_A into Equation 5.41 yields the resultant dipole moment of spacecraft A, in components resolved on the global frame:

$$\hat{\mu}_A = n_S A_S \begin{bmatrix} i_{A_1} & i_{A_2} & i_{A_3} \end{bmatrix} \begin{bmatrix} R_1^T(\alpha_1) & R_2^T(\alpha_2) & R_3^T(\alpha_3) \end{bmatrix} \begin{Bmatrix} \hat{e}_x \\ \hat{e}_y \\ \hat{e}_z \end{Bmatrix} \quad (5.43)$$

Similarly, the resultant dipole moment of spacecraft B may be expressed as:

$$\hat{\mu}_B = n_S A_S \begin{bmatrix} i_{B_1} & i_{B_2} & i_{B_3} \end{bmatrix} \begin{bmatrix} R_1^T(\beta_1) & R_2^T(\beta_2) & R_3^T(\beta_3) \end{bmatrix} \begin{Bmatrix} \hat{e}_x \\ \hat{e}_y \\ \hat{e}_z \end{Bmatrix} \quad (5.44)$$

Hence the products of terms premultiplying $\begin{bmatrix} \hat{e}_x & \hat{e}_y & \hat{e}_z \end{bmatrix}^T$ in Equations 5.43 and 5.44 represent the cartesian coordinates of $\hat{\mu}_A$ and $\hat{\mu}_B$, respectively, resolved on the global frame, \hat{e}_G .

5.3.2 Calculation of Electromagnetic Forces and Torques

We now consider the EM forces and torques (loads) exerted on one spacecraft by another, due to the interaction of their magnetic fields. If we first write a general expression for the loads on one spacecraft due to the magnetic field of another spacecraft, we can then superimpose these expressions to determine the loads on the spacecraft due to the fields of all other spacecraft in the array.

Consider spacecraft A and B. With the magnetic dipole moments, $\vec{\mu}_A$ and $\vec{\mu}_B$, as defined in Section 5.3.1, the force and torque exerted on the EMs of spacecraft A by those of spacecraft B are, respectively [22]:

$$\vec{F}_{AB} = \vec{\mu}_A \bullet \nabla \vec{B}_B|_A \quad (5.45)$$

$$\vec{T}_{AB} = \vec{\mu}_A \times \vec{B}_B|_A \quad (5.46)$$

where ∇ represents the gradient operator¹, \vec{B}_B represents the spatially varying magnetic field due to $\vec{\mu}_B$, and $\cdot|_A$ indicates evaluation of the field at the location of spacecraft A.

The field due to $\vec{\mu}_B$ at an arbitrary position $\vec{\xi} = \xi \hat{e}_\xi$ relative to spacecraft B is:

$$\vec{B}_B(\vec{\xi}) = \frac{\mu_0}{4\pi\xi^3} [-\vec{\mu}_B + 3(\vec{\mu}_B \bullet \hat{e}_\xi) \hat{e}_\xi] \quad (5.47)$$

where $\mu_0 = 4\pi \cdot 10^{-7}$ T·m/A is the permeability of free space.

We assume that $2r$ is the distance between spacecraft A and B, and \hat{e}_r is the unit vector pointing from spacecraft B to spacecraft A. Then from Equation 5.47, the field due to $\vec{\mu}_B$ at the location of spacecraft A is:

$$\vec{B}_B|_A = \frac{\mu_0}{4\pi(2r)^3} [-\vec{\mu}_B + 3(\vec{\mu}_B \bullet \hat{e}_r) \hat{e}_r] \quad (5.48)$$

where:

$$2r = \sqrt{(x_{AG} - x_{BG})^2 + (y_{AG} - y_{BG})^2 + (z_{AG} - z_{BG})^2} \quad (5.49)$$

1. Note when performing the gradient operation on $\vec{B}_B|_A$ in Equation 5.45 that the origin of the gradient operator must be placed at the location of $\vec{\mu}_B$, rather than at the global origin.

$$\hat{e}_r = \frac{1}{2r} \begin{bmatrix} x_{AG} - x_{BG} & y_{AG} - y_{BG} & z_{AG} - z_{BG} \end{bmatrix} \begin{Bmatrix} \hat{e}_x \\ \hat{e}_y \\ \hat{e}_z \end{Bmatrix} \quad (5.50)$$

Note that $\hat{\vec{B}}_A|_B$, the field due to $\vec{\mu}_A$ at the location of spacecraft B, may be determined by simply replacing $\vec{\mu}_B$ with $\vec{\mu}_A$ in Equation 5.48.

Finally, evaluating Equations 5.45 and 5.48 yields:

$$\hat{\vec{F}}_{AB} = \frac{3\mu_0}{64\pi r^4} \left[(\vec{\mu}_A \bullet \vec{\mu}_B) \hat{e}_r + (\vec{\mu}_A \bullet \hat{e}_r) \vec{\mu}_B + (\vec{\mu}_B \bullet \hat{e}_r) \vec{\mu}_A - 5(\vec{\mu}_A \bullet \hat{e}_r)(\vec{\mu}_B \bullet \hat{e}_r) \hat{e}_r \right] \quad (5.51)$$

and evaluating Equations 5.46 and 5.48 yields:

$$\hat{\vec{T}}_{AB} = \vec{\mu}_A \times \frac{\mu_0}{4\pi(2r)^3} [-\vec{\mu}_B + 3(\vec{\mu}_B \bullet \hat{e}_r) \hat{e}_r] \quad (5.52)$$

Thus to calculate the forces and torques exerted on the EMs of spacecraft A due to those of spacecraft B, we simply substitute $\vec{\mu}_A$, $\vec{\mu}_B$, $2r$, and \hat{e}_r from Equations 5.43, 5.44, 5.49, and 5.50, respectively, into Equations 5.51 and 5.52.

5.4 Nonlinear Equations of Motion

In this section, we use Kane's method to formulate the nonlinear equations of motion for the system described above. Kane's method was reviewed in Chapter 4, and more detailed information on the method is provided in *Dynamics: Theory and Applications* by Kane et al. [20].

5.4.1 Generalized Coordinates and Generalized Speeds

Referring to the degrees of freedom introduced in Section 5.2.3, we now define the generalized coordinates according to Kane's method. Table 5.3 lists the generalized coordinates for spacecraft A in the EMFF array.

TABLE 5.3 Generalized Coordinates for Spacecraft A and RW-3

Generalized Coordinate	Degree of Freedom	Description
q_1	x_{AG}	x Position of Spacecraft A Relative to Global Frame
q_2	y_{AG}	y Position of Spacecraft A Relative to Global Frame
q_3	z_{AG}	z Position of Spacecraft A Relative to Global Frame
q_4	x_{CA}	x Position of RW-3 Relative to Spacecraft Frame A
q_5	y_{CA}	y Position of RW-3 Relative to Spacecraft Frame A
q_6	z_{CA}	z Position of RW-3 Relative to Spacecraft Frame A
q_7	α_3	1 st Euler Angle Rotation of Spacecraft A (about \hat{a}_3)
q_8	α_2	2 nd Euler Angle Rotation of Spacecraft A (about \hat{a}_2)
q_9	α_1	3 rd Euler Angle Rotation of Spacecraft A (about \hat{a}_1)
q_{10}	γ_2	1 st Euler Angle Rotation of RW-3 (about \hat{c}_2)
q_{11}	γ_1	2 nd Euler Angle Rotation of RW-3 (about \hat{c}_1)
q_{12}	δ_3	3 rd Euler Angle Rotation of RW-3 (about \hat{d}_3)

In methods such as Lagrange's method, we would now specify generalized velocities as the time derivatives of the generalized coordinates. Using Kane's method, however, we specify *generalized speeds*, which are linear combinations of the generalized velocities. This allows us to specify generalized speeds as, for instance, the components of a body's angular velocity vector, instead of as the time derivatives of its Euler angles. (We demonstrated in Table 5.2 that the former are linear combinations of the latter.) We will find in the following section that this greatly simplifies the derivation of the rotational equations of motion for a body, since determining the partial angular velocities becomes trivial. The generalized speeds are thus defined in Table 5.4. Notice that the generalized speeds (u_7 - u_{12}) for the rotational degrees of freedom are linear combinations of the corresponding

generalized velocities (the time derivatives of the Euler angles), while the generalized speeds ($u_1 - u_6$) for the translational degrees of freedom are simply equal to the corresponding generalized velocities.

TABLE 5.4 Generalized Speeds for Spacecraft A and RW-3

Generalized Speed	Definition
u_1	\dot{x}_{AG}
u_2	\dot{y}_{AG}
u_3	\dot{z}_{AG}
u_4	\dot{x}_{CA}
u_5	\dot{y}_{CA}
u_6	\dot{z}_{CA}
u_7	$G \omega_1^A$
u_8	$G \omega_2^A$
u_9	$G \omega_3^A$
u_{10}	$G \omega_1^D$
u_{11}	$G \omega_2^D$
u_{12}	$G \omega_3^D$

5.4.2 Partial Velocities and Partial Angular Velocities

The partial velocities and partial angular velocities, defined in Section 4.2.3, may now be determined by inspection of the velocity vectors ($\overset{G_A}{v}$ and $\overset{G_C}{v}$) and the angular velocity vectors ($\overset{G}{\omega}^A$ and $\overset{G}{\omega}^D$), defined respectively in Equations 5.29, 5.35, 5.25, and 5.20/5.28.

The partial velocities corresponding to $\overset{G_A}{v}$ are:

$$\overset{G_A}{v}_1 = \hat{e}_x, \quad \overset{G_A}{v}_2 = \hat{e}_y, \quad \overset{G_A}{v}_3 = \hat{e}_z \quad (5.53)$$

$$\overset{G_A}{v}_i = 0, \quad i = 4, 5, \dots, 12 \quad (5.54)$$

The partial velocities corresponding to ${}^G v^C$ are:

$${}^G v_1^C = \hat{e}_x, \quad {}^G v_2^C = \hat{e}_y, \quad {}^G v_3^C = \hat{e}_z \quad (5.55)$$

$${}^G v_4^C = \hat{a}_1, \quad {}^G v_5^C = \hat{a}_2, \quad {}^G v_6^C = \hat{a}_3 \quad (5.56)$$

$${}^G v_7^C = y_{CA} \hat{a}_3 - z_{CA} \hat{a}_2, \quad {}^G v_8^C = z_{CA} \hat{a}_1 - x_{CA} \hat{a}_3, \quad {}^G v_9^C = x_{CA} \hat{a}_2 - y_{CA} \hat{a}_1 \quad (5.57)$$

$${}^G v_i^C = 0, \quad i = 10, 11, 12 \quad (5.58)$$

The partial velocities corresponding to ${}^G \omega^A$ are:

$${}^G \omega_i^A = 0, \quad i = 1, 2, \dots, 6, 10, 11, 12 \quad (5.59)$$

$${}^G \omega_7^A = \hat{a}_1, \quad {}^G \omega_8^A = \hat{a}_2, \quad {}^G \omega_9^A = \hat{a}_3 \quad (5.60)$$

The partial velocities corresponding to ${}^G \omega^D$ are:

$${}^G \omega_i^D = 0, \quad i = 1, 2, \dots, 6 \quad (5.61)$$

$${}^G \omega_7^D = \hat{a}_1, \quad {}^G \omega_8^D = \hat{a}_2, \quad {}^G \omega_9^D = \hat{a}_3 \quad (5.62)$$

$${}^G \omega_{10}^D = \hat{d}_1, \quad {}^G \omega_{11}^D = \hat{d}_2, \quad {}^G \omega_{12}^D = \hat{d}_3 \quad (5.63)$$

Notice that it was trivial to determine the partial angular velocities by inspection of Equations 5.25, 5.20 and 5.28, rather than 5.19 and 5.24. This is due to the fact that the angular velocity vector components, not the time derivatives of the Euler angles, were chosen as generalized speeds in Section 5.4.1.

5.4.3 Generalized Forces

Generalized Active Forces

We consider four main types of active loads:

- forces and torques caused by the electromagnetic (EM) interactions between spacecraft
- miscellaneous external forces and torques, which represent unknown disturbances
- forces and torques caused by the springs at the spacecraft-reaction wheel (RW) interface, and
- motor torques, which are exerted on the RW to control its spin rate.

Expressions for the *EM forces and torques* were developed in Section 5.3. Assuming the EM loads may be calculated as a function of the relative positions and attitudes of the spacecraft using Equations 5.51 and 5.52, we denote the force on spacecraft A due to the EMs on another spacecraft, B, as:

$$\begin{aligned}\vec{F}_{AB} &= \left[F_{AB,x} \ F_{AB,y} \ F_{AB,z} \right] \left\{ \begin{array}{c} \hat{e}_x \\ \hat{e}_y \\ \hat{e}_z \end{array} \right\} \\ &= \left[F_{AB,1} \ F_{AB,2} \ F_{AB,3} \right] \left\{ \begin{array}{c} \hat{a}_1 \\ \hat{a}_2 \\ \hat{a}_3 \end{array} \right\}\end{aligned}\tag{5.64}$$

where the former expression represents components resolved on the global coordinate frame, and the latter expression represents components resolved on the body-fixed frame of spacecraft A. Recall that expressions relating the various coordinate frames were given in Section 5.2.4.

Similarly, the torque on spacecraft A due to the EMs on spacecraft B may be denoted:

$$\begin{aligned}\dot{\vec{T}}_{AB} &= \left[\begin{array}{ccc} T_{AB,x} & T_{AB,y} & T_{AB,z} \end{array} \right] \left\{ \begin{array}{c} \hat{e}_x \\ \hat{e}_y \\ \hat{e}_z \end{array} \right\} \\ &= \left[\begin{array}{ccc} T_{AB,1} & T_{AB,2} & T_{AB,3} \end{array} \right] \left\{ \begin{array}{c} \hat{a}_1 \\ \hat{a}_2 \\ \hat{a}_3 \end{array} \right\}\end{aligned}\quad (5.65)$$

Note that the EM force specified in Equation 5.64 is assumed to be applied at the center of mass of spacecraft A (excluding the RW mass). If the EM force is applied elsewhere, it can be represented as an equivalent force through the center of mass, plus the torque that would result from the offset of the true loading point from the center of mass. (We treat the spring forces similarly below, since they are applied at the spacecraft-RW interface, and not at the centers of mass of the two bodies.)

Similarly, without characterizing the *miscellaneous external forces* on the spacecraft bus and reaction wheel, respectively, we denote them as:

$$\begin{aligned}\dot{\vec{F}}_A^{ext} &= \left[\begin{array}{ccc} F_{A,x}^{ext} & F_{A,y}^{ext} & F_{A,z}^{ext} \end{array} \right] \left\{ \begin{array}{c} \hat{e}_x \\ \hat{e}_y \\ \hat{e}_z \end{array} \right\} \\ &= \left[\begin{array}{ccc} F_{A,1}^{ext} & F_{A,2}^{ext} & F_{A,3}^{ext} \end{array} \right] \left\{ \begin{array}{c} \hat{a}_1 \\ \hat{a}_2 \\ \hat{a}_3 \end{array} \right\}\end{aligned}\quad (5.66)$$

$$\begin{aligned}\hat{\mathbf{F}}_{RW}^{ext} &= \left[F_{RW,x}^{ext} \ F_{RW,y}^{ext} \ F_{RW,z}^{ext} \right] \begin{Bmatrix} \dot{\hat{\mathbf{e}}}_x \\ \dot{\hat{\mathbf{e}}}_y \\ \dot{\hat{\mathbf{e}}}_z \end{Bmatrix} \\ &= \left[F_{RW,1}^{ext} \ F_{RW,2}^{ext} \ F_{RW,3}^{ext} \right] \begin{Bmatrix} \dot{\hat{\mathbf{a}}}_1 \\ \dot{\hat{\mathbf{a}}}_2 \\ \dot{\hat{\mathbf{a}}}_3 \end{Bmatrix}\end{aligned}\quad (5.67)$$

Analogous disturbance torques, $\hat{\mathbf{T}}_A^{ext}$ and $\hat{\mathbf{T}}_{RW}^{ext}$, may also be defined. These variables will be useful to a user who would like to simulate a given set of disturbances. Random or deterministic loading profiles may then be substituted for these external loads in the final equations of motion. Additionally, RW-induced disturbance forces and torques may be captured in the system model by substituting them for the terms $\hat{\mathbf{F}}_{RW}^{ext}$ and $\hat{\mathbf{T}}_{RW}^{ext}$, respectively.

Next, we must characterize the *spring forces and moments*. As described in Section 5.2.1, the interface between each spacecraft and its RW is modeled as a five-degree-of-freedom (DOF) spring, with three translational stiffnesses and two rotational stiffnesses (about axes perpendicular to the reaction wheel's spin axis). The translational stiffnesses are denoted k_1 , k_2 , and k_3 , along the body-fixed $\hat{\mathbf{a}}_1$, $\hat{\mathbf{a}}_2$, and $\hat{\mathbf{a}}_3$ axes, respectively. The rotational stiffnesses are denoted k_4 and k_5 , about the body-fixed $\hat{\mathbf{a}}_1$ and $\hat{\mathbf{a}}_2$ axes, respectively.

Recalling the definition in Equation 5.6 of the position of the RW relative to spacecraft A, we define the *nominal value* of this position vector to be the one in which no spring forces act:

$$\dot{\vec{r}}_{CA,0} = \begin{bmatrix} 0 & 0 & z_{CA,0} \end{bmatrix} \begin{Bmatrix} \hat{\vec{a}}_1 \\ \hat{\vec{a}}_2 \\ \hat{\vec{a}}_3 \end{Bmatrix} \quad (5.68)$$

In other words, we make the assumption that when the reaction wheel is “at rest” relative to the spacecraft bus, its center of mass lies directly “above” that of the spacecraft, at a distance $z_{CA,0}$ along the $\hat{\vec{a}}_3$ axis from the spacecraft center of mass. Then any relative position other than this nominal one causes the following spring forces to be exerted on the spacecraft bus:

$$\dot{\vec{F}}_A^s = \begin{bmatrix} F_{A,1}^s & F_{A,2}^s & F_{A,3}^s \end{bmatrix} \begin{Bmatrix} \hat{\vec{a}}_1 \\ \hat{\vec{a}}_2 \\ \hat{\vec{a}}_3 \end{Bmatrix} = \begin{bmatrix} k_1 x_{CA} & k_2 y_{CA} & k_3(z_{CA} - z_{CA,0}) \end{bmatrix} \begin{Bmatrix} \hat{\vec{a}}_1 \\ \hat{\vec{a}}_2 \\ \hat{\vec{a}}_3 \end{Bmatrix} \quad (5.69)$$

The spring forces exerted on the reaction wheel are simply equal in magnitude and opposite in direction to those exerted on the spacecraft bus:

$$\dot{\vec{F}}_{RW}^s = -\dot{\vec{F}}_A^s \quad (5.70)$$

Note that the spring forces, $\dot{\vec{F}}_A^s$ and $\dot{\vec{F}}_{RW}^s$, are applied to the spacecraft bus and the reaction wheel, respectively, at their common interface point. Hence we must express each spring force as an equivalent force *applied to the center of mass* of the respective body, *along with the torque resulting from the offset of the body's interface point from its center of mass*. To simplify this expression, we make the assumption that the interface point of the spacecraft lies a distance z_{iA} directly along the spacecraft's $\hat{\vec{a}}_3$ axis, and similarly, the interface point of the reaction wheel lies a distance z_{iC} directly along the reaction wheel's $\hat{\vec{c}}_3$ axis. (z_{iC} will likely be a negative value, or opposite in sign from z_{iA} , as can be seen from inspection of Figure 5.1.) Then the “interface offset” spring torque on the spacecraft is:

$$\vec{T}_A^{s,o} = z_{iA} \hat{a}_3 \times \vec{F}_A^s \quad (5.71)$$

and the “interface offset” spring torque on the reaction wheel is:

$$\vec{T}_{RW}^{s,o} = z_{iC} \hat{c}_3 \times \vec{F}_A^s \quad (5.72)$$

To determine the torques applied by the rotational springs, we first make the assumption that the two rotational spring stiffnesses are equal in value:

$$k_4 = k_5 \quad (5.73)$$

The result of this assumption is that the “restoring” spring torque is proportional to one angle, γ_0 , which is defined as the angle between the RW’s spin axis, \hat{c}_3 , and the body-fixed axis, \hat{a}_3 , of spacecraft A. To define γ_0 , we recognize that:

$$\cos(\gamma_0) = \hat{c}_3 \cdot \hat{a}_3 \quad (5.74)$$

where, from Equation 5.15,

$$\begin{aligned} \hat{c}_3 &= \begin{bmatrix} 0 & 0 & 1 \end{bmatrix} \hat{e}_C = \begin{bmatrix} 0 & 0 & 1 \end{bmatrix} R_1^T(\gamma_1) R_2^T(\gamma_2) \hat{e}_A \\ &= \cos(\gamma_1) \sin(\gamma_2) \hat{a}_1 - \sin(\gamma_1) \hat{a}_2 + \cos(\gamma_1) \cos(\gamma_2) \hat{a}_3 \end{aligned} \quad (5.75)$$

Hence:

$$\hat{c}_3 \cdot \hat{a}_3 = \cos(\gamma_1) \cos(\gamma_2) \quad (5.76)$$

and from Equations 5.74 and 5.76,

$$\gamma_0 = \arccos[\cos(\gamma_1) \cos(\gamma_2)] \quad (5.77)$$

To define the direction of the spring torque on the spacecraft bus, we recognize that the torque will act about the same axis (but in the opposite direction) as that which the RW spin axis (\hat{c}_3) rotates about relative to the spacecraft axis \hat{a}_3 . Hence the spring torque vector is perpendicular to both \hat{c}_3 and \hat{a}_3 , and its direction is:

$$\frac{\dot{T}_A^s}{T_A} = - \frac{\hat{c}_3 \times \hat{a}_3}{|\hat{c}_3 \times \hat{a}_3|} = \frac{\begin{bmatrix} \sin(\gamma_1) & \cos(\gamma_1)\sin(\gamma_2) & 0 \end{bmatrix}}{\sqrt{\cos^2(\gamma_1)\sin^2(\gamma_2) + \sin^2(\gamma_1)}} \hat{e}_A \quad (5.78)$$

The resulting spring torque on spacecraft A is then:

$$\begin{aligned} \dot{T}_A^s &= -k_4\gamma_0 \frac{\hat{c}_3 \times \hat{a}_3}{|\hat{c}_3 \times \hat{a}_3|} \\ &= \frac{k_4\cos[\cos(\gamma_1)\cos(\gamma_2)]}{\sqrt{\cos^2(\gamma_1)\sin^2(\gamma_2) + \sin^2(\gamma_1)}} \begin{bmatrix} \sin(\gamma_1) & \cos(\gamma_1)\sin(\gamma_2) & 0 \end{bmatrix} \hat{e}_A \end{aligned} \quad (5.79)$$

Clearly the spring torque is zero when $\gamma_1 = \gamma_2 = 0$ (and therefore $\gamma_0 = 0$). In this case, the spin axis of the RW (\hat{c}_3) is aligned with \hat{a}_3 .

The spring torque exerted *on the reaction wheel* is simply equal in magnitude and opposite in direction to that exerted on the spacecraft bus:

$$\dot{T}_{RW}^s = -\dot{T}_A^s \quad (5.80)$$

Finally, we consider the *torque exerted by a motor* to spin the reaction wheel relative to the spacecraft. The motor for RW-3 is oriented such that its spin axis aligns with the spacecraft's \hat{a}_3 axis. It provides a torque, $T_{Am_3}\hat{a}_3$, on RW-3, and therefore provides an opposite reaction torque, $-T_{Am_3}\hat{a}_3$, on the spacecraft.

Now we reconsider RW-1 and RW-2, the two additional RWs whose spin axes are aligned with the spacecraft's \hat{a}_1 and \hat{a}_2 axes, respectively. We repeat for emphasis that because the nominal trajectory of the array will be a steady-state spin maneuver within the \hat{e}_x , \hat{e}_y plane, and because RW-3 will store the majority of the array's angular momentum, we consider only the gyrostiffening of that RW in this analysis. However, to control the attitude of the spacecraft about all axes, we must account for the actuator capability of RW-1 and RW-2, without necessarily modeling their nonlinear dynamics.¹ The additional RWs are thus modeled as actuators by introducing motor torques (T_{Am_1} and T_{Am_2} , respectively)

into the equations of motion. Thus the torques *on the spacecraft* due to the motors of RW-1 and RW-2 are $-T_{Am_1}\hat{a}_1$ and $-T_{Am_2}\hat{a}_2$, respectively.

Note that analogous motor torques may be defined for every other spacecraft in the array and its associated RWs. For instance, spacecraft B will experience motor torques $-T_{Bm_1}\hat{b}_1$, $-T_{Bm_2}\hat{b}_2$, and $-T_{Bm_3}\hat{b}_3$.

With all of the active forces and torques (EM, external, spring, and motor) described above, and the partial velocities and partial angular velocities described in Section 5.4.2, we now express the *generalized active forces* (defined in Equation 4.17) for spacecraft A and its RW as:

$$\begin{aligned} F_1 = & (c\alpha_2 c\alpha_3)(F_{AB,1} + F_{A,1}^{ext} + F_{RW,1}^{ext}) \\ & + (s\alpha_1 s\alpha_2 c\alpha_3 - c\alpha_1 s\alpha_3)(F_{AB,2} + F_{A,2}^{ext} + F_{RW,2}^{ext}) \\ & + (c\alpha_1 s\alpha_2 c\alpha_3 + s\alpha_1 s\alpha_3)(F_{AB,3} + F_{A,3}^{ext} + F_{RW,3}^{ext}) \end{aligned} \quad (5.81)$$

$$\begin{aligned} F_2 = & (c\alpha_2 s\alpha_3)(F_{AB,1} + F_{A,1}^{ext} + F_{RW,1}^{ext}) \\ & + (s\alpha_1 s\alpha_2 s\alpha_3 + c\alpha_1 c\alpha_3)(F_{AB,2} + F_{A,2}^{ext} + F_{RW,2}^{ext}) \\ & + (c\alpha_1 s\alpha_2 s\alpha_3 - s\alpha_1 c\alpha_3)(F_{AB,3} + F_{A,3}^{ext} + F_{RW,3}^{ext}) \end{aligned} \quad (5.82)$$

$$\begin{aligned} F_3 = & (-s\alpha_2)(F_{AB,1} + F_{A,1}^{ext} + F_{RW,1}^{ext}) \\ & + (s\alpha_1 c\alpha_2)(F_{AB,2} + F_{A,2}^{ext} + F_{RW,2}^{ext}) \\ & + (c\alpha_1 c\alpha_2)(F_{AB,3} + F_{A,3}^{ext} + F_{RW,3}^{ext}) \end{aligned} \quad (5.83)$$

$$F_4 = -k_1 x_{CA} + F_{RW,1}^{ext} \quad (5.84)$$

-
- For any future analyses that require the gyrostiffening of all reaction wheels to be modeled, it would be simple to append the rigid-body dynamics of additional RWs by studying the derivation and resulting equations for the first RW, as developed in this chapter, and then repeating the process for additional RWs.

$$F_5 = -k_2 y_{CA} + F_{RW,2}^{ext} \quad (5.85)$$

$$F_6 = -k_3(z_{CA} - z_{CA,0}) + F_{RW,3}^{ext} \quad (5.86)$$

$$\begin{aligned} F_7 = & [-z_{CA}] [-k_2 y_{CA} + F_{RW,2}^{ext}] \\ & + [-y_{CA}] [-k_3(z_{CA} - z_{CA,0}) + F_{RW,3}^{ext}] \\ & + z_{iC}[-s\gamma_1 k_3(z_{CA} - z_{CA,0}) - c\gamma_1 c\gamma_2 k_2 y_{CA}] - z_{iA} k_2 y_{CA} \\ & + T_{AB,1} + T_{A,1}^{ext} + T_{RW,1}^{ext} - T_{Am_1} \end{aligned} \quad (5.87)$$

$$\begin{aligned} F_8 = & [z_{CA}] [-k_1 x_{CA} + F_{RW,1}^{ext}] \\ & + [-x_{CA}] [-k_3(z_{CA} - z_{CA,0}) + F_{RW,3}^{ext}] \\ & + z_{iC}[-c\gamma_1 s\gamma_2 k_3(z_{CA} - z_{CA,0}) + c\gamma_1 c\gamma_2 k_1 x_{CA}] + z_{iA} k_1 x_{CA} \\ & + T_{AB,2} + T_{A,2}^{ext} + T_{RW,2}^{ext} - T_{Am_2} \end{aligned} \quad (5.88)$$

$$\begin{aligned} F_9 = & [-y_{CA}] [-k_1 x_{CA} + F_{RW,1}^{ext}] \\ & + [x_{CA}] [-k_2 y_{CA} + F_{RW,2}^{ext}] \\ & + z_{iC}[c\gamma_1 s\gamma_2 k_2 y_{CA} + s\gamma_1 k_1 x_{CA}] \\ & + T_{AB,3} + T_{A,3}^{ext} + T_{RW,3}^{ext} \end{aligned} \quad (5.89)$$

$$\begin{aligned} F_{10} = & (s\gamma_1 s\gamma_2 s\delta_3 + c\gamma_2 c\delta_3) T_{RW,1} \\ & + (c\gamma_1 s\delta_3) T_{RW,2} \\ & + (s\gamma_1 c\gamma_2 s\delta_3 - s\gamma_2 c\delta_3) T_{RW,3} \end{aligned} \quad (5.90)$$

$$\begin{aligned} F_{11} = & (s\gamma_1 s\gamma_2 c\delta_3 - c\gamma_2 s\delta_3) T_{RW,1} \\ & + (c\gamma_1 c\delta_3) T_{RW,2} \\ & + (s\gamma_1 c\gamma_2 c\delta_3 + s\gamma_2 s\delta_3) T_{RW,3} \end{aligned} \quad (5.91)$$

$$\begin{aligned} F_{12} = & (\cos \gamma_1 \sin \gamma_2) T_{RW,1} \\ & + (-\sin \gamma_1) T_{RW,2} \\ & + (\cos \gamma_1 \cos \gamma_2) T_{RW,3} \end{aligned} \quad (5.92)$$

where \cos denotes the cosine function, \sin denotes the sine function, and:

$$T_{RW,1} \equiv -k_4 s \gamma_1 \frac{\cos(\cos \gamma_1 \cos \gamma_2)}{\sqrt{\sin^2 \gamma_1 + \cos^2 \gamma_1 \sin^2 \gamma_2}} + z_{iC} [-\sin \gamma_1 k_3 (z_{CA} - z_{CA,0}) - \cos \gamma_1 \cos \gamma_2 k_2 y_{CA}] + T_{RW,1}^{ext} \quad (5.93)$$

$$T_{RW,2} \equiv -k_4 \cos \gamma_1 s \gamma_2 \frac{\cos(\cos \gamma_1 \cos \gamma_2)}{\sqrt{\sin^2 \gamma_1 + \cos^2 \gamma_1 \sin^2 \gamma_2}} + z_{iC} [-\cos \gamma_1 \sin \gamma_2 k_3 (z_{CA} - z_{CA,0}) + \cos \gamma_1 \cos \gamma_2 k_1 x_{CA}] + T_{RW,2}^{ext} \quad (5.94)$$

$$T_{RW,3} \equiv z_{iC} [\cos \gamma_1 \sin \gamma_2 k_2 y_{CA} + \sin \gamma_1 k_1 x_{CA}] + T_{RW,3}^{ext} + T_{Am_3} \quad (5.95)$$

Generalized Inertia Forces

The first step in defining the inertia forces is to define the accelerations of the bodies in the system. The acceleration of the center of mass of the spacecraft bus is:

$$\frac{G_{\Delta A}}{a} = \frac{G_{\dot{\Delta}A}}{v} = \left[\begin{array}{ccc} \ddot{x}_{AG} & \ddot{y}_{AG} & \ddot{z}_{AG} \end{array} \right] \left\{ \begin{array}{c} \hat{e}_x \\ \hat{e}_y \\ \hat{e}_z \end{array} \right\} \quad (5.96)$$

where the velocity, $\frac{G_{\Delta A}}{v}$, was defined in Equation 5.29. The acceleration of the center of mass of the reaction wheel is:

$$\begin{aligned}
 \overset{G}{\ddot{\alpha}}^C = \overset{G}{v}^C = & \left[\begin{array}{c} \ddot{x}_{AG} \ddot{y}_{AG} \ddot{z}_{AG} \end{array} \right] \left\{ \begin{array}{c} \hat{e}_x \\ \hat{e}_y \\ \hat{e}_z \end{array} \right\} \\
 & + \left[\begin{array}{c} \dot{\hat{a}}_1 \\ \dot{\hat{a}}_2 \\ \dot{\hat{a}}_3 \end{array} \right] + 2 \left[\begin{array}{c} \overset{G}{\omega}^A \times \hat{a}_1 \\ \overset{G}{\omega}^A \times \hat{a}_2 \\ \overset{G}{\omega}^A \times \hat{a}_3 \end{array} \right] \\
 & + \left[\begin{array}{c} \overset{G}{\omega}^A \times (\overset{G}{\omega}^A \times \hat{a}_1) \\ \overset{G}{\omega}^A \times (\overset{G}{\omega}^A \times \hat{a}_2) \\ \overset{G}{\omega}^A \times (\overset{G}{\omega}^A \times \hat{a}_3) \end{array} \right] + \left[\begin{array}{c} \overset{G}{\dot{\omega}}^A \times \hat{a}_1 \\ \overset{G}{\dot{\omega}}^A \times \hat{a}_2 \\ \overset{G}{\dot{\omega}}^A \times \hat{a}_3 \end{array} \right]
 \end{aligned} \tag{5.97}$$

where the velocity, $\overset{G}{v}^C$, was defined in Equation 5.35. From inspection of the right-hand side of Equation 5.97, we find:

- the first term represents *the acceleration of A relative to the inertial frame, G*,
- the second term represents *the acceleration of C relative to A*,
- the third term represents the *coriolis acceleration of C*,
- the fourth term represents the *centripetal acceleration of C*, and
- the fifth term represents the *angular acceleration of C relative to A*.

The first, fourth, and fifth terms, together, represent the *carrying acceleration of A at C*, or the acceleration of the fixed point in A that coincides with the location of the center of mass of C.

Equation 5.97 may be expanded as:

$$\begin{aligned}
 \overset{G_{\Delta C}}{\vec{a}} = & \left[\begin{array}{c} \ddot{x}_{AG} \quad \ddot{y}_{AG} \quad \ddot{z}_{AG} \end{array} \right] \left\{ \begin{array}{c} \hat{\vec{e}}_x \\ \hat{\vec{e}}_y \\ \hat{\vec{e}}_z \end{array} \right\} \\
 + & \left\{ \begin{array}{c} \ddot{x}_{CA} + 2(\overset{G}{\omega}_2^A \dot{z}_{CA} - \overset{G}{\omega}_3^A \dot{y}_{CA}) + \overset{G}{\omega}_2^A (\overset{G}{\omega}_1^A y_{CA} - \overset{G}{\omega}_2^A x_{CA}) \\ \quad + \overset{G}{\omega}_3^A (\overset{G}{\omega}_1^A z_{CA} - \overset{G}{\omega}_3^A x_{CA}) + \overset{G}{\dot{\omega}}_2^A z_{CA} - \overset{G}{\dot{\omega}}_3^A y_{CA} \\ \ddot{y}_{CA} + 2(\overset{G}{\omega}_3^A \dot{x}_{CA} - \overset{G}{\omega}_1^A \dot{z}_{CA}) + \overset{G}{\omega}_3^A (\overset{G}{\omega}_2^A z_{CA} - \overset{G}{\omega}_3^A y_{CA}) \\ \quad + \overset{G}{\omega}_1^A (\overset{G}{\omega}_2^A x_{CA} - \overset{G}{\omega}_1^A y_{CA}) + \overset{G}{\dot{\omega}}_3^A x_{CA} - \overset{G}{\dot{\omega}}_1^A z_{CA} \\ \ddot{z}_{CA} + 2(\overset{G}{\omega}_1^A \dot{y}_{CA} - \overset{G}{\omega}_2^A \dot{x}_{CA}) + \overset{G}{\omega}_1^A (\overset{G}{\omega}_3^A x_{CA} - \overset{G}{\omega}_1^A z_{CA}) \\ \quad + \overset{G}{\omega}_2^A (\overset{G}{\omega}_3^A y_{CA} - \overset{G}{\omega}_2^A z_{CA}) + \overset{G}{\dot{\omega}}_1^A y_{CA} - \overset{G}{\dot{\omega}}_2^A x_{CA} \end{array} \right\}^T \\
 & \left\{ \begin{array}{c} \hat{\vec{a}}_1 \\ \hat{\vec{a}}_2 \\ \hat{\vec{a}}_3 \end{array} \right\} \quad (5.98)
 \end{aligned}$$

With the accelerations of the spacecraft and RW relative to the inertial frame, we can now express the inertia forces of the two bodies, as defined by Equation 4.24. The inertia force on the spacecraft is thus:

$$\overset{\Delta A}{\vec{F}_A} * \equiv -m_A \overset{G_{\Delta A}}{\vec{a}} \quad (5.99)$$

where m_A is the spacecraft mass (exclusive of the reaction wheel mass), and $\overset{G_{\Delta A}}{\vec{a}}$ is the inertial acceleration of the spacecraft center of mass, as defined in Equation 5.96.

Similarly, the inertia force on the reaction wheel is:

$$\overset{\Delta C}{\vec{F}_C} * \equiv -m_C \overset{G_{\Delta C}}{\vec{a}} \quad (5.100)$$

where m_C is the reaction wheel mass, and $\overset{G_{\Delta C}}{\vec{a}}$ is the inertial acceleration of the reaction wheel, as defined in Equation 5.98.

Expressions for the inertia torques on the bodies were given in Equation 4.25. Assuming \hat{e}_A and \hat{e}_C are principal axes of the spacecraft and reaction wheel, respectively, we can use the expression in Equation 4.26. Hence the inertia torque on the spacecraft bus is:

$$\begin{aligned}\dot{\tilde{T}}_A^* \equiv & -[{}^G\dot{\omega}_1^A I_1^A - {}^G\omega_2^A {}^G\omega_3^A (I_2^A - I_3^A)]\hat{a}_1 \\ & -[{}^G\dot{\omega}_2^A I_2^A - {}^G\omega_3^A {}^G\omega_1^A (I_3^A - I_1^A)]\hat{a}_2 \\ & -[{}^G\dot{\omega}_3^A I_3^A - {}^G\omega_1^A {}^G\omega_2^A (I_1^A - I_2^A)]\hat{a}_3\end{aligned}\quad (5.101)$$

where I_1^A , I_2^A , and I_3^A are the moments of inertia of spacecraft A about its body-fixed \hat{a}_1 , \hat{a}_2 , and \hat{a}_3 axes, respectively. The inertia torque on the reaction wheel is:

$$\begin{aligned}\dot{\tilde{T}}_D^* \equiv & -[{}^G\dot{\omega}_1^D I_1^D - {}^G\omega_2^D {}^G\omega_3^D (I_2^D - I_3^D)]\hat{d}_1 \\ & -[{}^G\dot{\omega}_2^D I_2^D - {}^G\omega_3^D {}^G\omega_1^D (I_3^D - I_1^D)]\hat{d}_2 \\ & -[{}^G\dot{\omega}_3^D I_3^D - {}^G\omega_1^D {}^G\omega_2^D (I_1^D - I_2^D)]\hat{d}_3\end{aligned}\quad (5.102)$$

where I_1^D , I_2^D , and I_3^D are the moments of inertia of the reaction wheel about its body-fixed \hat{d}_1 , \hat{d}_2 , and \hat{d}_3 axes, respectively. Assuming an axially symmetric flywheel ($I_1^D = I_2^D$), Equation 5.102 reduces to:

$$\begin{aligned}\dot{\tilde{T}}_D^* \equiv & -[{}^G\dot{\omega}_1^D I_1^D - {}^G\omega_2^D {}^G\omega_3^D (I_2^D - I_3^D)]\hat{d}_1 \\ & -[{}^G\dot{\omega}_2^D I_2^D - {}^G\omega_3^D {}^G\omega_1^D (I_3^D - I_1^D)]\hat{d}_2 \\ & -[{}^G\dot{\omega}_3^D I_3^D]\hat{d}_3\end{aligned}\quad (5.103)$$

With the inertia forces described in Equations 5.99 and 5.100, and the inertia torques described in Equations 5.101 and 5.103, we now express the *generalized inertia forces* (defined in Equation 4.17) for spacecraft A and its RW as:

$$\begin{aligned}
F_1^* = & - (m_A + m_C) \ddot{x}_{AG} - m_C \left\{ (\text{c}\alpha_2 \text{c}\alpha_3) \left(\left(\frac{G_{\Delta C}}{a} - \frac{G_{\Delta A}}{a} \right) \cdot \hat{a}_1 \right) \right. \\
& + (\text{s}\alpha_1 \text{s}\alpha_2 \text{c}\alpha_3 - \text{c}\alpha_1 \text{s}\alpha_3) \left(\left(\frac{G_{\Delta C}}{a} - \frac{G_{\Delta A}}{a} \right) \cdot \hat{a}_2 \right) \\
& \left. + (\text{c}\alpha_1 \text{s}\alpha_2 \text{c}\alpha_3 + \text{s}\alpha_1 \text{s}\alpha_3) \left(\left(\frac{G_{\Delta C}}{a} - \frac{G_{\Delta A}}{a} \right) \cdot \hat{a}_3 \right) \right\}
\end{aligned} \quad (5.104)$$

$$\begin{aligned}
F_2^* = & - (m_A + m_C) \ddot{y}_{AG} - m_C \left\{ (\text{c}\alpha_2 \text{s}\alpha_3) \left(\left(\frac{G_{\Delta C}}{a} - \frac{G_{\Delta A}}{a} \right) \cdot \hat{a}_1 \right) \right. \\
& + (\text{s}\alpha_1 \text{s}\alpha_2 \text{s}\alpha_3 + \text{c}\alpha_1 \text{c}\alpha_3) \left(\left(\frac{G_{\Delta C}}{a} - \frac{G_{\Delta A}}{a} \right) \cdot \hat{a}_2 \right) \\
& \left. + (\text{c}\alpha_1 \text{s}\alpha_2 \text{s}\alpha_3 - \text{s}\alpha_1 \text{c}\alpha_3) \left(\left(\frac{G_{\Delta C}}{a} - \frac{G_{\Delta A}}{a} \right) \cdot \hat{a}_3 \right) \right\}
\end{aligned} \quad (5.105)$$

$$\begin{aligned}
F_3^* = & - (m_A + m_C) \ddot{z}_{AG} - m_C \left\{ (-\text{s}\alpha_2) \left(\left(\frac{G_{\Delta C}}{a} - \frac{G_{\Delta A}}{a} \right) \cdot \hat{a}_1 \right) \right. \\
& + (\text{s}\alpha_1 \text{c}\alpha_2) \left(\left(\frac{G_{\Delta C}}{a} - \frac{G_{\Delta A}}{a} \right) \cdot \hat{a}_2 \right) \\
& \left. + (\text{c}\alpha_1 \text{c}\alpha_2) \left(\left(\frac{G_{\Delta C}}{a} - \frac{G_{\Delta A}}{a} \right) \cdot \hat{a}_3 \right) \right\}
\end{aligned} \quad (5.106)$$

$$F_4^* = -m_C \left\{ \text{c}\alpha_2 \text{c}\alpha_3 \ddot{x}_{AG} + \text{c}\alpha_2 \text{s}\alpha_3 \ddot{y}_{AG} - \text{s}\alpha_2 \ddot{z}_{AG} + \left(\frac{G_{\Delta C}}{a} - \frac{G_{\Delta A}}{a} \right) \cdot \hat{a}_1 \right\} \quad (5.107)$$

$$\begin{aligned}
F_5^* = & -m_C \left\{ (\text{s}\alpha_1 \text{s}\alpha_2 \text{c}\alpha_3 - \text{c}\alpha_1 \text{s}\alpha_3) \ddot{x}_{AG} + (\text{s}\alpha_1 \text{s}\alpha_2 \text{s}\alpha_3 + \text{c}\alpha_1 \text{c}\alpha_3) \ddot{y}_{AG} \right. \\
& \left. + \text{s}\alpha_1 \text{c}\alpha_2 \ddot{z}_{AG} + \left(\frac{G_{\Delta C}}{a} - \frac{G_{\Delta A}}{a} \right) \cdot \hat{a}_2 \right\}
\end{aligned} \quad (5.108)$$

$$\begin{aligned}
F_6^* = & -m_C \left\{ (\text{c}\alpha_1 \text{s}\alpha_2 \text{c}\alpha_3 + \text{s}\alpha_1 \text{s}\alpha_3) \ddot{x}_{AG} + (\text{c}\alpha_1 \text{s}\alpha_2 \text{s}\alpha_3 - \text{s}\alpha_1 \text{c}\alpha_3) \ddot{y}_{AG} \right. \\
& \left. + \text{c}\alpha_1 \text{c}\alpha_2 \ddot{z}_{AG} + \left(\frac{G_{\Delta C}}{a} - \frac{G_{\Delta A}}{a} \right) \cdot \hat{a}_3 \right\}
\end{aligned} \quad (5.109)$$

$$\begin{aligned}
F_7^* = & \\
& - [m_C z_{CA}] [(\text{s}\alpha_1 \text{s}\alpha_2 \text{c}\alpha_3 - \text{c}\alpha_1 \text{s}\alpha_3) \ddot{x}_{AG} + (\text{s}\alpha_1 \text{s}\alpha_2 \text{s}\alpha_3 + \text{c}\alpha_1 \text{c}\alpha_3) \ddot{y}_{AG} + \text{s}\alpha_1 \text{c}\alpha_2 \ddot{z}_{AG} + \left(\frac{G_{\Delta C}}{a} - \frac{G_{\Delta A}}{a} \right) \cdot \hat{a}_2] \\
& + [m_C y_{CA}] [(\text{c}\alpha_1 \text{s}\alpha_2 \text{c}\alpha_3 + \text{s}\alpha_1 \text{s}\alpha_3) \ddot{x}_{AG} + (\text{c}\alpha_1 \text{s}\alpha_2 \text{s}\alpha_3 - \text{s}\alpha_1 \text{c}\alpha_3) \ddot{y}_{AG} + \text{c}\alpha_1 \text{c}\alpha_2 \ddot{z}_{AG} + \left(\frac{G_{\Delta C}}{a} - \frac{G_{\Delta A}}{a} \right) \cdot \hat{a}_3] \\
& - {}^G \dot{\omega}_1^A I_1^A + {}^G \dot{\omega}_2^A {}^G \dot{\omega}_3^A (I_2^A - I_3^A) \\
& - [s\gamma_1 s\gamma_2 s\delta_3 + c\gamma_2 c\delta_3] [{}^G \dot{\omega}_1^D I_1^D - {}^G \dot{\omega}_2^D {}^G \dot{\omega}_3^D (I_2^D - I_3^D)] \\
& - [s\gamma_1 s\gamma_2 c\delta_3 - c\gamma_2 s\delta_3] [{}^G \dot{\omega}_2^D I_2^D - {}^G \dot{\omega}_3^D {}^G \dot{\omega}_1^D (I_3^D - I_1^D)] \\
& - [c\gamma_1 s\gamma_2] [{}^G \dot{\omega}_3^D I_3^D]
\end{aligned} \quad (5.110)$$

$$\begin{aligned}
F_8^* = & \\
[m_C z_{CA}] & [(\text{ca}_2 \text{ca}_3) \ddot{x}_{AG} + (\text{ca}_2 \text{s}\alpha_3) \ddot{y}_{AG} - \text{s}\alpha_2 \ddot{z}_{AG} + (\frac{G_{\Delta C}}{\dot{a}} - \frac{G_{\Delta A}}{\dot{a}}) \cdot \hat{a}_1] \\
-[m_C x_{CA}] & [(\text{ca}_1 \text{s}\alpha_2 \text{ca}_3 + \text{s}\alpha_1 \text{s}\alpha_3) \ddot{x}_{AG} + (\text{ca}_1 \text{s}\alpha_2 \text{s}\alpha_3 - \text{s}\alpha_1 \text{ca}_3) \ddot{y}_{AG} + \text{ca}_1 \text{ca}_2 \ddot{z}_{AG} + (\frac{G_{\Delta C}}{\dot{a}} - \frac{G_{\Delta A}}{\dot{a}}) \cdot \hat{a}_3] \\
& - \frac{G_{\dot{\omega}}^A}{\dot{\omega}_2} I_2^A + \frac{G_{\omega}}{\dot{\omega}_3} \frac{G_{\omega}}{\dot{\omega}_1} (I_3^A - I_1^A) \\
& - [\text{c}\gamma_1 \text{s}\delta_3] [\frac{G_{\dot{\omega}}^D}{\dot{\omega}_1} I_1^D - \frac{G_{\omega}}{\dot{\omega}_2} \frac{G_{\omega}}{\dot{\omega}_3} (I_2^D - I_3^D)] \\
& - [\text{c}\gamma_1 \text{c}\delta_3] [\frac{G_{\dot{\omega}}^D}{\dot{\omega}_2} I_2^D - \frac{G_{\omega}}{\dot{\omega}_3} \frac{G_{\omega}}{\dot{\omega}_1} (I_3^D - I_1^D)] \\
& + [\text{s}\gamma_1] [\frac{G_{\dot{\omega}}^D}{\dot{\omega}_3} I_3^D]
\end{aligned} \tag{5.111}$$

$$\begin{aligned}
F_9^* = & \\
-[m_C y_{CA}] & [(\text{ca}_2 \text{ca}_3) \ddot{x}_{AG} + (\text{ca}_2 \text{s}\alpha_3) \ddot{y}_{AG} - \text{s}\alpha_2 \ddot{z}_{AG} + (\frac{G_{\Delta C}}{\dot{a}} - \frac{G_{\Delta A}}{\dot{a}}) \cdot \hat{a}_1] \\
+[m_C x_{CA}] & [(\text{s}\alpha_1 \text{s}\alpha_2 \text{ca}_3 - \text{ca}_1 \text{s}\alpha_3) \ddot{x}_{AG} + (\text{s}\alpha_1 \text{s}\alpha_2 \text{s}\alpha_3 + \text{ca}_1 \text{ca}_3) \ddot{y}_{AG} + \text{s}\alpha_1 \text{ca}_2 \ddot{z}_{AG} + (\frac{G_{\Delta C}}{\dot{a}} - \frac{G_{\Delta A}}{\dot{a}}) \cdot \hat{a}_2] \\
& - \frac{G_{\dot{\omega}}^A}{\dot{\omega}_3} I_3^A + \frac{G_{\omega}}{\dot{\omega}_1} \frac{G_{\omega}}{\dot{\omega}_2} (I_1^A - I_2^A) \\
& - [\text{s}\gamma_1 \text{c}\gamma_2 \text{s}\delta_3 - \text{s}\gamma_2 \text{c}\delta_3] [\frac{G_{\dot{\omega}}^D}{\dot{\omega}_1} I_1^D - \frac{G_{\omega}}{\dot{\omega}_2} \frac{G_{\omega}}{\dot{\omega}_3} (I_2^D - I_3^D)] \\
& - [\text{s}\gamma_1 \text{c}\gamma_2 \text{c}\delta_3 + \text{s}\gamma_2 \text{s}\delta_3] [\frac{G_{\dot{\omega}}^D}{\dot{\omega}_2} I_2^D - \frac{G_{\omega}}{\dot{\omega}_3} \frac{G_{\omega}}{\dot{\omega}_1} (I_3^D - I_1^D)] \\
& - [\text{c}\gamma_1 \text{c}\gamma_2] [\frac{G_{\dot{\omega}}^D}{\dot{\omega}_3} I_3^D]
\end{aligned} \tag{5.112}$$

$$F_{10}^* = - \frac{G_{\dot{\omega}}^D}{\dot{\omega}_1} I_1^D + \frac{G_{\omega}}{\dot{\omega}_2} \frac{G_{\omega}}{\dot{\omega}_3} (I_2^D - I_3^D) \tag{5.113}$$

$$F_{11}^* = - \frac{G_{\dot{\omega}}^D}{\dot{\omega}_2} I_2^D + \frac{G_{\omega}}{\dot{\omega}_3} \frac{G_{\omega}}{\dot{\omega}_1} (I_3^D - I_1^D) \tag{5.114}$$

$$F_{12}^* = - \frac{G_{\dot{\omega}}^D}{\dot{\omega}_3} I_3^D \tag{5.115}$$

where:

$$\begin{aligned}
(\frac{G_{\Delta C}}{\dot{a}} - \frac{G_{\Delta A}}{\dot{a}}) \cdot \hat{a}_1 = & \ddot{x}_{CA} + 2(G_{\omega_2^A} \dot{z}_{CA} - G_{\omega_3^A} \dot{y}_{CA}) + G_{\omega_2^A} (G_{\omega_1^A} y_{CA} - G_{\omega_2^A} x_{CA}) \\
& + G_{\omega_3^A} (G_{\omega_1^A} z_{CA} - G_{\omega_3^A} x_{CA}) + G_{\dot{\omega}_2^A} z_{CA} - G_{\dot{\omega}_3^A} y_{CA}
\end{aligned} \tag{5.116}$$

$$\begin{aligned}
(\frac{G_{\Delta C}}{\dot{a}} - \frac{G_{\Delta A}}{\dot{a}}) \cdot \hat{a}_2 = & \ddot{y}_{CA} + 2(G_{\omega_3^A} \dot{x}_{CA} - G_{\omega_1^A} \dot{z}_{CA}) + G_{\omega_3^A} (G_{\omega_2^A} z_{CA} - G_{\omega_3^A} y_{CA}) \\
& + G_{\omega_1^A} (G_{\omega_2^A} x_{CA} - G_{\omega_1^A} y_{CA}) + G_{\dot{\omega}_3^A} x_{CA} - G_{\dot{\omega}_1^A} z_{CA}
\end{aligned} \tag{5.117}$$

$$\begin{aligned} \left(\frac{G_{\Delta C}}{a} - \frac{G_{\Delta A}}{a} \right) \cdot \hat{a}_3 &= \ddot{z}_{CA} + 2(G_{\omega_1^A} \dot{y}_{CA} - G_{\omega_2^A} \dot{x}_{CA}) + G_{\omega_1^A} (G_{\omega_3^A} x_{CA} - G_{\omega_1^A} z_{CA}) \\ &\quad + G_{\omega_2^A} (G_{\omega_3^A} y_{CA} - G_{\omega_2^A} z_{CA}) + G_{\dot{\omega}_1^A} y_{CA} - G_{\dot{\omega}_2^A} x_{CA} \end{aligned} \quad (5.118)$$

5.4.4 Nonlinear Equations of Motion

The final step to deriving the nonlinear equations of motion for the system is now performed. We simply substitute the generalized active and inertia forces from Section 5.4.3 into Equation 4.31. The result is the following 12 equations of motion that describe the behavior of spacecraft A and its reaction wheels (RWs). Further, the analogous sets of equations for all other spacecraft in the array can be obtained easily by substituting the corresponding degrees of freedom for those vehicles and their RWs into the equations for spacecraft A. Hence for spacecraft A, we arrive at the following 12 equations of motion:

$$\begin{aligned} &(m_A + m_C) \ddot{x}_{AG} + m_C \left\{ \begin{aligned} &[c\alpha_2 c\alpha_3] \cdot \\ &[\ddot{x}_{CA} + G_{\omega_2^A} (G_{\omega_1^A} y_{CA} - G_{\omega_2^A} x_{CA}) + G_{\omega_3^A} (G_{\omega_1^A} z_{CA} - G_{\omega_3^A} x_{CA}) + 2(G_{\omega_2^A} \dot{z}_{CA} - G_{\omega_3^A} \dot{y}_{CA}) + G_{\dot{\omega}_2^A} z_{CA} - G_{\dot{\omega}_3^A} y_{CA}] \\ &+ [s\alpha_1 s\alpha_2 c\alpha_3 - c\alpha_1 s\alpha_3] \cdot \\ &[\ddot{y}_{CA} + G_{\omega_3^A} (G_{\omega_2^A} z_{CA} - G_{\omega_3^A} y_{CA}) + G_{\omega_1^A} (G_{\omega_2^A} x_{CA} - G_{\omega_1^A} y_{CA}) + 2(G_{\omega_3^A} \dot{x}_{CA} - G_{\omega_1^A} \dot{z}_{CA}) + G_{\dot{\omega}_3^A} x_{CA} - G_{\dot{\omega}_1^A} z_{CA}] \end{aligned} \right. \\ &+ [c\alpha_1 s\alpha_2 c\alpha_3 + s\alpha_1 s\alpha_3] \cdot \\ &[\ddot{z}_{CA} + G_{\omega_1^A} (G_{\omega_3^A} x_{CA} - G_{\omega_1^A} z_{CA}) + G_{\omega_2^A} (G_{\omega_3^A} y_{CA} - G_{\omega_2^A} z_{CA}) + 2(G_{\omega_1^A} \dot{y}_{CA} - G_{\omega_2^A} \dot{x}_{CA}) + G_{\dot{\omega}_1^A} y_{CA} - G_{\dot{\omega}_2^A} x_{CA}] \left. \right\} \\ &= (c\alpha_2 c\alpha_3) (F_{AB,1} + F_{A,1}^{ext} + F_{RW,1}^{ext}) \\ &\quad + (s\alpha_1 s\alpha_2 c\alpha_3 - c\alpha_1 s\alpha_3) (F_{AB,2} + F_{A,2}^{ext} + F_{RW,2}^{ext}) \\ &\quad + (c\alpha_1 s\alpha_2 c\alpha_3 + s\alpha_1 s\alpha_3) (F_{AB,3} + F_{A,3}^{ext} + F_{RW,3}^{ext}) \end{aligned} \quad (5.119)$$

$$\begin{aligned}
& (m_A + m_C)\ddot{y}_{AG} + m_C \left\{ \begin{array}{l} [\text{c}\alpha_2 s\alpha_3] \cdot \\ [\text{s}\alpha_1 s\alpha_2 s\alpha_3 + \text{c}\alpha_1 c\alpha_3] \cdot \\ [\ddot{x}_{CA} + {}^G\omega_2^A({}^G\omega_1^A y_{CA} - {}^G\omega_2^A x_{CA}) + {}^G\omega_3^A({}^G\omega_1^A z_{CA} - {}^G\omega_3^A x_{CA}) + 2({}^G\omega_2^A \dot{z}_{CA} - {}^G\omega_3^A \dot{y}_{CA}) + {}^G\dot{\omega}_2^A z_{CA} - {}^G\dot{\omega}_3^A y_{CA}] \\ + [\text{s}\alpha_1 s\alpha_2 s\alpha_3 + \text{c}\alpha_1 c\alpha_3] \cdot \\ [{}^G\ddot{y}_{CA} + {}^G\omega_3^A({}^G\omega_2^A z_{CA} - {}^G\omega_3^A y_{CA}) + {}^G\omega_1^A({}^G\omega_2^A x_{CA} - {}^G\omega_1^A y_{CA}) + 2({}^G\omega_3^A \dot{x}_{CA} - {}^G\omega_1^A \dot{z}_{CA}) + {}^G\dot{\omega}_3^A x_{CA} - {}^G\dot{\omega}_1^A z_{CA}] \end{array} \right. \\
& \quad \left. + [\text{c}\alpha_1 s\alpha_2 s\alpha_3 - \text{s}\alpha_1 c\alpha_3] \cdot \right. \\
& \quad \left. [{}^G\ddot{z}_{CA} + {}^G\omega_1^A({}^G\omega_3^A x_{CA} - {}^G\omega_1^A z_{CA}) + {}^G\omega_2^A({}^G\omega_3^A y_{CA} - {}^G\omega_2^A z_{CA}) + 2({}^G\omega_1^A \dot{y}_{CA} - {}^G\omega_2^A \dot{x}_{CA}) + {}^G\dot{\omega}_1^A y_{CA} - {}^G\dot{\omega}_2^A x_{CA}] \right\} \\
& = (\text{c}\alpha_2 s\alpha_3)(F_{AB,1} + F_{A,1}^{ext} + F_{RW,1}^{ext}) \\
& + (\text{s}\alpha_1 s\alpha_2 s\alpha_3 + \text{c}\alpha_1 c\alpha_3)(F_{AB,2} + F_{A,2}^{ext} + F_{RW,2}^{ext}) \\
& + (\text{c}\alpha_1 s\alpha_2 s\alpha_3 - \text{s}\alpha_1 c\alpha_3)(F_{AB,3} + F_{A,3}^{ext} + F_{RW,3}^{ext})
\end{aligned} \tag{5.120}$$

$$\begin{aligned}
& (m_A + m_C)\ddot{z}_{AG} + m_C \left\{ \begin{array}{l} [-s\alpha_2] \cdot \\ [\text{c}\alpha_1 c\alpha_2] \cdot \\ [\ddot{x}_{CA} + {}^G\omega_2^A({}^G\omega_1^A y_{CA} - {}^G\omega_2^A x_{CA}) + {}^G\omega_3^A({}^G\omega_1^A z_{CA} - {}^G\omega_3^A x_{CA}) + 2({}^G\omega_2^A \dot{z}_{CA} - {}^G\omega_3^A \dot{y}_{CA}) + {}^G\dot{\omega}_2^A z_{CA} - {}^G\dot{\omega}_3^A y_{CA}] \\ + [\text{s}\alpha_1 c\alpha_2] \cdot \\ [{}^G\ddot{y}_{CA} + {}^G\omega_3^A({}^G\omega_2^A z_{CA} - {}^G\omega_3^A y_{CA}) + {}^G\omega_1^A({}^G\omega_2^A x_{CA} - {}^G\omega_1^A y_{CA}) + 2({}^G\omega_3^A \dot{x}_{CA} - {}^G\omega_1^A \dot{z}_{CA}) + {}^G\dot{\omega}_3^A x_{CA} - {}^G\dot{\omega}_1^A z_{CA}] \end{array} \right. \\
& \quad \left. + [\text{c}\alpha_1 c\alpha_2] \cdot \right. \\
& \quad \left. [{}^G\ddot{z}_{CA} + {}^G\omega_1^A({}^G\omega_3^A x_{CA} - {}^G\omega_1^A z_{CA}) + {}^G\omega_2^A({}^G\omega_3^A y_{CA} - {}^G\omega_2^A z_{CA}) + 2({}^G\omega_1^A \dot{y}_{CA} - {}^G\omega_2^A \dot{x}_{CA}) + {}^G\dot{\omega}_1^A y_{CA} - {}^G\dot{\omega}_2^A x_{CA}] \right\} \\
& = (-s\alpha_2)(F_{AB,1} + F_{A,1}^{ext} + F_{RW,1}^{ext}) \\
& + (\text{s}\alpha_1 c\alpha_2)(F_{AB,2} + F_{A,2}^{ext} + F_{RW,2}^{ext}) \\
& + (\text{c}\alpha_1 c\alpha_2)(F_{AB,3} + F_{A,3}^{ext} + F_{RW,3}^{ext})
\end{aligned} \tag{5.121}$$

$$\begin{aligned}
& m_C [\text{c}\alpha_2 c\alpha_3 \ddot{x}_{AG} + \text{c}\alpha_2 s\alpha_3 \ddot{y}_{AG} - \text{s}\alpha_2 \ddot{z}_{AG} \\
& + \ddot{x}_{CA} + {}^G\omega_2^A({}^G\omega_1^A y_{CA} - {}^G\omega_2^A x_{CA}) + {}^G\omega_3^A({}^G\omega_1^A z_{CA} - {}^G\omega_3^A x_{CA}) + 2({}^G\omega_2^A \dot{z}_{CA} - {}^G\omega_3^A \dot{y}_{CA}) + {}^G\dot{\omega}_2^A z_{CA} - {}^G\dot{\omega}_3^A y_{CA}] \\
& = -k_1 x_{CA} + F_{RW,1}^{ext}
\end{aligned} \tag{5.122}$$

$$\begin{aligned}
& m_C [(\text{s}\alpha_1 s\alpha_2 c\alpha_3 - \text{c}\alpha_1 s\alpha_3) \ddot{x}_{AG} + (\text{s}\alpha_1 s\alpha_2 s\alpha_3 + \text{c}\alpha_1 c\alpha_3) \ddot{y}_{AG} + \text{s}\alpha_1 c\alpha_2 \ddot{z}_{AG} \\
& + \ddot{y}_{CA} + {}^G\omega_3^A({}^G\omega_2^A z_{CA} - {}^G\omega_3^A y_{CA}) + {}^G\omega_1^A({}^G\omega_2^A x_{CA} - {}^G\omega_1^A y_{CA}) + 2({}^G\omega_3^A \dot{x}_{CA} - {}^G\omega_1^A \dot{z}_{CA}) + {}^G\dot{\omega}_3^A x_{CA} - {}^G\dot{\omega}_1^A z_{CA}] \\
& = -k_2 y_{CA} + F_{RW,2}^{ext}
\end{aligned} \tag{5.123}$$

$$\begin{aligned}
& m_C [(c\alpha_1 s\alpha_2 c\alpha_3 + s\alpha_1 s\alpha_3) \ddot{x}_{AG} + (c\alpha_1 s\alpha_2 s\alpha_3 - s\alpha_1 c\alpha_3) \ddot{y}_{AG} + c\alpha_1 c\alpha_2 \ddot{z}_{AG} \\
& + \ddot{z}_{CA} + {}^G\omega_1^A ({}^G\omega_3^A x_{CA} - {}^G\omega_1^A z_{CA}) + {}^G\omega_2^A ({}^G\omega_3^A y_{CA} - {}^G\omega_2^A z_{CA}) + 2({}^G\omega_1^A \dot{x}_{CA} - {}^G\omega_2^A \dot{z}_{CA}) + {}^G\dot{\omega}_1^A y_{CA} - {}^G\dot{\omega}_2^A x_{CA}] \quad (5.124) \\
& = -k_3(z_{CA} - z_{CA,0}) + F_{RW,3}^{ext}
\end{aligned}$$

$$\begin{aligned}
& [m_C z_{CA}] [(s\alpha_1 s\alpha_2 c\alpha_3 - c\alpha_1 s\alpha_3) \ddot{x}_{AG} + (s\alpha_1 s\alpha_2 s\alpha_3 + c\alpha_1 c\alpha_3) \ddot{y}_{AG} + s\alpha_1 c\alpha_2 \ddot{z}_{AG} \\
& + \ddot{y}_{CA} + {}^G\omega_3^A ({}^G\omega_2^A z_{CA} - {}^G\omega_3^A y_{CA}) + {}^G\omega_1^A ({}^G\omega_2^A x_{CA} - {}^G\omega_1^A y_{CA}) + 2({}^G\omega_3^A \dot{x}_{CA} - {}^G\omega_1^A \dot{z}_{CA}) + {}^G\dot{\omega}_3^A x_{CA} - {}^G\dot{\omega}_1^A z_{CA}] \\
& - [m_C y_{CA}] [(c\alpha_1 s\alpha_2 c\alpha_3 + s\alpha_1 s\alpha_3) \ddot{x}_{AG} + (c\alpha_1 s\alpha_2 s\alpha_3 - s\alpha_1 c\alpha_3) \ddot{y}_{AG} + c\alpha_1 c\alpha_2 \ddot{z}_{AG} \\
& + \ddot{z}_{CA} + {}^G\omega_1^A ({}^G\omega_3^A x_{CA} - {}^G\omega_1^A z_{CA}) + {}^G\omega_2^A ({}^G\omega_3^A y_{CA} - {}^G\omega_2^A z_{CA}) + 2({}^G\omega_1^A \dot{y}_{CA} - {}^G\omega_2^A \dot{x}_{CA}) + {}^G\dot{\omega}_1^A y_{CA} - {}^G\dot{\omega}_2^A x_{CA}] \\
& + {}^G\dot{\omega}_1^A I_1^A - {}^G\omega_2^A {}^G\omega_3^A (I_2^A - I_3^A) \\
& + [s\gamma_1 s\gamma_2 s\delta_3 + c\gamma_2 c\delta_3] [{}^G\dot{\omega}_1^D I_1^D - {}^G\omega_2^D {}^G\omega_3^D (I_2^D - I_3^D)] \quad (5.125) \\
& + [s\gamma_1 s\gamma_2 c\delta_3 - c\gamma_2 s\delta_3] [{}^G\dot{\omega}_2^D I_2^D - {}^G\omega_3^D {}^G\omega_1^D (I_3^D - I_1^D)] \\
& + [c\gamma_1 s\gamma_2] [{}^G\dot{\omega}_3^D I_3^D] \\
& = [-z_{CA}] [-k_2 y_{CA} + F_{RW,2}^{ext}] \\
& + [-y_{CA}] [-k_3(z_{CA} - z_{CA,0}) + F_{RW,3}^{ext}] \\
& + z_{iC} [-s\gamma_1 k_3(z_{CA} - z_{CA,0}) - c\gamma_1 c\gamma_2 k_2 y_{CA}] - z_{iA} k_2 y_{CA} \\
& + T_{AB,1} + T_{A,1}^{ext} + T_{RW,1}^{ext} - T_{Am_1}
\end{aligned}$$

$$\begin{aligned}
& -[m_C z_{CA}] [(c\alpha_2 c\alpha_3) \ddot{x}_{AG} + (c\alpha_2 s\alpha_3) \ddot{y}_{AG} - s\alpha_2 \ddot{z}_{AG} \\
& + \ddot{x}_{CA} + {}^G\omega_2^A ({}^G\omega_1^A y_{CA} - {}^G\omega_2^A x_{CA}) + {}^G\omega_3^A ({}^G\omega_1^A z_{CA} - {}^G\omega_3^A x_{CA}) + 2({}^G\omega_2^A \dot{z}_{CA} - {}^G\omega_3^A \dot{y}_{CA}) + {}^G\dot{\omega}_2^A z_{CA} - {}^G\dot{\omega}_3^A y_{CA}] \\
& + [m_C x_{CA}] [(c\alpha_1 s\alpha_2 c\alpha_3 + s\alpha_1 s\alpha_3) \ddot{x}_{AG} + (c\alpha_1 s\alpha_2 s\alpha_3 - s\alpha_1 c\alpha_3) \ddot{y}_{AG} + c\alpha_1 c\alpha_2 \ddot{z}_{AG} \\
& + \ddot{z}_{CA} + {}^G\omega_1^A ({}^G\omega_3^A x_{CA} - {}^G\omega_1^A z_{CA}) + {}^G\omega_2^A ({}^G\omega_3^A y_{CA} - {}^G\omega_2^A z_{CA}) + 2({}^G\omega_1^A \dot{y}_{CA} - {}^G\omega_2^A \dot{x}_{CA}) + {}^G\dot{\omega}_1^A y_{CA} - {}^G\dot{\omega}_2^A x_{CA}] \\
& + {}^G\dot{\omega}_2^A I_2^A - {}^G\omega_3^A {}^G\omega_1^A (I_3^A - I_1^A) \\
& + [c\gamma_1 s\delta_3] [{}^G\dot{\omega}_1^D I_1^D - {}^G\omega_2^D {}^G\omega_3^D (I_2^D - I_3^D)] \quad (5.126) \\
& + [c\gamma_1 c\delta_3] [{}^G\dot{\omega}_2^D I_2^D - {}^G\omega_3^D {}^G\omega_1^D (I_3^D - I_1^D)] \\
& - [s\gamma_1] [{}^G\dot{\omega}_3^D I_3^D] \\
& = [-z_{CA}] [-k_1 x_{CA} + F_{RW,1}^{ext}] \\
& + [-x_{CA}] [-k_3(z_{CA} - z_{CA,0}) + F_{RW,3}^{ext}] \\
& + z_{iC} [-c\gamma_1 s\gamma_2 k_3(z_{CA} - z_{CA,0}) + c\gamma_1 c\gamma_2 k_1 x_{CA}] + z_{iA} k_1 x_{CA} \\
& + T_{AB,2} + T_{A,2}^{ext} + T_{RW,2}^{ext} - T_{Am_2}
\end{aligned}$$

$$\begin{aligned}
& [m_C y_{CA}] [(c\alpha_2 c\alpha_3) \ddot{x}_{AG} + (c\alpha_2 s\alpha_3) \ddot{y}_{AG} - s\alpha_2 \ddot{z}_{AG} \\
& \quad + \ddot{x}_{CA} + {}^G\omega_2^A ({}^G\omega_1^A y_{CA} - {}^G\omega_2^A x_{CA}) + {}^G\omega_3^A ({}^G\omega_1^A z_{CA} - {}^G\omega_3^A x_{CA}) + 2({}^G\omega_2^A \dot{z}_{CA} - {}^G\omega_3^A \dot{x}_{CA}) + {}^G\dot{\omega}_2^A z_{CA} - {}^G\dot{\omega}_3^A y_{CA}] \\
& - [m_C x_{CA}] [(s\alpha_1 s\alpha_2 c\alpha_3 - c\alpha_1 s\alpha_3) \ddot{x}_{AG} + (s\alpha_1 s\alpha_2 s\alpha_3 + c\alpha_1 c\alpha_3) \ddot{y}_{AG} + s\alpha_1 c\alpha_2 \ddot{z}_{AG} \\
& \quad + \ddot{y}_{CA} + {}^G\omega_3^A ({}^G\omega_2^A z_{CA} - {}^G\omega_3^A y_{CA}) + {}^G\omega_1^A ({}^G\omega_2^A x_{CA} - {}^G\omega_1^A y_{CA}) + 2({}^G\omega_3^A \dot{x}_{CA} - {}^G\omega_1^A \dot{z}_{CA}) + {}^G\dot{\omega}_3^A x_{CA} - {}^G\dot{\omega}_1^A z_{CA}] \\
& \quad + {}^G\dot{\omega}_3^A I_3^A - {}^G\omega_1^A {}^G\omega_2^A (I_1^A - I_2^A) \\
& \quad + [s\gamma_1 c\gamma_2 s\delta_3 - s\gamma_2 c\delta_3] [{}^G\dot{\omega}_1^D I_1^D - {}^G\omega_2^D {}^G\omega_3^D (I_2^D - I_3^D)] \\
& \quad + [s\gamma_1 c\gamma_2 c\delta_3 + s\gamma_2 s\delta_3] [{}^G\dot{\omega}_2^D I_2^D - {}^G\omega_3^D {}^G\omega_1^D (I_3^D - I_1^D)] \\
& \quad + [c\gamma_1 c\gamma_2] [{}^G\dot{\omega}_3^D I_3^D] \\
& = [-y_{CA}] [-k_1 x_{CA} + F_{RW,1}^{ext}] \\
& \quad + [x_{CA}] [-k_2 y_{CA} + F_{RW,2}^{ext}] \\
& \quad + z_{iC} [c\gamma_1 s\gamma_2 k_2 y_{CA} + s\gamma_1 k_1 x_{CA}] \\
& \quad + T_{AB,3} + T_{A,3}^{ext} + T_{RW,3}^{ext}
\end{aligned} \tag{5.127}$$

$$\begin{aligned}
& {}^G\dot{\omega}_1^D I_1^D - {}^G\omega_2^D {}^G\omega_3^D (I_2^D - I_3^D) \\
& = \{s\gamma_1 s\gamma_2 s\delta_3 + c\gamma_2 c\delta_3\} \left\{ -k_4 s\gamma_1 \frac{\text{acos}(c\gamma_1 c\gamma_2)}{\sqrt{s^2 \gamma_1 + c^2 \gamma_1 s^2 \gamma_2}} + z_{iC} [-s\gamma_1 k_3 (z_{CA} - z_{CA,0}) - c\gamma_1 c\gamma_2 k_2 y_{CA}] + T_{RW,1}^{ext} \right\} \\
& \quad + \{c\gamma_1 s\delta_3\} \left\{ -k_4 c\gamma_1 s\gamma_2 \frac{\text{acos}(c\gamma_1 c\gamma_2)}{\sqrt{s^2 \gamma_1 + c^2 \gamma_1 s^2 \gamma_2}} + z_{iC} [-c\gamma_1 s\gamma_2 k_3 (z_{CA} - z_{CA,0}) + c\gamma_1 c\gamma_2 k_1 x_{CA}] + T_{RW,2}^{ext} \right\} \\
& \quad + \{s\gamma_1 c\gamma_2 s\delta_3 - s\gamma_2 c\delta_3\} \left\{ z_{iC} [c\gamma_1 s\gamma_2 k_2 y_{CA} + s\gamma_1 k_1 x_{CA}] + T_{RW,3}^{ext} + T_{Am_3} \right\}
\end{aligned} \tag{5.128}$$

$$\begin{aligned}
& {}^G\dot{\omega}_2^D I_2^D - {}^G\omega_3^D {}^G\omega_1^D (I_3^D - I_1^D) \\
& = \{s\gamma_1 s\gamma_2 c\delta_3 - c\gamma_2 s\delta_3\} \left\{ -k_4 s\gamma_1 \frac{\text{acos}(c\gamma_1 c\gamma_2)}{\sqrt{s^2 \gamma_1 + c^2 \gamma_1 s^2 \gamma_2}} + z_{iC} [-s\gamma_1 k_3 (z_{CA} - z_{CA,0}) - c\gamma_1 c\gamma_2 k_2 y_{CA}] + T_{RW,1}^{ext} \right\} \\
& \quad + \{c\gamma_1 c\delta_3\} \left\{ -k_4 c\gamma_1 s\gamma_2 \frac{\text{acos}(c\gamma_1 c\gamma_2)}{\sqrt{s^2 \gamma_1 + c^2 \gamma_1 s^2 \gamma_2}} + z_{iC} [-c\gamma_1 s\gamma_2 k_3 (z_{CA} - z_{CA,0}) + c\gamma_1 c\gamma_2 k_1 x_{CA}] + T_{RW,2}^{ext} \right\} \\
& \quad + \{s\gamma_1 c\gamma_2 c\delta_3 + s\gamma_2 s\delta_3\} \left\{ z_{iC} [c\gamma_1 s\gamma_2 k_2 y_{CA} + s\gamma_1 k_1 x_{CA}] + T_{RW,3}^{ext} + T_{Am_3} \right\}
\end{aligned} \tag{5.129}$$

$$\begin{aligned}
& {}^G \dot{\omega}_3^D \, I_3^D \\
= & \{c\gamma_1 s\gamma_2\} \left\{ -k_4 s\gamma_1 \frac{a \cos(c\gamma_1 c\gamma_2)}{\sqrt{s^2 \gamma_1 + c^2 \gamma_1 s^2 \gamma_2}} + z_{iC}[-s\gamma_1 k_3(z_{CA} - z_{CA,0}) - c\gamma_1 c\gamma_2 k_2 y_{CA}] + T_{RW,1}^{ext} \right\} \\
& + \{-s\gamma_1\} \left\{ -k_4 c\gamma_1 s\gamma_2 \frac{a \cos(c\gamma_1 c\gamma_2)}{\sqrt{s^2 \gamma_1 + c^2 \gamma_1 s^2 \gamma_2}} + z_{iC}[-c\gamma_1 s\gamma_2 k_3(z_{CA} - z_{CA,0}) + c\gamma_1 c\gamma_2 k_1 x_{CA}] + T_{RW,2}^{ext} \right\} \\
& + \{c\gamma_1 c\gamma_2\} \left\{ z_{iC}[c\gamma_1 s\gamma_2 k_2 y_{CA} + s\gamma_1 k_1 x_{CA}] + T_{RW,3}^{ext} + T_{Am_3} \right\}
\end{aligned} \tag{5.130}$$

where c denotes the cosine function, and s denotes the sine function.

We interpret the equations of motion in the following way:

- Equations 5.119-5.121 describe the motion of the entire spacecraft-RW system relative to the inertial frame, \hat{e}_G . The three equations represent the components of the forces and accelerations resolved on the \hat{e}_x , \hat{e}_y , and \hat{e}_z axes, respectively.
- Equations 5.122-5.124 describe the motion of RW-3 relative to the spacecraft bus. The three equations represent the components of the forces and accelerations resolved on the \hat{a}_1 , \hat{a}_2 , and \hat{a}_3 axes, respectively.
- Equations 5.125-5.127 describe the attitude dynamics of the entire spacecraft-RW system. The three equations represent the components of the torques and angular accelerations resolved on the \hat{a}_1 , \hat{a}_2 , and \hat{a}_3 axes, respectively.
- Equations 5.128-5.130 describe the attitude dynamics of RW-3. The three equations represent the components of the torques and angular accelerations resolved on the \hat{d}_1 , \hat{d}_2 , and \hat{d}_3 axes, respectively.

Hence the 12 equations of motion for spacecraft A and its reaction wheels are represented by Equations 5.119-5.130. Note that similar equations will describe the behavior of each additional spacecraft in the array. The sets of equations are then coupled to each other by the electromagnetic forces and torques, which are functions of the *relative* degrees of freedom between the various spacecraft, as described in Section 5.3.

5.4.5 Nonlinear Equations of Motion with Infinite Spring Stiffness

Finally, we consider a similar system with rigid connections between each spacecraft and its reaction wheels (RWs). The spring interfaces were modeled above to capture the flexibility of reaction wheels, which often causes an amplification of reaction wheel disturbances in real systems. Since our concern here (and in the simulation in Chapter 7) is not reaction wheel disturbances, but rather the rigid-body dynamics of an EMFF system, we rewrite the equations in Section 5.4.4 assuming infinitely stiff springs (rigid connections).

The result is the loss of the following degrees of freedom:

- the x_{CA} , y_{CA} , and z_{CA} translations of RW-3 relative to the spacecraft
- the γ_1 and γ_2 rotations of RW-3 relative to the spacecraft

Hence we are setting $x_{CA} = x_{CA,0} = 0$, $y_{CA} = y_{CA,0} = 0$, and $z_{CA} = z_{CA,0}$ where $z_{CA,0}$ was defined in Equation 5.68. Further, although RW-3 is still free to rotate through angle δ_3 about its spin axis, \hat{d}_3 , relative to the spacecraft, its rotations γ_1 and γ_2 about \hat{c}_1 and \hat{c}_2 , respectively, relative to the spacecraft, are constrained to zero.

With these assumptions, the equations of motion in Section 5.4.4 reduce to the following set of equations:

$$\begin{aligned}
 & (m_A + m_C)\ddot{x}_{AG} + m_C z_{CA,0} \left\{ \begin{array}{l} [c\alpha_2 c\alpha_3] [{}^G\omega_3^A {}^G\omega_1^A + {}^G\dot{\omega}_2^A] \\ + [s\alpha_1 s\alpha_2 c\alpha_3 - c\alpha_1 s\alpha_3] [{}^G\omega_3^A {}^G\omega_2^A - {}^G\dot{\omega}_1^A] \\ + [-c\alpha_1 s\alpha_2 c\alpha_3 - s\alpha_1 s\alpha_3] [({}^G\omega_1^A)^2 + ({}^G\omega_2^A)^2] \end{array} \right\} \quad (5.131) \\
 & = (c\alpha_2 c\alpha_3)(F_{AB,1}^{ext} + F_{A,1}^{ext} + F_{RW,1}^{ext}) \\
 & + (s\alpha_1 s\alpha_2 c\alpha_3 - c\alpha_1 s\alpha_3)(F_{AB,2}^{ext} + F_{A,2}^{ext} + F_{RW,2}^{ext}) \\
 & + (c\alpha_1 s\alpha_2 c\alpha_3 + s\alpha_1 s\alpha_3)(F_{AB,3}^{ext} + F_{A,3}^{ext} + F_{RW,3}^{ext})
 \end{aligned}$$

$$\begin{aligned}
& (m_A + m_C)\ddot{y}_{AG} + m_C z_{CA,0} \left\{ [c\alpha_2 s\alpha_3][{}^G\omega_3^A {}^G\omega_1^A + {}^G\dot{\omega}_2^A] \right. \\
& \quad + [s\alpha_1 s\alpha_2 s\alpha_3 + c\alpha_1 c\alpha_3][{}^G\omega_3^A {}^G\omega_2^A - {}^G\dot{\omega}_1^A] \\
& \quad \left. + [s\alpha_1 c\alpha_3 - c\alpha_1 s\alpha_2 s\alpha_3][({}^G\omega_1^A)^2 + ({}^G\omega_2^A)^2] \right\} \\
& = (c\alpha_2 s\alpha_3)(F_{AB,1} + F_{A,1}^{ext} + F_{RW,1}^{ext}) \\
& \quad + (s\alpha_1 s\alpha_2 s\alpha_3 + c\alpha_1 c\alpha_3)(F_{AB,2} + F_{A,2}^{ext} + F_{RW,2}^{ext}) \\
& \quad + (c\alpha_1 s\alpha_2 s\alpha_3 - s\alpha_1 c\alpha_3)(F_{AB,3} + F_{A,3}^{ext} + F_{RW,3}^{ext})
\end{aligned} \tag{5.132}$$

$$\begin{aligned}
& (m_A + m_C)\ddot{z}_{AG} + m_C z_{CA,0} \left\{ [-s\alpha_2][{}^G\omega_3^A {}^G\omega_1^A + {}^G\dot{\omega}_2^A] \right. \\
& \quad + [s\alpha_1 c\alpha_2][{}^G\omega_3^A {}^G\omega_2^A - {}^G\dot{\omega}_1^A] \\
& \quad \left. + [-c\alpha_1 c\alpha_2][({}^G\omega_1^A)^2 + ({}^G\omega_2^A)^2] \right\} \\
& = (-s\alpha_2)(F_{AB,1} + F_{A,1}^{ext} + F_{RW,1}^{ext}) \\
& \quad + (s\alpha_1 c\alpha_2)(F_{AB,2} + F_{A,2}^{ext} + F_{RW,2}^{ext}) \\
& \quad + (c\alpha_1 c\alpha_2)(F_{AB,3} + F_{A,3}^{ext} + F_{RW,3}^{ext})
\end{aligned} \tag{5.133}$$

$$\begin{aligned}
& [m_C z_{CA,0}][(s\alpha_1 s\alpha_2 c\alpha_3 - c\alpha_1 s\alpha_3) \ddot{x}_{AG} + (s\alpha_1 s\alpha_2 s\alpha_3 + c\alpha_1 c\alpha_3) \ddot{y}_{AG} + s\alpha_1 c\alpha_2 \ddot{z}_{AG}] \\
& \quad - [m_C z_{CA,0}^2][{}^G\dot{\omega}_1^A - {}^G\omega_3^A {}^G\omega_2^A] \\
& \quad + {}^G\dot{\omega}_1^A I_1^A - {}^G\omega_2^A {}^G\omega_3^A (I_2^A - I_3^A) \\
& \quad + [c\delta_3][{}^G\dot{\omega}_1^A I_1^P - {}^G\omega_2^A ({}^G\omega_3^A + \dot{\delta}_3) (I_2^P - I_3^P)] \\
& \quad + [-s\delta_3][{}^G\dot{\omega}_2^A I_2^P - {}^G\omega_1^A ({}^G\omega_3^A + \dot{\delta}_3) (I_3^P - I_1^P)] \\
& = T_{AB,1} + T_{A,1}^{ext} + T_{RW,1}^{ext} - T_{Am_1} - z_{CA,0} F_{RW,2}^{ext}
\end{aligned} \tag{5.134}$$

$$\begin{aligned}
& -[m_C z_{CA,0}][(\mathbf{c}\alpha_2\mathbf{c}\alpha_3)\ddot{x}_{AG} + (\mathbf{c}\alpha_2\mathbf{s}\alpha_3)\ddot{y}_{AG} - \mathbf{s}\alpha_2\ddot{z}_{AG}] \\
& -[m_C z_{CA,0}^2][{}^G\dot{\omega}_2^A + {}^G\omega_3^A {}^G\omega_1^A] \\
& + {}^G\dot{\omega}_2^A I_2^A - {}^G\omega_3^A {}^G\omega_1^A (I_3^A - I_1^A) \\
& + [\mathbf{s}\delta_3][{}^G\dot{\omega}_1^A I_1^D - {}^G\omega_2^A ({}^G\omega_3^A + \dot{\delta}_3) (I_2^D - I_3^D)] \\
& + [\mathbf{c}\delta_3][{}^G\dot{\omega}_2^A I_2^D - {}^G\omega_1^A ({}^G\omega_3^A + \dot{\delta}_3) (I_3^D - I_1^D)] \\
& = T_{AB,2} + T_{A,2}^{ext} + T_{RW,2}^{ext} - T_{Am_2} + z_{CA,0} F_{RW,1}^{ext}
\end{aligned} \tag{5.135}$$

$${}^G\dot{\omega}_3^A I_3^A - {}^G\omega_1^A {}^G\omega_2^A (I_1^A - I_2^A) + ({}^G\dot{\omega}_3^A + \ddot{\delta}_3) I_3^D = T_{AB,3} + T_{A,3}^{ext} + T_{RW,3}^{ext} \tag{5.136}$$

$$({}^G\dot{\omega}_3^A + \ddot{\delta}_3) I_3^D = T_{RW,3}^{ext} + T_{Am_3} \tag{5.137}$$

5.5 Summary and Conclusions

In this chapter, we have defined the geometry for a three-dimensional, multi-spacecraft electromagnetic formation flying array, in which each spacecraft has three orthogonal electromagnetic actuators and three orthogonal reaction wheels. We have also developed from first principles the *nonlinear dynamic equations of motion* (the evaluation model) of this system using Kane's method.

The major contributions of this chapter are:

- We have developed a new framework for modeling the dynamics of formation flying spacecraft with electromagnetic actuators, including the introduction of standardized notation, descriptions of the system's degrees of freedom, and a derivation of expressions for the system's kinematics.
- We have developed from first principles the dynamic equations of motion for a multi-body electromagnetic formation flying array.
- Our model includes the nonlinear dynamics (the gyroscopic stiffening effect) of the reaction wheels that store the array's angular momentum.
- The equations also account for external disturbances to the system, and allow us to capture reaction wheel disturbances in the system model.

The following steps will be taken in Chapter 6 to further develop this work:

- The equations will be expressed for a two-spacecraft array, and then will be linearized about a nominal trajectory (a steady-state spin maneuver) to yield the *linearized dynamic equations of motion* (the design model).
- A *stability analysis* will be performed, in which the eigenvalues of the linearized system are determined and analyzed for dynamic stability. The eigenvectors will also be examined to indicate the “mode shapes” of motion of the system.
- A *controllability analysis* will be performed to ensure that the given set of actuators is sufficient to fully control the dynamics of the system.
- An *optimal controller will be designed* using the linearized equations and the given set of actuators described above.

Finally, in Chapter 7, the resulting controller will be used to perform a *closed-loop time simulation* of the system, using both the linearized design model and the original, nonlinear evaluation model. The success of the controller will be determined by the performance of the nonlinear simulation.

Chapter 6

ELECTROMAGNETIC FORMATION FLIGHT DYNAMICS ANALYSIS

In this chapter, we apply the nonlinear equations of motion derived in Chapter 5 to a two-spacecraft electromagnetic formation flying (EMFF) array. We define the nominal trajectory of the array to be a steady-state spin maneuver about a common origin, a maneuver that is useful for deep-space interferometry applications. We then proceed to linearize the nonlinear equations of motion about this trajectory. The resulting linearized set of equations will be referred to as the *design model*.

With the design model, we first check the *stability* and *controllability* of the system. We then proceed to *design a linear controller* for the system. In Chapter 7, this linear controller will be implemented with the original nonlinear equations, or the *evaluation model*, to form the closed-loop dynamics of this system, and the closed-loop dynamics will be simulated. In this way, we will be able to assess the effectiveness of the linear controller on the nonlinear dynamics of the system.

This chapter is organized as follows:

- In Section 6.1, we briefly review the system under consideration.
- In Section 6.2, the system's nominal operating trajectory is defined, and the nonlinear equations are linearized about this nominal trajectory.
- In Section 6.3, a *stability analysis* of the linearized equations of motion is presented. The eigenvalues of the linearized system are determined and analyzed for dynamic stability. They are investigated for dependence on RW gyrostiffening terms, and the degree of gyrostiffening in the system is

assessed based on these results. The eigenvectors are also examined to indicate the “modes” of motion of the system.

- In Section 6.4, a *controllability analysis* is presented to determine whether the given set of actuators is sufficient to fully control the dynamics of the system. Various actuator configurations are investigated.
- In Section 6.5, an *optimal controller* is designed based on the linearized dynamics and the given set of actuators.
- In Section 6.6, key results and contributions are summarized.

6.1 System Description

We begin by reviewing the geometry and characteristics of the system being considered. Chapter 5 describes the nonlinear dynamics of an n -spacecraft EMFF system, where each spacecraft has three orthogonal electromagnets, oriented along the body-fixed \hat{a}_1 , \hat{a}_2 , and \hat{a}_3 axes, respectively, and three orthogonal reaction wheels, whose spin axes align with \hat{a}_1 , \hat{a}_2 , and \hat{a}_3 , respectively. These electromagnets (EMs) and reaction wheels (RWs) are used as actuators to control the relative positions and absolute attitudes of the spacecraft.

The linearized system that we will consider consists only of $n = 2$ spacecraft, which we denote as spacecraft A and B. The two-spacecraft array is depicted in Figure 6.1. The \hat{e}_x , \hat{e}_y , \hat{e}_z coordinate frame in Figure 6.1 is the same global frame, \hat{e}_G , defined for the derivation of the nonlinear equations of motion in Section 5.2.2 and depicted in Figure 5.2. We also consider the spherical frame shown in Figure 6.1, defined as:

$$\hat{e}_S \equiv \left\{ \begin{array}{c} \hat{e}_r \\ \hat{e}_\phi \\ \hat{e}_\psi \end{array} \right\} \quad (6.1)$$

\hat{e}_S is a global, curvilinear coordinate frame. Because it is a global frame, the distance r and the angles ϕ and ψ (all shown in Figure 6.1) are measured with respect to \hat{e}_G . ψ is thus defined as the angle between the position vector to spacecraft A (\vec{r}_{AG}) and the \hat{e}_x , \hat{e}_y plane, and ϕ is defined as the angle between \hat{e}_x and the projection of \vec{r}_{AG} onto the \hat{e}_x , \hat{e}_y

plane. Further, because \hat{e}_S is a curvilinear frame, its unit vectors ($\hat{e}_r, \hat{e}_\phi, \hat{e}_\psi$) move with spacecraft A to form a *local* frame whose origin lies at the center of mass of spacecraft A, as depicted in Figure 6.2. These unit vectors are not fixed to the body in that they do not rotate or “tilt” with the spacecraft; rather, the spacecraft rotates *relative* to this frame.

As shown in Figure 6.2, \hat{e}_r always aligns with the position vector, \hat{r}_{AG} , of spacecraft A relative to the origin of the global frame. Hence if spacecraft A lies on the surface of an imaginary sphere of radius r centered at the origin of the global frame, the \hat{e}_r vector is perpendicular to the spherical surface. The \hat{e}_ϕ vector is tangent to the spherical surface, parallel to the local line of constant *latitude*. The \hat{e}_ψ vector is also tangent to the spherical surface, parallel to the local line of constant *longitude*, thus completing the orthogonal frame.

Similar to the relationship between \hat{e}_G and \hat{e}_A in Section 5.2.4, we relate \hat{e}_G to the curvilinear frame, \hat{e}_S as:

$$\hat{e}_G = R_3(\phi)R_2(-\psi)\hat{e}_S \quad (6.2)$$

or conversely, as:

$$\hat{e}_S = R_2^T(-\psi)R_3^T(\phi)\hat{e}_G = R_2(\psi)R_3^T(\phi)\hat{e}_G \quad (6.3)$$

where the rotation matrices R_2 and R_3 were defined in Section 5.2.4.

Now we consider the degrees of freedom of this two-spacecraft array. Recall the degrees of freedom that were defined in Section 5.2.3 for an n -spacecraft array:

- x_{AG}, y_{AG} , and z_{AG} are components of the position vector of spacecraft A, resolved on the cartesian coordinate axes, \hat{e}_x, \hat{e}_y , and \hat{e}_z .
- α_3, α_2 , and α_1 are the Euler angle rotations of spacecraft A about its body-fixed \hat{a}_3, \hat{a}_2 , and \hat{a}_1 axes, respectively. (The Euler angles are defined such that when they are zero, the \hat{e}_A frame is aligned with \hat{e}_G .)
- δ_3 is the rotation angle of RW-3 on spacecraft A about \hat{d}_3 , the body-fixed axis on the RW that is nominally aligned with the \hat{a}_3 axis.

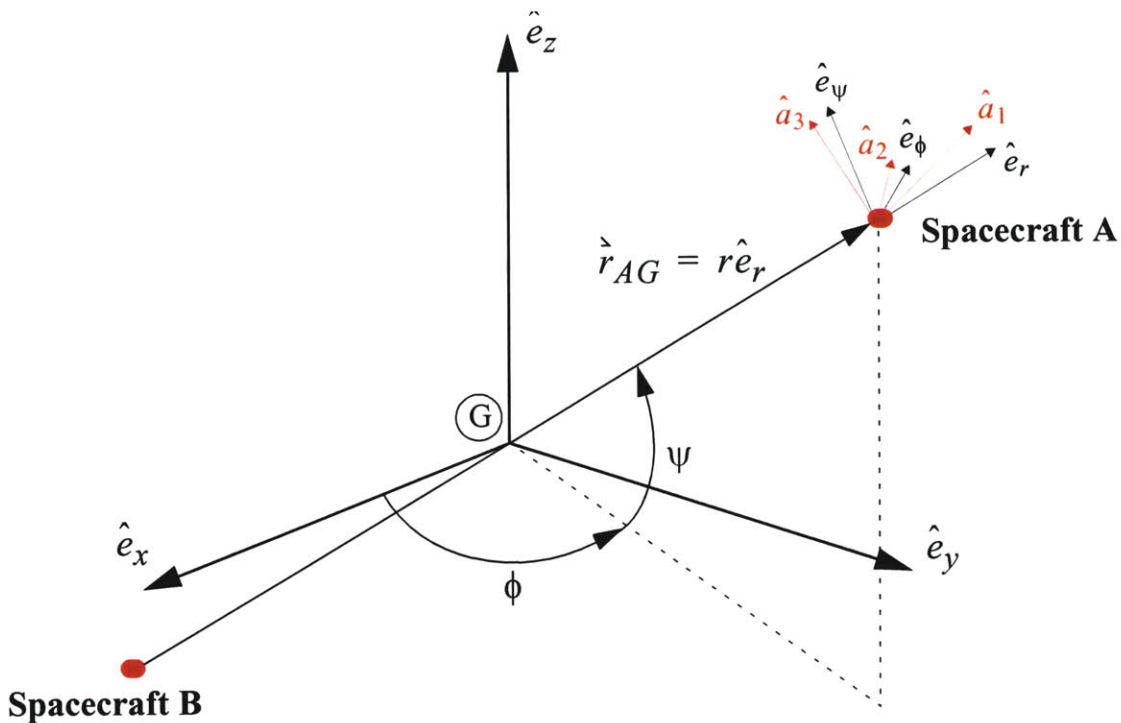


Figure 6.1 Geometry of Two-Spacecraft EMFF Array

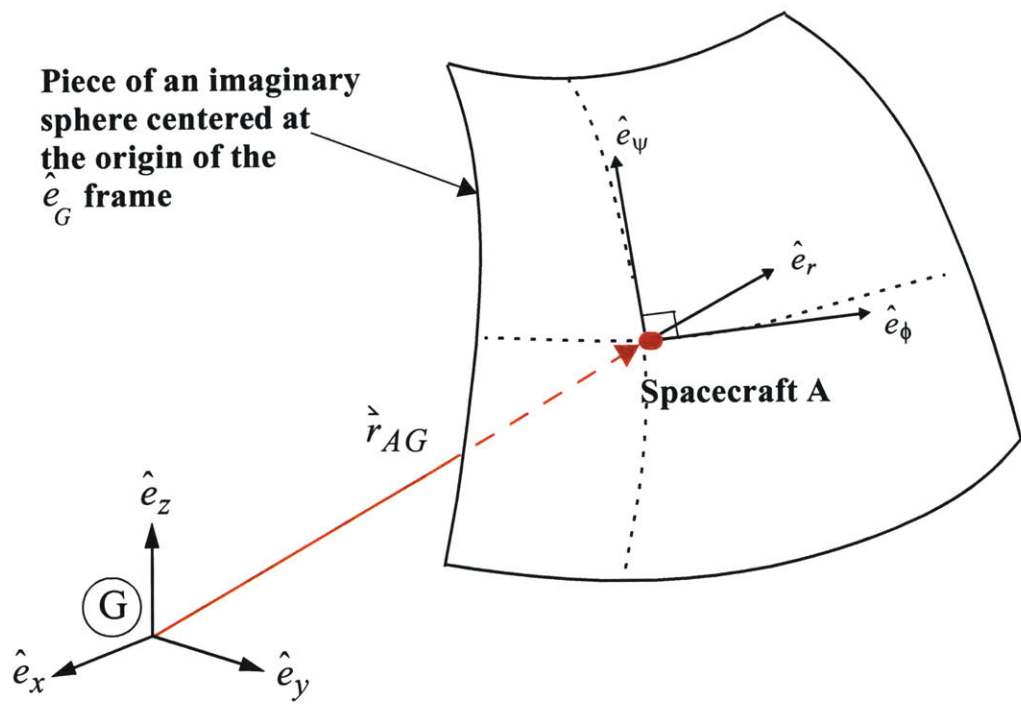


Figure 6.2 Local Curvilinear Coordinate Frame at Spacecraft A

- Finally, analogous variables exist to characterize the positions and attitudes of all the remaining spacecraft in the array. For instance, spacecraft B would be characterized by three position variables (x_{BG} , y_{BG} , and z_{BG}), three Euler angles (β_3 , β_2 , and β_1 about body-fixed b_3 , b_2 , and b_1 axes, respectively), and an RW rotation angle (ε_3).

The position vector, \hat{r}_{AG} , was defined in Equation 5.5 with components (x_{AG} , y_{AG} , and z_{AG}) resolved on the global frame, \hat{e}_G . As depicted in Figure 6.1, \hat{r}_{AG} can also be resolved on the spherical coordinate frame, as:

$$\begin{aligned} \hat{r}_{AG} &= \begin{bmatrix} x_{AG} & y_{AG} & z_{AG} \end{bmatrix} \begin{Bmatrix} \hat{e}_x \\ \hat{e}_y \\ \hat{e}_z \end{Bmatrix} = \begin{bmatrix} x_{AG} & y_{AG} & z_{AG} \end{bmatrix} \hat{e}_G \\ &= \begin{bmatrix} r & 0 & 0 \end{bmatrix} \begin{Bmatrix} \hat{e}_r \\ \hat{e}_\phi \\ \hat{e}_\psi \end{Bmatrix} = \begin{bmatrix} r & 0 & 0 \end{bmatrix} \hat{e}_S \end{aligned} \quad (6.4)$$

where \hat{e}_G and \hat{e}_S are related by Equations 6.2 and 6.3. Using spherical coordinates, the position of spacecraft A is thus characterized by the distance, r , from the origin of \hat{e}_G , and the direction from the origin to the \hat{e}_r , \hat{e}_ϕ , \hat{e}_ψ triad, defined by the angles ϕ and ψ .

Substituting Equation 6.3 for \hat{e}_S into Equation 6.4, we can define the following relationships between the cartesian and spherical coordinates of the position vector:

$$x_{AG} = r \cos \psi \cos \phi \quad (6.5)$$

$$y_{AG} = r \cos \psi \sin \phi \quad (6.6)$$

$$z_{AG} = r \sin \psi \quad (6.7)$$

Conversely, we find from geometry (and the definitions of ϕ and ψ on page 124):

$$r = \sqrt{x_{AG}^2 + y_{AG}^2 + z_{AG}^2} \quad (6.8)$$

$$\phi = \text{atan}\left(\frac{y_{AG}}{x_{AG}}\right) \quad (6.9)$$

$$\psi = \text{atan}\left(\frac{z_{AG}}{\sqrt{x_{AG}^2 + y_{AG}^2}}\right) \quad (6.10)$$

With these definitions, we return to the set of nonlinear equations developed in Chapter 5 for an n -spacecraft EMFF array, and we make the following assumptions:

1. We treat the interface between each spacecraft bus and its RWs as an infinitely stiff spring, or a rigid connection.
2. We neglect external forces and torques on the RWs, since we are more concerned with the rigid-body dynamics of the system than the system's response to RW disturbances.
3. We neglect the external loads on the spacecraft bus, since we will attempt to demonstrate closed-loop control of the linearized system without yet accounting for noise or continual external disturbances. An initial external disturbance will be modeled as a non-zero initial condition, and we will simulate the free response, due to only internal (EM, RW) forces and torques.
4. We neglect the RW offset distance from the center of mass of the spacecraft bus ($z_{CA,0} = 0$) without loss of generality. The term is not highly influential to the dynamics of the system, and neglecting it will simplify the linearization of the nonlinear equations, as well as the subsequent simulations.
5. We treat spacecraft A and B as being identical in mass and geometric properties. Doing so will still capture the essential dynamics of the system, while simplifying the linearization and simulation of the nonlinear equations of motion.

With these assumptions, the nonlinear equations of motion in Chapter 5 reduce to the following, for each spacecraft in the array:

$$\begin{aligned} (m_A + m_C)\ddot{x}_{AG} &= (c\alpha_2 c\alpha_3)(F_{AB,1}) \\ &+ (s\alpha_1 s\alpha_2 c\alpha_3 - c\alpha_1 s\alpha_3)(F_{AB,2}) \\ &+ (c\alpha_1 s\alpha_2 c\alpha_3 + s\alpha_1 s\alpha_3)(F_{AB,3}) \end{aligned} \quad (6.11)$$

$$\begin{aligned}
(m_A + m_C)\ddot{y}_{AG} = & (c\alpha_2 s\alpha_3)(F_{AB,1}) \\
& + (s\alpha_1 s\alpha_2 s\alpha_3 + c\alpha_1 c\alpha_3)(F_{AB,2}) \\
& + (c\alpha_1 s\alpha_2 s\alpha_3 - s\alpha_1 c\alpha_3)(F_{AB,3})
\end{aligned} \tag{6.12}$$

$$\begin{aligned}
(m_A + m_C)\ddot{z}_{AG} = & (-s\alpha_2)(F_{AB,1}) \\
& + (s\alpha_1 c\alpha_2)(F_{AB,2}) \\
& + (c\alpha_1 c\alpha_2)(F_{AB,3})
\end{aligned} \tag{6.13}$$

$$\begin{aligned}
& {}^G\dot{\omega}_1^A I_1^A - {}^G\omega_2^A {}^G\omega_3^A (I_2^A - I_3^A) \\
& + [c\delta_3] [{}^G\dot{\omega}_1^A I_1^D - {}^G\omega_2^A ({}^G\omega_3^A + \dot{\delta}_3) (I_2^D - I_3^D)] \\
& + [-s\delta_3] [{}^G\dot{\omega}_2^A I_2^D - {}^G\omega_1^A ({}^G\omega_3^A + \dot{\delta}_3) (I_3^D - I_1^D)] \\
& = T_{AB,1} - T_{Am_1}
\end{aligned} \tag{6.14}$$

$$\begin{aligned}
& {}^G\dot{\omega}_2^A I_2^A - {}^G\omega_3^A {}^G\omega_1^A (I_3^A - I_1^A) \\
& + [s\delta_3] [{}^G\dot{\omega}_1^A I_1^D - {}^G\omega_2^A ({}^G\omega_3^A + \dot{\delta}_3) (I_2^D - I_3^D)] \\
& + [c\delta_3] [{}^G\dot{\omega}_2^A I_2^D - {}^G\omega_1^A ({}^G\omega_3^A + \dot{\delta}_3) (I_3^D - I_1^D)] \\
& = T_{AB,2} - T_{Am_2}
\end{aligned} \tag{6.15}$$

$${}^G\dot{\omega}_3^A I_3^A - {}^G\omega_1^A {}^G\omega_2^A (I_1^A - I_2^A) = T_{AB,3} - T_{Am_3} \tag{6.16}$$

$$({}^G\dot{\omega}_3^A + \ddot{\delta}_3) I_3^D = T_{Am_3} \tag{6.17}$$

where all of the variables in these equations are defined in Chapter 5.

In this chapter, we will linearize these equations for a two-spacecraft array. Because of assumptions 2, 3, and 5 above, and because the nominal trajectory will be a steady-state spin of two spacecraft about their common center, the center of mass of the array will remain fixed in space, and will always coincide with the origin of the global frame. Hence spacecraft B will nominally lie opposite spacecraft A with respect to the global reference

frame, \hat{e}_G . If spacecraft A lies at coordinates (r, ϕ, ψ) , where $-\frac{\pi}{2} \leq \psi < \frac{\pi}{2}$, then spacecraft B lies at coordinates $(r, \phi + \pi, -\psi)$, so that:

$$r_B = r_A = r, \quad \phi_B = \phi_A + \pi = \phi + \pi, \quad -\psi_B = \psi_A = \psi \quad (6.18)$$

Since the position of spacecraft B is thus constrained to be opposite that of spacecraft A, and we have redefined the position of spacecraft A using curvilinear coordinates, we revisit the set of variables defined on page 125, and we revise that set to be:

- r, ϕ , and ψ are curvilinear coordinates defining the position vector of spacecraft A.
- α_3, α_2 , and α_1 are the Euler angle rotations of spacecraft A about its body-fixed \hat{a}_3, \hat{a}_2 , and \hat{a}_1 axes, respectively. (The Euler angles are defined such that when they are zero, the \hat{e}_A frame is aligned with \hat{e}_G .)
- δ_3 is the rotation angle of RW-3 on spacecraft A about \hat{d}_3 , the body-fixed axis on the RW that is nominally aligned with the \hat{a}_3 axis.
- The position coordinates of spacecraft B are determined using 6.18, and are not considered to be independent variables.
- β_3, β_2 , and β_1 are the Euler angle rotations of spacecraft B about its body-fixed \hat{b}_3, \hat{b}_2 , and \hat{b}_1 axes, respectively. (The Euler angles are defined such that when they are zero, the \hat{e}_B frame is aligned with \hat{e}_G .)
- ε_3 is the rotation angle of RW-3 on spacecraft B about \hat{e}_3 , the body-fixed axis on the RW that is nominally aligned with the \hat{b}_3 axis.

This revised set thus consists of 11 independent variables: three to describe the position and three to describe the attitude of spacecraft A, one to describe the RW-3 rotation angle on spacecraft A, three to describe the attitude of spacecraft B, and one to describe the RW-3 rotation angle on spacecraft B. We arrange these 11 degrees of freedom in a column matrix, \tilde{x} :

$$\tilde{x} = \begin{bmatrix} r & \phi & \psi & \alpha_1 & \alpha_2 & \alpha_3 & \delta_3 & \beta_1 & \beta_2 & \beta_3 & \varepsilon_3 \end{bmatrix}^T \quad (6.19)$$

We now return to Equations 6.11-6.13, the nonlinear equations that describe the position of each spacecraft, and transform them to curvilinear coordinates. This will facilitate the

linearization process in Section 6.2. Recalling the relationships in Equations 5.14 and 5.64, we can rewrite Equations 6.11-6.13 as:

$$(m_A + m_C)\ddot{x}_{AG} = F_{AB,x} \quad (6.20)$$

$$(m_A + m_C)\ddot{y}_{AG} = F_{AB,y} \quad (6.21)$$

$$(m_A + m_C)\ddot{z}_{AG} = F_{AB,z} \quad (6.22)$$

or equivalently as:

$$(m_A + m_C)\ddot{\vec{r}}_{AG} = \ddot{\vec{F}}_{AB} \quad (6.23)$$

where $\ddot{\vec{F}}_{AB}$ may be expressed by Equation 5.64, or as:

$$\begin{aligned} \ddot{\vec{F}}_{AB} &= \left[\begin{array}{c} F_{AB,x} \\ F_{AB,y} \\ F_{AB,z} \end{array} \right] \left\{ \begin{array}{c} \hat{e}_x \\ \hat{e}_y \\ \hat{e}_z \end{array} \right\} \\ &= \left[\begin{array}{c} F_{AB,1} \\ F_{AB,2} \\ F_{AB,3} \end{array} \right] \left\{ \begin{array}{c} \hat{a}_1 \\ \hat{a}_2 \\ \hat{a}_3 \end{array} \right\} \quad (6.24) \\ &= \left[\begin{array}{c} F_{AB,r} \\ F_{AB,\phi} \\ F_{AB,\psi} \end{array} \right] \left\{ \begin{array}{c} \hat{e}_r \\ \hat{e}_\phi \\ \hat{e}_\psi \end{array} \right\} \end{aligned}$$

and $\ddot{\vec{r}}_{AG}$ may be expressed by twice differentiating Equation 6.4:

$$\begin{aligned}
\ddot{\vec{r}}_{AG} &= \left[\begin{array}{c} \ddot{x}_{AG} \quad \ddot{y}_{AG} \quad \ddot{z}_{AG} \end{array} \right] \hat{e}_G \\
&= \left[\begin{array}{c} \ddot{r} \quad 0 \quad 0 \end{array} \right] \hat{e}_S + 2 \left[\begin{array}{c} \dot{r} \quad 0 \quad 0 \end{array} \right] \dot{\hat{e}}_S + \left[\begin{array}{c} r \quad 0 \quad 0 \end{array} \right] \ddot{\hat{e}}_S \\
&= \left\{ \begin{array}{c} \ddot{r} - r\dot{\psi}^2 - r\dot{\phi}^2 \cos^2 \psi \\ r\ddot{\phi} \cos \psi + 2r\dot{\phi} \cos \psi - 2r\dot{\phi}\dot{\psi} \sin \psi \\ r\ddot{\psi} + 2r\dot{\psi} + r\dot{\phi}^2 \sin \psi \cos \psi \end{array} \right\}^T \hat{e}_S
\end{aligned} \tag{6.25}$$

Hence using Equations 6.23-6.25, we rewrite Equations 6.11-6.13 as:

$$(m_A + m_C)(\ddot{r} - r\dot{\psi}^2 - r\dot{\phi}^2 \cos^2 \psi) = F_{AB,r} \tag{6.26}$$

$$(m_A + m_C)(r\ddot{\phi} \cos \psi + 2r\dot{\phi} \cos \psi - 2r\dot{\phi}\dot{\psi} \sin \psi) = F_{AB,\phi} \tag{6.27}$$

$$(m_A + m_C)(r\ddot{\psi} + 2r\dot{\psi} + r\dot{\phi}^2 \sin \psi \cos \psi) = F_{AB,\psi} \tag{6.28}$$

Recall that in order for the electromagnetic forces between two spacecraft to be calculated using Equation 5.51, the magnetic moment vectors, $\hat{\mu}_A$ and $\hat{\mu}_B$, must first be transformed from components resolved on the spacecraft's body-fixed frame (\hat{e}_A) to components resolved on the global frame (\hat{e}_G) using Equations 5.43 and 5.44 and the rotation matrices in Section 5.2.4. Further, Equations 6.26-6.28 require that the resulting force vector be transformed from components resolved on the global frame (\hat{e}_G) to components resolved on the curvilinear frame (\hat{e}_S) using Equation 6.2.

$$\begin{aligned}
\vec{F}_{AB} &= \left[\begin{array}{c} F_{AB,x} \quad F_{AB,y} \quad F_{AB,z} \end{array} \right] \hat{e}_G \\
&= \left[\begin{array}{c} F_{AB,x} \quad F_{AB,y} \quad F_{AB,z} \end{array} \right] R_3(\phi)R_2(-\psi)\hat{e}_S \\
&= \left[\begin{array}{c} F_{AB,r} \quad F_{AB,\phi} \quad F_{AB,\psi} \end{array} \right] \hat{e}_S
\end{aligned} \tag{6.29}$$

$$\Rightarrow \left[\begin{array}{c} F_{AB,r} \quad F_{AB,\phi} \quad F_{AB,\psi} \end{array} \right] = \left[\begin{array}{c} F_{AB,x} \quad F_{AB,y} \quad F_{AB,z} \end{array} \right] R_3(\phi)R_2(-\psi) \tag{6.30}$$

Hence with all of the required products of rotation matrices (which are functions of the sines and cosines of the Euler angles and the curvilinear coordinate angles), the resulting force expressions on the right-hand sides of Equations 6.26-6.28 are quite complicated, nonlinear expressions.

Similarly, Equations 6.14-6.17 involve very complicated, nonlinear expressions. On the left-hand sides, the angular velocity components must be replaced with expressions involving the Euler angles, as defined in Table 5.2, and the angular acceleration components must be replaced with the corresponding derivatives of the angular velocity components. The resulting expressions for the left-hand sides of Equations 6.14-6.17 are very lengthy, complicated, nonlinear expressions. Note that similar expressions exist for spacecraft B, where the Euler angles β_1 , β_2 , and β_3 are simply substituted in place of α_1 , α_2 , and α_3 .

On the right-hand sides of Equations 6.14-6.16, the torques are expressed as components resolved on the body-fixed frame. Hence the magnetic moments must be transformed from the body-fixed to the global frame using Equations 5.43 and 5.44, and the resulting torques (calculated using Equation 5.52) must then be transformed from the global frame back to the body-fixed frame using Equation 5.11:

$$\begin{aligned}\vec{T}_{AB} &= \left[\begin{array}{ccc} T_{AB,x} & T_{AB,y} & T_{AB,z} \end{array} \right] \hat{\mathbf{e}}_G \\ &= \left[\begin{array}{ccc} T_{AB,x} & T_{AB,y} & T_{AB,z} \end{array} \right] R_3(\alpha_3)R_2(\alpha_2)R_1(\alpha_1) \hat{\mathbf{e}}_A \\ &= \left[\begin{array}{ccc} T_{AB,1} & T_{AB,2} & T_{AB,3} \end{array} \right] \hat{\mathbf{e}}_A\end{aligned}\quad (6.31)$$

$$\Rightarrow \left[\begin{array}{ccc} T_{AB,1} & T_{AB,2} & T_{AB,3} \end{array} \right] = \left[\begin{array}{ccc} T_{AB,x} & T_{AB,y} & T_{AB,z} \end{array} \right] R_3(\alpha_3)R_2(\alpha_2)R_1(\alpha_1) \quad (6.32)$$

The result, again, is several products of nonlinear terms in the Euler angles. Note that similar transformations must be made for the forces and torques on spacecraft B, where the magnetic moments must first be transformed to global components, and the resulting

forces and torques must be transformed back to curvilinear and body-fixed components, respectively. When transforming the torques on spacecraft B back to the body-fixed components, the Euler angles β_1 , β_2 , and β_3 will be used in place of α_1 , α_2 , and α_3 in Equation 6.32:

$$\begin{bmatrix} T_{BA,1} & T_{BA,2} & T_{BA,3} \end{bmatrix} = \begin{bmatrix} T_{BA,x} & T_{BA,y} & T_{BA,z} \end{bmatrix} R_3(\beta_3)R_2(\beta_2)R_1(\beta_1) \quad (6.33)$$

6.2 Linearized Equations of Motion

6.2.1 Nominal Trajectory

As explained earlier in this chapter, the nominal trajectory for the two-spacecraft EMFF array will be a steady-state spin maneuver of the two vehicles about the array center.¹ While spinning, the vehicles should maintain a constant separation distance, $2r_0$, remain within the global \hat{e}_x , \hat{e}_y plane, and spin at a steady rate, $\dot{\phi}_0$, about their array center. Further, the nominal attitude of each spacecraft is such that the \hat{a}_1 and \hat{b}_1 axes of spacecraft A and B, respectively, remain aligned with \hat{e}_r , and thus that the EMs aligned with \hat{a}_1 and \hat{b}_1 on spacecraft A and B, respectively, point toward the center of the array and align with each other. For this to occur, spacecraft A and B must rotate about their body-fixed \hat{a}_3 and \hat{b}_3 axes, respectively, by the same angle, ϕ , that the array rotates about its center point. Further, the \hat{a}_3 and \hat{b}_3 axes must nominally remain aligned with the global \hat{e}_z axis (and thus remain perpendicular to the \hat{e}_x , \hat{e}_y plane of rotation). In order for this to occur, the remaining Euler angles of the two spacecraft (α_1 , α_2 , β_1 , and β_2) must nominally be zero.

The nominal spacecraft attitudes can also be visualized in the following way: both spacecraft are nominally oriented such that their body-fixed frames (\hat{e}_A and \hat{e}_B , respectively) align with the curvilinear frame, \hat{e}_S , and therefore also nominally align with each other.

1. The transient dynamics required to transform a system at rest to one spinning about its centerpoint are discussed briefly in Appendix E, as well as in references [2, 39].

Because the spacecraft positions nominally remain within the \hat{e}_x, \hat{e}_y plane, ψ is nominally zero, and the \hat{e}_r, \hat{e}_ϕ plane nominally coincides with the \hat{e}_x, \hat{e}_y plane.

With this description of the nominal trajectory, and the degree-of-freedom matrix defined in Equation 6.19, we write the *nominal* degree-of-freedom matrix, \tilde{x}_0 , as:

$$\tilde{x}_0 = \begin{Bmatrix} r \\ \dot{\phi} \\ \psi \\ \alpha_1 \\ \alpha_2 \\ \alpha_3 \\ \delta_3 \\ \beta_1 \\ \beta_2 \\ \beta_3 \\ \varepsilon_3 \end{Bmatrix}_0 = \begin{Bmatrix} r_0 \\ \dot{\phi}_0 t \\ 0 \\ 0 \\ 0 \\ \dot{\phi}_0 t \\ \delta_{3,0} \\ 0 \\ 0 \\ \dot{\phi}_0 t \\ \varepsilon_{3,0} \end{Bmatrix} \quad (6.34)$$

where all subscripts “0” indicate the nominal values, and the values $\delta_{3,0}$ and $\varepsilon_{3,0}$ will be defined in Section 6.2.3 using the principle of conservation of angular momentum.

If we now define $\dot{\tilde{x}}$ to be a column matrix containing the time-derivatives of the degrees of freedom then we define the nominal value of $\dot{\tilde{x}}$ to be:

$$\dot{\tilde{x}}_0 = \begin{Bmatrix} \dot{r} \\ \dot{\phi} \\ \dot{\psi} \\ \dot{\alpha}_1 \\ \dot{\alpha}_2 \\ \dot{\alpha}_3 \\ \dot{\delta}_3 \\ \dot{\beta}_1 \\ \dot{\beta}_2 \\ \dot{\beta}_3 \\ \dot{\varepsilon}_3 \end{Bmatrix}_0 = \begin{Bmatrix} 0 \\ \dot{\phi}_0 \\ 0 \\ 0 \\ 0 \\ \dot{\phi}_0 \\ \dot{\delta}_{3,0} \\ 0 \\ 0 \\ \dot{\phi}_0 \\ \dot{\varepsilon}_{3,0} \end{Bmatrix} \quad (6.35)$$

where the values $\dot{\delta}_{3,0}$ and $\dot{\varepsilon}_{3,0}$ will be defined in Section 6.2.3.

It is important to note that Equations 6.34 and 6.35 define the *nominal array trajectory*, so that any displacements or rotations *relative to these nominal values* correspond to perturbed motion. Hence we write \tilde{x} and $\dot{\tilde{x}}$ as the nominal values, plus perturbations from the nominal values:

$$\tilde{x} = x_0 + \Delta\tilde{x} \quad (6.36)$$

$$\dot{\tilde{x}} = \dot{x}_0 + \dot{\Delta}\tilde{x} \quad (6.37)$$

where the perturbations are:

$$\Delta \tilde{\mathbf{x}} = \begin{Bmatrix} \Delta r \\ \Delta \phi \\ \Delta \psi \\ \Delta \alpha_1 \\ \Delta \alpha_2 \\ \Delta \alpha_3 \\ \Delta \delta_3 \\ \Delta \beta_1 \\ \Delta \beta_2 \\ \Delta \beta_3 \\ \Delta \varepsilon_3 \end{Bmatrix} \quad \text{and} \quad \dot{\Delta \tilde{\mathbf{x}}} = \begin{Bmatrix} \Delta \dot{r} \\ \Delta \dot{\phi} \\ \Delta \dot{\psi} \\ \Delta \dot{\alpha}_1 \\ \Delta \dot{\alpha}_2 \\ \Delta \dot{\alpha}_3 \\ \Delta \dot{\delta}_3 \\ \Delta \dot{\beta}_1 \\ \Delta \dot{\beta}_2 \\ \Delta \dot{\beta}_3 \\ \Delta \dot{\varepsilon}_3 \end{Bmatrix} \quad (6.38)$$

6.2.2 Nominal Control

Having defined the nominal degrees of freedom and their derivatives, we can derive an expression for the nominal control, which is the set of control values (magnetic moments and reaction wheel torques) that would be required to maintain the nominal trajectory in a disturbance-free environment.

Substituting the nominal trajectory, defined by Equations 6.34 and 6.35, into the nonlinear equations of motion (Equations 6.26-6.28 and 6.14-6.17), we write the nominal (steady-state) dynamics as:

$$(m_A + m_C)(-r_0 \dot{\phi}_0^2) = F_{AB, r, 0} \quad (6.39)$$

$$0 = F_{AB, \phi, 0} \quad (6.40)$$

$$0 = F_{AB, \psi, 0} \quad (6.41)$$

$$0 = T_{AB, 1, 0} - T_{Am_1, 0} \quad (6.42)$$

$$0 = T_{AB,2,0} - T_{Am_2,0} \quad (6.43)$$

$$0 = T_{AB,3,0} - T_{Am_3,0} \quad (6.44)$$

$$0 = T_{Am_3,0} \quad (6.45)$$

From Equations 6.40-6.45, we conclude that all RW motor torques are nominally zero, and all EM forces and torques are nominally zero, with the exception of the radial force component, $F_{AB,r}$.

The nominal value, $F_{AB,r,0}$, of the radial force is calculated by creating the full nonlinear expression for the radial force, as defined by Equations 5.43, 5.44, 5.51 and 6.30, and substituting the nominal values for the degrees of freedom and their derivatives into the resulting expression. First we define nominal values for the magnetic moments in Equations 5.41 and 5.42:

$$\begin{aligned}\hat{\mu}_{A_i,0} &= \mu_{A_i,0} \hat{a}_i, \quad i = 1, 2, 3 \\ \hat{\mu}_{B_i,0} &= \mu_{B_i,0} \hat{b}_i\end{aligned} \quad (6.46)$$

so that the nominal value of the radial force is:

$$F_{AB,r,0} = -\frac{3\mu_0\mu_{A_1,0}\mu_{B_1,0}}{32\pi r_0^4} \quad (6.47)$$

Substituting Equation 6.47 into Equation 6.39 yields:

$$(m_A + m_C)r_0 \dot{\phi}_0^2 = \frac{3\mu_0\mu_{A_1,0}\mu_{B_1,0}}{32\pi r_0^4} \quad (6.48)$$

On the right-hand side of 6.48, we have the control applied in the steady-state. This expression is equivalent to the attractive force exerted on each spacecraft when both spacecraft are in their nominal positions and orientations, and steady-state magnetic

moments, $\mu_{A_i,0}$ and $\mu_{B_i,0}$, are applied. On the left-hand side, we have the centripetal load needed to maintain each spacecraft in a steady-state spin when no disturbances are present. Hence Equation 6.48 is essentially a steady-state force-balance equation, indicating that the attractive electromagnetic force provides the steady-state centripetal load of the spinning system.

With this result, and the fact that the remaining EM force and torque components are zero, we conclude that:

$$\begin{aligned}\dot{\mu}_{A_i,0} &= 0 \\ \dot{\mu}_{B_i,0} &= 0\end{aligned}, \quad i = 2, 3 \quad (6.49)$$

In other words, when the array is following its nominal trajectory without any external disturbances, the EMs oriented along \hat{a}_2 , \hat{a}_3 , \hat{b}_2 , and \hat{b}_3 are nominally unpowered.

Further, from Equation 6.48, we solve for the nominal values of the EMs oriented along \hat{a}_1 and \hat{b}_1 , respectively. Assuming they have equal nominal strengths, $\mu_{A_1,0} = \mu_{B_1,0}$, the nominal values are:

$$\mu_{A_1,0} = \sqrt{(m_A + m_C) \frac{32\pi r_0^5 \dot{\phi}_0^2}{3\mu_0}} \quad (6.50)$$

Similar to the matrix of degrees of freedom and their derivatives, we define a column matrix of control values, \mathbf{u} , that may be defined as nominal values, \mathbf{u}_0 , plus perturbations, $\Delta\mathbf{u}$:

$$\mathbf{u} = \mathbf{u}_0 + \Delta\mathbf{u} \quad (6.51)$$

where the control matrix and perturbations are:

$$\boldsymbol{u} = \left\{ \begin{array}{l} \mu_{A_1} \\ \mu_{A_2} \\ \mu_{A_3} \\ \mu_{B_1} \\ \mu_{B_2} \\ \mu_{B_3} \\ T_{Am_1} \\ T_{Am_2} \\ T_{Am_3} \\ T_{Bm_1} \\ T_{Bm_2} \\ T_{Bm_3} \end{array} \right\} \text{ and } \Delta \boldsymbol{u} = \left\{ \begin{array}{l} \Delta \mu_{A_1} \\ \Delta \mu_{A_2} \\ \Delta \mu_{A_3} \\ \Delta \mu_{B_1} \\ \Delta \mu_{B_2} \\ \Delta \mu_{B_3} \\ \Delta T_{Am_1} \\ \Delta T_{Am_2} \\ \Delta T_{Am_3} \\ \Delta T_{Bm_1} \\ \Delta T_{Bm_2} \\ \Delta T_{Bm_3} \end{array} \right\} \quad (6.52)$$

respectively, and the nominal control values are:

where $\mu_{A_1, 0}$ is defined in Equation 6.50.

6.2.3 Conservation of Angular Momentum

We now attempt to define $\delta_{3, 0}$, $\varepsilon_{3, 0}$, $\dot{\delta}_{3, 0}$, and $\dot{\varepsilon}_{3, 0}$ (all introduced in Section 6.2.1) by using the principle of conservation of angular momentum. We begin with $\dot{\delta}_{3, 0}$, which is the nominal spin-rate of RW-3, the RW aligned with \hat{a}_3 , on spacecraft A.

Recall that RW-3 nominally stores the angular momentum of the spinning array. Hence for the nominal trajectory, the array spins at a constant angular velocity, $\dot{\phi}_0$, and RW-3 also spins at a constant rate in order to store the constant angular momentum of the array. In other words, the sum of the angular momentum stored in RW-3 on spacecraft A and B is *equal in magnitude and opposite in direction* to the angular momentum of the two-spacecraft array as it rotates about its own center of mass. Nominally the two spacecraft would assume a circular trajectory in the global \hat{e}_x , \hat{e}_y plane ($\psi = 0$), so that the conservation of angular momentum is expressed as:

$$2I_3^D(\dot{\delta}_{3, 0} + \dot{\phi}_0) + 2[I_3^A + (m_A + m_C)r_0^2]\dot{\phi}_0 = 0 \quad (6.54)$$

or more simply,

$$I_3^D\dot{\delta}_{3, 0} + [(I_3^A + I_3^D) + (m_A + m_C)r_0^2]\dot{\phi}_0 = 0 \quad (6.55)$$

The steady-state spin-rate of RW-3 on spacecraft A is then:

$$\dot{\delta}_{3, 0} = -\dot{\phi}_0 \frac{(I_3^A + I_3^D) + (m_A + m_C)r_0^2}{I_3^D} \quad (6.56)$$

where I_3^D is the mass-moment of inertia of RW-3 about its spin axis, I_3^A is the mass-moment of inertia of spacecraft A about its body-fixed \hat{a}_3 -axis, m_A and m_C are the masses of the spacecraft and RW-3, respectively, and r_0 is the nominal array radius. Notice that in order for Equation 6.54 to be satisfied, $\dot{\phi}_0$ and $\dot{\delta}_{3, 0}$ must be opposite in

sign; in other words, if the array is spinning counterclockwise such that $\dot{\phi}_0 > 0$, the RW will spin clockwise such that $\dot{\delta}_{3,0} < 0$.

Because we have made the assumption that spacecraft A and B are identical in mass and geometric properties, we can assume that their RWs nominally store equal amounts of the array's angular momentum. Hence:

$$\dot{\varepsilon}_{3,0} = \dot{\delta}_{3,0} \quad (6.57)$$

where $\dot{\delta}_{3,0}$ is defined by Equation 6.56.

For any realistic formation flight geometry with multiple spacecraft separated at large distances, the inertia of the array will be much larger than the inertias of the individual vehicles (with their RWs) about the body-fixed \hat{a}_3 -axes, so that:

$$(m_A + m_C)r_0^2 \gg I_3^A + I_3^D \quad (6.58)$$

Equation 6.55 can thus be reasonably approximated as:

$$I_3^D \dot{\delta}_{3,0} + (m_A + m_C)r_0^2 \dot{\phi}_0 = 0 \quad (6.59)$$

6.2.4 Linearization of Equations

We now linearize the system's nonlinear equations of motion (Equations 6.26-6.28 and 6.14-6.17) by assuming that *all motions are small relative to the nominal trajectory* defined in Section 6.2.1. We thus substitute for each degree of freedom and its derivative a nominal value, as defined by Equations 6.34 and 6.35, plus a perturbation to the nominal value. Similarly, we substitute for each control variable a nominal value, as defined by Equation 6.53, plus a perturbation to the nominal value. Then since a linearized set of equations will capture only first-order dynamics, all second order and higher products of perturbations are set to zero, yielding relationships that involve only constants and first order perturbation terms. This is equivalent to taking a first-order Taylor Series expansion of the equations about the nominal trajectory and nominal control values. We make the

simplifying assumption that the spacecraft and RW are axially symmetric ($I_1^A = I_2^A$ and $I_1^P = I_2^P$), and recalling the assumption that spacecraft A and B are identical in mass and geometric properties, we arrive at the following 11 linearized equations, written in matrix form:

$$\begin{aligned}
 & \begin{bmatrix} 1 & 0 & 0 & 0 & 0 & 0 & 0 & 0 & 0 & 0 \\ 0 & r_0 & 0 & 0 & 0 & 0 & 0 & 0 & 0 & 0 \\ 0 & 0 & r_0 & 0 & 0 & 0 & 0 & 0 & 0 & 0 \\ 0 & 0 & 0 & I_1^A + I_1^D & 0 & 0 & 0 & 0 & 0 & 0 \\ 0 & 0 & 0 & 0 & I_1^A + I_1^D & 0 & 0 & 0 & 0 & 0 \\ 0 & 0 & 0 & 0 & 0 & I_3^A & 0 & 0 & 0 & 0 \\ 0 & 0 & 0 & 0 & 0 & 0 & I_3^D & 0 & 0 & 0 \\ 0 & 0 & 0 & 0 & 0 & 0 & 0 & I_1^A + I_1^D & 0 & 0 \\ 0 & 0 & 0 & 0 & 0 & 0 & 0 & 0 & I_1^A + I_1^D & 0 \\ 0 & 0 & 0 & 0 & 0 & 0 & 0 & 0 & 0 & I_3^A \end{bmatrix} \begin{Bmatrix} \Delta\ddot{r} \\ \Delta\ddot{\phi} \\ \Delta\ddot{\psi} \\ \Delta\ddot{\alpha}_1 \\ \Delta\ddot{\alpha}_2 \\ \Delta\ddot{\alpha}_3 \\ \Delta\ddot{\delta}_3 \\ \Delta\ddot{\beta}_1 \\ \Delta\ddot{\beta}_2 \\ \Delta\ddot{\beta}_3 \\ \Delta\ddot{\epsilon}_3 \end{Bmatrix} \\
 & + \begin{bmatrix} 0 & -2r_0\dot{\phi}_0 & 0 & 0 & 0 & 0 & 0 & 0 & 0 & 0 \\ 2\dot{\phi}_0 & 0 & 0 & 0 & 0 & 0 & 0 & 0 & 0 & 0 \\ 0 & 0 & 0 & 0 & 0 & 0 & 0 & 0 & 0 & 0 \\ 0 & 0 & 0 & 0 & -c_4 & 0 & 0 & 0 & 0 & 0 \\ 0 & 0 & 0 & c_4 & 0 & 0 & 0 & 0 & 0 & 0 \\ 0 & 0 & 0 & 0 & 0 & 0 & 0 & 0 & 0 & 0 \\ 0 & 0 & 0 & 0 & 0 & 0 & 0 & 0 & 0 & 0 \\ 0 & 0 & 0 & 0 & 0 & 0 & 0 & -c_4 & 0 & 0 \\ 0 & 0 & 0 & 0 & 0 & 0 & c_4 & 0 & 0 & 0 \\ 0 & 0 & 0 & 0 & 0 & 0 & 0 & 0 & 0 & 0 \end{bmatrix} \begin{Bmatrix} \Delta\dot{r} \\ \Delta\dot{\phi} \\ \Delta\dot{\psi} \\ \Delta\dot{\alpha}_1 \\ \Delta\dot{\alpha}_2 \\ \Delta\dot{\alpha}_3 \\ \Delta\dot{\delta}_3 \\ \Delta\dot{\beta}_1 \\ \Delta\dot{\beta}_2 \\ \Delta\dot{\beta}_3 \\ \Delta\dot{\epsilon}_3 \end{Bmatrix} \\
 & + \begin{bmatrix} -5\dot{\phi}_0^2 & 0 & 0 & 0 & 0 & 0 & 0 & 0 & 0 & 0 \\ 0 & -2c_1 & 0 & 0 & 0 & c_1 & 0 & 0 & 0 & c_1 \\ 0 & 0 & -4c_1 & 0 & -c_1 & 0 & 0 & 0 & -c_1 & 0 \\ 0 & 0 & 0 & -c_5 & 0 & 0 & 0 & 0 & 0 & 0 \\ 0 & 0 & -3c_0 & 0 & -(c_5 + 2c_0) & 0 & 0 & 0 & -c_0 & 0 \\ 0 & 3c_0 & 0 & 0 & 0 & -2c_0 & 0 & 0 & 0 & -c_0 \\ 0 & \frac{-3c_0 I_3^D}{I_3^A} & 0 & 0 & 0 & \frac{2c_0 I_3^D}{I_3^A} & 0 & 0 & 0 & \frac{c_0 I_3^D}{I_3^A} \\ 0 & 0 & 0 & 0 & 0 & 0 & 0 & -c_5 & 0 & 0 \\ 0 & 0 & -3c_0 & 0 & -c_0 & 0 & 0 & 0 & -(c_5 + 2c_0) & 0 \\ 0 & 3c_0 & 0 & 0 & 0 & -c_0 & 0 & 0 & 0 & -2c_0 \\ 0 & \frac{-3c_0 I_3^D}{I_3^A} & 0 & 0 & 0 & \frac{c_0 I_3^D}{I_3^A} & 0 & 0 & 0 & \frac{2c_0 I_3^D}{I_3^A} \end{bmatrix} = \tilde{F}\Delta u
 \end{aligned} \tag{6.60}$$

where:

$$\tilde{F}\Delta\mathbf{u} = \begin{bmatrix} c_2 & 0 & 0 & c_2 & 0 & 0 & 0 & 0 & 0 & 0 & 0 & 0 \\ 0 & -\frac{c_2}{2} & 0 & 0 & -\frac{c_2}{2} & 0 & 0 & 0 & 0 & 0 & 0 & 0 \\ 0 & 0 & -\frac{c_2}{2} & 0 & 0 & -\frac{c_2}{2} & 0 & 0 & 0 & 0 & 0 & 0 \\ 0 & 0 & 0 & 0 & 0 & 0 & -1 & 0 & 0 & 0 & 0 & 0 \\ 0 & 0 & -2c_3 & 0 & 0 & -c_3 & 0 & -1 & 0 & 0 & 0 & 0 \\ 0 & 2c_3 & 0 & 0 & c_3 & 0 & 0 & 0 & -1 & 0 & 0 & 0 \\ 0 & \frac{-2c_3 I_3^P}{I_3^A} & 0 & 0 & \frac{-c_3 I_3^P}{I_3^A} & 0 & 0 & 0 & \frac{I_3^A + I_3^P}{I_3^A} & 0 & 0 & 0 \\ 0 & 0 & 0 & 0 & 0 & 0 & 0 & 0 & 0 & -1 & 0 & 0 \\ 0 & 0 & -c_3 & 0 & 0 & -2c_3 & 0 & 0 & 0 & 0 & -1 & 0 \\ 0 & c_3 & 0 & 0 & 2c_3 & 0 & 0 & 0 & 0 & 0 & 0 & -1 \\ 0 & \frac{-c_3 I_3^P}{I_3^A} & 0 & 0 & \frac{-2c_3 I_3^P}{I_3^A} & 0 & 0 & 0 & 0 & 0 & \frac{I_3^A + I_3^P}{I_3^A} & \end{bmatrix} \begin{Bmatrix} \Delta\mu_{A_1} \\ \Delta\mu_{A_2} \\ \Delta\mu_{A_3} \\ \Delta\mu_{B_1} \\ \Delta\mu_{B_2} \\ \Delta\mu_{B_3} \\ \Delta T_{Am_1} \\ \Delta T_{Am_2} \\ \Delta T_{Am_3} \\ \Delta T_{Bm_1} \\ \Delta T_{Bm_2} \\ \Delta T_{Bm_3} \end{Bmatrix} \quad (6.61)$$

and:

$$c_0 \equiv \frac{-(m_A + m_C)r_0^2\dot{\phi}_0^2}{3}, \quad c_1 \equiv \frac{-r_0\dot{\phi}_0^2}{2}, \quad c_2 \equiv -\dot{\phi}_0 \sqrt{\frac{3\mu_0}{32\pi(m_A + m_C)r_0^3}} \quad (6.62)$$

$$c_3 \equiv \frac{(m_A + m_C)r_0}{3}c_2 = -\dot{\phi}_0 \sqrt{\frac{\mu_0(m_A + m_C)}{96\pi r_0}} \quad (6.63)$$

$$c_4 = (2(I_1^A + I_1^D) + (m_A + m_C)r_0^2)\dot{\phi}_0, \quad c_5 = (I_1^A + I_1^D + (m_A + m_C)r_0^2)\dot{\phi}_0^2 \quad (6.64)$$

Notice in Equation 6.60 that the dynamics of the spacecraft (equations for $\Delta\ddot{r}$, $\Delta\ddot{\phi}$, $\Delta\ddot{\psi}$, $\Delta\ddot{\alpha}_1$, $\Delta\ddot{\alpha}_2$, $\Delta\ddot{\alpha}_3$, $\Delta\ddot{\beta}_1$, $\Delta\ddot{\beta}_2$, and $\Delta\ddot{\beta}_3$) are independent of the states of the RWs ($\Delta\delta_3$ and $\Delta\varepsilon_3$), although the reverse is not true. Hence we can reduce the set of Equations for the spacecraft dynamics to:

$$\begin{aligned}
 & \left[\begin{array}{ccccccc} 1 & 0 & 0 & 0 & 0 & 0 & 0 \\ 0 & r_0 & 0 & 0 & 0 & 0 & 0 \\ 0 & 0 & r_0 & 0 & 0 & 0 & 0 \\ 0 & 0 & 0 & I_1^A + I_1^D & 0 & 0 & 0 \\ 0 & 0 & 0 & 0 & I_1^A + I_1^D & 0 & 0 \\ 0 & 0 & 0 & 0 & 0 & I_3^A & 0 \\ 0 & 0 & 0 & 0 & 0 & 0 & I_1^A + I_1^D \\ 0 & 0 & 0 & 0 & 0 & 0 & I_1^A + I_1^D \\ 0 & 0 & 0 & 0 & 0 & 0 & I_3^A \end{array} \right] \left\{ \begin{array}{l} \Delta \ddot{r} \\ \Delta \ddot{\phi} \\ \Delta \ddot{\psi} \\ \Delta \ddot{\alpha}_1 \\ \Delta \ddot{\alpha}_2 \\ \Delta \ddot{\alpha}_3 \\ \Delta \ddot{\beta}_1 \\ \Delta \ddot{\beta}_2 \\ \Delta \ddot{\beta}_3 \end{array} \right\} \\
 & + \left[\begin{array}{ccccccc} 0 & -2r_0 \dot{\phi}_0 & 0 & 0 & 0 & 0 & 0 \\ 2\dot{\phi}_0 & 0 & 0 & 0 & 0 & 0 & 0 \\ 0 & 0 & 0 & 0 & 0 & 0 & 0 \\ 0 & 0 & 0 & 0 & -c_4 & 0 & 0 \\ 0 & 0 & 0 & c_4 & 0 & 0 & 0 \\ 0 & 0 & 0 & 0 & 0 & 0 & 0 \\ 0 & 0 & 0 & 0 & 0 & 0 & -c_4 \\ 0 & 0 & 0 & 0 & 0 & c_4 & 0 \\ 0 & 0 & 0 & 0 & 0 & 0 & 0 \end{array} \right] \left\{ \begin{array}{l} \Delta \dot{r} \\ \Delta \dot{\phi} \\ \Delta \dot{\psi} \\ \Delta \dot{\alpha}_1 \\ \Delta \dot{\alpha}_2 \\ \Delta \dot{\alpha}_3 \\ \Delta \dot{\beta}_1 \\ \Delta \dot{\beta}_2 \\ \Delta \dot{\beta}_3 \end{array} \right\} \quad (6.65) \\
 & + \left[\begin{array}{ccccccc} -5\dot{\phi}_0^2 & 0 & 0 & 0 & 0 & 0 & 0 \\ 0 & -2c_1 & 0 & 0 & 0 & c_1 & 0 \\ 0 & 0 & -4c_1 & 0 & -c_1 & 0 & 0 \\ 0 & 0 & 0 & -c_5 & 0 & 0 & 0 \\ 0 & 0 & -3c_0 & 0 & -(c_5 + 2c_0) & 0 & -c_0 \\ 0 & 3c_0 & 0 & 0 & 0 & -2c_0 & 0 \\ 0 & 0 & 0 & 0 & 0 & 0 & -c_5 \\ 0 & 0 & -3c_0 & 0 & -c_0 & 0 & -(c_5 + 2c_0) \\ 0 & 3c_0 & 0 & 0 & 0 & -c_0 & 0 \end{array} \right] \left\{ \begin{array}{l} \Delta r \\ \Delta \phi \\ \Delta \psi \\ \Delta \alpha_1 \\ \Delta \alpha_2 \\ \Delta \alpha_3 \\ \Delta \beta_1 \\ \Delta \beta_2 \\ \Delta \beta_3 \end{array} \right\} = F \Delta \mathbf{u}
 \end{aligned}$$

where:

$$F\Delta u = \begin{bmatrix} c_2 & 0 & 0 & c_2 & 0 & 0 & 0 & 0 & 0 & 0 & 0 & 0 \\ 0 & -\frac{c_2}{2} & 0 & 0 & -\frac{c_2}{2} & 0 & 0 & 0 & 0 & 0 & 0 & 0 \\ 0 & 0 & -\frac{c_2}{2} & 0 & 0 & -\frac{c_2}{2} & 0 & 0 & 0 & 0 & 0 & 0 \\ 0 & 0 & 0 & 0 & 0 & 0 & -1 & 0 & 0 & 0 & 0 & 0 \\ 0 & 0 & -2c_3 & 0 & 0 & -c_3 & 0 & -1 & 0 & 0 & 0 & 0 \\ 0 & 2c_3 & 0 & 0 & c_3 & 0 & 0 & 0 & -1 & 0 & 0 & 0 \\ 0 & 0 & 0 & 0 & 0 & 0 & 0 & 0 & 0 & -1 & 0 & 0 \\ 0 & 0 & -c_3 & 0 & 0 & -2c_3 & 0 & 0 & 0 & 0 & -1 & 0 \\ 0 & c_3 & 0 & 0 & 2c_3 & 0 & 0 & 0 & 0 & 0 & 0 & -1 \end{bmatrix} \begin{Bmatrix} \Delta\mu_{A_1} \\ \Delta\mu_{A_2} \\ \Delta\mu_{A_3} \\ \Delta\mu_{B_1} \\ \Delta\mu_{B_2} \\ \Delta\mu_{B_3} \\ \Delta T_{Am_1} \\ \Delta T_{Am_2} \\ \Delta T_{Am_3} \\ \Delta T_{Bm_1} \\ \Delta T_{Bm_2} \\ \Delta T_{Bm_3} \end{Bmatrix} \quad (6.66)$$

The reaction wheel dynamics, which are dependent on the spacecraft states, may then be determined by the relations (from Equations 6.60 and 6.61):

$$\begin{aligned} & \begin{bmatrix} I_3^D & 0 \\ 0 & I_3^D \end{bmatrix} \begin{Bmatrix} \Delta\ddot{\delta}_3 \\ \Delta\ddot{\epsilon}_3 \end{Bmatrix} + \begin{bmatrix} \frac{-3c_0 I_3^D}{I_3^A} & \frac{2c_0 I_3^D}{I_3^A} & \frac{c_0 I_3^D}{I_3^A} \\ \frac{-3c_0 I_3^D}{I_3^A} & \frac{c_0 I_3^D}{I_3^A} & \frac{2c_0 I_3^D}{I_3^A} \end{bmatrix} \begin{Bmatrix} \Delta\phi \\ \Delta\alpha_3 \\ \Delta\beta_3 \end{Bmatrix} \\ &= \begin{bmatrix} \frac{-2c_3 I_3^D}{I_3^A} & \frac{-c_3 I_3^D}{I_3^A} & \frac{I_3^A + I_3^D}{I_3^A} & 0 \\ \frac{-c_3 I_3^D}{I_3^A} & \frac{-2c_3 I_3^D}{I_3^A} & 0 & \frac{I_3^A + I_3^D}{I_3^A} \end{bmatrix} \begin{Bmatrix} \Delta\mu_{A_2} \\ \Delta\mu_{B_2} \\ \Delta T_{Am_3} \\ \Delta T_{Bm_3} \end{Bmatrix} \end{aligned} \quad (6.67)$$

Notice that Equations 6.65-6.66 form a 9×9 second-order matrix equation of the form:

$$M\ddot{\tilde{x}} + C\dot{\tilde{x}} + K\tilde{x} = F\Delta u \quad (6.68)$$

where $\Delta\tilde{x}$, defined originally in Equation 6.38, is now redefined as:

$$\Delta\tilde{x} = \begin{Bmatrix} \Delta r \\ \Delta\phi \\ \Delta\psi \\ \Delta\alpha_1 \\ \Delta\alpha_2 \\ \Delta\alpha_3 \\ \Delta\beta_1 \\ \Delta\beta_2 \\ \Delta\beta_3 \end{Bmatrix} \quad (6.69)$$

and from Equation 6.52, Δu is defined as:

$$\Delta u = \begin{Bmatrix} \Delta\mu_{A_1} \\ \Delta\mu_{A_2} \\ \Delta\mu_{A_3} \\ \Delta\mu_{B_1} \\ \Delta\mu_{B_2} \\ \Delta\mu_{B_3} \\ \Delta T_{Am_1} \\ \Delta T_{Am_2} \\ \Delta T_{Am_3} \\ \Delta T_{Bm_1} \\ \Delta T_{Bm_2} \\ \Delta T_{Bm_3} \end{Bmatrix} \quad (6.70)$$

It follows that:

$$K = \begin{bmatrix} -5\dot{\phi}_0^2 & 0 & 0 & 0 & 0 & 0 & 0 & 0 \\ 0 & -2c_1 & 0 & 0 & 0 & c_1 & 0 & 0 \\ 0 & 0 & -4c_1 & 0 & -c_1 & 0 & 0 & -c_1 \\ 0 & 0 & 0 & -c_5 & 0 & 0 & 0 & 0 \\ 0 & 0 & -3c_0 & 0 & -(c_5 + 2c_0) & 0 & 0 & -c_0 \\ 0 & 3c_0 & 0 & 0 & 0 & -2c_0 & 0 & 0 \\ 0 & 0 & 0 & 0 & 0 & 0 & -c_5 & 0 \\ 0 & 0 & -3c_0 & 0 & -c_0 & 0 & 0 & -(c_5 + 2c_0) \\ 0 & 3c_0 & 0 & 0 & 0 & -c_0 & 0 & 0 \end{bmatrix} \quad (6.73)$$

$$F = \begin{bmatrix} c_2 & 0 & 0 & c_2 & 0 & 0 & 0 & 0 & 0 & 0 & 0 & 0 \\ 0 & -\frac{c_2}{2} & 0 & 0 & -\frac{c_2}{2} & 0 & 0 & 0 & 0 & 0 & 0 & 0 \\ 0 & 0 & -\frac{c_2}{2} & 0 & 0 & -\frac{c_2}{2} & 0 & 0 & 0 & 0 & 0 & 0 \\ 0 & 0 & 0 & 0 & 0 & 0 & -1 & 0 & 0 & 0 & 0 & 0 \\ 0 & 0 & -2c_3 & 0 & 0 & -c_3 & 0 & -1 & 0 & 0 & 0 & 0 \\ 0 & 2c_3 & 0 & 0 & c_3 & 0 & 0 & 0 & -1 & 0 & 0 & 0 \\ 0 & 0 & 0 & 0 & 0 & 0 & 0 & 0 & 0 & -1 & 0 & 0 \\ 0 & 0 & -c_3 & 0 & 0 & -2c_3 & 0 & 0 & 0 & 0 & -1 & 0 \\ 0 & c_3 & 0 & 0 & 2c_3 & 0 & 0 & 0 & 0 & 0 & 0 & -1 \end{bmatrix} \quad (6.74)$$

Equation 6.68 may be expressed equivalently in first order form:

$$\dot{\Delta x} = A\Delta x + B\Delta u \quad (6.75)$$

where:

$$A = \begin{bmatrix} 0 & I \\ -M^{-1}K & -M^{-1}C \end{bmatrix} \quad (6.76)$$

$$B = \begin{bmatrix} 0 \\ M^{-1}F \end{bmatrix} \quad (6.77)$$

$$\Delta x = \left\{ \begin{array}{l} \Delta \tilde{x} \\ \dot{\Delta \tilde{x}} \\ \ddot{\Delta \tilde{x}} \end{array} \right\} \quad (6.78)$$

I represents an $n/2 \times n/2$ identity matrix, where $n/2 = 9$ is the number of independent degrees of freedom in the system. Δx represents the *state* of the system and is an $n \times 1$ column matrix, where $n = 18$ is the number of state variables (twice the number of degrees of freedom). From the definition in Equation 6.78, we see that the state represents a perturbation of the degrees of freedom and their derivatives from the nominal values, x_0 and \dot{x}_0 , respectively.

Notice that the damping matrix, C , contains skew-symmetric gyrostiffening terms, $\pm c_4$, as shown in Equations 6.65 and 6.72. These terms are due to the gyroscopic stiffening behavior of the RW's spinning flywheel. Although they are expressed in terms of the array spin rate, then may equivalently be expressed in terms of the flywheel's spin rate, using the conservation of angular momentum as expressed in Equation 6.55. When the flywheel is at rest (and thus the array is at rest), these terms vanish, and the gyroscopic stiffening phenomenon no longer occurs, as expected. These terms are captured in the model because we have chosen to model the nonlinear dynamics of RW-3. Similar terms would exist if we appended to the model the nonlinear dynamics of the two other RWs.

6.3 Stability Analysis of Linearized Dynamics

6.3.1 System Eigenvalues

We now investigate the stability of the open-loop, linearized dynamics in Equation 6.65. The A matrix is formed using the definitions in Equations 6.76 and 6.71-6.73. Then the

“eig” command provided in the Matlab symbolic toolbox yields the following eigenvalues for the linearized two-spacecraft dynamics:

$$\lambda_{1,2} = 0 \quad (6.79)$$

$$\lambda_{13,14} = \pm ir_0\dot{\phi}_0 \sqrt{\frac{m}{3I_3^A}} \quad (6.80)$$

$$\lambda_{15,16} = \pm \dot{\phi}_0 \sqrt{\frac{-mr_0^2 + \sqrt{(mr_0^2 + 2I_3^A)^2 + (4I_3^A)^2}}{2I_3^A}} \quad (6.81)$$

$$\lambda_{17,18} = \pm i\dot{\phi}_0 \sqrt{\frac{mr_0^2 + \sqrt{(mr_0^2 + 2I_3^A)^2 + (4I_3^A)^2}}{2I_3^A}} \quad (6.82)$$

where $m = m_A + m_C$. Note that $\lambda_3 - \lambda_{12}$ are very complicated expressions and are omitted here for brevity. Symbolic expressions for all 18 eigenvalues are given in Appendix B.

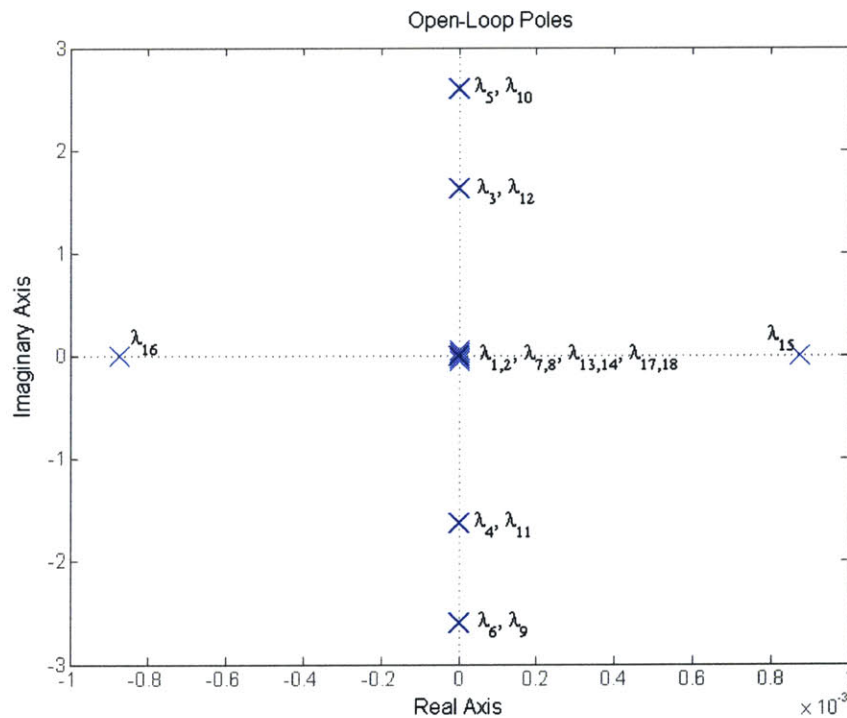
To represent the dynamics of a physical system, we now substitute sample values into the A matrix and calculate the corresponding numerical eigenvalues and eigenvectors. The chosen system is a two-spacecraft array with mass and geometric properties on the order of those anticipated for NASA’s forthcoming Terrestrial Planet Finder (TPF) mission. These values are shown in Table 6.1. The numerical eigenvalues based on these geometric and mass properties are shown in the pole-zero map in Figure 6.3.

From Figure 6.3, we see that one eigenvalue is strictly stable, one is strictly unstable, two lie at the origin, and the remainder are marginally stable, lying on the imaginary axis. Note that only one pole is strictly unstable. Hence if we can design a controller that will stabilize this mode, we will have a good chance of controlling the entire system.

It is also interesting to note that the 16 non-zero eigenvalues increase in magnitude as the spin rate of the array increases. Hence the unstable pole, λ_{15} , moves further into the

TABLE 6.1 Physical Parameters Used to Plot the Eigenvalues in Figure 6.3.

Parameter	Description	Assigned Value
r_0	Nominal Array Radius	7.5 m (15 m separation)
m_A	Spacecraft Mass	600 kg
m_C	Reaction Wheel Mass	~8.9 kg
I_3^A	Spacecraft Inertia About z-Axis	10 kg-m ²
I_1^A	Spacecraft Inertia About Radial Axes	7 kg-m ²
I_3^D	Reaction Wheel Inertia About z-Axis	~0.1 kg-m ²
I_1^D	Reaction Wheel Inertia About Radial Axes	~0.08 kg-m ²
$\dot{\phi}_0$	Nominal Array Spin Rate	1 revolution / 2 hours

**Figure 6.3** Pole-Zero Map for Two-Spacecraft EMFF Array, Using Geometric Values in Table 6.1.

right-half complex plane with increased steady-spin rate of the array. Also, as the ratio of mr_0^2 to I_3^A increases (the system behaves more like a point-mass pendulum), the value of λ_{15} approaches $\dot{\phi}_0$, the spin rate of the array.

6.3.2 System Mode Shapes

The corresponding eigenvectors of this system are found to be:

$$\phi_{1,2} = \begin{Bmatrix} 0 \\ 1 \\ 0 \\ 0 \\ 0 \\ -0.262 \\ \pm 0.262i \\ 1 \\ 0 \\ 0 \\ 0 \\ 0 \\ 0 \\ 0 \\ 0 \\ 0 \\ 0 \\ 0 \\ 0 \\ 0 \\ 0 \end{Bmatrix}, \quad \phi_{3,4} = \begin{Bmatrix} 0 \\ 0 \\ 0 \\ 0 \\ -0.262 \\ \mp 0.262i \\ 0 \\ 0 \\ 0 \\ 0 \\ 0 \\ 0 \\ 0 \\ 0 \\ 0 \\ 0 \\ 0 \\ 0 \\ 0 \\ 0 \end{Bmatrix}, \quad \phi_{5,6} = \begin{Bmatrix} 0 \\ 0.180 \\ \pm 0.180i \\ 0 \\ 0 \\ -0.180 \\ \mp 0.180i \\ 0 \\ 0 \\ 0 \\ 0 \\ 0 \\ 0 \\ 0 \\ 0 \\ 0 \\ 0 \\ 0 \\ 0 \end{Bmatrix}, \quad \phi_{7,8} = \begin{Bmatrix} 0 \\ 0 \\ 0 \\ 0 \\ 0 \\ 0 \\ 0 \\ 0 \\ 0 \\ 0 \\ 0 \\ 0 \\ 0 \\ 0 \\ 0 \\ 0 \\ 0 \\ 0 \\ 0 \\ 0 \end{Bmatrix}, \quad \phi_{9,10} = \begin{Bmatrix} 0 \\ 0 \\ 0 \\ 0 \\ -0.180 \\ \pm 0.180i \\ 0 \\ 0 \\ 0 \\ 0 \\ 0 \\ 0 \\ 0 \\ 0 \\ 0 \\ 0 \\ 0 \\ 0 \\ 0 \\ 0 \end{Bmatrix} \quad (6.83)$$

$$\phi_{11,12} = \begin{Bmatrix} 0 \\ 0 \\ 0 \\ -0.262 \\ \pm 0.262i \\ 0 \\ -0.262 \\ \pm 0.262i \\ 0 \\ 0 \\ 0 \\ 0 \\ 0 \\ 0 \\ 0 \\ 0 \\ 0 \\ 0 \\ 0 \\ 0 \end{Bmatrix}, \quad \phi_{13,14} = \begin{Bmatrix} 0 \\ 0 \\ 0 \\ 0 \\ -0.707 \\ 0 \\ 0 \\ 0 \\ 0 \\ 0 \\ 0 \\ 0 \\ 0 \\ 0 \\ 0 \\ 0 \\ 0 \\ 0 \\ 0 \\ 0 \end{Bmatrix}, \quad \phi_{15,16} = \begin{Bmatrix} 0.908 \\ \mp 0.242 \\ 0 \\ 0 \\ 0 \\ 0 \\ 0 \\ 0 \\ 0 \\ 0 \\ 0 \\ 0 \\ 0 \\ 0 \\ 0 \\ 0 \\ 0 \\ 0 \\ 0 \\ 0 \end{Bmatrix}, \quad \phi_{17,18} = \begin{Bmatrix} \pm 0.0001i \\ -0.0002 \\ 0 \\ 0 \\ 0 \\ 0 \\ 0 \\ 0 \\ 0 \\ 0 \\ 0 \\ 0 \\ 0 \\ 0 \\ 0 \\ 0 \\ 0 \\ 0 \\ 0 \\ 0 \end{Bmatrix}$$

By comparing the rows of each eigenvector to the state matrix defined by Equations 6.78 and 6.69, we can interpret the mode shapes physically. The first two eigenvectors, $\phi_{1,2}$,

represent free-body modes of the array, in which the array rotates through an arbitrary angle, $\Delta\phi$, about the global \hat{e}_z axis, while the spacecraft bodies rotate by the same angle about the body-fixed \hat{a}_3 and \hat{b}_3 axes, respectively, but do not rotate about \hat{a}_1 , \hat{a}_2 , \hat{b}_1 , or \hat{b}_2 . Eigenvectors $\phi_3 - \phi_6$ and $\phi_9 - \phi_{12}$ represent sinusoidal “tipping” of both spacecraft about their respective \hat{a}_1 , \hat{a}_2 and \hat{b}_1 , \hat{b}_2 axes. Eigenvectors $\phi_{7,8}$ represent a sinusoidal tipping of the entire array through an angle $\Delta\psi$. Notice that the values for $\Delta\alpha_2$ and $\Delta\beta_2$ are much smaller than that for $\Delta\psi$ and are not sinusoidal, so that the spacecraft bodies do not effectively tip with the entire array. Eigenvectors $\phi_{13,14}$ represent sinusoidal, out-of-phase rotations of spacecraft A and B about the \hat{a}_3 and \hat{b}_3 axes, respectively. Eigenvectors $\phi_{15,16}$ represent the unstable mode of the system and its counterpart stable mode. In the unstable mode, the array radius increases, while the spin rate decreases, and the angles $\Delta\alpha_3$ and $\Delta\beta_3$ decrease at the same rate as the array angle, $\Delta\phi$. Finally, eigenvectors $\phi_{17,18}$ are similar to $\phi_{13,14}$, except that the rotations $\Delta\alpha_3$ and $\Delta\beta_3$ are in phase, and there is also a small component associated with the array radius, Δr , and angle, $\Delta\phi$. The fact that the derivatives of Δr and $\Delta\phi$ do not appear in $\phi_{17,18}$ may be purely numerical, since the values may be an order of magnitude smaller than those displayed.

6.4 Controllability Analysis of Linearized Dynamics

6.4.1 Full Degree-of-Freedom, Full Actuator System

We now consider the controllability of the two-vehicle EMFF array being discussed in this chapter. Like the stability of the system, which was discussed in Section 6.3.1, we assess the controllability using the linearized representation of the system’s dynamics in Equation 6.75.

To assess the controllability, we form the “controllability matrix,” defined as [23]:

$$C = \begin{bmatrix} B & AB & A^2B & \dots & A^{n-1}B \end{bmatrix} \quad (6.84)$$

Recall that the system described in Equation 6.75 is represented by nine degrees of freedom, or $n = 18$ state variables. From linear control theory, we know that the system is only controllable if $\text{rank}(C) = n$.

Substituting A and B as defined by 6.76-6.77 and 6.71-6.74 into 6.84, we obtain the controllability matrix. Testing the rank using the Matlab “rank” command yields:

$$\text{rank}(C) = 18 = n \quad (6.85)$$

From Equation 6.85, we see that all 18 states (all nine degrees of freedom) of our linearized system are controllable. Further, because even the unstable modes are controllable, this result implies that our system is also stabilizable [23].

This result is not surprising, since we have *nine degrees of freedom* (three translational degrees of freedom and six rotational degrees of freedom), and *twelve actuators* (three EMs per vehicle and three RWs per vehicle). Note that because the EMs create forces and torques only by interacting with other EMs, the six EM actuators may be thought of as three actuator pairs. These three pairs, in addition to the six RW actuators in the system, still yield a number of actuators equal to the number of degrees of freedom of the system.

6.4.2 Full Degree-of-Freedom, Reduced Actuator System

It is also interesting to consider the same system with a reduced set of actuators. Specifically, we consider that each vehicle has three RWs, but only one EM actuator. Hence our modified actuator vector is:

$$\Delta \mathbf{u} = \begin{Bmatrix} \Delta \mu_{A_1} \\ \Delta \mu_{B_1} \\ \Delta T_{Am_1} \\ \Delta T_{Am_2} \\ \Delta T_{Am_3} \\ \Delta T_{Bm_1} \\ \Delta T_{Bm_2} \\ \Delta T_{Bm_3} \end{Bmatrix} \quad (6.86)$$

where the second and third EMs for each spacecraft have been removed (the second, third, fifth, and sixth rows of $\Delta \mathbf{u}$ in Equation 6.70). Hence the corresponding columns of B (Equation 6.77) must be struck, accordingly, to form a modified actuator influence matrix. A controllability check of the modified controllability matrix then demonstrates that:

$$\text{rank}(C) = 18 = n \quad (6.87)$$

Hence the modified controllability matrix still has full rank, and **the modified system is fully controllable, even with the reduced set of actuators!** At first glance, this is a very promising result. A great deal of expense could be saved by requiring only one EM per vehicle instead of three, while still maintaining the system's controllability. However, upon close inspection of the definition of controllability, such a system would not necessarily have the ability to track a desired state trajectory. Controllability, as determined by the rank test, guarantees that the system can move from a given initial state to any other desired state in a finite amount of time [23]. However, no conditions are placed upon the intermediate trajectory of the state between the initial and final times. Hence with only one EM per vehicle, we may attain any desired state in a finite amount of time, but cannot necessarily prescribe the state trajectory at all times. Further, to avoid a single-point failure of the system, it is useful to retain redundancy of the actuators, and therefore to retain three EMs on each vehicle.

6.4.3 Reduced Degree-of-Freedom, Reduced Actuator System

Now we consider a simplified version of the *geometry*, in which the system has only four degrees of freedom, Δr , $\Delta\phi$, $\Delta\alpha_3$, and $\Delta\beta_3$, and thus eight state variables. In this case, the vehicles are allowed to translate within the \hat{e}_x , \hat{e}_y plane, but are constrained to rotate only about axes perpendicular to the system's plane of rotation, so that the reduced set of degrees of freedom is:

$$\Delta \tilde{x} = \begin{Bmatrix} \Delta r \\ \Delta\phi \\ \Delta\alpha_3 \\ \Delta\beta_3 \end{Bmatrix} \quad (6.88)$$

We modify the dynamics in Equation 6.75 by striking the rows and columns of the A matrix, as well as the rows of the B matrix, associated with the removed degrees of freedom. We also consider that the system has a reduced set of actuators: only one EM and one RW on each spacecraft, so that the reduced actuator vector is:

$$\Delta u = \begin{Bmatrix} \Delta\mu_{A_1} \\ \Delta\mu_{B_1} \\ \Delta T_{Am_3} \\ \Delta T_{Bm_3} \end{Bmatrix} \quad (6.89)$$

We thus strike the corresponding columns of the B matrix. We then assemble the modified A and B matrices using Equation 6.84 to form the modified controllability matrix. Finally, the rank test of the controllability matrix yields:

$$\text{rank}(C) = 8 = n \quad (6.90)$$

Hence this simplified system is, indeed, fully controllable. This result is not surprising, since this modified system has four degrees of freedom and four actuators (one EM and one RW on each spacecraft). This result could be useful for the development of a two-

dimensional EMFF testbed. For instance, if two test vehicles are placed on a planar testing facility (such as an optical bench or a flat floor), and each vehicle is equipped with two orthogonal electromagnets whose axes of symmetry are parallel to the plane of the testbed, and one reaction wheel whose spin axis is perpendicular to this plane, then this testbed will be fully controllable. Such a testbed would be very useful in demonstrating the EMFF concept using a ground-based facility.

6.5 Optimal Control Design Using Linearized Dynamics

As we have demonstrated that our system is controllable in Section 6.4, we now proceed to design a controller for the system.

In control design, the simplest solution is often the best. Clearly our system is highly nonlinear, both spatially, in the electromagnetic forces and moments, as well as rotationally in the rigid-body attitude dynamics of the bodies. The linearized set of equations is an idealized representation of the dynamics, accurate only for states and controls very near to the nominal values. However, if linear control can successfully stabilize and control this nonlinear, unstable system, it will greatly simplify the control design and implementation process compared to using nonlinear control techniques. For this reason, we attempt to apply linear control to this system.

We take a standard linear quadratic regulator (LQR) approach to the problem, which may be summarized as minimizing the following performance index [23]:

$$J = \int_0^{\infty} [\Delta\mathbf{x}^T(t)R_x\Delta\mathbf{x}(t) + \Delta\mathbf{u}^T(t)R_u\Delta\mathbf{u}(t)]dt \quad (6.91)$$

where R_x is an $n \times n$ symmetric, positive semi-definite matrix of state penalties, R_u is a $p \times p$ symmetric, positive definite matrix of control penalties, and $p = 12$ is the number of control variables.

The feedback control that minimizes Equation 6.91 is:

$$\Delta \mathbf{u} = -K\Delta \mathbf{x} \quad (6.92)$$

where the state gain matrix, K , is:

$$K = -R_u^{-1}B^T P \quad (6.93)$$

and P is the solution of the matrix Riccati equation:

$$A^T P + PA - PBR_u^{-1}B^T P + R_x = 0 \quad (6.94)$$

The solution to Equations 6.91-6.94 is implemented using the Matlab Control Toolbox [24]. The state penalty matrix was chosen to be diagonal, with components as listed in Table 6.2. Three different sets of control penalties were chosen: “cheap” penalties in which actuators may be used liberally, “reasonable” penalties in which actuators are used in moderation, and “expensive” penalties in which actuator use is highly penalized and therefore used sparingly. The reasonable penalties are listed in Table 6.3. The cheap penalties are one hundredth of the reasonable penalties, and the expensive penalties are one hundred times the reasonable penalties.

Solving Equations 6.91-6.94 and inserting the control in Equation 6.92 into the linearized equations (Equation 6.75) yields the *closed-loop linearized dynamics*:

$$\dot{\Delta \mathbf{x}} = A\Delta \mathbf{x} + B\Delta \mathbf{u} = A\Delta \mathbf{x} - BK\Delta \mathbf{x} = (A - BK)\Delta \mathbf{x} = A_{CL}\Delta \mathbf{x} \quad (6.95)$$

where $A_{CL} = A - BK$ is the closed-loop dynamic matrix. The gain matrices, K , for cheap, reasonable, and expensive control are listed in Appendix C.

Similar to the stability analysis of A in Section 6.3.1, we now assess the stability of A_{CL} by solving for the closed-loop eigenvalues using the Matlab software. The corresponding eigenvalues are shown in Figure 6.4 for all three control levels: cheap, reasonable, and expensive control. In all three cases, the closed-loop linearized dynamics are stable, since all closed-loop eigenvalues lie in the left-half complex plane. Although some eigenvalues

TABLE 6.2 State Penalties for LQR Control Design

State Variable	Associated Penalty
Δr	5
$\Delta \phi$	45
$\Delta \psi$	45
$\Delta \alpha_1$	5
$\Delta \alpha_2$	25
$\Delta \alpha_3$	8
$\Delta \beta_1$	5
$\Delta \beta_2$	25
$\Delta \beta_3$	8
$\Delta \dot{r}$	10^{-2}
$\Delta \dot{\phi}$	5
$\Delta \dot{\psi}$	10^{-2}
$\Delta \dot{\alpha}_1$	10^{-2}
$\Delta \dot{\alpha}_2$	10^{-2}
$\Delta \dot{\alpha}_3$	10^{-2}
$\Delta \dot{\beta}_1$	10^{-2}
$\Delta \dot{\beta}_2$	10^{-2}
$\Delta \dot{\beta}_3$	10^{-2}

are much closer to the imaginary axis than others, they are all strictly stable. Notice the wide range of magnitudes of the eigenvalues; this will be taken into consideration in the simulations in Chapter 7.

Note that to form the *closed-loop nonlinear dynamics*, we simply replace the actuator terms in Equations 6.26-6.28 and 6.14-6.17 with the control in Equation 6.92.

The controller designed in this chapter will be implemented in Chapter 7, where we will simulate both the nonlinear and linearized closed-loop dynamics. While *simulations* will be used to demonstrate closed-loop control of the full-degree-of-freedom system, we will validate the closed-loop control *experimentally* on a reduced-degree-of-freedom airtrack system in Appendix D. We will also introduce a higher fidelity testbed (similar to the sys-

TABLE 6.3 Actuator Penalties for LQR Control Design

Control Variable	“Reasonable” Penalty
$\Delta\mu_{A_1}$	10^{-10}
$\Delta\mu_{A_2}$	10^{-12}
$\Delta\mu_{A_3}$	10^{-12}
$\Delta\mu_{B_1}$	10^{-10}
$\Delta\mu_{B_2}$	10^{-12}
$\Delta\mu_{B_3}$	10^{-12}
ΔT_{Am_1}	10^{-4}
ΔT_{Am_2}	10^{-4}
ΔT_{Am_3}	3
ΔT_{Bm_1}	10^{-4}
ΔT_{Bm_2}	10^{-4}
ΔT_{Bm_3}	3

tem described in Section 6.4.3), and we will suggest future experiments that may be performed using this testbed.

6.6 Summary and Conclusions

In this chapter, we have:

- linearized the nonlinear dynamics of Chapter 5 for a specific, two-spacecraft EMFF system.
- performed a *stability analysis* of the linearized design model, in which the eigenvalues of the linearized system were determined and analyzed for dynamic stability.
- performed a *controllability analysis* of the linearized design model, which demonstrated that the system under consideration is indeed fully controllable, and thus stabilizable.
- *designed an optimal controller* using the linear optimal control techniques and the linearized design model.

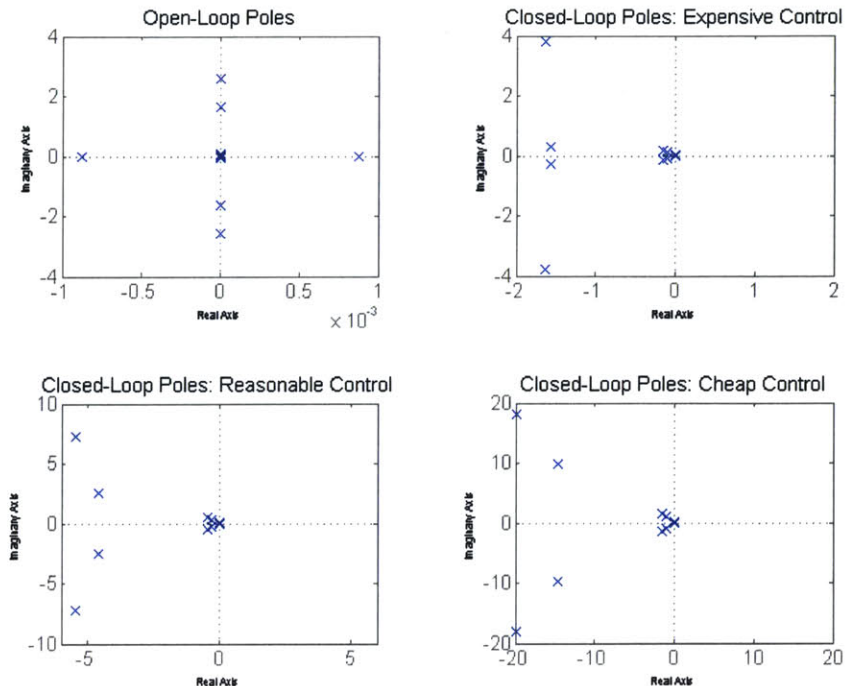


Figure 6.4 Open-Loop and Closed-Loop Eigenvalues of the Linearized Design Model

- performed a *stability analysis of the closed-loop nonlinear dynamics* (or evaluation model) and demonstrated that they are indeed stable.

The controller designed in this chapter will be used in Chapter 7 to perform a *closed-loop time simulation* of the system, using both the linearized design model and the original, nonlinear evaluation model. The success of the controller will then be determined by the performance of the nonlinear simulation.

The contributions of this chapter are:

- We have derived and presented a *linearized* set of dynamics for an EMFF system.
- We have shown that an EMFF system undergoing a steady-state spin maneuver is an *unstable* system, but that it is *controllable* using the given set of actuators, and it is therefore *stabilizable*. This is a very important result, since it is critical to the feasibility of EMFF.

- We have demonstrated that such a system becomes increasingly unstable with increased array spin rate. This result is intuitive, but we have confirmed it mathematically.
- The eigenvectors have been determined, and they represent “modes” of motion of the system. We have learned that a critical, unstable mode corresponds to the separation distance between vehicles and with the “clock angle” of the array.

Chapter 7

ELECTROMAGNETIC FORMATION FLIGHT CONTROL SIMULATIONS

7.1 Introduction

In Chapter 6, the nonlinear equations of motion for an electromagnetic formation flying (EMFF) array were applied to a two-spacecraft array and were linearized about a nominal operating trajectory. The linearized set of dynamics was used to design a linear controller, and therefore serves as a *design model* of the dynamics. In this chapter, we return to the nonlinear equations of motion, apply the linear control designed in Chapter 6 to form the *closed-loop* nonlinear dynamics, and then simulate these dynamics to demonstrate the effectiveness of the linear controller on the nonlinear dynamics. For this reason, the nonlinear dynamics serve as an *evaluation model* for assessing the closed-loop behavior of the system.

7.2 Dynamics Simulation Method

7.2.1 Simulation Tools

Two different methods are used to simulate the closed-loop dynamics, and both methods are implemented using the Matlab software.

First, the nonlinear closed-loop dynamics are simulated using a differential equation simulation function, “ode15s” [24]. This is a built-in “stiff” solver in Matlab, useful for integrating differential equations with widely varying time constants. Because our closed-

loop design model has poles of widely varying magnitude, as depicted in Figure 6.4, a stiff solver proves more stable and accurate than non-stiff solvers.

In addition to simulating the closed-loop nonlinear equations, we also simulate the closed-loop linearized equations to assess the difference between the two sets of dynamics. We expect the linearized equations to be an accurate representation of the nonlinear equations in a regime close to the nominal trajectory, but that this approximation becomes less accurate as the state and control variables move away from their nominal values. To simulate the linearized equations, we use the Matlab “lsim” command, which is a function designed specifically to integrate first order differential equations (in the form of Equation 6.95).

7.2.2 Simulation Approach

Having selected the tools we will use to simulate the closed-loop dynamics, we now define our approach. As explained in Chapters 5 and 6, the EMFF array will nominally operate in a steady-state spin mode for scientific data collection. Thus our controller has been designed to:

- provide the centripetal acceleration to each vehicle in the spinning array, using electromagnets to generate forces on the vehicles, and
- maintain the nominal trajectory, even in the presence of disturbances (and therefore to “reject” disturbances).

One way of simulating the closed-loop dynamics would thus be to simulate the response to external disturbances. However, this would require that we first characterize the disturbances, and it would yield a time response of the system that is dependent on the input sources and the characteristics with which they are modeled.

We instead take another approach. Instead of simulating the response to specific disturbances, we simulate the free response of the system due to non-zero initial conditions. In this manner, we are able to assess the response of the system to off-nominal conditions. This is similar to applying disturbances and attempting to reject them; instead, we simply

impose initial conditions that differ from the nominal conditions and assess the resulting behavior (dynamics and stability) of the system.

In this case, our primary concern is maintaining the nominal separation distance between the vehicles. As we observed in Section 6.3.2, the unstable mode of the open-loop dynamics involves a divergence of the radial separation distance from its nominal value. Hence to demonstrate the stability of our closed-loop system, it would be useful to perturb the radial separation distance from the nominal value and witness the free-response of the system to this off-nominal initial condition. It is important to note that we focus on the separation distance as our variable of interest because of its role in the system stability; however, other “disturbances” may be simulated in a similar manner by applying off-nominal initial conditions to the other degrees of freedom of the system.

7.3 Simulation Results

The first step in simulating the system is to verify that our simulation tools and dynamic models “make sense.” To do so, we apply a very small initial condition on the radial separation distance. We then expect the nonlinear and linear dynamics simulations to be nearly identical, since the states are very close to the nominal trajectory of the system and therefore lie in a regime where the linear dynamics should accurately represent the nonlinear dynamics. This is represented in Figure 7.1, where each degree of the freedom of the system is plotted as a function of time. (Note that the deviations, Δx , from the nominal values are plotted, as opposed to the values themselves, x .) Clearly the radial separation distance is perturbed by a small amount at the initial time, and the controller causes this variable to return to its nominal value. (In other words, the perturbation, Δr , from nominal, returns to zero.) Notice that the simulations of the nonlinear and linearized dynamics are nearly identical, as expected for these very small (and nearly nominal) initial conditions.

The next step is to apply a larger initial disturbance to the system to investigate the limitations of our control system, as well as the differences between the two representations of

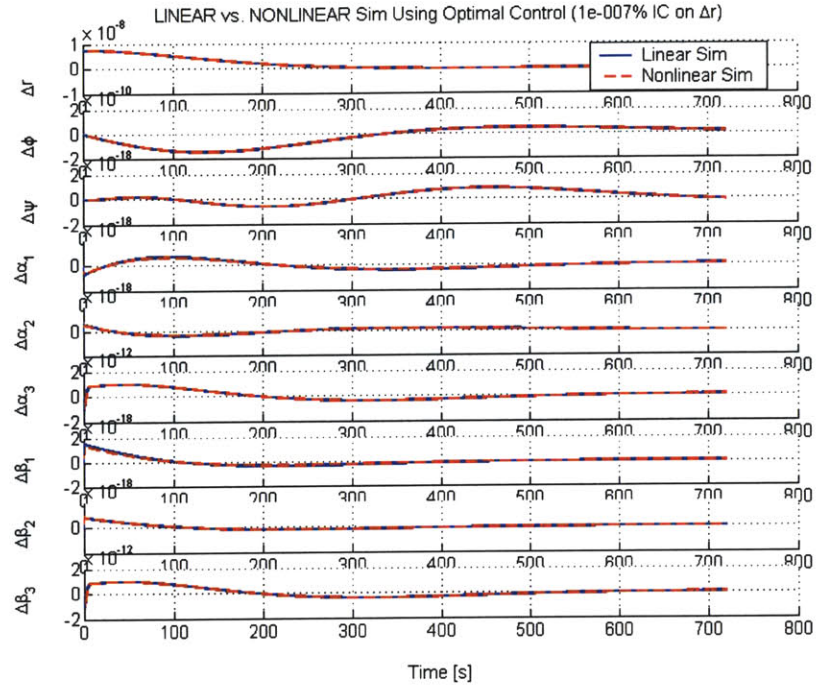


Figure 7.1 Dynamic Simulation with Very Small Initial Conditions: State Responses

the dynamics. Figure 7.2 shows the simulation results with a 10% initial condition displacement on the radial separation distance. Recall from Table 6.1 that the nominal separation radius is 7.5 meters. Hence this initial condition represents a 0.75-meter initial displacement from the nominal separation radius (equivalent to an initial separation radius of 8.25 meters). While this is a significant initial displacement (that tests the limits of the linear model), we see that the controller performs well, and the closed-loop dynamics remain stable.

Figure 7.3 shows the time histories of the actuator signals used to control the system. The state and control penalties in Chapter 6 were chosen so that the magnitudes of the actuator signals would all remain physically realizable. We see that this is indeed the case. It is simple to see that we can create magnetic moments on the order of 10^5 Ampere-meters². For instance, using Equation 5.36, we find that running 100 Amperes through 600 turns of superconductive wire, with a coil radius of 0.75 meters would yield a magnetic moment of $\sim 10^5$ Ampere-meters². This is currently achievable with commercially available wire

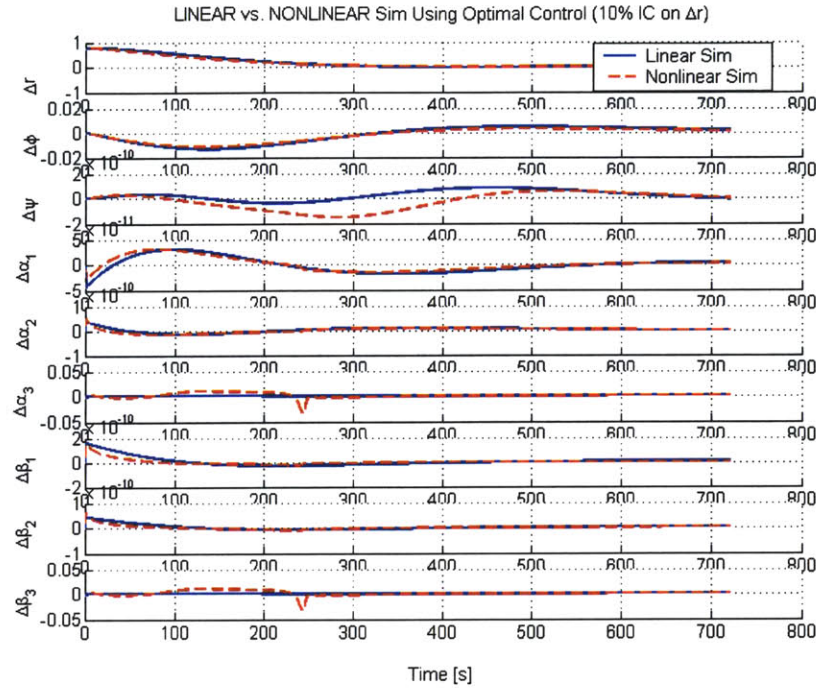


Figure 7.2 Dynamic Simulation with 10% Initial Condition on Δr : State Responses

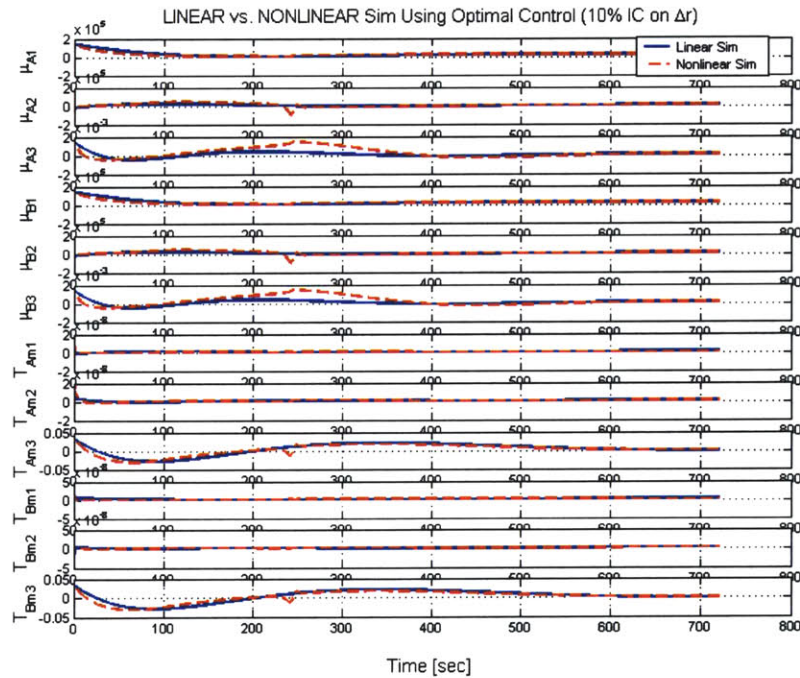


Figure 7.3 Dynamic Simulation with 10% Initial Condition on Δr : Actuator Signals

[25], but future state-of-the art wire will be even more enabling. As for the reaction wheel torques, low-mass reaction wheels have been demonstrated with motor torques on the order of 140 milli-Newton-meters [26]. Hence our actuator signals are of reasonable magnitude. (Note that although the states are plotted as deviations from nominal values, the controls are plotted as the actual magnitudes of the actuator signals, so that we may assess whether these values are physically realistic.)

In Figures 7.4 and 7.5, we plot the analogous state and actuator responses corresponding to an initial 35% (or \sim 2.6-meter) deviation of Δr . We recognize that despite the spatial nonlinearity of the electromagnetic actuators, the system remains stable, even at a very large displacement from the nominal trajectory. Clearly the dynamics of the nonlinear equations are now distinctly different from their idealized (linearized) counterparts, as expected.

Finally, in Figures 7.6 and 7.7, we find that the system eventually becomes unstable when a 40% initial condition is placed on the separation radius. It is interesting to observe, contrary to intuition, that the instability occurs in the rotational degrees of freedom, $\Delta\alpha_3$ and $\Delta\beta_3$, as opposed to in the radial separation variable, which we might expect to diverge. By increasing the actuator capability of RW-3 on each spacecraft, we could increase the stability margin of this system and likely operate successfully, even with this 40% initial condition on Δr . *Hence the limitation in this case is actually on the torque capability of the reaction wheel motors, as opposed to the electromagnetic actuators.* This is very encouraging for the prospects of using electromagnets for relative control of formation flying arrays, since they do not seem to be the limiting factor on stability in systems similar to the one considered here.

7.4 Summary and Conclusions

In this chapter, we have introduced the computational tools used for the dynamic simulations, explained the simulation approach and the assumptions about the initial conditions,

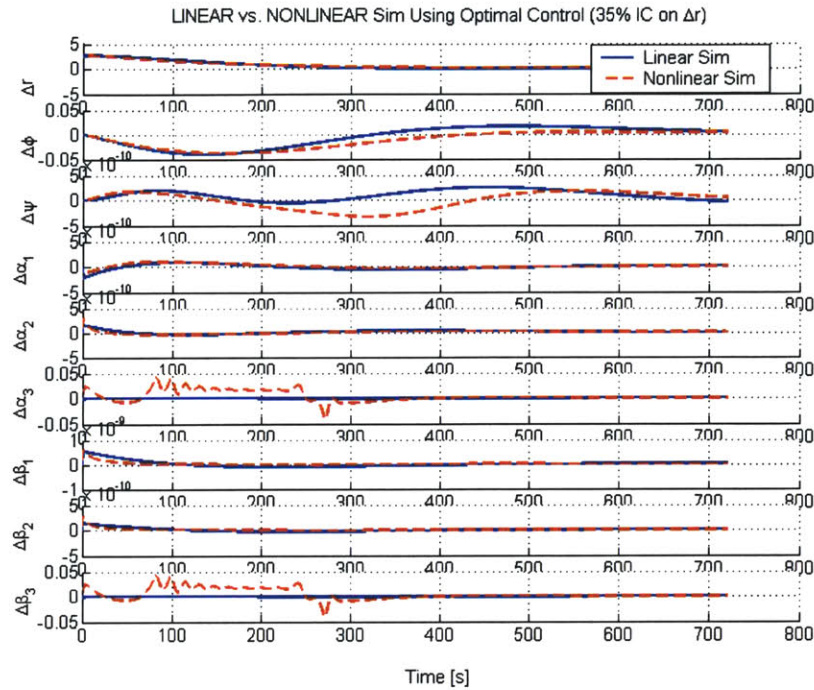


Figure 7.4 Dynamic Simulation with 35% Initial Condition on Δr : State Responses

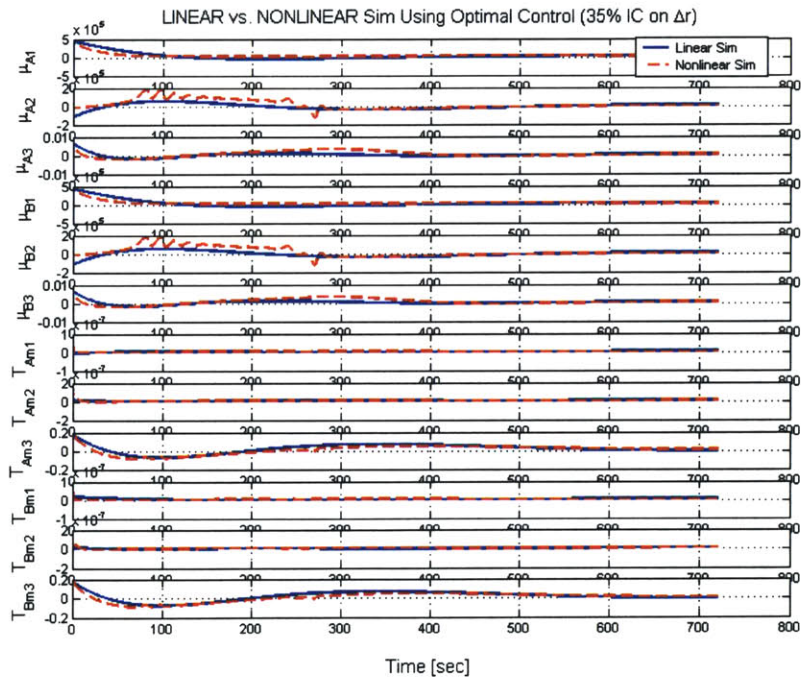


Figure 7.5 Dynamic Simulation with 35% Initial Condition on Δr : Actuator Signals

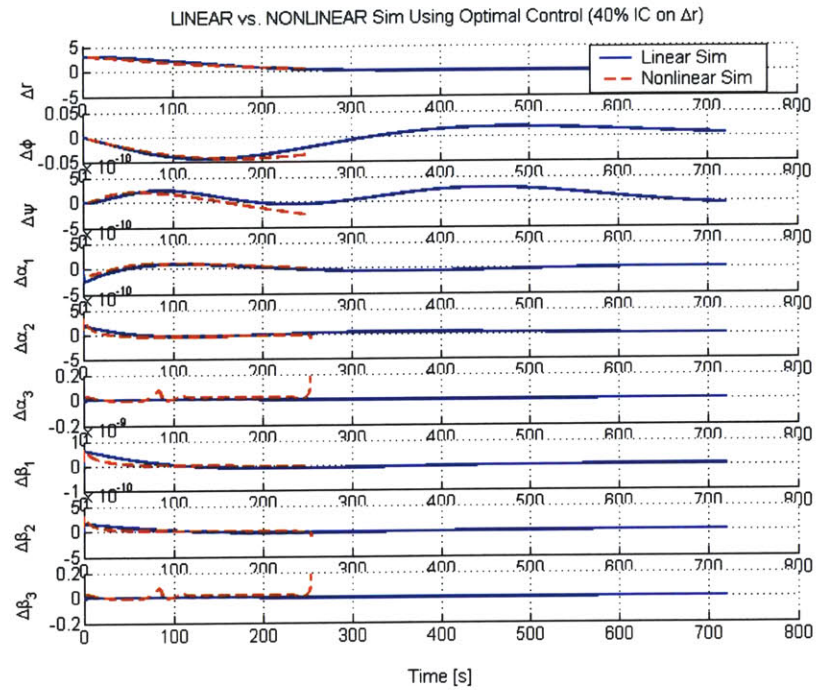


Figure 7.6 Dynamic Simulation with 40% Initial Condition on Δr : State Responses

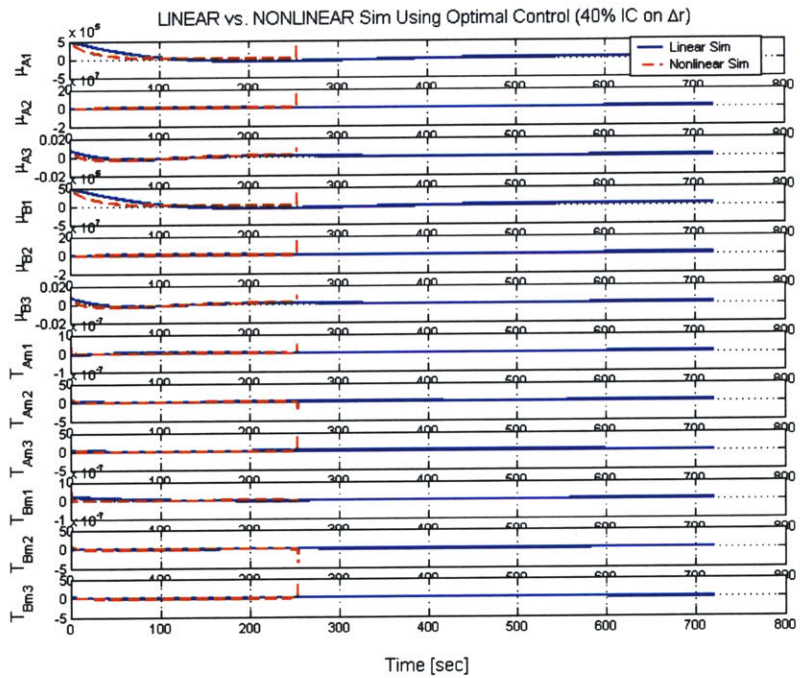


Figure 7.7 Dynamic Simulation with 40% Initial Condition on Δr : Actuator Signals

and simulated both the nonlinear and the linearized dynamics of a two-vehicle EMFF system, subject to non-zero initial conditions.

The major contributions of this chapter are:

- We have demonstrated via simulation that a closed-loop EMFF system is indeed stabilizable, despite the instability of its open-loop dynamics.
- We have demonstrated that for a system similar to a TPF-class mission, the actuator strengths required to stabilize and control an EMFF system in the presence of disturbances are physically realizable. This is a key contribution, since it is essential to demonstrating the feasibility and practicability of EMFF.
- We have demonstrated via simulation that linear optimal control has great potential to be applied to EMFF systems, even in regimes that are significantly different from the nominal trajectory. Although higher fidelity, non-linear control techniques may be investigated in the future, simple linear control has proven effective.
- We have determined that the spatial nonlinearity of the electromagnetic actuators may not be the limiting factor in determining the closed-loop stability of spinning EMFF arrays. This indicates that the electromagnetic actuators are indeed effective, even beyond their linear regime.
- We have shown that in EMFF systems similar to the one considered here, the torque capability of the reaction wheel motors may be the limiting factor in maintaining the system's stability. Hence reaction wheels with high-torque motors should be used for EMFF applications.

Because EMFF eliminates thruster contaminants, it is very promising for use on separated-spacecraft interferometry missions, such as a formation flying Terrestrial Planet Finder. Finally, EMFF has the potential to greatly extend the lifetime of a mission, since the mission lifetime is no longer constrained by a finite thruster fuel supply.

Chapter 8

CONCLUSIONS AND RECOMMENDATIONS

8.1 Thesis Summary

The work presented in this thesis is summarized briefly by chapter:

- In Chapter 2, a coupled disturbance analysis method for structurally connected space-based interferometers is presented. The analysis method corrects the “mis-match” in boundary conditions that occurs during reaction wheel (RW) disturbance testing by creating a “load filter” from estimates of the spacecraft’s and reaction wheel’s interface accelerances.
- In Chapter 3, we validated the coupled disturbance analysis method on representative hardware, the Micro-Precision Interferometer (MPI) testbed at NASA’s Jet Propulsion Laboratory.
- Chapter 4 provides a detailed review of Kane’s method for the formulation of a system’s dynamic equations of motion.
- In Chapter 5, we define the geometry for a three-dimensional, multi-spacecraft electromagnetic formation flying array, in which each spacecraft has three orthogonal electromagnetic actuators and three orthogonal reaction wheels. We also develop from first principles the nonlinear dynamic equations of motion (the evaluation model) of this system using Kane’s method.
- In Chapter 6, we linearize the nonlinear dynamics of Chapter 5 for a specific, two-spacecraft electromagnetic formation flight (EMFF) system to form the linearized design model. We then perform a *stability analysis* of the linearized system, in which the eigenvalues are determined and shown to be unstable. We also perform a *controllability analysis*, which demonstrates that the system under consideration is indeed fully controllable, and thus stabilizable. Finally, an optimal controller is designed for the linearized design

model using the linear optimal control techniques, and a closed-loop stability analysis demonstrates that the closed-loop dynamics are stable.

- In Chapter 7, closed-loop time simulations of the EMFF system are performed, using both the linearized and the nonlinear dynamics. In each simulation, the initial state is perturbed, and the system’s free response to the non-zero initial conditions is observed.

8.2 Thesis Contributions

The key contributions of this thesis are summarized here by chapter.

In Chapter 2, the primary contribution is the derivation of a new, coupled disturbance analysis method that includes the gyroscopic stiffening effects of a spinning reaction wheel. This method will improve our prediction capability for precision space missions, such as NASA’s forthcoming Space Interferometry Mission, which has very strict tolerances on its optical performance metrics. With this new, high-fidelity method of predicting SIM’s optical on-orbit performance prior to launch, we will be able to accurately assess SIM’s behavior and to ensure the success of the mission and its ability to acquire scientific goals. The coupled disturbance analysis method has been adopted by the SIM integrated modeling team and may prove to be a valuable analysis tool in future precision space telescope missions.

In Chapter 3, we validated this analysis method on an interferometer-testbed system at NASA’s Jet Propulsion Laboratory. We demonstrated that:

- predictions using this coupling method are superior to previous predictions that do not account for dynamic coupling between the two bodies.
- on the MPI testbed, the simplest load filter, one containing only three scalar force filters, yields the largest improvement compared to the decoupled method. Higher-fidelity models, including moment filters of MPI and the RW and moment filters that include the RW’s gyroscopic dynamics, do not add a visible improvement to the simple force filter analysis, and therefore their complexity may be avoided.
- the cross-spectral density reaction wheel disturbance terms are influential, and should not be neglected as previously done.

In Chapter 5, we:

- developed a new framework for modeling the dynamics of formation flying spacecraft that use electromagnets (EMs) as relative position actuators. This includes the introduction of a standardized notation, descriptions of the system's degrees of freedom, and a derivation of expressions for the system's kinematics.
- developed from first principles the dynamic equations of motion for a multi-body electromagnetic formation flying array. Our model includes the non-linear dynamics (the gyroscopic stiffening effect) of the reaction wheels that store a great deal of the array's angular momentum. The equations also account for perturbations from the system's nominal state, and allow us to capture reaction wheel disturbances in the system model.

In Chapter 6, we presented a linearized set of dynamics for an EMFF system. We then analyzed the linearized EMFF equations of motion to show that:

- an EMFF system undergoing a steady-state spin maneuver has *unstable* dynamics, and the system becomes increasingly unstable with increased array spin rate.
- the critical, unstable mode corresponds to the separation distance between vehicles and the “clock angle” of the array.
- all modes other than the rigid body modes and the unstable radial separation mode are oscillatory and undamped.
- such a system is controllable with three EMs and three RWs per vehicle (and even with only one EM and three RWs per vehicle). This is of great importance, since it provides the first step in proving the feasibility of this EMFF control concept for multi-spacecraft systems.
- the system is *controllable* using the given set of actuators, and is therefore *stabilizable*. This is a very important result, since it is critical to the feasibility of EMFF.

In Chapter 7, we:

- developed a simulation environment (a toolbox of interdependent Matlab functions) for testing electromagnetic control algorithms on two-vehicle electromagnetic formation flying systems.
- demonstrated via simulation that a closed-loop spinning EMFF system is indeed stabilizable, despite the instability of its open-loop dynamics.

- demonstrated that for a system similar to a TPF-class mission, the actuator strengths required to stabilize and control an EMFF system in the presence of disturbances are physically realizable. This is a key contribution, since it is essential to demonstrating the feasibility and practicability of EMFF.
- demonstrated via simulation that linear control has great potential to be applied to EMFF systems, even in regimes that are significantly different from the nominal trajectory. Although higher fidelity, nonlinear control techniques may be investigated in the future, simple linear control has proven effective.
- determined that the spatial nonlinearity of the electromagnetic actuators may not be the limiting factor in determining the closed-loop stability of spinning EMFF arrays, and hence that the electromagnetic actuators are indeed effective, even beyond their linear regime.
- showed that in EMFF systems similar to the one considered here, the torque capability of the reaction wheel motors may be the limiting factor in maintaining the system's stability. Hence reaction wheels with high-torque motors should be used for EMFF applications.

8.3 Recommendations for Future Work

In the first part of this thesis, we demonstrated that gyroscopic stiffening of the reaction wheel was not largely influential *for the system under consideration*, the MPI testbed. It would be useful in the future to develop a non-dimensional parameter (or set of parameters) to characterize the influence of gyroscopic stiffening on a given spacecraft-RW system. This parameter may include terms such as the mass and inertias of the RW, the mass and inertias of the spacecraft, and the spin rate of the flywheel. It could help indicate for a given system whether it would be beneficial to model the gyroscopic accelerance of the RW when predicting the coupled system's performance.

The work documented in the remainder of this thesis investigates a novel concept, the use of electromagnets as relative position actuators for formation flying spacecraft. As there are several directions one may take in demonstrating the feasibility of a new concept, we have taken the basic approach of deriving the dynamics and showing that some type of simple linear control is indeed effective in controlling the system. We stress that the aim of this work has been to demonstrate that the concept is *feasible*. Once we are convinced

of the feasibility, much interesting work remains to be done, since we must still determine the most efficient and enabling ways to implement EMFF.

The following are some suggestions of work that may be done to further develop the EMFF concept.

- Investigate other control techniques, in addition to linear control. For instance, investigate the use of nonlinear control methods, such as gain scheduling and adaptive control, on an EMFF system. Simulate these techniques to assess their benefits and limitations relative to linear control.
- Characterize realistic disturbance environments for a deep-space EMFF system, and investigate the system's response to such external disturbances.
- Perform a rigorous nonlinear stability analysis, and determine analytical expressions for the system's stability limitations.
- Linearize the equations of motion for an array containing more than two spacecraft. Then design a controller and simulate the resulting closed-loop equations to investigate whether EMFF proves as successful for larger arrays as it is for a two-vehicle array.
- Implement both linear and other control techniques on representative hardware, such as the EMFF testbed developed in the Space Systems Laboratory at the Massachusetts Institute of Technology. Demonstrate disturbance rejection (regulation), as well as tracking in the presence of disturbances. Also, demonstrate operation of the system in its steady-state spin mode.

8.4 Concluding Remarks

The results in this thesis have been enormously positive. First, we have demonstrated that a coupled disturbance analysis method does indeed predict the performance of a structurally connected space interferometer more accurately than the decoupled disturbance analysis method. This result has already been adopted by the SIM integrated modeling team at NASA's JPL, where the analysis code from this work has been distributed. This method will endow analysts with increased confidence in their on-orbit performance predictions for SIM prior to launch, and therefore will directly benefit the flight program.

We have also made great strides in demonstrating the feasibility and benefits of EMFF. We have demonstrated that EMFF has the ability to control a formation flight system,

even one with unstable dynamics, and that the required actuator magnitudes are within the limits of what is physically achievable. This result, coupled with the fact that EMFF will eliminate many of the detrimental aspects associated with thrusters, is very encouraging for the future of formation flight, and demonstrates that EMFF may be an attractive candidate architecture for NASA's TPF mission.

REFERENCES

1. Jet Propulsion Laboratory, *Space Interferometry Mission (SIM)*, URL <<http://sim.jpl.nasa.gov>>.
2. E.M.C. Kong, *Spacecraft Formation Flight Exploiting Potential Fields*, Ph.D. thesis, Massachusetts Institute of Technology, February 2002.
3. K-C. Liu, *Stochastic Performance Analysis and Staged Control System Designs for Space Based Interferometers*, SM Thesis, Massachusetts Institute of Technology, May 2003.
4. Jet Propulsion Laboratory, *Terrestrial Planet Finder Mission*, URL <<http://tpf.jpl.nasa.gov>>.
5. C.A. Beichman, N.J. Woolf, and C.A. Lindensmith, Eds., *The Terrestrial Planet Finder (TPF): A NASA Origins Program to Search for Habitable Planets*, May 1999, JPL Publication 99-003.
6. L.M. Elias, *A Structurally Coupled Disturbance Analysis Method Using Dynamic Mass Measurement Techniques, with Application to Spacecraft-Reaction Wheel Systems*, Master's thesis, Massachusetts Institute of Technology, March 2001.
7. R.A. Masterson, *Development and Validation of Empirical and Analytical Reaction Wheel Disturbance Models*, SM Thesis, Massachusetts Institute of Technology, June 1999.
8. I. Basdogan, F. Dekens, and G.W. Neat, "A Model Validation Study of the Wave Front Tip/Tilt System Using the Micro-Precision Interferometer," *Proceedings of the IEEE Aerospace Conference*, Snowmass, CO, April 1999.
9. I. Basdogan, R. Grogan, A. Kissil, N. Sigrist, and L. Sievers, "Preliminary Optical Performance Analysis of the Space Interferometer Mission Using an Integrated Modeling Methodology," *Proceedings of the 6th Biennial Symposium on Active Control of Vibration and Noise*, The 2000 International Mechanical Engineering Congress and Exposition, Orlando, FL, November 2000.
10. S.R. Ploen, "Analysis of MPI/RWA Dynamic Coupling via Mechanical Impedance Methods," *Jet Propulsion Laboratory Engineering Memorandum 3455-01-001*, January 4, 2001.
11. J. Enright, M. Hilstad, A. Saenz-Otero, and D. Miller, "The SPHERES Guest Scientist Program: Collaborative Science on the ISS," To be presented at the 2004 IEEE Aerospace Conference, Big Sky, MT, March 2004, IEEEAC #1296.
12. F.H. Bauer, K. Hartman, J.P. How, J. Bristow, D. Weidow, and F. Busse, "Enabling Spacecraft Formation Flying through Spaceborne GPS and Enhanced Automation Technologies," *Proceedings of the ION-GPS Conference*, Nashville, TN, September 1999, pp. 369-383.

13. P.K.C. Wang, F.Y. Hadaegh, and K. Lau, "Synchronized Formation Rotation and Attitude Control of Multiple Free-Flying Spacecraft," *Journal of Guidance, Control, and Dynamics* **22**, pp. 28-35, January 1999.
14. R.S. Smith and F.Y. Hadaegh, "Control Topologies for Deep Space Formation Flying Spacecraft," *Proceedings of the 2002 American Control Conference*, pp. 2836-2841, Anchorage, AK, May 2002.
15. E.M.C. Kong, D.W. Kwon, S.A. Schweighart, L.M. Elias, R.J. Sedwick, and D.W. Miller, "Electromagnetic Formation Flight for Multi-Satellite Arrays," Accepted for upcoming publication in the *Journal of Spacecraft and Rockets*, 2003.
16. L.M. Elias, F. Dekens, L. Sievers, and T. Neville, "A methodology for 'Modeling' the Mechanical Interaction between a Reaction Wheel and a Flexible Structure," *Proceedings of the SPIE Astronomical Telescopes and Instrumentation Conference*, Waikoloa, HI, 22-28 August 2002.
17. L.M. Elias, "A Coupled Disturbance Analysis Method Using Dynamic Mass Measurement Techniques," *Proceedings of the 43rd Annual AIAA/ASME/ASCE/AHS/ASC Structures, Structural Dynamics, and Materials Conference*, Denver, CO, April 2002, AIAA Paper 2002-1252.
18. D.J. Ewins, *Modal Testing: Theory, Practice, and Application*, Second Edition, Research Studies Press Ltd., 2000.
19. J.W. Melody and G.W. Neat, "Integrated Modeling Methodology Validation Using the Micro-Precision Interferometer Testbed," *Proceedings of the 35th IEEE Conference on Decision and Control* **4**, pp. 4222-4227, December 1996.
20. T.R. Kane and D.A. Levinson, *Dynamics: Theory and Applications*, McGraw-Hill, Inc., 1985.
21. D. Halliday, R. Resnick, and K.S. Krane, *Physics*, 4th ed., John Wiley and Sons, 1992.
22. M.S. Schwartz, *Principles of Electrodynamics*, Dover Publications, Inc., 1987.
23. P.R. Belanger, *Control Engineering: A Modern Approach*, Saunders College Publishing, 1995.
24. The Mathworks, Inc., Matlab Software and Control Toolbox User's Manuals.
25. American Superconductor, *American Superconductor*, URL <www.amsuper.com>.
26. E. Ahronovich and M. Balling, "Reaction Wheel and Drive Electronics for LeoStar Class Vehicles," *Proceedings of the 12th Annual AIAA/USU Conference on Small Satellites*, Logan, Utah, 31 August - 3 September 1998, SSC98-I-5.
27. Elias, L.M., Kong, E.M., and Miller, D.W., "An Investigation of Electromagnetic Control for Formation Flight Applications," *Proceedings of the SPIE Astronomical Telescopes and Instrumentation Conference*, Waikoloa, Hawaii, August 2002.

28. L.M. Elias, "Two-Spacecraft EMFF Nonlinear Equations of Motion, Including Gyrostiffening," Internal MIT-SSL Memo, Revised December 2002.
29. L.M. Elias, "Validation of a Coupled Reaction Wheel Disturbance Analysis Method for the MPI Testbed at JPL. Summary of Work: June 2001 - May 2002," *Jet Propulsion Laboratory Internal Document: Unofficial Interoffice Memorandum*, May 31, 2002.
30. R. Grogan, "Summary of Reaction Wheel Analysis Validation," *Jet Propulsion Laboratory Internal Document: Interoffice Memorandum 3411-01-000 SIM*, July 2, 2001.
31. L.M. Elias, "Summary of Work: JPL Summer 2001," *Jet Propulsion Laboratory Internal Document: Unofficial Interoffice Memorandum*, August 31, 2001.
32. A. Aviles, J. Bolivar, B. Bosch, et. al., "Volume II: Design Appendix, Project EMFFORCE," Final Design Document for the MIT Course 16 2002-2003 Capstone Design Course, Spring 2003.
33. N.M.M. Maia, J.M.M. Silva, J. He, N.A.J. Lieven, R.M. Lin, G.W. Skingle, W. To, and A.P.V. Urgueira, *Theoretical and Experimental Modal Analysis*, Research Studies Press Ltd., 1997.
34. P.H. Wirsching, T.L. Paez, and H. Ortiz, *Random Vibrations: Theory and Practice*, John Wiley & Sons, Inc., 1995.
35. T.R. Kane, P.W. Likins, and D.A. Levinson, *Spacecraft Dynamics*, McGraw-Hill, Inc., 1983.
36. T.R. Kane and D.A. Levinson, "Multibody Dynamics," *Journal of Applied Mechanics* **50**, pp. 1071-1078, December 1983.
37. D.L. Mingori, "Lagrange's Equations, Hamilton's Equations, and Kane's Equations: Interrelations, Energy Integrals, and a Variational Principle," *Journal of Applied Mechanics (Transactions of the ASME)* **62**, pp. 505-510, June 1995.
38. L.M. Elias, Doctoral General Exam, Written Response to Question Posed by Professor David W. Miller, 27 January 2003.
39. D.W. Miller, R.J. Sedwick, E.M. Kong, and S. Schweighart, "Electromagnetic Formation Flight for Sparse Aperture Telescopes," *Proceedings of the 2002 IEEE Aerospace Conference*, Big Sky, MT, March 9-16, 2002, IEEEAC Paper #418.
40. P.C. Hughes, *Spacecraft Attitude Dynamics*, John Wiley and Sons, 1986.
41. J.L. Junkins and J.D. Turner, *Optimal Spacecraft Rotational Maneuvers*, Elsevier Science Publishers B.V., 1986.
42. K. Zhou with J.C. Doyle, *Essentials of Robust Control*, Prentice-Hall, Inc., 1998.
43. B.N. Agrawal, *Design of Geosynchronous Spacecraft*, Prentice-Hall, Inc., 1986.

44. G.W. Housner and D.E. Hudson, *Applied Mechanics Dynamics*, Litton Educational Publishing, Inc., 1959.
45. V. Kapila, A.G. Sparks, J.M. Buffington, and Q. Yan, "Spacecraft Formation Flying: Dynamics and Control," *Proceedings of the American Control Conference*, San Diego, California, June 1999.
46. L. Meirovitch, *Introduction to Dynamics and Control*, John Wiley & Sons, Inc., 1985.
47. R.J. Sedwick, R.J., D.W. Miller, and E.M.C. Kong, "Mitigation of Differential Perturbations in Clusters of Formation Flying Satellites," *AAS 99-124*, 1999.
48. J.E. Slotine, J.E. and W. Li, *Applied Nonlinear Control*, Prentice-Hall, Inc., 1991.
49. W.T. Thomson, *Introduction to Space Dynamics*, John Wiley & Sons, Inc., 1961.
50. S. Timoshenko, S. and D.H. Young, *Advanced Dynamics*, McGraw-Hill Book Company, Inc., 1948.

Appendix A

EMPIRICAL FORCE FILTERS

We now investigate “empirical filters,” formed from experimental data using a reaction wheel (RW) and the Micro-Precision Interferometer (MPI) testbed at NASA’s Jet Propulsion Laboratory (JPL). Empirical filters are formed from *measured disturbances* by taking the ratio of *coupled* disturbance spectra (measured with the RW mounted on MPI) to *blocked* spectra (measured with the RW mounted to a rigid surface). This ratio provides an estimate of how the analytical filters *should* appear when calculated from the free-body accelerances of the RW and MPI.

We form the three force and three moment empirical filters by dividing the coupled disturbance spectra by the blocked disturbance spectra. Since each spectrum, $\Phi_{F_i F_i}(\omega, \Omega)$ for $i = 1, 2, \dots, 6$, is a function of frequency (ω) and wheel spin rate (Ω), the resulting empirical filters are also frequency- and wheel-speed-dependent. The empirical F_x filter is shown in Figure A.1, and the M_x filter is shown in Figure A.2. Each filter is plotted as a function of frequency (x-axis) and wheel spin rate (y-axis), with its magnitude (in decibels) indicated by the neighboring color scale. The color-scale limits have been truncated to improve the signal-to-noise ratio. Thus a few very large peaks have magnitudes “off the scale” in order to avoid eclipsing the remaining data.

Notice that the empirical filters in Figures A.1 and A.2 appear to be dependent on the reaction wheel’s spin rate, as well as on frequency. Further, the peak values of the empirical filters are over an order of magnitude larger than their analytical equivalents in Chapter 3.

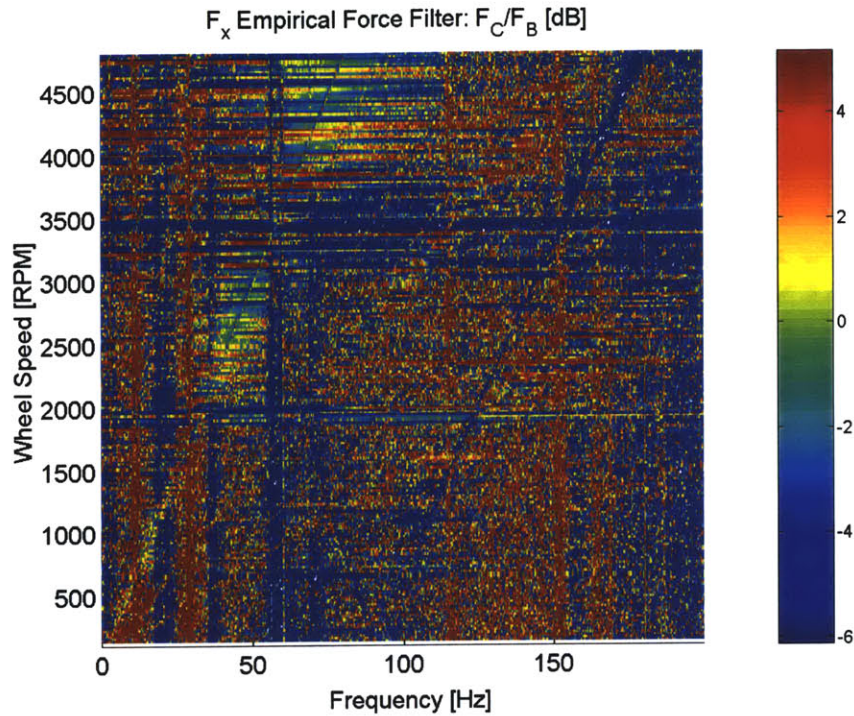


Figure A.1 F_x Empirical Force Filter

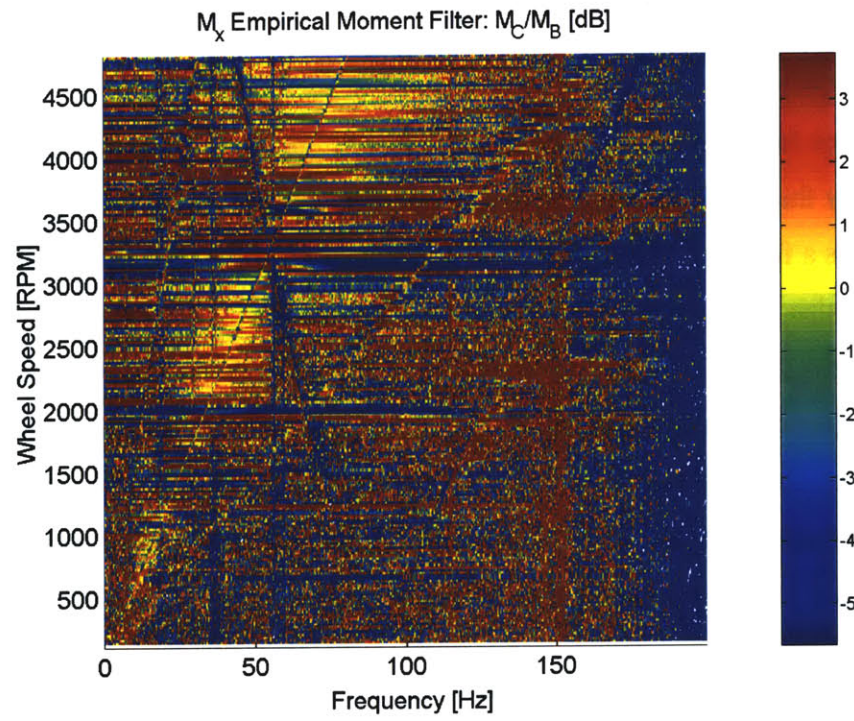


Figure A.2 M_x Empirical Moment Filter.

These differences between the empirical and analytical filters appear because the empirical magnitudes are not entirely trustworthy. Recall that a blocked spectrum expressed in the frequency-versus-wheel-speed domain is mostly noise, with localized regions of signal due to tonal (harmonic) disturbances and structural (constant-frequency) modes of the RW, as shown in Figure 3.5. Thus an empirical filter is essentially the division of a coupled spectrum by noise *in all but the localized signal regions*. Hence the general trend of the empirical filters is correct, but the peak values are inaccurate.

It would be useful to improve the numerical accuracy of the empirical filters in the future, but for now, we confirm their general correctness by using them in a coupled disturbance analysis. Since the empirical filters are the true ratios of coupled-to-blocked disturbance spectra, filtering the blocked spectra should return the coupled spectra, and the resulting filtered prediction should be identical to an unfiltered prediction using the coupled spectra. Previous analyses have demonstrated that this is true [31], so despite our concerns about the peak magnitudes, the empirical filters may be used in the future to help us understand some of the traits our analytical filters should capture.

Appendix B

TWO-VEHICLE EMFF SYMBOLIC EIGENVALUES

The eigenvalues of a two-spacecraft EMFF array were discussed in Section 6.3.1. The full, symbolic expressions for the eigenvalues are shown here for reference.

$$\lambda_{1,2} = 0, 0$$

$$\lambda_{3,4} = +/- \frac{1}{6} \sqrt{I1^6} \left(- (12 \cdot I1^2 \cdot \phi d0 - 6 \cdot m \cdot r0^2 \cdot I1 + 3 \cdot r0^4 \cdot m^2 \cdot \phi d0 + 13 \cdot r0^2 \cdot m \cdot I1 \cdot \phi d0 - 6 \cdot I1^2 - (\phi d0 \cdot (78 \cdot m^3 \cdot r0^6 \cdot I1 \cdot \phi d0 - 36 \cdot m^3 \cdot r0^6 \cdot I1 - 288 \cdot m \cdot r0^2 \cdot I1^3 + 312 \cdot I1^3 \cdot \phi d0 \cdot m \cdot r0^2 + 9 \cdot r0^8 \cdot m^4 \cdot \phi d0 - 180 \cdot m^2 \cdot r0^4 \cdot I1^2 - 144 \cdot I1^4 + 144 \cdot I1^4 \cdot \phi d0 + 241 \cdot I1^2 \cdot \phi d0 \cdot r0^4 \cdot m^2))^{1/2}) \right)^{(1/2)}$$

$$\lambda_{5,6} = +/- \frac{1}{6} \sqrt{I1^6} \left(- \phi d0 \cdot (12 \cdot I1^2 \cdot \phi d0 - 6 \cdot m \cdot r0^2 \cdot I1 + 3 \cdot r0^4 \cdot m^2 \cdot \phi d0 + 13 \cdot r0^2 \cdot m \cdot I1 \cdot \phi d0 - 6 \cdot I1^2 + (\phi d0 \cdot (78 \cdot m^3 \cdot r0^6 \cdot I1 \cdot \phi d0 - 36 \cdot m^3 \cdot r0^6 \cdot I1 - 288 \cdot m \cdot r0^2 \cdot I1^3 + 312 \cdot I1^3 \cdot \phi d0 \cdot m \cdot r0^2 + 9 \cdot r0^8 \cdot m^4 \cdot \phi d0 - 180 \cdot m^2 \cdot r0^4 \cdot I1^2 - 144 \cdot I1^4 + 144 \cdot I1^4 \cdot \phi d0 + 241 \cdot I1^2 \cdot \phi d0 \cdot r0^4 \cdot m^2))^{1/2}) \right)^{(1/2)}$$

$$\begin{aligned} \lambda_7 = & \frac{1}{6} \sqrt{I1} \left(- 8 \cdot r0^12 \cdot m^6 \cdot \phi d0^3 - 24 \cdot I1^5 \cdot m \cdot r0^2 - 8 \cdot I1^3 \cdot m^3 \cdot r0^6 - 24 \cdot I1^4 \cdot m^2 \cdot r0^4 - 8 \cdot I1^6 + 288 \cdot I1^6 \cdot \phi d0^2 - 288 \cdot I1^6 \cdot \phi d0 - 348 \cdot I1^3 \cdot m^3 \cdot r0^6 \cdot \phi d0 + 1752 \cdot I1^3 \cdot r0^6 \cdot m^3 \cdot \phi d0^2 - 672 \cdot I1^2 \cdot r0^8 \cdot m^4 \cdot \phi d0^3 - 1756 \cdot I1^3 \cdot r0^6 \cdot m^3 \cdot \phi d0^3 - 804 \cdot I1^4 \cdot \phi d0 \cdot r0^4 \cdot m^2 + 492 \cdot I1^2 \cdot r0^8 \cdot m^4 \cdot \phi d0^2 - 60 \cdot I1^2 \cdot r0^8 \cdot m^4 \cdot \phi d0 + 1692 \cdot I1^5 \cdot \phi d0^2 \cdot r0^2 \cdot m - 804 \cdot I1^5 \cdot \phi d0 \cdot m \cdot r0^2 + 2712 \cdot I1^4 \cdot r0^4 \cdot m^2 \cdot \phi d0^2 - 936 \cdot I1^5 \cdot \phi d0^3 \cdot r0^2 \cdot m - 2124 \cdot I1^4 \cdot r0^4 \cdot m^2 \cdot \phi d0^3 + 48 \cdot r0^10 \cdot m^5 \cdot \phi d0^2 \cdot I1 - 120 \cdot r0^10 \cdot m^5 \cdot \phi d0^3 \cdot I1 + 12 \cdot 3^{1/2} \cdot (- \phi d0 \cdot (\phi d0 - 1) \cdot (4 \cdot \phi d0^4 \cdot m^8 \cdot r0^16 + 46 \cdot m^7 \cdot r0^14 \cdot I1 \cdot \phi d0^3 + 76 \cdot r0^14 \cdot m^7 \cdot \phi d0^4 \cdot I1 - 52 \cdot m^5 \cdot r0^10 \cdot I1^3 \cdot \phi d0 - 221 \cdot m^6 \cdot r0^12 \cdot I1^2 \cdot \phi d0^2 + 16 \cdot I1^8 + 600 \cdot I1^7 \cdot \phi d0 \cdot m \cdot r0^2 + 244 \cdot m^2 \cdot r0^4 \cdot I1^6 - 1064 \cdot I1^3 \cdot \phi d0^2 \cdot r0^10 \cdot m^5 + 143 \cdot I1^2 \cdot \phi d0^3 \cdot r0^12 \cdot m^6 + 974 \cdot I1^5 \cdot \phi d0 \cdot r0^6 \cdot m^3 + 345 \cdot I1^4 \cdot \phi d0 \cdot r0^8 \cdot m^4 + 1107 \cdot I1^6 \cdot \phi d0 \cdot r0^4 \cdot m^2 - 5062 \cdot r0^6 \cdot m^3 \cdot \phi d0^3 \cdot I1^5 - 5400 \cdot r0^4 \cdot m^2 \cdot \phi d0^3 \cdot I1^6 - 2412 \cdot r0^6 \cdot m^3 \cdot \phi d0^2 \cdot I1^5 - 2305 \cdot r0^8 \cdot m^4 \cdot \phi d0^2 \cdot I1^4 - 1011 \cdot r0^4 \cdot m^2 \cdot \phi d0^2 \cdot I1^6 + 2414 \cdot r0^10 \cdot m^5 \cdot \phi d0^4 \cdot I1^3 - 210 \cdot r0^10 \cdot m^5 \cdot \phi d0^3 \cdot I1^3 + 589 \cdot r0^12 \cdot m^6 \cdot \phi d0^4 \cdot I1^2 + 2112 \cdot I1^7 \cdot \phi d0^4 \cdot r0^2 \cdot m + 340 \cdot m^3 \cdot r0^6 \cdot I1^5 + 96 \cdot m^2 \cdot r0^2 \cdot I1^7 + 280 \cdot m^4 \cdot r0^8 \cdot I1^4 + 5661 \cdot r0^8 \cdot m^4 \cdot \phi d0^4 \cdot I1^4 + 5764 \cdot r0^4 \cdot m^2 \cdot \phi d0^4 \cdot I1^6 + 7672 \cdot r0^6 \cdot m^3 \cdot \phi d0^4 \cdot I1^5 - 2181 \cdot r0^8 \cdot m^4 \cdot \phi d0^3 \cdot I1^4 - 12 \cdot r0^14 \cdot m^7 \cdot \phi d0^2 \cdot I1 + 4 \cdot r0^16 \cdot m^8 \cdot \phi d0^3 - 75 \cdot r0^12 \cdot m^6 \cdot \phi d0 \cdot I1^2 - 18 \cdot I1 \cdot \phi d0 \cdot r0^14 \cdot m^7 + \right) \right)^{(1/2)}$$

$$\begin{aligned}
& \phi d0^2 * r0^16 * m^8 + 36 * I1^2 * r0^12 * m^6 + 4 * m^7 * r0^14 * I1 - m^8 * r0^16 * \phi d0 + 80 * I1^7 * \phi d0^2 * m * r0^2 \\
& - 2720 * I1^7 * \phi d0^3 * m * r0^2 + 136 * I1^3 * r0^10 * m^5 + 128 * \phi d0^2 * I1^8 + 128 * I1^8 * \phi d0 - \\
& 512 * I1^8 * \phi d0^3 + 256 * I1^8 * \phi d0^4)^(1/2) * I1^2)^(1/3) * 3^(1/2) * 2^(1/2) * ((- 8 * r0^12 * m^6 * \phi d0^3 - \\
& 24 * I1^5 * m * r0^2 - 8 * I1^3 * m^3 * r0^6 - 24 * I1^4 * m^2 * r0^4 - 8 * I1^6 + 288 * I1^6 * \phi d0^2 - 288 * I1^6 * \phi d0 - \\
& 348 * I1^3 * m^3 * r0^6 * \phi d0 + 1752 * I1^3 * r0^6 * m^3 * \phi d0^2 - 672 * I1^2 * r0^8 * m^4 * \phi d0^3 - \\
& 1756 * I1^3 * r0^6 * m^3 * \phi d0^3 - 804 * I1^4 * \phi d0 * r0^4 * m^2 + 492 * I1^2 * r0^8 * m^4 * \phi d0^2 - \\
& 60 * I1^2 * r0^8 * m^4 * \phi d0 + 1692 * I1^5 * \phi d0^2 * r0^2 * m - 804 * I1^5 * \phi d0 * m * r0^2 + \\
& 2712 * I1^4 * r0^4 * m^2 * \phi d0^2 - 936 * I1^5 * \phi d0^3 * r0^2 * m - 2124 * I1^4 * r0^4 * m^2 * \phi d0^3 + \\
& 48 * r0^10 * m^5 * \phi d0^2 * I1 - 120 * r0^10 * m^5 * \phi d0^3 * I1 + 12 * 3^(1/2) * (- \phi d0 * (\phi d0 - \\
& 1) * (4 * \phi d0 * 4 * m^8 * r0^16 + 46 * m^7 * r0^14 * I1 * \phi d0^3 + 76 * r0^14 * m^7 * \phi d0^4 * I1 - \\
& 52 * m^5 * r0^10 * I1^3 * \phi d0 - 221 * m^6 * r0^12 * I1^2 * \phi d0^2 + 16 * I1^8 + 600 * I1^7 * \phi d0 * m * r0^2 + \\
& 244 * m^2 * r0^4 * I1^6 - 1064 * I1^3 * \phi d0^2 * r0^10 * m^5 + 143 * I1^2 * \phi d0^3 * r0^12 * m^6 + \\
& 974 * I1^5 * \phi d0 * r0^6 * m^3 + 345 * I1^4 * \phi d0 * r0^8 * m^4 + 1107 * I1^6 * \phi d0 * r0^4 * m^2 - \\
& 5062 * r0^6 * m^3 * \phi d0^3 * I1^5 - 5400 * r0^4 * m^2 * \phi d0^3 * I1^6 - 2412 * r0^6 * m^3 * \phi d0^2 * I1^5 - \\
& 2305 * r0^8 * m^4 * \phi d0^2 * I1^4 - 1011 * r0^4 * m^2 * \phi d0^2 * I1^6 + 2414 * r0^10 * m^5 * \phi d0^4 * I1^3 - \\
& 210 * r0^10 * m^5 * \phi d0^3 * I1^3 + 589 * r0^12 * m^6 * \phi d0^4 * I1^2 + 2112 * I1^7 * \phi d0^4 * r0^2 * m + \\
& 340 * m^3 * r0^6 * I1^5 + 96 * m^2 * r0^2 * I1^7 + 280 * m^4 * r0^8 * I1^4 + 5661 * r0^8 * m^4 * \phi d0^4 * I1^4 + \\
& 5764 * r0^4 * m^2 * \phi d0^4 * I1^6 + 7672 * r0^6 * m^3 * \phi d0^4 * I1^5 - 2181 * r0^8 * m^4 * \phi d0^3 * I1^4 - \\
& 12 * r0^14 * m^7 * \phi d0^2 * I1 + 4 * r0^16 * m^8 * \phi d0^3 - 75 * r0^12 * m^6 * \phi d0 * I1^2 - 18 * I1 * \phi d0 * r0^14 * m^7 + \\
& \phi d0^2 * r0^16 * m^8 + 36 * I1^2 * r0^12 * m^6 + 4 * m^7 * r0^14 * I1 - m^8 * r0^16 * \phi d0 + 80 * I1^7 * \phi d0^2 * m * r0^2 \\
& - 2720 * I1^7 * \phi d0^3 * m * r0^2 + 136 * I1^3 * r0^10 * m^5 + 128 * \phi d0^2 * I1^8 + 128 * I1^8 * \phi d0 - \\
& 512 * I1^8 * \phi d0^3 + 256 * I1^8 * \phi d0^4)^(1/2) * I1^2)^(1/3) * \phi d0 * (4 * r0^8 * m^4 * \phi d0^2 + (- \\
& 8 * r0^12 * m^6 * \phi d0^3 - 24 * I1^5 * m * r0^2 - 8 * I1^3 * m^3 * r0^6 - 24 * I1^4 * m^2 * r0^4 - 8 * I1^6 + \\
& 288 * I1^6 * \phi d0^2 - 288 * I1^6 * \phi d0 - 348 * I1^3 * m^3 * r0^6 * \phi d0 + 1752 * I1^3 * r0^6 * m^3 * \phi d0^2 - \\
& 672 * I1^2 * r0^8 * m^4 * \phi d0^3 - 1756 * I1^3 * r0^6 * m^3 * \phi d0^3 - 804 * I1^4 * \phi d0 * r0^4 * m^2 + \\
& 492 * I1^2 * r0^8 * m^4 * \phi d0^2 - 60 * I1^2 * r0^8 * m^4 * \phi d0 + 1692 * I1^5 * \phi d0^2 * r0^2 * m - \\
& 804 * I1^5 * \phi d0 * m * r0^2 + 2712 * I1^4 * r0^4 * m^2 * \phi d0^2 - 936 * I1^5 * \phi d0^3 * r0^2 * m - \\
& 2124 * I1^4 * r0^4 * m^2 * \phi d0^3 + 48 * r0^10 * m^5 * \phi d0^2 * I1 - 120 * r0^10 * m^5 * \phi d0^3 * I1 + 12 * 3^(1/2) * (- \\
& \phi d0 * (\phi d0 - 1) * (4 * \phi d0 * 4 * m^8 * r0^16 + 46 * m^7 * r0^14 * I1 * \phi d0^3 + 76 * r0^14 * m^7 * \phi d0^4 * I1 - \\
& 52 * m^5 * r0^10 * I1^3 * \phi d0 - 221 * m^6 * r0^12 * I1^2 * \phi d0^2 + 16 * I1^8 + 600 * I1^7 * \phi d0 * m * r0^2 + \\
& 244 * m^2 * r0^4 * I1^6 - 1064 * I1^3 * \phi d0^2 * r0^10 * m^5 + 143 * I1^2 * \phi d0^3 * r0^12 * m^6 + \\
& 974 * I1^5 * \phi d0 * r0^6 * m^3 + 345 * I1^4 * \phi d0 * r0^8 * m^4 + 1107 * I1^6 * \phi d0 * r0^4 * m^2 - \\
& 5062 * r0^6 * m^3 * \phi d0^3 * I1^5 - 5400 * r0^4 * m^2 * \phi d0^3 * I1^6 - 2412 * r0^6 * m^3 * \phi d0^2 * I1^5 - \\
& 2305 * r0^8 * m^4 * \phi d0^2 * I1^4 - 1011 * r0^4 * m^2 * \phi d0^2 * I1^6 + 2414 * r0^10 * m^5 * \phi d0^4 * I1^3 - \\
& 210 * r0^10 * m^5 * \phi d0^3 * I1^3 + 589 * r0^12 * m^6 * \phi d0^4 * I1^2 + 2112 * I1^7 * \phi d0^4 * r0^2 * m + \\
& 340 * m^3 * r0^6 * I1^5 + 96 * m^2 * r0^2 * I1^7 + 280 * m^4 * r0^8 * I1^4 + 5661 * r0^8 * m^4 * \phi d0^4 * I1^4 + \\
& 5764 * r0^4 * m^2 * \phi d0^4 * I1^6 + 7672 * r0^6 * m^3 * \phi d0^4 * I1^5 - 2181 * r0^8 * m^4 * \phi d0^3 * I1^4 - \\
& 12 * r0^14 * m^7 * \phi d0^2 * I1 + 4 * r0^16 * m^8 * \phi d0^3 - 75 * r0^12 * m^6 * \phi d0 * I1^2 - 18 * I1 * \phi d0 * r0^14 * m^7 + \\
& \phi d0^2 * r0^16 * m^8 + 36 * I1^2 * r0^12 * m^6 + 4 * m^7 * r0^14 * I1 - m^8 * r0^16 * \phi d0 + 80 * I1^7 * \phi d0^2 * m * r0^2 \\
& - 2720 * I1^7 * \phi d0^3 * m * r0^2 + 136 * I1^3 * r0^10 * m^5 + 128 * \phi d0^2 * I1^8 + 128 * I1^8 * \phi d0 - \\
& 512 * I1^8 * \phi d0^3 + 256 * I1^8 * \phi d0^4)^(1/2) * I1^2)^(2/3) + 124 * r0^4 * m^2 * \phi d0^2 * I1^2 + 48 * I1^4 * \phi d0^2 + \\
& 132 * I1^3 * \phi d0^2 * r0^2 * m - 84 * I1^2 * \phi d0 * r0^4 * m^2 - 116 * I1^3 * \phi d0 * m * r0^2 - 48 * I1^4 * \phi d0 + \\
& 8 * m * r0^2 * I1^3 + 4 * m^2 * r0^4 * I1^2 + 4 * I1^4 + 40 * r0^6 * m^3 * \phi d0^2 * I1 - 16 * m^3 * r0^6 * I1 * \phi d0 - 10 * (- \\
& 8 * r0^12 * m^6 * \phi d0^3 - 24 * I1^5 * m * r0^2 - 8 * I1^3 * m^3 * r0^6 - 24 * I1^4 * m^2 * r0^4 - 8 * I1^6 + \\
& 288 * I1^6 * \phi d0^2 - 288 * I1^6 * \phi d0 - 348 * I1^3 * m^3 * r0^6 * \phi d0 + 1752 * I1^3 * r0^6 * m^3 * \phi d0^2 - \\
& 672 * I1^2 * r0^8 * m^4 * \phi d0^3 - 1756 * I1^3 * r0^6 * m^3 * \phi d0^3 - 804 * I1^4 * \phi d0 * r0^4 * m^2 + \\
& 492 * I1^2 * r0^8 * m^4 * \phi d0^2 - 60 * I1^2 * r0^8 * m^4 * \phi d0 + 1692 * I1^5 * \phi d0^2 * r0^2 * m -
\end{aligned}$$

804*I1^5*fd0*m*r0^2 + 2712*I1^4*r0^4*m^2*fd0^2 - 936*I1^5*fd0^3*r0^2*m -
 2124*I1^4*r0^4*m^2*fd0^3 + 48*r0^10*m^5*fd0^2*I1 - 120*r0^10*m^5*fd0^3*I1 + 12*I3^(1/2)*(-
 fd0*(fd0 - 1)*(4*fd0^4*m^8*r0^16 + 46*m^7*r0^14*I1*fd0^3 + 76*r0^14*m^7*fd0^4*I1 -
 52*m^5*r0^10*I1^3*fd0 - 221*m^6*r0^12*I1^2*fd0^2 + 16*I1^8 + 600*I1^7*fd0*m*r0^2 +
 244*m^2*r0^4*I1^6 - 1064*I1^3*fd0^2*r0^10*m^5 + 143*I1^2*fd0^3*r0^12*m^6 +
 974*I1^5*fd0*r0^6*m^3 + 345*I1^4*fd0*r0^8*m^4 + 1107*I1^6*fd0*r0^4*m^2 -
 5062*r0^6*m^3*fd0^3*I1^5 - 5400*r0^4*m^2*fd0^3*I1^6 - 2412*r0^6*m^3*fd0^2*I1^5 -
 2305*r0^8*m^4*fd0^2*I1^4 - 1011*r0^4*m^2*fd0^2*I1^6 + 2414*r0^10*m^5*fd0^4*I1^3 -
 210*r0^10*m^5*fd0^3*I1^3 + 589*r0^12*m^6*fd0^4*I1^2 + 2112*I1^7*fd0^4*r0^2*m +
 340*m^3*r0^6*I1^5 + 96*m^2*r0^2*I1^7 + 280*m^4*r0^8*I1^4 + 5661*r0^8*m^4*fd0^4*I1^4 +
 5764*r0^4*m^2*fd0^4*I1^6 + 7672*r0^6*m^3*fd0^4*I1^5 - 2181*r0^8*m^4*fd0^3*I1^4 -
 12*r0^14*m^7*fd0^2*I1 + 4*r0^16*m^8*fd0^3 - 75*r0^12*m^6*fd0*I1^2 - 18*I1*fd0*r0^14*m^7 +
 fd0^2*r0^16*m^8 + 36*I1^2*r0^12*m^6 + 4*m^7*r0^14*I1 - m^8*r0^16*fd0 + 80*I1^7*fd0^2*m*r0^2
 - 2720*I1^7*fd0^3*m*r0^2 + 136*I1^3*r0^10*m^5 + 128*fd0^2*I1^8 + 128*I1^8*fd0 -
 512*I1^8*fd0^3 + 256*I1^8*fd0^4))^(1/2)*I1^2)^(1/3)*r0^2*m*I1*fd0 - 12*(-8*r0^12*m^6*fd0^3 -
 24*I1^5*m*r0^2 - 8*I1^3*m^3*r0^6 - 24*I1^4*m^2*r0^4 - 8*I1^6 + 288*I1^6*fd0^2 - 288*I1^6*fd0 -
 348*I1^3*m^3*r0^6*fd0 + 1752*I1^3*r0^6*m^3*fd0^2 - 672*I1^2*r0^8*m^4*fd0^3 -
 1756*I1^3*r0^6*m^3*fd0^3 - 804*I1^4*fd0*r0^4*m^2 + 492*I1^2*r0^8*m^4*fd0^2 -
 60*I1^2*r0^8*m^4*fd0 + 1692*I1^5*fd0^2*r0^2*m - 804*I1^5*fd0*m*r0^2 +
 2712*I1^4*r0^4*m^2*fd0^2 - 936*I1^5*fd0^3*r0^2*m - 2124*I1^4*r0^4*m^2*fd0^3 +
 48*r0^10*m^5*fd0^2*I1 - 120*r0^10*m^5*fd0^3*I1 + 12*I3^(1/2)*(-fd0*(fd0 -
 1)*(4*fd0^4*m^8*r0^16 + 46*m^7*r0^14*I1*fd0^3 + 76*r0^14*m^7*fd0^4*I1 -
 52*m^5*r0^10*I1^3*fd0 - 221*m^6*r0^12*I1^2*fd0^2 + 16*I1^8 + 600*I1^7*fd0*m*r0^2 +
 244*m^2*r0^4*I1^6 - 1064*I1^3*fd0^2*r0^10*m^5 + 143*I1^2*fd0^3*r0^12*m^6 +
 974*I1^5*fd0*r0^6*m^3 + 345*I1^4*fd0*r0^8*m^4 + 1107*I1^6*fd0*r0^4*m^2 -
 5062*r0^6*m^3*fd0^3*I1^5 - 5400*r0^4*m^2*fd0^3*I1^6 - 2412*r0^6*m^3*fd0^2*I1^5 -
 2305*r0^8*m^4*fd0^2*I1^4 - 1011*r0^4*m^2*fd0^2*I1^6 + 2414*r0^10*m^5*fd0^4*I1^3 -
 210*r0^10*m^5*fd0^3*I1^3 + 589*r0^12*m^6*fd0^4*I1^2 + 2112*I1^7*fd0^4*r0^2*m +
 340*m^3*r0^6*I1^5 + 96*m^2*r0^2*I1^7 + 280*m^4*r0^8*I1^4 + 5661*r0^8*m^4*fd0^4*I1^4 +
 5764*r0^4*m^2*fd0^4*I1^6 + 7672*r0^6*m^3*fd0^4*I1^5 - 2181*r0^8*m^4*fd0^3*I1^4 -
 12*r0^14*m^7*fd0^2*I1 + 4*r0^16*m^8*fd0^3 - 75*r0^12*m^6*fd0*I1^2 - 18*I1*fd0*r0^14*m^7 +
 fd0^2*r0^16*m^8 + 36*I1^2*r0^12*m^6 + 4*m^7*r0^14*I1 - m^8*r0^16*fd0 + 80*I1^7*fd0^2*m*r0^2
 - 2720*I1^7*fd0^3*m*r0^2 + 136*I1^3*r0^10*m^5 + 128*fd0^2*I1^8 + 128*I1^8*fd0 -
 512*I1^8*fd0^3 + 256*I1^8*fd0^4))^(1/2)*I1^2)^(1/3)*I1^2*fd0 - 2*(-8*r0^12*m^6*fd0^3 -
 24*I1^5*m*r0^2 - 8*I1^3*m^3*r0^6 - 24*I1^4*m^2*r0^4 - 8*I1^6 + 288*I1^6*fd0^2 - 288*I1^6*fd0 -
 348*I1^3*m^3*r0^6*fd0 + 1752*I1^3*r0^6*m^3*fd0^2 - 672*I1^2*r0^8*m^4*fd0^3 -
 1756*I1^3*r0^6*m^3*fd0^3 - 804*I1^4*fd0*r0^4*m^2 + 492*I1^2*r0^8*m^4*fd0^2 -
 60*I1^2*r0^8*m^4*fd0 + 1692*I1^5*fd0^2*r0^2*m - 804*I1^5*fd0*m*r0^2 +
 2712*I1^4*r0^4*m^2*fd0^2 - 936*I1^5*fd0^3*r0^2*m - 2124*I1^4*r0^4*m^2*fd0^3 +
 48*r0^10*m^5*fd0^2*I1 - 120*r0^10*m^5*fd0^3*I1 + 12*I3^(1/2)*(-fd0*(fd0 -
 1)*(4*fd0^4*m^8*r0^16 + 46*m^7*r0^14*I1*fd0^3 + 76*r0^14*m^7*fd0^4*I1 -
 52*m^5*r0^10*I1^3*fd0 - 221*m^6*r0^12*I1^2*fd0^2 + 16*I1^8 + 600*I1^7*fd0*m*r0^2 +
 244*m^2*r0^4*I1^6 - 1064*I1^3*fd0^2*r0^10*m^5 + 143*I1^2*fd0^3*r0^12*m^6 +
 974*I1^5*fd0*r0^6*m^3 + 345*I1^4*fd0*r0^8*m^4 + 1107*I1^6*fd0*r0^4*m^2 -
 5062*r0^6*m^3*fd0^3*I1^5 - 5400*r0^4*m^2*fd0^3*I1^6 - 2412*r0^6*m^3*fd0^2*I1^5 -
 2305*r0^8*m^4*fd0^2*I1^4 - 1011*r0^4*m^2*fd0^2*I1^6 + 2414*r0^10*m^5*fd0^4*I1^3 -
 210*r0^10*m^5*fd0^3*I1^3 + 589*r0^12*m^6*fd0^4*I1^2 + 2112*I1^7*fd0^4*r0^2*m +

$$\begin{aligned}
& 340*m^3*r0^6*I1^5 + 96*m*r0^2*I1^7 + 280*m^4*r0^8*I1^4 + 5661*r0^8*m^4*phi0^4*I1^4 + \\
& 5764*r0^4*m^2*phi0^4*I1^6 + 7672*r0^6*m^3*phi0^4*I1^5 - 2181*r0^8*m^4*phi0^3*I1^4 - \\
& 12*r0^14*m^7*phi0^2*I1 + 4*r0^16*m^8*phi0^3 - 75*r0^12*m^6*phi0^2*I1^2 - 18*I1*phi0*r0^14*m^7 + \\
& phi0^2*r0^16*m^8 + 36*I1^2*r0^12*m^6 + 4*m^7*r0^14*I1 - m^8*r0^16*phi0 + 80*I1^7*phi0^2*m*r0^2 \\
& - 2720*I1^7*phi0^3*m*r0^2 + 136*I1^3*r0^10*m^5 + 128*phi0^2*I1^8 + 128*I1^8*phi0 - \\
& 512*I1^8*phi0^3 + 256*I1^8*phi0^4))^(1/2)*I1^2)^(1/3)*r0^4*m^2*phi0 + 4*(-8*r0^12*m^6*phi0^3 - \\
& 24*I1^5*m*r0^2 - 8*I1^3*m^3*r0^6 - 24*I1^4*m^2*r0^4 - 8*I1^6 + 288*I1^6*phi0^2 - 288*I1^6*phi0 - \\
& 348*I1^3*m^3*r0^6*phi0 + 1752*I1^3*r0^6*m^3*phi0^2 - 672*I1^2*r0^8*m^4*phi0^3 - \\
& 1756*I1^3*r0^6*m^3*phi0^3 - 804*I1^4*phi0*r0^4*m^2 + 492*I1^2*r0^8*m^4*phi0^2 - \\
& 60*I1^2*r0^8*m^4*phi0 + 1692*I1^5*phi0^2*r0^2*m - 804*I1^5*phi0*m*r0^2 + \\
& 2712*I1^4*r0^4*m^2*phi0^2 - 936*I1^5*phi0^3*r0^2*m - 2124*I1^4*r0^4*m^2*phi0^3 + \\
& 48*r0^10*m^5*phi0^2*I1 - 120*r0^10*m^5*phi0^3*I1 + 12*3^(1/2)*(-phi0*(phi0 - \\
& 1)*(4*phi0^4*m^8*r0^16 + 46*m^7*r0^14*I1*phi0^3 + 76*r0^14*m^7*phi0^4*I1 - \\
& 52*m^5*r0^10*I1^3*phi0 - 221*m^6*r0^12*I1^2*phi0^2 + 16*I1^8 + 600*I1^7*phi0*m*r0^2 + \\
& 244*m^2*r0^4*I1^6 - 1064*I1^3*phi0^2*r0^10*m^5 + 143*I1^2*phi0^3*r0^12*m^6 + \\
& 974*I1^5*phi0*r0^6*m^3 + 345*I1^4*phi0*r0^8*m^4 + 1107*I1^6*phi0*r0^4*m^2 - \\
& 5062*r0^6*m^3*phi0^3*I1^5 - 5400*r0^4*m^2*phi0^3*I1^6 - 2412*r0^6*m^3*phi0^2*I1^5 - \\
& 2305*r0^8*m^4*phi0^2*I1^4 - 1011*r0^4*m^2*phi0^2*I1^6 + 2414*r0^10*m^5*phi0^4*I1^3 - \\
& 210*r0^10*m^5*phi0^3*I1^3 + 589*r0^12*m^6*phi0^4*I1^2 + 2112*I1^7*phi0^4*r0^2*m + \\
& 340*m^3*r0^6*I1^5 + 96*m*r0^2*I1^7 + 280*m^4*r0^8*I1^4 + 5661*r0^8*m^4*phi0^4*I1^4 + \\
& 5764*r0^4*m^2*phi0^4*I1^6 + 7672*r0^6*m^3*phi0^4*I1^5 - 2181*r0^8*m^4*phi0^3*I1^4 - \\
& 12*r0^14*m^7*phi0^2*I1 + 4*r0^16*m^8*phi0^3 - 75*r0^12*m^6*phi0^2*I1^2 - 18*I1*phi0*r0^14*m^7 + \\
& phi0^2*r0^16*m^8 + 36*I1^2*r0^12*m^6 + 4*m^7*r0^14*I1 - m^8*r0^16*phi0 + 80*I1^7*phi0^2*m*r0^2 \\
& - 2720*I1^7*phi0^3*m*r0^2 + 136*I1^3*r0^10*m^5 + 128*phi0^2*I1^8 + 128*I1^8*phi0 - \\
& 512*I1^8*phi0^3 + 256*I1^8*phi0^4))^(1/2)*I1^2)^(1/3)*r0^2*I1^4 + 4*I1^2*(-8*r0^12*m^6*phi0^3 - \\
& 24*I1^5*m*r0^2 - 8*I1^3*m^3*r0^6 - 24*I1^4*m^2*r0^4 - 8*I1^6 + 288*I1^6*phi0^2 - 288*I1^6*phi0 - \\
& 348*I1^3*m^3*r0^6*phi0 + 1752*I1^3*r0^6*m^3*phi0^2 - 672*I1^2*r0^8*m^4*phi0^3 - \\
& 1756*I1^3*r0^6*m^3*phi0^3 - 804*I1^4*phi0*r0^4*m^2 + 492*I1^2*r0^8*m^4*phi0^2 - \\
& 60*I1^2*r0^8*m^4*phi0 + 1692*I1^5*phi0^2*r0^2*m - 804*I1^5*phi0*m*r0^2 + \\
& 2712*I1^4*r0^4*m^2*phi0^2 - 936*I1^5*phi0^3*r0^2*m - 2124*I1^4*r0^4*m^2*phi0^3 + \\
& 48*r0^10*m^5*phi0^2*I1 - 120*r0^10*m^5*phi0^3*I1 + 12*3^(1/2)*(-phi0*(phi0 - \\
& 1)*(4*phi0^4*m^8*r0^16 + 46*m^7*r0^14*I1*phi0^3 + 76*r0^14*m^7*phi0^4*I1 - \\
& 52*m^5*r0^10*I1^3*phi0 - 221*m^6*r0^12*I1^2*phi0^2 + 16*I1^8 + 600*I1^7*phi0*m*r0^2 + \\
& 244*m^2*r0^4*I1^6 - 1064*I1^3*phi0^2*r0^10*m^5 + 143*I1^2*phi0^3*r0^12*m^6 + \\
& 974*I1^5*phi0*r0^6*m^3 + 345*I1^4*phi0*r0^8*m^4 + 1107*I1^6*phi0*r0^4*m^2 - \\
& 5062*r0^6*m^3*phi0^3*I1^5 - 5400*r0^4*m^2*phi0^3*I1^6 - 2412*r0^6*m^3*phi0^2*I1^5 - \\
& 2305*r0^8*m^4*phi0^2*I1^4 - 1011*r0^4*m^2*phi0^2*I1^6 + 2414*r0^10*m^5*phi0^4*I1^3 - \\
& 210*r0^10*m^5*phi0^3*I1^3 + 589*r0^12*m^6*phi0^4*I1^2 + 2112*I1^7*phi0^4*r0^2*m + \\
& 340*m^3*r0^6*I1^5 + 96*m*r0^2*I1^7 + 280*m^4*r0^8*I1^4 + 5661*r0^8*m^4*phi0^4*I1^4 + \\
& 5764*r0^4*m^2*phi0^4*I1^6 + 7672*r0^6*m^3*phi0^4*I1^5 - 2181*r0^8*m^4*phi0^3*I1^4 - \\
& 12*r0^14*m^7*phi0^2*I1 + 4*r0^16*m^8*phi0^3 - 75*r0^12*m^6*phi0^2*I1^2 - 18*I1*phi0*r0^14*m^7 + \\
& phi0^2*r0^16*m^8 + 36*I1^2*r0^12*m^6 + 4*m^7*r0^14*I1 - m^8*r0^16*phi0 + 80*I1^7*phi0^2*m*r0^2 \\
& - 2720*I1^7*phi0^3*m*r0^2 + 136*I1^3*r0^10*m^5 + 128*phi0^2*I1^8 + 128*I1^8*phi0 - \\
& 512*I1^8*phi0^3 + 256*I1^8*phi0^4))^(1/2)*I1^2)^(1/3))
\end{aligned}$$

$$\begin{aligned}
\lambda_8 = & -1/6/I1/(-8*r0^12*m^6*phi0^3 - 24*I1^5*m*r0^2 - 8*I1^3*m^3*r0^6 - 24*I1^4*m^2*r0^4 - 8*I1^6 \\
& + 288*I1^6*phi0^2 - 288*I1^6*phi0 - 348*I1^3*m^3*r0^6*phi0 + 1752*I1^3*r0^6*m^3*phi0^2 -
\end{aligned}$$

672*I1^2*r0^8*m^4*fd0^3 - 1756*I1^3*r0^6*m^3*fd0^3 - 804*I1^4*fd0*r0^4*m^2 +
 492*I1^2*r0^8*m^4*fd0^2 - 60*I1^2*r0^8*m^4*fd0 + 1692*I1^5*fd0^2*r0^2*m -
 804*I1^5*fd0*m*r0^2 + 2712*I1^4*r0^4*m^2*fd0^2 - 936*I1^5*fd0^3*r0^2*m -
 2124*I1^4*r0^4*m^2*fd0^3 + 48*r0^10*m^5*fd0^2*I1 - 120*r0^10*m^5*fd0^3*I1 + 12*3^(1/2)*(-
 fd0*(fd0 - 1)*(4*fd0^4*m^8*r0^16 + 46*m^7*r0^14*I1*fd0^3 + 76*r0^14*m^7*fd0^4*I1 -
 52*m^5*r0^10*I1^3*fd0 - 221*m^6*r0^12*I1^2*fd0^2 + 16*I1^8 + 600*I1^7*fd0*m*r0^2 +
 244*m^2*r0^4*I1^6 - 1064*I1^3*fd0^2*r0^10*m^5 + 143*I1^2*fd0^3*r0^12*m^6 +
 974*I1^5*fd0*r0^6*m^3 + 345*I1^4*fd0*r0^8*m^4 + 1107*I1^6*fd0*r0^4*m^2 -
 5062*r0^6*m^3*fd0^3*I1^5 - 5400*r0^4*m^2*fd0^3*I1^6 - 2412*r0^6*m^3*fd0^2*I1^5 -
 2305*r0^8*m^4*fd0^2*I1^4 - 1011*r0^4*m^2*fd0^2*I1^6 + 2414*r0^10*m^5*fd0^4*I1^3 -
 210*r0^10*m^5*fd0^3*I1^3 + 589*r0^12*m^6*fd0^4*I1^2 + 2112*I1^7*fd0^4*r0^2*m +
 340*m^3*r0^6*I1^5 + 96*m*r0^2*I1^7 + 280*m^4*r0^8*I1^4 + 5661*r0^8*m^4*fd0^4*I1^4 +
 5764*r0^4*m^2*fd0^4*I1^6 + 7672*r0^6*m^3*fd0^4*I1^5 - 2181*r0^8*m^4*fd0^3*I1^4 -
 12*r0^14*m^7*fd0^2*I1 + 4*r0^16*m^8*fd0^3 - 75*r0^12*m^6*fd0*I1^2 - 18*I1*fd0*r0^14*m^7 +
 fd0^2*r0^16*m^8 + 36*I1^2*r0^12*m^6 + 4*m^7*r0^14*I1 - m^8*r0^16*fd0 + 80*I1^7*fd0^2*m*r0^2
 - 2720*I1^7*fd0^3*m*r0^2 + 136*I1^3*r0^10*m^5 + 128*fd0^2*I1^8 + 128*I1^8*fd0 -
 512*I1^8*fd0^3 + 256*I1^8*fd0^4))^(1/2)*I1^2)^(1/3)*3^(1/2)*2^(1/2)*((- 8*r0^12*m^6*fd0^3 -
 24*I1^5*m*r0^2 - 8*I1^3*m^3*r0^6 - 24*I1^4*m^2*r0^4 - 8*I1^6 + 288*I1^6*fd0^2 - 288*I1^6*fd0 -
 348*I1^3*m^3*r0^6*fd0 + 1752*I1^3*r0^6*m^3*fd0^2 - 672*I1^2*r0^8*m^4*fd0^3 -
 1756*I1^3*r0^6*m^3*fd0^3 - 804*I1^4*fd0*r0^4*m^2 + 492*I1^2*r0^8*m^4*fd0^2 -
 60*I1^2*r0^8*m^4*fd0 + 1692*I1^5*fd0^2*r0^2*m - 804*I1^5*fd0*m*r0^2 +
 2712*I1^4*r0^4*m^2*fd0^2 - 936*I1^5*fd0^3*r0^2*m - 2124*I1^4*r0^4*m^2*fd0^3 +
 48*r0^10*m^5*fd0^2*I1 - 120*r0^10*m^5*fd0^3*I1 + 12*3^(1/2)*(- fd0*(fd0 -
 1)*(4*fd0^4*m^8*r0^16 + 46*m^7*r0^14*I1*fd0^3 + 76*r0^14*m^7*fd0^4*I1 -
 52*m^5*r0^10*I1^3*fd0 - 221*m^6*r0^12*I1^2*fd0^2 + 16*I1^8 + 600*I1^7*fd0*m*r0^2 +
 244*m^2*r0^4*I1^6 - 1064*I1^3*fd0^2*r0^10*m^5 + 143*I1^2*fd0^3*r0^12*m^6 +
 974*I1^5*fd0*r0^6*m^3 + 345*I1^4*fd0*r0^8*m^4 + 1107*I1^6*fd0*r0^4*m^2 -
 5062*r0^6*m^3*fd0^3*I1^5 - 5400*r0^4*m^2*fd0^3*I1^6 - 2412*r0^6*m^3*fd0^2*I1^5 -
 2305*r0^8*m^4*fd0^2*I1^4 - 1011*r0^4*m^2*fd0^2*I1^6 + 2414*r0^10*m^5*fd0^4*I1^3 -
 210*r0^10*m^5*fd0^3*I1^3 + 589*r0^12*m^6*fd0^4*I1^2 + 2112*I1^7*fd0^4*r0^2*m +
 340*m^3*r0^6*I1^5 + 96*m*r0^2*I1^7 + 280*m^4*r0^8*I1^4 + 5661*r0^8*m^4*fd0^4*I1^4 +
 5764*r0^4*m^2*fd0^4*I1^6 + 7672*r0^6*m^3*fd0^4*I1^5 - 2181*r0^8*m^4*fd0^3*I1^4 -
 12*r0^14*m^7*fd0^2*I1 + 4*r0^16*m^8*fd0^3 - 75*r0^12*m^6*fd0*I1^2 - 18*I1*fd0*r0^14*m^7 +
 fd0^2*r0^16*m^8 + 36*I1^2*r0^12*m^6 + 4*m^7*r0^14*I1 - m^8*r0^16*fd0 + 80*I1^7*fd0^2*m*r0^2
 - 2720*I1^7*fd0^3*m*r0^2 + 136*I1^3*r0^10*m^5 + 128*fd0^2*I1^8 + 128*I1^8*fd0 -
 512*I1^8*fd0^3 + 256*I1^8*fd0^4))^(1/2)*I1^2)^(1/3)*fd0*(4*r0^8*m^4*fd0^2 + (-
 8*r0^12*m^6*fd0^3 - 24*I1^5*m*r0^2 - 8*I1^3*m^3*r0^6 - 24*I1^4*m^2*r0^4 - 8*I1^6 +
 288*I1^6*fd0^2 - 288*I1^6*fd0 - 348*I1^3*m^3*r0^6*fd0 + 1752*I1^3*r0^6*m^3*fd0^2 -
 672*I1^2*r0^8*m^4*fd0^3 - 1756*I1^3*r0^6*m^3*fd0^3 - 804*I1^4*fd0*r0^4*m^2 +
 492*I1^2*r0^8*m^4*fd0^2 - 60*I1^2*r0^8*m^4*fd0 + 1692*I1^5*fd0^2*r0^2*m -
 804*I1^5*fd0*m*r0^2 + 2712*I1^4*r0^4*m^2*fd0^2 - 936*I1^5*fd0^3*r0^2*m -
 2124*I1^4*r0^4*m^2*fd0^3 + 48*r0^10*m^5*fd0^2*I1 - 120*r0^10*m^5*fd0^3*I1 + 12*3^(1/2)*(-
 fd0*(fd0 - 1)*(4*fd0^4*m^8*r0^16 + 46*m^7*r0^14*I1*fd0^3 + 76*r0^14*m^7*fd0^4*I1 -
 52*m^5*r0^10*I1^3*fd0 - 221*m^6*r0^12*I1^2*fd0^2 + 16*I1^8 + 600*I1^7*fd0*m*r0^2 +
 244*m^2*r0^4*I1^6 - 1064*I1^3*fd0^2*r0^10*m^5 + 143*I1^2*fd0^3*r0^12*m^6 +
 974*I1^5*fd0*r0^6*m^3 + 345*I1^4*fd0*r0^8*m^4 + 1107*I1^6*fd0*r0^4*m^2 -
 5062*r0^6*m^3*fd0^3*I1^5 - 5400*r0^4*m^2*fd0^3*I1^6 - 2412*r0^6*m^3*fd0^2*I1^5 -

$2305^*r0^8*m^4*\phi d0^2*I1^4 - 1011^*r0^4*m^2*\phi d0^2*I1^6 + 2414^*r0^10*m^5*\phi d0^4*I1^3 -$
 $210^*r0^10*m^5*\phi d0^3*I1^3 + 589^*r0^12*m^6*\phi d0^4*I1^2 + 2112^*I1^7*\phi d0^4*r0^2*m +$
 $340^*m^3*r0^6*I1^5 + 96^*m^*r0^2*I1^7 + 280^*m^4*r0^8*I1^4 + 5661^*r0^8*m^4*\phi d0^4*I1^4 +$
 $5764^*r0^4*m^2*\phi d0^4*I1^6 + 7672^*r0^6*m^3*\phi d0^4*I1^5 - 2181^*r0^8*m^4*\phi d0^3*I1^4 -$
 $12^*r0^14*m^7*\phi d0^2*I1 + 4^*r0^16*m^8*\phi d0^3 - 75^*r0^12*m^6*\phi d0^2*I1^2 - 18^*I1^*\phi d0^*r0^14*m^7 +$
 $\phi d0^2*r0^16*m^8 + 36^*I1^2*r0^12*m^6 + 4^*m^7*r0^14*I1 - m^8*r0^16*\phi d0 + 80^*I1^7*\phi d0^2*m*r0^2 -$
 $- 2720^*I1^7*\phi d0^3*m*r0^2 + 136^*I1^3*r0^10*m^5 + 128^*\phi d0^2*I1^8 + 128^*I1^8*\phi d0 -$
 $512^*I1^8*\phi d0^3 + 256^*I1^8*\phi d0^4))^(1/2)*I1^2)^(2/3) + 124^*r0^4*m^2*\phi d0^2*I1^2 + 48^*I1^4*\phi d0^2 +$
 $132^*I1^3*\phi d0^2*r0^2*m - 84^*I1^2*\phi d0^*r0^4*m^2 - 116^*I1^3*\phi d0*m*r0^2 - 48^*I1^4*\phi d0 +$
 $8^*m^*r0^2*I1^3 + 4^*m^2*r0^4*I1^2 + 4^*I1^4 + 40^*r0^6*m^3*\phi d0^2*I1 - 16^*m^3*r0^6*I1*\phi d0 - 10^*(-$
 $8^*r0^12*m^6*\phi d0^3 - 24^*I1^5*m^*r0^2 - 8^*I1^3*m^3*r0^6 - 24^*I1^4*m^2*r0^4 - 8^*I1^6 +$
 $288^*I1^6*\phi d0^2 - 288^*I1^6*\phi d0 - 348^*I1^3*m^3*r0^6*\phi d0 + 1752^*I1^3*r0^6*m^3*\phi d0^2 -$
 $672^*I1^2*r0^8*m^4*\phi d0^3 - 1756^*I1^3*r0^6*m^3*\phi d0^3 - 804^*I1^4*\phi d0^*r0^4*m^2 +$
 $492^*I1^2*r0^8*m^4*\phi d0^2 - 60^*I1^2*r0^8*m^4*\phi d0 + 1692^*I1^5*\phi d0^2*r0^2*m -$
 $804^*I1^5*\phi d0*m*r0^2 + 2712^*I1^4*r0^4*m^2*\phi d0^2 - 936^*I1^5*\phi d0^3*r0^2*m -$
 $2124^*I1^4*r0^4*m^2*\phi d0^3 + 48^*r0^10*m^5*\phi d0^2*I1 - 120^*r0^10*m^5*\phi d0^3*I1 + 12^*3^(1/2)*(-$
 $\phi d0*(\phi d0 - 1)*(4^*\phi d0^4*m^8*r0^16 + 46^*m^7*r0^14*I1*\phi d0^3 + 76^*r0^14*m^7*\phi d0^4*I1 -$
 $52^*m^5*r0^10*I1^3*\phi d0 - 221^*m^6*r0^12*I1^2*\phi d0^2 + 16^*I1^8 + 600^*I1^7*\phi d0*m*r0^2 +$
 $244^*m^2*r0^4*I1^6 - 1064^*I1^3*\phi d0^2*r0^10*m^5 + 143^*I1^2*\phi d0^3*r0^12*m^6 +$
 $974^*I1^5*\phi d0*r0^6*m^3 + 345^*I1^4*\phi d0*r0^8*m^4 + 1107^*I1^6*\phi d0*r0^4*m^2 -$
 $5062^*r0^6*m^3*\phi d0^3*I1^5 - 5400^*r0^4*m^2*\phi d0^3*I1^6 - 2412^*r0^6*m^3*\phi d0^2*I1^5 -$
 $2305^*r0^8*m^4*\phi d0^2*I1^4 - 1011^*r0^4*m^2*\phi d0^2*I1^6 + 2414^*r0^10*m^5*\phi d0^4*I1^3 -$
 $210^*r0^10*m^5*\phi d0^3*I1^3 + 589^*r0^12*m^6*\phi d0^4*I1^2 + 2112^*I1^7*\phi d0^4*r0^2*m +$
 $340^*m^3*r0^6*I1^5 + 96^*m^*r0^2*I1^7 + 280^*m^4*r0^8*I1^4 + 5661^*r0^8*m^4*\phi d0^4*I1^4 +$
 $5764^*r0^4*m^2*\phi d0^4*I1^6 + 7672^*r0^6*m^3*\phi d0^4*I1^5 - 2181^*r0^8*m^4*\phi d0^3*I1^4 -$
 $12^*r0^14*m^7*\phi d0^2*I1 + 4^*r0^16*m^8*\phi d0^3 - 75^*r0^12*m^6*\phi d0^2*I1^2 - 18^*I1^*\phi d0^*r0^14*m^7 +$
 $\phi d0^2*r0^16*m^8 + 36^*I1^2*r0^12*m^6 + 4^*m^7*r0^14*I1 - m^8*r0^16*\phi d0 + 80^*I1^7*\phi d0^2*m*r0^2 -$
 $- 2720^*I1^7*\phi d0^3*m*r0^2 + 136^*I1^3*r0^10*m^5 + 128^*\phi d0^2*I1^8 + 128^*I1^8*\phi d0 -$
 $512^*I1^8*\phi d0^3 + 256^*I1^8*\phi d0^4))^(1/2)*I1^2)^(1/3)*r0^2*m*I1^*\phi d0 - 12^*(-8^*r0^12*m^6*\phi d0^3 -$
 $24^*I1^5*m^*r0^2 - 8^*I1^3*m^3*r0^6 - 24^*I1^4*m^2*r0^4 - 8^*I1^6 + 288^*I1^6*\phi d0^2 - 288^*I1^6*\phi d0 -$
 $348^*I1^3*m^3*r0^6*\phi d0 + 1752^*I1^3*r0^6*m^3*\phi d0^2 - 672^*I1^2*r0^8*m^4*\phi d0^3 -$
 $1756^*I1^3*r0^6*m^3*\phi d0^3 - 804^*I1^4*\phi d0*r0^4*m^2 + 492^*I1^2*r0^8*m^4*\phi d0^2 -$
 $60^*I1^2*r0^8*m^4*\phi d0 + 1692^*I1^5*\phi d0^2*r0^2*m - 804^*I1^5*\phi d0*m*r0^2 +$
 $2712^*I1^4*r0^4*m^2*\phi d0^2 - 936^*I1^5*\phi d0^3*r0^2*m - 2124^*I1^4*r0^4*m^2*\phi d0^3 +$
 $48^*r0^10*m^5*\phi d0^2*I1 - 120^*r0^10*m^5*\phi d0^3*I1 + 12^*3^(1/2)*(-\phi d0*(\phi d0 -$
 $1)^*(4^*\phi d0^4*m^8*r0^16 + 46^*m^7*r0^14*I1*\phi d0^3 + 76^*r0^14*m^7*\phi d0^4*I1 -$
 $52^*m^5*r0^10*I1^3*\phi d0 - 221^*m^6*r0^12*I1^2*\phi d0^2 + 16^*I1^8 + 600^*I1^7*\phi d0*m*r0^2 +$
 $244^*m^2*r0^4*I1^6 - 1064^*I1^3*\phi d0^2*r0^10*m^5 + 143^*I1^2*\phi d0^3*r0^12*m^6 +$
 $974^*I1^5*\phi d0*r0^6*m^3 + 345^*I1^4*\phi d0*r0^8*m^4 + 1107^*I1^6*\phi d0*r0^4*m^2 -$
 $5062^*r0^6*m^3*\phi d0^3*I1^5 - 5400^*r0^4*m^2*\phi d0^3*I1^6 - 2412^*r0^6*m^3*\phi d0^2*I1^5 -$
 $2305^*r0^8*m^4*\phi d0^2*I1^4 - 1011^*r0^4*m^2*\phi d0^2*I1^6 + 2414^*r0^10*m^5*\phi d0^4*I1^3 -$
 $210^*r0^10*m^5*\phi d0^3*I1^3 + 589^*r0^12*m^6*\phi d0^4*I1^2 + 2112^*I1^7*\phi d0^4*r0^2*m +$
 $340^*m^3*r0^6*I1^5 + 96^*m^*r0^2*I1^7 + 280^*m^4*r0^8*I1^4 + 5661^*r0^8*m^4*\phi d0^4*I1^4 +$
 $5764^*r0^4*m^2*\phi d0^4*I1^6 + 7672^*r0^6*m^3*\phi d0^4*I1^5 - 2181^*r0^8*m^4*\phi d0^3*I1^4 -$
 $12^*r0^14*m^7*\phi d0^2*I1 + 4^*r0^16*m^8*\phi d0^3 - 75^*r0^12*m^6*\phi d0^2*I1^2 - 18^*I1^*\phi d0^*r0^14*m^7 +$
 $\phi d0^2*r0^16*m^8 + 36^*I1^2*r0^12*m^6 + 4^*m^7*r0^14*I1 - m^8*r0^16*\phi d0 + 80^*I1^7*\phi d0^2*m*r0^2 -$
 $- 2720^*I1^7*\phi d0^3*m*r0^2 + 136^*I1^3*r0^10*m^5 + 128^*\phi d0^2*I1^8 + 128^*I1^8*\phi d0 -$

$512*I1^8*\phi d0^3 + 256*I1^8*\phi d0^4))^{(1/2)*I1^2}^{(1/3)*I1^2*\phi d0 - 2*(-8*r0^12*m^6*\phi d0^3 - 24*I1^5*m^r0^2 - 8*I1^3*m^3*r0^6 - 24*I1^4*m^2*r0^4 - 8*I1^6 + 288*I1^6*\phi d0^2 - 288*I1^6*\phi d0 - 348*I1^3*m^3*r0^6*\phi d0 + 1752*I1^3*r0^6*m^3*\phi d0^2 - 672*I1^2*r0^8*m^4*\phi d0^3 - 1756*I1^3*r0^6*m^3*\phi d0^3 - 804*I1^4*\phi d0^2*r0^4*m^2 + 492*I1^2*r0^8*m^4*\phi d0^2 - 60*I1^2*r0^8*m^4*\phi d0 + 1692*I1^5*\phi d0^2*r0^2*m - 804*I1^5*\phi d0*m*r0^2 + 2712*I1^4*r0^4*m^2*\phi d0^2 - 936*I1^5*\phi d0^3*r0^2*m - 2124*I1^4*r0^4*m^2*\phi d0^3 + 48*r0^10*m^5*\phi d0^2*I1 - 120*r0^10*m^5*\phi d0^3*I1 + 12*3^{(1/2)}*(-\phi d0*(\phi d0 - 1)*(4*\phi d0^4*m^8*r0^16 + 46*m^7*r0^14*I1*\phi d0^3 + 76*r0^14*m^7*\phi d0^4*I1 - 52*m^5*r0^10*I1^3*\phi d0 - 221*m^6*r0^12*I1^2*\phi d0^2 + 16*I1^8 + 600*I1^7*\phi d0*m*r0^2 + 244*m^2*r0^4*I1^6 - 1064*I1^3*\phi d0^2*r0^10*m^5 + 143*I1^2*\phi d0^3*r0^12*m^6 + 974*I1^5*\phi d0*r0^6*m^3 + 345*I1^4*\phi d0*r0^8*m^4 + 1107*I1^6*\phi d0*r0^4*m^2 - 5062*r0^6*m^3*\phi d0^3*I1^5 - 5400*r0^4*m^2*\phi d0^3*I1^6 - 2412*r0^6*m^3*\phi d0^2*I1^5 - 2305*r0^8*m^4*\phi d0^2*I1^4 - 1011*r0^4*m^2*\phi d0^2*I1^6 + 2414*r0^10*m^5*\phi d0^4*I1^3 - 210*r0^10*m^5*\phi d0^3*I1^3 + 589*r0^12*m^6*\phi d0^4*I1^2 + 2112*I1^7*\phi d0^4*r0^2*m + 340*m^3*r0^6*I1^5 + 96*m^r0^2*I1^7 + 280*m^4*r0^8*I1^4 + 5661*r0^8*m^4*\phi d0^4*I1^4 + 5764*r0^4*m^2*\phi d0^4*I1^6 + 7672*r0^6*m^3*\phi d0^4*I1^5 - 2181*r0^8*m^4*\phi d0^3*I1^4 - 12*r0^14*m^7*\phi d0^2*I1 + 4*r0^16*m^8*\phi d0^3 - 75*r0^12*m^6*\phi d0*I1^2 - 18*I1*\phi d0*r0^14*m^7 + \phi d0^2*r0^16*m^8 + 36*I1^2*r0^12*m^6 + 4*m^7*r0^14*I1 - m^8*r0^16*\phi d0 + 80*I1^7*\phi d0^2*m*r0^2 - 2720*I1^7*\phi d0^3*m*r0^2 + 136*I1^3*r0^10*m^5 + 128*\phi d0^2*I1^8 + 128*I1^8*\phi d0 - 512*I1^8*\phi d0^3 + 256*I1^8*\phi d0^4))^{(1/2)*I1^2}^{(1/3)*r0^4*m^2*\phi d0 + 4*(-8*r0^12*m^6*\phi d0^3 - 24*I1^5*m^r0^2 - 8*I1^3*m^3*r0^6 - 24*I1^4*m^2*r0^4 - 8*I1^6 + 288*I1^6*\phi d0^2 - 288*I1^6*\phi d0 - 348*I1^3*m^3*r0^6*\phi d0 + 1752*I1^3*r0^6*m^3*\phi d0^2 - 672*I1^2*r0^8*m^4*\phi d0^3 - 1756*I1^3*r0^6*m^3*\phi d0^3 - 804*I1^4*\phi d0*r0^4*m^2 + 492*I1^2*r0^8*m^4*\phi d0^2 - 60*I1^2*r0^8*m^4*\phi d0 + 1692*I1^5*\phi d0^2*r0^2*m - 804*I1^5*\phi d0*m*r0^2 + 2712*I1^4*r0^4*m^2*\phi d0^2 - 936*I1^5*\phi d0^3*r0^2*m - 2124*I1^4*r0^4*m^2*\phi d0^3 + 48*r0^10*m^5*\phi d0^2*I1 - 120*r0^10*m^5*\phi d0^3*I1 + 12*3^{(1/2)}*(-\phi d0*(\phi d0 - 1)*(4*\phi d0^4*m^8*r0^16 + 46*m^7*r0^14*I1*\phi d0^3 + 76*r0^14*m^7*\phi d0^4*I1 - 52*m^5*r0^10*I1^3*\phi d0 - 221*m^6*r0^12*I1^2*\phi d0^2 + 16*I1^8 + 600*I1^7*\phi d0*m*r0^2 + 244*m^2*r0^4*I1^6 - 1064*I1^3*\phi d0^2*r0^10*m^5 + 143*I1^2*\phi d0^3*r0^12*m^6 + 974*I1^5*\phi d0*r0^6*m^3 + 345*I1^4*\phi d0*r0^8*m^4 + 1107*I1^6*\phi d0*r0^4*m^2 - 5062*r0^6*m^3*\phi d0^3*I1^5 - 5400*r0^4*m^2*\phi d0^3*I1^6 - 2412*r0^6*m^3*\phi d0^2*I1^5 - 2305*r0^8*m^4*\phi d0^2*I1^4 - 1011*r0^4*m^2*\phi d0^2*I1^6 + 2414*r0^10*m^5*\phi d0^4*I1^3 - 210*r0^10*m^5*\phi d0^3*I1^3 + 589*r0^12*m^6*\phi d0^4*I1^2 + 2112*I1^7*\phi d0^4*r0^2*m + 340*m^3*r0^6*I1^5 + 96*m^r0^2*I1^7 + 280*m^4*r0^8*I1^4 + 5661*r0^8*m^4*\phi d0^4*I1^4 + 5764*r0^4*m^2*\phi d0^4*I1^6 + 7672*r0^6*m^3*\phi d0^4*I1^5 - 2181*r0^8*m^4*\phi d0^3*I1^4 - 12*r0^14*m^7*\phi d0^2*I1 + 4*r0^16*m^8*\phi d0^3 - 75*r0^12*m^6*\phi d0*I1^2 - 18*I1*\phi d0*r0^14*m^7 + \phi d0^2*r0^16*m^8 + 36*I1^2*r0^12*m^6 + 4*m^7*r0^14*I1 - m^8*r0^16*\phi d0 + 80*I1^7*\phi d0^2*m*r0^2 - 2720*I1^7*\phi d0^3*m*r0^2 + 136*I1^3*r0^10*m^5 + 128*\phi d0^2*I1^8 + 128*I1^8*\phi d0 - 512*I1^8*\phi d0^3 + 256*I1^8*\phi d0^4))^{(1/2)*I1^2}^{(1/3)*m^r0^2*I1 + 4*I1^2*(-8*r0^12*m^6*\phi d0^3 - 24*I1^5*m^r0^2 - 8*I1^3*m^3*r0^6 - 24*I1^4*m^2*r0^4 - 8*I1^6 + 288*I1^6*\phi d0^2 - 288*I1^6*\phi d0 - 348*I1^3*m^3*r0^6*\phi d0 + 1752*I1^3*r0^6*m^3*\phi d0^2 - 672*I1^2*r0^8*m^4*\phi d0^3 - 1756*I1^3*r0^6*m^3*\phi d0^3 - 804*I1^4*\phi d0*r0^4*m^2 + 492*I1^2*r0^8*m^4*\phi d0^2 - 60*I1^2*r0^8*m^4*\phi d0 + 1692*I1^5*\phi d0^2*r0^2*m - 804*I1^5*\phi d0*m*r0^2 + 2712*I1^4*r0^4*m^2*\phi d0^2 - 936*I1^5*\phi d0^3*r0^2*m - 2124*I1^4*r0^4*m^2*\phi d0^3 + 48*r0^10*m^5*\phi d0^2*I1 - 120*r0^10*m^5*\phi d0^3*I1 + 12*3^{(1/2)}*(-\phi d0*(\phi d0 - 1)*(4*\phi d0^4*m^8*r0^16 + 46*m^7*r0^14*I1*\phi d0^3 + 76*r0^14*m^7*\phi d0^4*I1 - 52*m^5*r0^10*I1^3*\phi d0 - 221*m^6*r0^12*I1^2*\phi d0^2 + 16*I1^8 + 600*I1^7*\phi d0*m*r0^2 +$

$244*m^2*r0^4*I1^6 - 1064*I1^3*fd0^2*r0^10*m^5 + 143*I1^2*fd0^3*r0^12*m^6 +$
 $974*I1^5*fd0^*r0^6*m^3 + 345*I1^4*fd0^*r0^8*m^4 + 1107*I1^6*fd0^*r0^4*m^2 -$
 $5062*r0^6*m^3*fd0^3*I1^5 - 5400*r0^4*m^2*fd0^3*I1^6 - 2412*r0^6*m^3*fd0^2*I1^5 -$
 $2305*r0^8*m^4*fd0^2*I1^4 - 1011*r0^4*m^2*fd0^2*I1^6 + 2414*r0^10*m^5*fd0^4*I1^3 -$
 $210*r0^10*m^5*fd0^3*I1^3 + 589*r0^12*m^6*fd0^4*I1^2 + 2112*I1^7*fd0^4*r0^2*m +$
 $340*m^3*r0^6*I1^5 + 96*m^*r0^2*I1^7 + 280*m^4*r0^8*I1^4 + 5661*r0^8*m^4*fd0^4*I1^4 +$
 $5764*r0^4*m^2*fd0^4*I1^6 + 7672*r0^6*m^3*fd0^4*I1^5 - 2181*r0^8*m^4*fd0^3*I1^4 -$
 $12*r0^14*m^7*fd0^2*I1 + 4*r0^16*m^8*fd0^3 - 75*r0^12*m^6*fd0^11^2 - 18*I1*fd0^*r0^14*m^7 +$
 $\phi d0^2*r0^16*m^8 + 36*I1^2*r0^12*m^6 + 4*m^7*r0^14*I1 - m^8*r0^16*fd0 + 80*I1^7*fd0^2*m^*r0^2 -$
 $- 2720*I1^7*fd0^3*m^*r0^2 + 136*I1^3*r0^10*m^5 + 128*fd0^2*I1^8 + 128*I1^8*fd0 -$
 $512*I1^8*fd0^3 + 256*I1^8*fd0^4))^(1/2)*I1^2)^(1/3)))^(1/2)$

$\lambda_9 = 1/6/I1*(-8*r0^12*m^6*fd0^3 - 24*I1^5*m^*r0^2 - 8*I1^3*m^3*r0^6 - 24*I1^4*m^2*r0^4 - 8*I1^6 +$
 $288*I1^6*fd0^2 - 288*I1^6*fd0 - 348*I1^3*m^3*r0^6*fd0 + 1752*I1^3*r0^6*m^3*fd0^2 -$
 $672*I1^2*r0^8*m^4*fd0^3 - 1756*I1^3*r0^6*m^3*fd0^3 - 804*I1^4*fd0^*r0^4*m^2 +$
 $492*I1^2*r0^8*m^4*fd0^2 - 60*I1^2*r0^8*m^4*fd0 + 1692*I1^5*fd0^2*r0^2*m -$
 $804*I1^5*fd0^*m^*r0^2 + 2712*I1^4*r0^4*m^2*fd0^2 - 936*I1^5*fd0^3*r0^2*m -$
 $2124*I1^4*r0^4*m^2*fd0^3 + 48*r0^10*m^5*fd0^2*I1 - 120*r0^10*m^5*fd0^3*I1 + 12*3^(1/2)*(-$
 $\phi d0*(\phi d0 - 1)*(4*fd0^4*m^8*r0^16 + 46*m^7*r0^14*I1*fd0^3 + 76*r0^14*m^7*fd0^4*I1 -$
 $52*m^5*r0^10*I1^3*fd0 - 221*m^6*r0^12*I1^2*fd0^2 + 16*I1^8 + 600*I1^7*fd0^*m^*r0^2 +$
 $244*m^2*r0^4*I1^6 - 1064*I1^3*fd0^2*r0^10*m^5 + 143*I1^2*fd0^3*r0^12*m^6 +$
 $974*I1^5*fd0^*r0^6*m^3 + 345*I1^4*fd0^*r0^8*m^4 + 1107*I1^6*fd0^*r0^4*m^2 -$
 $5062*r0^6*m^3*fd0^3*I1^5 - 5400*r0^4*m^2*fd0^3*I1^6 - 2412*r0^6*m^3*fd0^2*I1^5 -$
 $2305*r0^8*m^4*fd0^2*I1^4 - 1011*r0^4*m^2*fd0^2*I1^6 + 2414*r0^10*m^5*fd0^4*I1^3 -$
 $210*r0^10*m^5*fd0^3*I1^3 + 589*r0^12*m^6*fd0^4*I1^2 + 2112*I1^7*fd0^4*r0^2*m +$
 $340*m^3*r0^6*I1^5 + 96*m^*r0^2*I1^7 + 280*m^4*r0^8*I1^4 + 5661*r0^8*m^4*fd0^4*I1^4 +$
 $5764*r0^4*m^2*fd0^4*I1^6 + 7672*r0^6*m^3*fd0^4*I1^5 - 2181*r0^8*m^4*fd0^3*I1^4 -$
 $12*r0^14*m^7*fd0^2*I1 + 4*r0^16*m^8*fd0^3 - 75*r0^12*m^6*fd0^11^2 - 18*I1*fd0^*r0^14*m^7 +$
 $\phi d0^2*r0^16*m^8 + 36*I1^2*r0^12*m^6 + 4*m^7*r0^14*I1 - m^8*r0^16*fd0 + 80*I1^7*fd0^2*m^*r0^2 -$
 $- 2720*I1^7*fd0^3*m^*r0^2 + 136*I1^3*r0^10*m^5 + 128*fd0^2*I1^8 + 128*I1^8*fd0 -$
 $512*I1^8*fd0^3 + 256*I1^8*fd0^4))^(1/2)*I1^2)^(1/3)*3^(1/2)*((-8*r0^12*m^6*fd0^3 -$
 $24*I1^5*m^*r0^2 - 8*I1^3*m^3*r0^6 - 24*I1^4*m^2*r0^4 - 8*I1^6 + 288*I1^6*fd0^2 - 288*I1^6*fd0 -$
 $348*I1^3*m^3*r0^6*fd0 + 1752*I1^3*r0^6*m^3*fd0^2 - 672*I1^2*r0^8*m^4*fd0^3 -$
 $1756*I1^3*r0^6*m^3*fd0^3 - 804*I1^4*fd0^*r0^4*m^2 + 492*I1^2*r0^8*m^4*fd0^2 -$
 $60*I1^2*r0^8*m^4*fd0 + 1692*I1^5*fd0^2*r0^2*m - 804*I1^5*fd0^*m^*r0^2 +$
 $2712*I1^4*r0^4*m^2*fd0^2 - 936*I1^5*fd0^3*r0^2*m - 2124*I1^4*r0^4*m^2*fd0^3 +$
 $48*r0^10*m^5*fd0^2*I1 - 120*r0^10*m^5*fd0^3*I1 + 12*3^(1/2)*(-\phi d0*(\phi d0 -$
 $1)*(4*fd0^4*m^8*r0^16 + 46*m^7*r0^14*I1*fd0^3 + 76*r0^14*m^7*fd0^4*I1 -$
 $52*m^5*r0^10*I1^3*fd0 - 221*m^6*r0^12*I1^2*fd0^2 + 16*I1^8 + 600*I1^7*fd0^*m^*r0^2 +$
 $244*m^2*r0^4*I1^6 - 1064*I1^3*fd0^2*r0^10*m^5 + 143*I1^2*fd0^3*r0^12*m^6 +$
 $974*I1^5*fd0^*r0^6*m^3 + 345*I1^4*fd0^*r0^8*m^4 + 1107*I1^6*fd0^*r0^4*m^2 -$
 $5062*r0^6*m^3*fd0^3*I1^5 - 5400*r0^4*m^2*fd0^3*I1^6 - 2412*r0^6*m^3*fd0^2*I1^5 -$
 $2305*r0^8*m^4*fd0^2*I1^4 - 1011*r0^4*m^2*fd0^2*I1^6 + 2414*r0^10*m^5*fd0^4*I1^3 -$
 $210*r0^10*m^5*fd0^3*I1^3 + 589*r0^12*m^6*fd0^4*I1^2 + 2112*I1^7*fd0^4*r0^2*m +$
 $340*m^3*r0^6*I1^5 + 96*m^*r0^2*I1^7 + 280*m^4*r0^8*I1^4 + 5661*r0^8*m^4*fd0^4*I1^4 +$
 $5764*r0^4*m^2*fd0^4*I1^6 + 7672*r0^6*m^3*fd0^4*I1^5 - 2181*r0^8*m^4*fd0^3*I1^4 -$
 $12*r0^14*m^7*fd0^2*I1 + 4*r0^16*m^8*fd0^3 - 75*r0^12*m^6*fd0^11^2 - 18*I1*fd0^*r0^14*m^7 +$

$$\begin{aligned}
& \phi d0^2 * r0^16 * m^8 + 36 * I1^2 * r0^12 * m^6 + 4 * m^7 * r0^14 * I1 - m^8 * r0^16 * \phi d0 + 80 * I1^7 * \phi d0^2 * m^* r0^2 \\
& - 2720 * I1^7 * \phi d0^3 * m^* r0^2 + 136 * I1^3 * r0^10 * m^5 + 128 * \phi d0^2 * I1^8 + 128 * I1^8 * \phi d0 - \\
& 512 * I1^8 * \phi d0^3 + 256 * I1^8 * \phi d0^4))^{(1/2)} * I1^2)^{(1/3)} * \phi d0 * (i^3 * (1/2) * (-8 * r0^12 * m^6 * \phi d0^3 - \\
& 24 * I1^5 * m^* r0^2 - 8 * I1^3 * m^3 * r0^6 - 24 * I1^4 * m^2 * r0^4 - 8 * I1^6 + 288 * I1^6 * \phi d0^2 - 288 * I1^6 * \phi d0 - \\
& 348 * I1^3 * m^3 * r0^6 * \phi d0 + 1752 * I1^3 * r0^6 * m^3 * 3 * \phi d0^2 - 672 * I1^2 * r0^8 * m^4 * \phi d0^3 - \\
& 1756 * I1^3 * r0^6 * m^3 * \phi d0^3 - 804 * I1^4 * \phi d0 * r0^4 * m^2 + 492 * I1^2 * r0^8 * m^4 * \phi d0^2 - \\
& 60 * I1^2 * r0^8 * m^4 * \phi d0 + 1692 * I1^5 * \phi d0^2 * r0^2 * m - 804 * I1^5 * \phi d0 * m^* r0^2 + \\
& 2712 * I1^4 * r0^4 * m^2 * \phi d0^2 - 936 * I1^5 * \phi d0^3 * r0^2 * m - 2124 * I1^4 * r0^4 * m^2 * \phi d0^3 + \\
& 48 * r0^10 * m^5 * \phi d0^2 * I1 - 120 * r0^10 * m^5 * \phi d0^3 * I1 + 12 * 3^{(1/2)} * (-\phi d0 * (\phi d0 - \\
& 1) * (4 * \phi d0^4 * m^8 * r0^16 + 46 * m^7 * r0^14 * I1 * \phi d0^3 + 76 * r0^14 * m^7 * \phi d0^4 * I1 - \\
& 52 * m^5 * r0^10 * I1^3 * \phi d0 - 221 * m^6 * r0^12 * I1^2 * \phi d0^2 + 16 * I1^8 + 600 * I1^7 * \phi d0 * m^* r0^2 + \\
& 244 * m^2 * r0^4 * I1^6 - 1064 * I1^3 * \phi d0^2 * r0^10 * m^5 + 143 * I1^2 * \phi d0^3 * r0^12 * m^6 + \\
& 974 * I1^5 * \phi d0 * r0^6 * m^3 + 345 * I1^4 * \phi d0 * r0^8 * m^4 + 1107 * I1^6 * \phi d0 * r0^4 * m^2 - \\
& 5062 * r0^6 * m^3 * \phi d0^3 * I1^5 - 5400 * r0^4 * m^2 * \phi d0^3 * I1^6 - 2412 * r0^6 * m^3 * \phi d0^2 * I1^5 - \\
& 2305 * r0^8 * m^4 * \phi d0^2 * I1^4 - 1011 * r0^4 * m^2 * \phi d0^2 * I1^6 + 2414 * r0^10 * m^5 * \phi d0^4 * I1^3 - \\
& 210 * r0^10 * m^5 * \phi d0^3 * I1^3 + 589 * r0^12 * m^6 * \phi d0^4 * I1^2 + 2112 * I1^7 * \phi d0^4 * r0^2 * m + \\
& 340 * m^3 * r0^6 * I1^5 + 96 * m^* r0^2 * I1^7 + 280 * m^4 * r0^8 * I1^4 + 5661 * r0^8 * m^4 * \phi d0^4 * I1^4 + \\
& 5764 * r0^4 * m^2 * \phi d0^4 * I1^6 + 7672 * r0^6 * m^3 * \phi d0^4 * I1^5 - 2181 * r0^8 * m^4 * \phi d0^3 * I1^4 - \\
& 12 * r0^14 * m^7 * \phi d0^2 * I1 + 4 * r0^16 * m^8 * \phi d0^3 - 75 * r0^12 * m^6 * \phi d0 * I1^2 - 18 * I1 * \phi d0 * r0^14 * m^7 + \\
& \phi d0^2 * r0^16 * m^8 + 36 * I1^2 * r0^12 * m^6 + 4 * m^7 * r0^14 * I1 - m^8 * r0^16 * \phi d0 + 80 * I1^7 * \phi d0^2 * m^* r0^2 \\
& - 2720 * I1^7 * \phi d0^3 * m^* r0^2 + 136 * I1^3 * r0^10 * m^5 + 128 * \phi d0^2 * I1^8 + 128 * I1^8 * \phi d0 - \\
& 512 * I1^8 * \phi d0^3 + 256 * I1^8 * \phi d0^4))^{(1/2)} * I1^2)^{(2/3)} - 4 * i^3 * (1/2) * r0^8 * m^4 * \phi d0^2 - \\
& 40 * r0^6 * m^3 * \phi d0^2 * I1 + 16 * m^3 * r0^6 * I1 * \phi d0 + 116 * I1^3 * \phi d0 * m^* r0^2 - 132 * I1^3 * \phi d0^2 * r0^2 * m - \\
& 8 * m^* r0^2 * I1^3 - 4 * m^2 * r0^4 * I1^2 - 4 * r0^8 * m^4 * \phi d0^2 + 84 * I1^2 * \phi d0 * r0^4 * m^2 + 48 * I1^4 * \phi d0 - 4 * (\\
& - 8 * r0^12 * m^6 * \phi d0^3 - 24 * I1^5 * m^* r0^2 - 8 * I1^3 * m^3 * r0^6 - 24 * I1^4 * m^2 * r0^4 - 8 * I1^6 + \\
& 288 * I1^6 * \phi d0^2 - 288 * I1^6 * \phi d0 - 348 * I1^3 * m^3 * r0^6 * \phi d0 + 1752 * I1^3 * r0^6 * m^3 * \phi d0^2 - \\
& 672 * I1^2 * r0^8 * m^4 * \phi d0^3 - 1756 * I1^3 * r0^6 * m^3 * \phi d0^3 - 804 * I1^4 * \phi d0 * r0^4 * m^2 + \\
& 492 * I1^2 * r0^8 * m^4 * \phi d0^2 - 60 * I1^2 * r0^8 * m^4 * \phi d0 + 1692 * I1^5 * \phi d0^2 * r0^2 * m - \\
& 804 * I1^5 * \phi d0 * m^* r0^2 + 2712 * I1^4 * r0^4 * m^2 * \phi d0^2 - 936 * I1^5 * \phi d0^3 * r0^2 * m - \\
& 2124 * I1^4 * r0^4 * m^2 * \phi d0^3 + 48 * r0^10 * m^5 * \phi d0^2 * I1 - 120 * r0^10 * m^5 * \phi d0^3 * I1 + 12 * 3^{(1/2)} * (- \\
& \phi d0 * (\phi d0 - 1) * (4 * \phi d0^4 * m^8 * r0^16 + 46 * m^7 * r0^14 * I1 * \phi d0^3 + 76 * r0^14 * m^7 * \phi d0^4 * I1 - \\
& 52 * m^5 * r0^10 * I1^3 * \phi d0 - 221 * m^6 * r0^12 * I1^2 * \phi d0^2 + 16 * I1^8 + 600 * I1^7 * \phi d0 * m^* r0^2 + \\
& 244 * m^2 * r0^4 * I1^6 - 1064 * I1^3 * \phi d0^2 * r0^10 * m^5 + 143 * I1^2 * \phi d0^3 * r0^12 * m^6 + \\
& 974 * I1^5 * \phi d0 * r0^6 * m^3 + 345 * I1^4 * \phi d0 * r0^8 * m^4 + 1107 * I1^6 * \phi d0 * r0^4 * m^2 - \\
& 5062 * r0^6 * m^3 * \phi d0^3 * I1^5 - 5400 * r0^4 * m^2 * \phi d0^3 * I1^6 - 2412 * r0^6 * m^3 * \phi d0^2 * I1^5 - \\
& 2305 * r0^8 * m^4 * \phi d0^2 * I1^4 - 1011 * r0^4 * m^2 * \phi d0^2 * I1^6 + 2414 * r0^10 * m^5 * \phi d0^4 * I1^3 - \\
& 210 * r0^10 * m^5 * \phi d0^3 * I1^3 + 589 * r0^12 * m^6 * \phi d0^4 * I1^2 + 2112 * I1^7 * \phi d0^4 * r0^2 * m + \\
& 340 * m^3 * r0^6 * I1^5 + 96 * m^* r0^2 * I1^7 + 280 * m^4 * r0^8 * I1^4 + 5661 * r0^8 * m^4 * \phi d0^4 * I1^4 + \\
& 5764 * r0^4 * m^2 * \phi d0^4 * I1^6 + 7672 * r0^6 * m^3 * \phi d0^4 * I1^5 - 2181 * r0^8 * m^4 * \phi d0^3 * I1^4 - \\
& 12 * r0^14 * m^7 * \phi d0^2 * I1 + 4 * r0^16 * m^8 * \phi d0^3 - 75 * r0^12 * m^6 * \phi d0 * I1^2 - 18 * I1 * \phi d0 * r0^14 * m^7 + \\
& \phi d0^2 * r0^16 * m^8 + 36 * I1^2 * r0^12 * m^6 + 4 * m^7 * r0^14 * I1 - m^8 * r0^16 * \phi d0 + 80 * I1^7 * \phi d0^2 * m^* r0^2 \\
& - 2720 * I1^7 * \phi d0^3 * m^* r0^2 + 136 * I1^3 * r0^10 * m^5 + 128 * \phi d0^2 * I1^8 + 128 * I1^8 * \phi d0 - \\
& 512 * I1^8 * \phi d0^3 + 256 * I1^8 * \phi d0^4))^{(1/2)} * I1^2)^{(1/3)} * r0^4 * m^2 * \phi d0 + 8 * (-8 * r0^12 * m^6 * \phi d0^3 - \\
& 24 * I1^5 * m^* r0^2 - 8 * I1^3 * m^3 * r0^6 - 24 * I1^4 * m^2 * r0^4 - 8 * I1^6 + 288 * I1^6 * \phi d0^2 - 288 * I1^6 * \phi d0 - \\
& 348 * I1^3 * m^3 * r0^6 * \phi d0 + 1752 * I1^3 * r0^6 * m^3 * 3 * \phi d0^2 - 672 * I1^2 * r0^8 * m^4 * \phi d0^3 - \\
& 1756 * I1^3 * r0^6 * m^3 * \phi d0^3 - 804 * I1^4 * \phi d0 * r0^4 * m^2 + 492 * I1^2 * r0^8 * m^4 * \phi d0^2 - \\
& 60 * I1^2 * r0^8 * m^4 * \phi d0 + 1692 * I1^5 * \phi d0^2 * r0^2 * m - 804 * I1^5 * \phi d0 * m^* r0^2 +
\end{aligned}$$

$2712*I1^4*r0^4*m^2*phi0^2 - 936*I1^5*phi0^3*r0^2*m - 2124*I1^4*r0^4*m^2*phi0^3 +$
 $48*r0^10*m^5*phi0^2*I1 - 120*r0^10*m^5*phi0^3*I1 + 12*3^(1/2)*(-phi0*(phi0 -$
 $1)*(4*phi0^4*m^8*r0^16 + 46*m^7*r0^14*I1*phi0^3 + 76*r0^14*m^7*phi0^4*I1 -$
 $52*m^5*r0^10*I1^3*phi0 - 221*m^6*r0^12*I1^2*phi0^2 + 16*I1^8 + 600*I1^7*phi0*m*r0^2 +$
 $244*m^2*r0^4*I1^6 - 1064*I1^3*phi0^2*r0^10*m^5 + 143*I1^2*phi0^3*r0^12*m^6 +$
 $974*I1^5*phi0*r0^6*m^3 + 345*I1^4*phi0*r0^8*m^4 + 1107*I1^6*phi0*r0^4*m^2 -$
 $5062*r0^6*m^3*phi0^3*I1^5 - 5400*r0^4*m^2*phi0^3*I1^6 - 2412*r0^6*m^3*phi0^2*I1^5 -$
 $2305*r0^8*m^4*phi0^2*I1^4 - 1011*r0^4*m^2*phi0^2*I1^6 + 2414*r0^10*m^5*phi0^4*I1^3 -$
 $210*r0^10*m^5*phi0^3*I1^3 + 589*r0^12*m^6*phi0^4*I1^2 + 2112*I1^7*phi0^4*r0^2*m +$
 $340*m^3*r0^6*I1^5 + 96*m^2*r0^2*I1^7 + 280*m^4*r0^8*I1^4 + 5661*r0^8*m^4*phi0^4*I1^4 +$
 $5764*r0^4*m^2*phi0^4*I1^6 + 7672*r0^6*m^3*phi0^4*I1^5 - 2181*r0^8*m^4*phi0^3*I1^4 -$
 $12*r0^14*m^7*phi0^2*I1 + 4*r0^16*m^8*phi0^3 - 75*r0^12*m^6*phi0^2*I1^2 - 18*I1*phi0*r0^14*m^7 +$
 $phi0^2*r0^16*m^8 + 36*I1^2*r0^12*m^6 + 4*m^7*r0^14*I1 - m^8*r0^16*phi0 + 80*I1^7*phi0^2*m*r0^2 -$
 $- 2720*I1^7*phi0^3*m*r0^2 + 136*I1^3*r0^10*m^5 + 128*phi0^2*I1^8 + 128*I1^8*phi0 -$
 $512*I1^8*phi0^3 + 256*I1^8*phi0^4))^(1/2)*I1^2)*(1/3)*m^r0^2*I1 - 4*I1^4 - 24*(-8*r0^12*m^6*phi0^3 -$
 $- 24*I1^5*m*r0^2 - 8*I1^3*m^3*r0^6 - 24*I1^4*m^2*r0^4 - 8*I1^6 + 288*I1^6*phi0^2 - 288*I1^6*phi0 -$
 $348*I1^3*m^3*r0^6*phi0 + 1752*I1^3*r0^6*m^3*phi0^2 - 672*I1^2*r0^8*m^4*phi0^3 -$
 $1756*I1^3*r0^6*m^3*phi0^3 - 804*I1^4*phi0*r0^4*m^2 + 492*I1^2*r0^8*m^4*phi0^2 -$
 $60*I1^2*r0^8*m^4*phi0 + 1692*I1^5*phi0^2*r0^2*m - 804*I1^5*phi0*m*r0^2 +$
 $2712*I1^4*r0^4*m^2*phi0^2 - 936*I1^5*phi0^3*r0^2*m - 2124*I1^4*r0^4*m^2*phi0^3 +$
 $48*r0^10*m^5*phi0^2*I1 - 120*r0^10*m^5*phi0^3*I1 + 12*3^(1/2)*(-phi0*(phi0 -$
 $1)*(4*phi0^4*m^8*r0^16 + 46*m^7*r0^14*I1*phi0^3 + 76*r0^14*m^7*phi0^4*I1 -$
 $52*m^5*r0^10*I1^3*phi0 - 221*m^6*r0^12*I1^2*phi0^2 + 16*I1^8 + 600*I1^7*phi0*m*r0^2 +$
 $244*m^2*r0^4*I1^6 - 1064*I1^3*phi0^2*r0^10*m^5 + 143*I1^2*phi0^3*r0^12*m^6 +$
 $974*I1^5*phi0*r0^6*m^3 + 345*I1^4*phi0*r0^8*m^4 + 1107*I1^6*phi0*r0^4*m^2 -$
 $5062*r0^6*m^3*phi0^3*I1^5 - 5400*r0^4*m^2*phi0^3*I1^6 - 2412*r0^6*m^3*phi0^2*I1^5 -$
 $2305*r0^8*m^4*phi0^2*I1^4 - 1011*r0^4*m^2*phi0^2*I1^6 + 2414*r0^10*m^5*phi0^4*I1^3 -$
 $210*r0^10*m^5*phi0^3*I1^3 + 589*r0^12*m^6*phi0^4*I1^2 + 2112*I1^7*phi0^4*r0^2*m +$
 $340*m^3*r0^6*I1^5 + 96*m^2*r0^2*I1^7 + 280*m^4*r0^8*I1^4 + 5661*r0^8*m^4*phi0^4*I1^4 +$
 $5764*r0^4*m^2*phi0^4*I1^6 + 7672*r0^6*m^3*phi0^4*I1^5 - 2181*r0^8*m^4*phi0^3*I1^4 -$
 $12*r0^14*m^7*phi0^2*I1 + 4*r0^16*m^8*phi0^3 - 75*r0^12*m^6*phi0^2*I1^2 - 18*I1*phi0*r0^14*m^7 +$
 $phi0^2*r0^16*m^8 + 36*I1^2*r0^12*m^6 + 4*m^7*r0^14*I1 - m^8*r0^16*phi0 + 80*I1^7*phi0^2*m*r0^2 -$
 $- 2720*I1^7*phi0^3*m*r0^2 + 136*I1^3*r0^10*m^5 + 128*phi0^2*I1^8 + 128*I1^8*phi0 -$
 $512*I1^8*phi0^3 + 256*I1^8*phi0^4))^(1/2)*I1^2)*(1/3)*I1^2*phi0 - 48*I1^4*phi0^2 - 4*I1^3*(1/2)*I1^4 +$
 $8*I1^2*(-8*r0^12*m^6*phi0^3 - 24*I1^5*m*r0^2 - 8*I1^3*m^3*r0^6 - 24*I1^4*m^2*r0^4 - 8*I1^6 +$
 $288*I1^6*phi0^2 - 288*I1^6*phi0 - 348*I1^3*m^3*r0^6*phi0 + 1752*I1^3*r0^6*m^3*phi0^2 -$
 $672*I1^2*r0^8*m^4*phi0^3 - 1756*I1^3*r0^6*m^3*phi0^3 - 804*I1^4*phi0*r0^4*m^2 +$
 $492*I1^2*r0^8*m^4*phi0^2 - 60*I1^2*r0^8*m^4*phi0 + 1692*I1^5*phi0^2*r0^2*m -$
 $804*I1^5*phi0*m*r0^2 + 2712*I1^4*r0^4*m^2*phi0^2 - 936*I1^5*phi0^3*r0^2*m -$
 $2124*I1^4*r0^4*m^2*phi0^3 + 48*r0^10*m^5*phi0^2*I1 - 120*r0^10*m^5*phi0^3*I1 + 12*3^(1/2)*(-$
 $phi0*(phi0 - 1)*(4*phi0^4*m^8*r0^16 + 46*m^7*r0^14*I1*phi0^3 + 76*r0^14*m^7*phi0^4*I1 -$
 $52*m^5*r0^10*I1^3*phi0 - 221*m^6*r0^12*I1^2*phi0^2 + 16*I1^8 + 600*I1^7*phi0*m*r0^2 +$
 $244*m^2*r0^4*I1^6 - 1064*I1^3*phi0^2*r0^10*m^5 + 143*I1^2*phi0^3*r0^12*m^6 +$
 $974*I1^5*phi0*r0^6*m^3 + 345*I1^4*phi0*r0^8*m^4 + 1107*I1^6*phi0*r0^4*m^2 -$
 $5062*r0^6*m^3*phi0^3*I1^5 - 5400*r0^4*m^2*phi0^3*I1^6 - 2412*r0^6*m^3*phi0^2*I1^5 -$
 $2305*r0^8*m^4*phi0^2*I1^4 - 1011*r0^4*m^2*phi0^2*I1^6 + 2414*r0^10*m^5*phi0^4*I1^3 -$
 $210*r0^10*m^5*phi0^3*I1^3 + 589*r0^12*m^6*phi0^4*I1^2 + 2112*I1^7*phi0^4*r0^2*m +$

$$\begin{aligned}
& 340*m^3*r0^6*I1^5 + 96*m*r0^2*I1^7 + 280*m^4*r0^8*I1^4 + 5661*r0^8*m^4*phi0^4*I1^4 + \\
& 5764*r0^4*m^2*phi0^4*I1^6 + 7672*r0^6*m^3*phi0^4*I1^5 - 2181*r0^8*m^4*phi0^3*I1^4 - \\
& 12*r0^14*m^7*phi0^2*I1 + 4*r0^16*m^8*phi0^3 - 75*r0^12*m^6*phi0*I1^2 - 18*I1*phi0*r0^14*m^7 + \\
& phi0^2*r0^16*m^8 + 36*I1^2*r0^12*m^6 + 4*m^7*r0^14*I1 - m^8*r0^16*phi0 + 80*I1^7*phi0^2*m*r0^2 \\
& - 2720*I1^7*phi0^3*m*r0^2 + 136*I1^3*r0^10*m^5 + 128*phi0^2*I1^8 + 128*I1^8*phi0 - \\
& 512*I1^8*phi0^3 + 256*I1^8*phi0^4))^(1/2)*I1^2)^(1/3) - 20*(-8*r0^12*m^6*phi0^3 - 24*I1^5*m*r0^2 - \\
& 8*I1^3*m^3*r0^6 - 24*I1^4*m^2*r0^4 - 8*I1^6 + 288*I1^6*phi0^2 - 288*I1^6*phi0 - \\
& 348*I1^3*m^3*r0^6*phi0 + 1752*I1^3*r0^6*m^3*phi0^2 - 672*I1^2*r0^8*m^4*phi0^3 - \\
& 1756*I1^3*r0^6*m^3*phi0^3 - 804*I1^4*phi0*r0^4*m^2 + 492*I1^2*r0^8*m^4*phi0^2 - \\
& 60*I1^2*r0^8*m^4*phi0 + 1692*I1^5*phi0^2*r0^2*m - 804*I1^5*phi0*m*r0^2 + \\
& 2712*I1^4*r0^4*m^2*phi0^2 - 936*I1^5*phi0^3*r0^2*m - 2124*I1^4*r0^4*m^2*phi0^3 + \\
& 48*r0^10*m^5*phi0^2*I1 - 120*r0^10*m^5*phi0^3*I1 + 12*3^(1/2)*(-phi0*(phi0 - \\
& 1)*(4*phi0^4*m^8*r0^16 + 46*m^7*r0^14*I1*phi0^3 + 76*r0^14*m^7*phi0^4*I1 - \\
& 52*m^5*r0^10*I1^3*phi0 - 221*m^6*r0^12*I1^2*phi0^2 + 16*I1^8 + 600*I1^7*phi0*m*r0^2 + \\
& 244*m^2*r0^4*I1^6 - 1064*I1^3*phi0^2*r0^10*m^5 + 143*I1^2*phi0^3*r0^12*m^6 + \\
& 974*I1^5*phi0*r0^6*m^3 + 345*I1^4*phi0*r0^8*m^4 + 1107*I1^6*phi0*r0^4*m^2 - \\
& 5062*r0^6*m^3*phi0^3*I1^5 - 5400*r0^4*m^2*phi0^3*I1^6 - 2412*r0^6*m^3*phi0^2*I1^5 - \\
& 2305*r0^8*m^4*phi0^2*I1^4 - 1011*r0^4*m^2*phi0^2*I1^6 + 2414*r0^10*m^5*phi0^4*I1^3 - \\
& 210*r0^10*m^5*phi0^3*I1^3 + 589*r0^12*m^6*phi0^4*I1^2 + 2112*I1^7*phi0^4*r0^2*m + \\
& 340*m^3*r0^6*I1^5 + 96*m*r0^2*I1^7 + 280*m^4*r0^8*I1^4 + 5661*r0^8*m^4*phi0^4*I1^4 + \\
& 5764*r0^4*m^2*phi0^4*I1^6 + 7672*r0^6*m^3*phi0^4*I1^5 - 2181*r0^8*m^4*phi0^3*I1^4 - \\
& 12*r0^14*m^7*phi0^2*I1 + 4*r0^16*m^8*phi0^3 - 75*r0^12*m^6*phi0*I1^2 - 18*I1*phi0*r0^14*m^7 + \\
& phi0^2*r0^16*m^8 + 36*I1^2*r0^12*m^6 + 4*m^7*r0^14*I1 - m^8*r0^16*phi0 + 80*I1^7*phi0^2*m*r0^2 \\
& - 2720*I1^7*phi0^3*m*r0^2 + 136*I1^3*r0^10*m^5 + 128*phi0^2*I1^8 + 128*I1^8*phi0 - \\
& 512*I1^8*phi0^3 + 256*I1^8*phi0^4))^(1/2)*I1^2)^(1/3)*r0^2*m*I1*phi0 - 40*i^3^(1/ \\
& 2)*r0^6*m^3*phi0^2*I1 + 48*i^3^(1/2)*I1^4*phi0 - 48*i^3^(1/2)*I1^4*phi0^2 - (-8*r0^12*m^6*phi0^3 - \\
& 24*I1^5*m*r0^2 - 8*I1^3*m^3*r0^6 - 24*I1^4*m^2*r0^4 - 8*I1^6 + 288*I1^6*phi0^2 - 288*I1^6*phi0 - \\
& 348*I1^3*m^3*r0^6*phi0 + 1752*I1^3*r0^6*m^3*phi0^2 - 672*I1^2*r0^8*m^4*phi0^3 - \\
& 1756*I1^3*r0^6*m^3*phi0^3 - 804*I1^4*phi0*r0^4*m^2 + 492*I1^2*r0^8*m^4*phi0^2 - \\
& 60*I1^2*r0^8*m^4*phi0 + 1692*I1^5*phi0^2*r0^2*m - 804*I1^5*phi0*m*r0^2 + \\
& 2712*I1^4*r0^4*m^2*phi0^2 - 936*I1^5*phi0^3*r0^2*m - 2124*I1^4*r0^4*m^2*phi0^3 + \\
& 48*r0^10*m^5*phi0^2*I1 - 120*r0^10*m^5*phi0^3*I1 + 12*3^(1/2)*(-phi0*(phi0 - \\
& 1)*(4*phi0^4*m^8*r0^16 + 46*m^7*r0^14*I1*phi0^3 + 76*r0^14*m^7*phi0^4*I1 - \\
& 52*m^5*r0^10*I1^3*phi0 - 221*m^6*r0^12*I1^2*phi0^2 + 16*I1^8 + 600*I1^7*phi0*m*r0^2 + \\
& 244*m^2*r0^4*I1^6 - 1064*I1^3*phi0^2*r0^10*m^5 + 143*I1^2*phi0^3*r0^12*m^6 + \\
& 974*I1^5*phi0*r0^6*m^3 + 345*I1^4*phi0*r0^8*m^4 + 1107*I1^6*phi0*r0^4*m^2 - \\
& 5062*r0^6*m^3*phi0^3*I1^5 - 5400*r0^4*m^2*phi0^3*I1^6 - 2412*r0^6*m^3*phi0^2*I1^5 - \\
& 2305*r0^8*m^4*phi0^2*I1^4 - 1011*r0^4*m^2*phi0^2*I1^6 + 2414*r0^10*m^5*phi0^4*I1^3 - \\
& 210*r0^10*m^5*phi0^3*I1^3 + 589*r0^12*m^6*phi0^4*I1^2 + 2112*I1^7*phi0^4*r0^2*m + \\
& 340*m^3*r0^6*I1^5 + 96*m*r0^2*I1^7 + 280*m^4*r0^8*I1^4 + 5661*r0^8*m^4*phi0^4*I1^4 + \\
& 5764*r0^4*m^2*phi0^4*I1^6 + 7672*r0^6*m^3*phi0^4*I1^5 - 2181*r0^8*m^4*phi0^3*I1^4 - \\
& 12*r0^14*m^7*phi0^2*I1 + 4*r0^16*m^8*phi0^3 - 75*r0^12*m^6*phi0*I1^2 - 18*I1*phi0*r0^14*m^7 + \\
& phi0^2*r0^16*m^8 + 36*I1^2*r0^12*m^6 + 4*m^7*r0^14*I1 - m^8*r0^16*phi0 + 80*I1^7*phi0^2*m*r0^2 \\
& - 2720*I1^7*phi0^3*m*r0^2 + 136*I1^3*r0^10*m^5 + 128*phi0^2*I1^8 + 128*I1^8*phi0 - \\
& 512*I1^8*phi0^3 + 256*I1^8*phi0^4))^(1/2)*I1^2)^(2/3) + 16*i^3^(1/2)*r0^6*m^3*phi0*I1 - 4*i^3^(1/ \\
& 2)*I1^2*r0^4*m^2 - 8*i^3^(1/2)*I1^3*m*r0^2 - 124*i^3^(1/2)*r0^4*m^2*phi0^2*I1^2 - 132*i^3^(1/$$

$$2)*I1^3*fd0^2*r0^2*m + 84*i^3*(1/2)*I1^2*fd0*r0^4*m^2 + 116*i^3*(1/2)*I1^3*fd0*m*r0^2 - 124*r0^4*m^2*fd0^2*I1^2))^{(1/2)}$$

$$\begin{aligned}
\lambda_{10} = & -1/6/I1/(-8*r0^12*m^6*fd0^3 - 24*I1^5*m^r0^2 - 8*I1^3*m^3*r0^6 - 24*I1^4*m^2*r0^4 - \\
& 8*I1^6 + 288*I1^6*fd0^2 - 288*I1^6*fd0 - 348*I1^3*m^3*r0^6*fd0 + 1752*I1^3*r0^6*m^3*fd0^2 - \\
& 672*I1^2*r0^8*m^4*fd0^3 - 1756*I1^3*r0^6*m^3*fd0^3 - 804*I1^4*fd0^2*r0^4*m^2 + \\
& 492*I1^2*r0^8*m^4*fd0^2 - 60*I1^2*r0^8*m^4*fd0 + 1692*I1^5*fd0^2*r0^2*m - \\
& 804*I1^5*fd0^2*m^r0^2 + 2712*I1^4*r0^4*m^2*fd0^2 - 936*I1^5*fd0^3*r0^2*m - \\
& 2124*I1^4*r0^4*m^2*fd0^3 + 48*r0^10*m^5*fd0^2*I1 - 120*r0^10*m^5*fd0^3*I1 + 12*3^(1/2)*(- \\
& fd0*(fd0 - 1)*(4*fd0^4*m^8*r0^16 + 46*m^7*r0^14*I1*fd0^3 + 76*r0^14*m^7*fd0^4*I1 - \\
& 52*m^5*r0^10*I1^3*fd0 - 221*m^6*r0^12*I1^2*fd0^2 + 16*I1^8 + 600*I1^7*fd0^2*m^r0^2 + \\
& 244*m^2*r0^4*I1^6 - 1064*I1^3*fd0^2*r0^10*m^5 + 143*I1^2*fd0^3*r0^12*m^6 + \\
& 974*I1^5*fd0^2*r0^6*m^3 + 345*I1^4*fd0^2*r0^8*m^4 + 1107*I1^6*fd0^2*r0^4*m^2 - \\
& 5062*r0^6*m^3*fd0^3*I1^5 - 5400*r0^4*m^2*fd0^3*I1^6 - 2412*r0^6*m^3*fd0^2*I1^5 - \\
& 2305*r0^8*m^4*fd0^2*I1^4 - 1011*r0^4*m^2*fd0^2*I1^6 + 2414*r0^10*m^5*fd0^4*I1^3 - \\
& 210*r0^10*m^5*fd0^3*I1^3 + 589*r0^12*m^6*fd0^4*I1^2 + 2112*I1^7*fd0^4*r0^2*m + \\
& 340*m^3*r0^6*I1^5 + 96*m^r0^2*I1^7 + 280*m^4*r0^8*I1^4 + 5661*r0^8*m^4*fd0^4*I1^4 + \\
& 5764*r0^4*m^2*fd0^4*I1^6 + 7672*r0^6*m^3*fd0^4*I1^5 - 2181*r0^8*m^4*fd0^3*I1^4 - \\
& 12*r0^14*m^7*fd0^2*I1 + 4*r0^16*m^8*fd0^3 - 75*r0^12*m^6*fd0^2*I1^2 - 18*I1*fd0^2*r0^14*m^7 + \\
& fd0^2*r0^16*m^8 + 36*I1^2*r0^12*m^6 + 4*m^7*r0^14*I1 - m^8*r0^16*fd0 + 80*I1^7*fd0^2*m^r0^2 - \\
& 2720*I1^7*fd0^3*m^r0^2 + 136*I1^3*r0^10*m^5 + 128*fd0^2*I1^8 + 128*I1^8*fd0 - \\
& 512*I1^8*fd0^3 + 256*I1^8*fd0^4))^(1/2)*I1^2)^(1/3)*3^(1/2)*((-8*r0^12*m^6*fd0^3 - \\
& 24*I1^5*m^r0^2 - 8*I1^3*m^3*r0^6 - 24*I1^4*m^2*r0^4 - 8*I1^6 + 288*I1^6*fd0^2 - 288*I1^6*fd0 - \\
& 348*I1^3*m^3*r0^6*fd0 + 1752*I1^3*r0^6*m^3*fd0^2 - 672*I1^2*r0^8*m^4*fd0^3 - \\
& 1756*I1^3*r0^6*m^3*fd0^3 - 804*I1^4*fd0^2*r0^4*m^2 + 492*I1^2*r0^8*m^4*fd0^2 - \\
& 60*I1^2*r0^8*m^4*fd0 + 1692*I1^5*fd0^2*r0^2*m - 804*I1^5*fd0^2*m^r0^2 + \\
& 2712*I1^4*r0^4*m^2*fd0^2 - 936*I1^5*fd0^3*r0^2*m - 2124*I1^4*r0^4*m^2*fd0^3 + \\
& 48*r0^10*m^5*fd0^2*I1 - 120*r0^10*m^5*fd0^3*I1 + 12*3^(1/2)*(-fd0*(fd0 -
\end{aligned}$$

$$\begin{aligned}
 & 1)*(4*\phi d0^4*m^8*r0^16 + 46*m^7*r0^14*I1*\phi d0^3 + 76*r0^14*m^7*\phi d0^4*I1 - \\
 & 52*m^5*r0^10*I1^3*\phi d0 - 221*m^6*r0^12*I1^2*\phi d0^2 + 16*I1^8 + 600*I1^7*\phi d0*m*r0^2 + \\
 & 244*m^2*r0^4*I1^6 - 1064*I1^3*\phi d0^2*r0^10*m^5 + 143*I1^2*\phi d0^3*r0^12*m^6 + \\
 & 974*I1^5*\phi d0*r0^6*m^3 + 345*I1^4*\phi d0*r0^8*m^4 + 1107*I1^6*\phi d0*r0^4*m^2 - \\
 & 5062*r0^6*m^3*\phi d0^3*I1^5 - 5400*r0^4*m^2*\phi d0^3*I1^6 - 2412*r0^6*m^3*\phi d0^2*I1^5 - \\
 & 2305*r0^8*m^4*\phi d0^2*I1^4 - 1011*r0^4*m^2*\phi d0^2*I1^6 + 2414*r0^10*m^5*\phi d0^4*I1^3 - \\
 & 210*r0^10*m^5*\phi d0^3*I1^3 + 589*r0^12*m^6*\phi d0^4*I1^2 + 2112*I1^7*\phi d0^4*r0^2*m + \\
 & 340*m^3*r0^6*I1^5 + 96*m^2*r0^2*I1^7 + 280*m^4*r0^8*I1^4 + 5661*r0^8*m^4*\phi d0^4*I1^4 + \\
 & 5764*r0^4*m^2*\phi d0^4*I1^6 + 7672*r0^6*m^3*\phi d0^4*I1^5 - 2181*r0^8*m^4*\phi d0^3*I1^4 - \\
 & 12*r0^14*m^7*\phi d0^2*I1 + 4*r0^16*m^8*\phi d0^3 - 75*r0^12*m^6*\phi d0*I1^2 - 18*I1*\phi d0*r0^14*m^7 + \\
 & \phi d0^2*r0^16*m^8 + 36*I1^2*r0^12*m^6 + 4*m^7*r0^14*I1 - m^8*r0^16*\phi d0 + 80*I1^7*\phi d0^2*m*r0^2 \\
 & - 2720*I1^7*\phi d0^3*m*r0^2 + 136*I1^3*r0^10*m^5 + 128*\phi d0^2*I1^8 + 128*I1^8*\phi d0 - \\
 & 512*I1^8*\phi d0^3 + 256*I1^8*\phi d0^4))^(1/2)*I1^2)^(2/3) - 4*i^3*(1/2)*r0^8*m^4*\phi d0^2 - \\
 & 40*r0^6*m^3*\phi d0^2*I1 + 16*m^3*r0^6*I1*\phi d0 + 116*I1^3*\phi d0*m*r0^2 - 132*I1^3*\phi d0^2*r0^2*m - \\
 & 8*m^2*I1^3 - 4*m^2*r0^4*I1^2 - 4*r0^8*m^4*\phi d0^2 + 84*I1^2*\phi d0*r0^4*m^2 + 48*I1^4*\phi d0 - 4* \\
 & - 8*r0^12*m^6*\phi d0^3 - 24*I1^5*m^2*r0^2 - 8*I1^3*m^3*r0^6 - 24*I1^4*m^2*r0^4 - 8*I1^6 + \\
 & 288*I1^6*\phi d0^2 - 288*I1^6*\phi d0 - 348*I1^3*m^3*r0^6*\phi d0 + 1752*I1^3*r0^6*m^3*\phi d0^2 - \\
 & 672*I1^2*r0^8*m^4*\phi d0^3 - 1756*I1^3*r0^6*m^3*\phi d0^3 - 804*I1^4*\phi d0*r0^4*m^2 + \\
 & 492*I1^2*r0^8*m^4*\phi d0^2 - 60*I1^2*r0^8*m^4*\phi d0 + 1692*I1^5*\phi d0^2*r0^2*m - \\
 & 804*I1^5*\phi d0*m*r0^2 + 2712*I1^4*r0^4*m^2*\phi d0^2 - 936*I1^5*\phi d0^3*r0^2*m - \\
 & 2124*I1^4*r0^4*m^2*\phi d0^3 + 48*r0^10*m^5*\phi d0^2*I1 - 120*r0^10*m^5*\phi d0^3*I1 + 12*I3^(1/2)*(- \\
 & \phi d0*(\phi d0 - 1)*(4*\phi d0^4*m^8*r0^16 + 46*m^7*r0^14*I1*\phi d0^3 + 76*r0^14*m^7*\phi d0^4*I1 - \\
 & 52*m^5*r0^10*I1^3*\phi d0 - 221*m^6*r0^12*I1^2*\phi d0^2 + 16*I1^8 + 600*I1^7*\phi d0*m*r0^2 + \\
 & 244*m^2*r0^4*I1^6 - 1064*I1^3*\phi d0^2*r0^10*m^5 + 143*I1^2*\phi d0^3*r0^12*m^6 + \\
 & 974*I1^5*\phi d0*r0^6*m^3 + 345*I1^4*\phi d0*r0^8*m^4 + 1107*I1^6*\phi d0*r0^4*m^2 - \\
 & 5062*r0^6*m^3*\phi d0^3*I1^5 - 5400*r0^4*m^2*\phi d0^3*I1^6 - 2412*r0^6*m^3*\phi d0^2*I1^5 - \\
 & 2305*r0^8*m^4*\phi d0^2*I1^4 - 1011*r0^4*m^2*\phi d0^2*I1^6 + 2414*r0^10*m^5*\phi d0^4*I1^3 - \\
 & 210*r0^10*m^5*\phi d0^3*I1^3 + 589*r0^12*m^6*\phi d0^4*I1^2 + 2112*I1^7*\phi d0^4*r0^2*m + \\
 & 340*m^3*r0^6*I1^5 + 96*m^2*r0^2*I1^7 + 280*m^4*r0^8*I1^4 + 5661*r0^8*m^4*\phi d0^4*I1^4 + \\
 & 5764*r0^4*m^2*\phi d0^4*I1^6 + 7672*r0^6*m^3*\phi d0^4*I1^5 - 2181*r0^8*m^4*\phi d0^3*I1^4 - \\
 & 12*r0^14*m^7*\phi d0^2*I1 + 4*r0^16*m^8*\phi d0^3 - 75*r0^12*m^6*\phi d0*I1^2 - 18*I1*\phi d0*r0^14*m^7 + \\
 & \phi d0^2*r0^16*m^8 + 36*I1^2*r0^12*m^6 + 4*m^7*r0^14*I1 - m^8*r0^16*\phi d0 + 80*I1^7*\phi d0^2*m*r0^2 \\
 & - 2720*I1^7*\phi d0^3*m*r0^2 + 136*I1^3*r0^10*m^5 + 128*\phi d0^2*I1^8 + 128*I1^8*\phi d0 - \\
 & 512*I1^8*\phi d0^3 + 256*I1^8*\phi d0^4))^(1/2)*I1^2)^(1/3)*r0^4*m^2*\phi d0 + 8*(-8*r0^12*m^6*\phi d0^3 - \\
 & 24*I1^5*m^2*r0^2 - 8*I1^3*m^3*r0^6 - 24*I1^4*m^2*r0^4 - 8*I1^6 + 288*I1^6*\phi d0^2 - 288*I1^6*\phi d0 - \\
 & 348*I1^3*m^3*r0^6*\phi d0 + 1752*I1^3*r0^6*m^3*\phi d0^2 - 672*I1^2*r0^8*m^4*\phi d0^3 - \\
 & 1756*I1^3*r0^6*m^3*\phi d0^3 - 804*I1^4*\phi d0*r0^4*m^2 + 492*I1^2*r0^8*m^4*\phi d0^2 - \\
 & 60*I1^2*r0^8*m^4*\phi d0 + 1692*I1^5*\phi d0^2*r0^2*m - 804*I1^5*\phi d0*m*r0^2 + \\
 & 2712*I1^4*r0^4*m^2*\phi d0^2 - 936*I1^5*\phi d0^3*r0^2*m - 2124*I1^4*r0^4*m^2*\phi d0^3 + \\
 & 48*r0^10*m^5*\phi d0^2*I1 - 120*r0^10*m^5*\phi d0^3*I1 + 12*I3^(1/2)*(-\phi d0*(\phi d0 - \\
 & 1)*(4*\phi d0^4*m^8*r0^16 + 46*m^7*r0^14*I1*\phi d0^3 + 76*r0^14*m^7*\phi d0^4*I1 - \\
 & 52*m^5*r0^10*I1^3*\phi d0 - 221*m^6*r0^12*I1^2*\phi d0^2 + 16*I1^8 + 600*I1^7*\phi d0*m*r0^2 + \\
 & 244*m^2*r0^4*I1^6 - 1064*I1^3*\phi d0^2*r0^10*m^5 + 143*I1^2*\phi d0^3*r0^12*m^6 + \\
 & 974*I1^5*\phi d0*r0^6*m^3 + 345*I1^4*\phi d0*r0^8*m^4 + 1107*I1^6*\phi d0*r0^4*m^2 - \\
 & 5062*r0^6*m^3*\phi d0^3*I1^5 - 5400*r0^4*m^2*\phi d0^3*I1^6 - 2412*r0^6*m^3*\phi d0^2*I1^5 - \\
 & 2305*r0^8*m^4*\phi d0^2*I1^4 - 1011*r0^4*m^2*\phi d0^2*I1^6 + 2414*r0^10*m^5*\phi d0^4*I1^3 - \\
 & 210*r0^10*m^5*\phi d0^3*I1^3 + 589*r0^12*m^6*\phi d0^4*I1^2 + 2112*I1^7*\phi d0^4*r0^2*m +
 \end{aligned}$$

$$\begin{aligned}
& 340*m^3*r0^6*I1^5 + 96*m*r0^2*I1^7 + 280*m^4*r0^8*I1^4 + 5661*r0^8*m^4*phi0^4*I1^4 + \\
& 5764*r0^4*m^2*phi0^4*I1^6 + 7672*r0^6*m^3*phi0^4*I1^5 - 2181*r0^8*m^4*phi0^3*I1^4 - \\
& 12*r0^14*m^7*phi0^2*I1 + 4*r0^16*m^8*phi0^3 - 75*r0^12*m^6*phi0^4*I1^2 - 18*I1*phi0*r0^14*m^7 + \\
& phi0^2*r0^16*m^8 + 36*I1^2*r0^12*m^6 + 4*m^7*r0^14*I1 - m^8*r0^16*phi0 + 80*I1^7*phi0^2*m*r0^2 \\
& - 2720*I1^7*phi0^3*m*r0^2 + 136*I1^3*r0^10*m^5 + 128*phi0^2*I1^8 + 128*I1^8*phi0 - \\
& 512*I1^8*phi0^3 + 256*I1^8*phi0^4))^(1/2)*I1^2)^(1/3)*m*r0^2*I1 - 4*I1^4 - 24*(-8*r0^12*m^6*phi0^3 \\
& - 24*I1^5*m*r0^2 - 8*I1^3*m^3*r0^6 - 24*I1^4*m^2*r0^4 - 8*I1^6 + 288*I1^6*phi0^2 - 288*I1^6*phi0 - \\
& 348*I1^3*m^3*r0^6*phi0 + 1752*I1^3*r0^6*m^3*phi0^2 - 672*I1^2*r0^8*m^4*phi0^3 - \\
& 1756*I1^3*r0^6*m^3*phi0^3 - 804*I1^4*phi0*r0^4*m^2 + 492*I1^2*r0^8*m^4*phi0^2 - \\
& 60*I1^2*r0^8*m^4*phi0 + 1692*I1^5*phi0^2*r0^2*m - 804*I1^5*phi0*m*r0^2 + \\
& 2712*I1^4*r0^4*m^2*phi0^2 - 936*I1^5*phi0^3*r0^2*m - 2124*I1^4*r0^4*m^2*phi0^3 + \\
& 48*r0^10*m^5*phi0^2*I1 - 120*r0^10*m^5*phi0^3*I1 + 12*3^(1/2)*(-phi0*(phi0 - \\
& 1)*(4*phi0^4*m^8*r0^16 + 46*m^7*r0^14*I1*phi0^3 + 76*r0^14*m^7*phi0^4*I1 - \\
& 52*m^5*r0^10*I1^3*phi0 - 221*m^6*r0^12*I1^2*phi0^2 + 16*I1^8 + 600*I1^7*phi0*m*r0^2 + \\
& 244*m^2*r0^4*I1^6 - 1064*I1^3*phi0^2*r0^10*m^5 + 143*I1^2*phi0^3*r0^12*m^6 + \\
& 974*I1^5*phi0*r0^6*m^3 + 345*I1^4*phi0*r0^8*m^4 + 1107*I1^6*phi0*r0^4*m^2 - \\
& 5062*r0^6*m^3*phi0^3*I1^5 - 5400*r0^4*m^2*phi0^3*I1^6 - 2412*r0^6*m^3*phi0^2*I1^5 - \\
& 2305*r0^8*m^4*phi0^2*I1^4 - 1011*r0^4*m^2*phi0^2*I1^6 + 2414*r0^10*m^5*phi0^4*I1^3 - \\
& 210*r0^10*m^5*phi0^3*I1^3 + 589*r0^12*m^6*phi0^4*I1^2 + 2112*I1^7*phi0^4*r0^2*m + \\
& 340*m^3*r0^6*I1^5 + 96*m*r0^2*I1^7 + 280*m^4*r0^8*I1^4 + 5661*r0^8*m^4*phi0^4*I1^4 + \\
& 5764*r0^4*m^2*phi0^4*I1^6 + 7672*r0^6*m^3*phi0^4*I1^5 - 2181*r0^8*m^4*phi0^3*I1^4 - \\
& 12*r0^14*m^7*phi0^2*I1 + 4*r0^16*m^8*phi0^3 - 75*r0^12*m^6*phi0^4*I1^2 - 18*I1*phi0*r0^14*m^7 + \\
& phi0^2*r0^16*m^8 + 36*I1^2*r0^12*m^6 + 4*m^7*r0^14*I1 - m^8*r0^16*phi0 + 80*I1^7*phi0^2*m*r0^2 \\
& - 2720*I1^7*phi0^3*m*r0^2 + 136*I1^3*r0^10*m^5 + 128*phi0^2*I1^8 + 128*I1^8*phi0 - \\
& 512*I1^8*phi0^3 + 256*I1^8*phi0^4))^(1/2)*I1^2)^(1/3)*I1^2*phi0 - 48*I1^4*phi0^2 - 4*i*3^(1/2)*I1^4 + \\
& 8*I1^2*(-8*r0^12*m^6*phi0^3 - 24*I1^5*m*r0^2 - 8*I1^3*m^3*r0^6 - 24*I1^4*m^2*r0^4 - 8*I1^6 + \\
& 288*I1^6*phi0^2 - 288*I1^6*phi0 - 348*I1^3*m^3*r0^6*phi0 + 1752*I1^3*r0^6*m^3*phi0^2 - \\
& 672*I1^2*r0^8*m^4*phi0^3 - 1756*I1^3*r0^6*m^3*phi0^3 - 804*I1^4*phi0*r0^4*m^2 + \\
& 492*I1^2*r0^8*m^4*phi0^2 - 60*I1^2*r0^8*m^4*phi0 + 1692*I1^5*phi0^2*r0^2*m - \\
& 804*I1^5*phi0*m*r0^2 + 2712*I1^4*r0^4*m^2*phi0^2 - 936*I1^5*phi0^3*r0^2*m - \\
& 2124*I1^4*r0^4*m^2*phi0^3 + 48*r0^10*m^5*phi0^2*I1 - 120*r0^10*m^5*phi0^3*I1 + 12*3^(1/2)*(- \\
& phi0*(phi0 - 1)*(4*phi0^4*m^8*r0^16 + 46*m^7*r0^14*I1*phi0^3 + 76*r0^14*m^7*phi0^4*I1 - \\
& 52*m^5*r0^10*I1^3*phi0 - 221*m^6*r0^12*I1^2*phi0^2 + 16*I1^8 + 600*I1^7*phi0*m*r0^2 + \\
& 244*m^2*r0^4*I1^6 - 1064*I1^3*phi0^2*r0^10*m^5 + 143*I1^2*phi0^3*r0^12*m^6 + \\
& 974*I1^5*phi0*r0^6*m^3 + 345*I1^4*phi0*r0^8*m^4 + 1107*I1^6*phi0*r0^4*m^2 - \\
& 5062*r0^6*m^3*phi0^3*I1^5 - 5400*r0^4*m^2*phi0^3*I1^6 - 2412*r0^6*m^3*phi0^2*I1^5 - \\
& 2305*r0^8*m^4*phi0^2*I1^4 - 1011*r0^4*m^2*phi0^2*I1^6 + 2414*r0^10*m^5*phi0^4*I1^3 - \\
& 210*r0^10*m^5*phi0^3*I1^3 + 589*r0^12*m^6*phi0^4*I1^2 + 2112*I1^7*phi0^4*r0^2*m + \\
& 340*m^3*r0^6*I1^5 + 96*m*r0^2*I1^7 + 280*m^4*r0^8*I1^4 + 5661*r0^8*m^4*phi0^4*I1^4 + \\
& 5764*r0^4*m^2*phi0^4*I1^6 + 7672*r0^6*m^3*phi0^4*I1^5 - 2181*r0^8*m^4*phi0^3*I1^4 - \\
& 12*r0^14*m^7*phi0^2*I1 + 4*r0^16*m^8*phi0^3 - 75*r0^12*m^6*phi0^4*I1^2 - 18*I1*phi0*r0^14*m^7 + \\
& phi0^2*r0^16*m^8 + 36*I1^2*r0^12*m^6 + 4*m^7*r0^14*I1 - m^8*r0^16*phi0 + 80*I1^7*phi0^2*m*r0^2 \\
& - 2720*I1^7*phi0^3*m*r0^2 + 136*I1^3*r0^10*m^5 + 128*phi0^2*I1^8 + 128*I1^8*phi0 - \\
& 512*I1^8*phi0^3 + 256*I1^8*phi0^4))^(1/2)*I1^2)^(1/3) - 20*(-8*r0^12*m^6*phi0^3 - 24*I1^5*m*r0^2 - \\
& 8*I1^3*m^3*r0^6 - 24*I1^4*m^2*r0^4 - 8*I1^6 + 288*I1^6*phi0^2 - 288*I1^6*phi0 - \\
& 348*I1^3*m^3*r0^6*phi0 + 1752*I1^3*r0^6*m^3*phi0^2 - 672*I1^2*r0^8*m^4*phi0^3 - \\
& 1756*I1^3*r0^6*m^3*phi0^3 - 804*I1^4*phi0*r0^4*m^2 + 492*I1^2*r0^8*m^4*phi0^2 -$$

60*I1^2*r0^8*m^4*fd0 + 1692*I1^5*fd0^2*r0^2*m - 804*I1^5*fd0*m*r0^2 +
 2712*I1^4*r0^4*m^2*fd0^2 - 936*I1^5*fd0^3*r0^2*m - 2124*I1^4*r0^4*m^2*fd0^3 +
 48*r0^10*m^5*fd0^2*I1 - 120*r0^10*m^5*fd0^3*I1 + 12*3^(1/2)*(- fd0*(fd0 -
 1)*(4*fd0^4*m^8*r0^16 + 46*m^7*r0^14*I1*fd0^3 + 76*r0^14*m^7*fd0^4*I1 -
 52*m^5*r0^10*I1^3*fd0 - 221*m^6*r0^12*I1^2*fd0^2 + 16*I1^8 + 600*I1^7*fd0*m*r0^2 +
 244*m^2*r0^4*I1^6 - 1064*I1^3*fd0^2*r0^10*m^5 + 143*I1^2*fd0^3*r0^12*m^6 +
 974*I1^5*fd0*r0^6*m^3 + 345*I1^4*fd0*r0^8*m^4 + 1107*I1^6*fd0*r0^4*m^2 -
 5062*r0^6*m^3*fd0^3*I1^5 - 5400*r0^4*m^2*fd0^3*I1^6 - 2412*r0^6*m^3*fd0^2*I1^5 -
 2305*r0^8*m^4*fd0^2*I1^4 - 1011*r0^4*m^2*fd0^2*I1^6 + 2414*r0^10*m^5*fd0^4*I1^3 -
 210*r0^10*m^5*fd0^3*I1^3 + 589*r0^12*m^6*fd0^4*I1^2 + 2112*I1^7*fd0^4*r0^2*m +
 340*m^3*r0^6*I1^5 + 96*m^2*r0^2*I1^7 + 280*m^4*r0^8*I1^4 + 5661*r0^8*m^4*fd0^4*I1^4 +
 5764*r0^4*m^2*fd0^4*I1^6 + 7672*r0^6*m^3*fd0^4*I1^5 - 2181*r0^8*m^4*fd0^3*I1^4 -
 12*r0^14*m^7*fd0^2*I1 + 4*r0^16*m^8*fd0^3 - 75*r0^12*m^6*fd0*I1^2 - 18*I1*fd0*r0^14*m^7 +
 fd0^2*r0^16*m^8 + 36*I1^2*r0^12*m^6 + 4*m^7*r0^14*I1 - m^8*r0^16*fd0 + 80*I1^7*fd0^2*m*r0^2
 - 2720*I1^7*fd0^3*m*r0^2 + 136*I1^3*r0^10*m^5 + 128*fd0^2*I1^8 + 128*I1^8*fd0 -
 512*I1^8*fd0^3 + 256*I1^8*fd0^4))^(1/2)*I1^2)^(1/3)*r0^2*m*I1*fd0 - 40*i^3^(1/
 2)*r0^6*m^3*fd0^2*I1 + 48*i^3^(1/2)*I1^4*fd0 - 48*i^3^(1/2)*I1^4*fd0^2 - (- 8*r0^12*m^6*fd0^3 -
 24*I1^5*m^2*r0^2 - 8*I1^3*m^3*r0^6 - 24*I1^4*m^2*r0^4 - 8*I1^6 + 288*I1^6*fd0^2 - 288*I1^6*fd0 -
 348*I1^3*m^3*r0^6*fd0 + 1752*I1^3*r0^6*m^3*fd0^2 - 672*I1^2*r0^8*m^4*fd0^3 -
 1756*I1^3*r0^6*m^3*fd0^3 - 804*I1^4*fd0*r0^4*m^2 + 492*I1^2*r0^8*m^4*fd0^2 -
 60*I1^2*r0^8*m^4*fd0 + 1692*I1^5*fd0^2*r0^2*m - 804*I1^5*fd0*m*r0^2 +
 2712*I1^4*r0^4*m^2*fd0^2 - 936*I1^5*fd0^3*r0^2*m - 2124*I1^4*r0^4*m^2*fd0^3 +
 48*r0^10*m^5*fd0^2*I1 - 120*r0^10*m^5*fd0^3*I1 + 12*3^(1/2)*(- fd0*(fd0 -
 1)*(4*fd0^4*m^8*r0^16 + 46*m^7*r0^14*I1*fd0^3 + 76*r0^14*m^7*fd0^4*I1 -
 52*m^5*r0^10*I1^3*fd0 - 221*m^6*r0^12*I1^2*fd0^2 + 16*I1^8 + 600*I1^7*fd0*m*r0^2 +
 244*m^2*r0^4*I1^6 - 1064*I1^3*fd0^2*r0^10*m^5 + 143*I1^2*fd0^3*r0^12*m^6 +
 974*I1^5*fd0*r0^6*m^3 + 345*I1^4*fd0*r0^8*m^4 + 1107*I1^6*fd0*r0^4*m^2 -
 5062*r0^6*m^3*fd0^3*I1^5 - 5400*r0^4*m^2*fd0^3*I1^6 - 2412*r0^6*m^3*fd0^2*I1^5 -
 2305*r0^8*m^4*fd0^2*I1^4 - 1011*r0^4*m^2*fd0^2*I1^6 + 2414*r0^10*m^5*fd0^4*I1^3 -
 210*r0^10*m^5*fd0^3*I1^3 + 589*r0^12*m^6*fd0^4*I1^2 + 2112*I1^7*fd0^4*r0^2*m +
 340*m^3*r0^6*I1^5 + 96*m^2*r0^2*I1^7 + 280*m^4*r0^8*I1^4 + 5661*r0^8*m^4*fd0^4*I1^4 +
 5764*r0^4*m^2*fd0^4*I1^6 + 7672*r0^6*m^3*fd0^4*I1^5 - 2181*r0^8*m^4*fd0^3*I1^4 -
 12*r0^14*m^7*fd0^2*I1 + 4*r0^16*m^8*fd0^3 - 75*r0^12*m^6*fd0*I1^2 - 18*I1*fd0*r0^14*m^7 +
 fd0^2*r0^16*m^8 + 36*I1^2*r0^12*m^6 + 4*m^7*r0^14*I1 - m^8*r0^16*fd0 + 80*I1^7*fd0^2*m*r0^2
 - 2720*I1^7*fd0^3*m*r0^2 + 136*I1^3*r0^10*m^5 + 128*fd0^2*I1^8 + 128*I1^8*fd0 -
 512*I1^8*fd0^3 + 256*I1^8*fd0^4))^(1/2)*I1^2)^(2/3) + 16*i^3^(1/2)*r0^6*m^3*fd0*I1 - 4*i^3^(1/
 2)*I1^2*r0^4*m^2 - 8*i^3^(1/2)*I1^3*m^2*r0^2 - 124*i^3^(1/2)*r0^4*m^2*fd0^2*I1^2 - 132*i^3^(1/
 2)*I1^3*fd0^2*r0^2*m + 84*i^3^(1/2)*I1^2*fd0*r0^4*m^2 + 116*i^3^(1/2)*I1^3*fd0*m*r0^2 -
 124*r0^4*m^2*fd0^2*I1^2))^(1/2)

$$\begin{aligned}
 \lambda_{11} = & 1/6/I1/(- 8*r0^12*m^6*fd0^3 - 24*I1^5*m^2*r0^2 - 8*I1^3*m^3*r0^6 - 24*I1^4*m^2*r0^4 - 8*I1^6 \\
 & + 288*I1^6*fd0^2 - 288*I1^6*fd0 - 348*I1^3*m^3*r0^6*fd0 + 1752*I1^3*r0^6*m^3*fd0^2 - \\
 & 672*I1^2*r0^8*m^4*fd0^3 - 1756*I1^3*r0^6*m^3*fd0^3 - 804*I1^4*fd0*r0^4*m^2 + \\
 & 492*I1^2*r0^8*m^4*fd0^2 - 60*I1^2*r0^8*m^4*fd0 + 1692*I1^5*fd0^2*r0^2*m - \\
 & 804*I1^5*fd0*m*r0^2 + 2712*I1^4*r0^4*m^2*fd0^2 - 936*I1^5*fd0^3*r0^2*m - \\
 & 2124*I1^4*r0^4*m^2*fd0^3 + 48*r0^10*m^5*fd0^2*I1 - 120*r0^10*m^5*fd0^3*I1 + 12*3^(1/2)*(- \\
 & fd0*(fd0 - 1)*(4*fd0^4*m^8*r0^16 + 46*m^7*r0^14*I1*fd0^3 + 76*r0^14*m^7*fd0^4*I1 - \\
 & 52*m^5*r0^10*I1^3*fd0 - 221*m^6*r0^12*I1^2*fd0^2 + 16*I1^8 + 600*I1^7*fd0*m*r0^2 + \\
 & 244*m^2*r0^4*I1^6 - 1064*I1^3*fd0^2*r0^10*m^5 + 143*I1^2*fd0^3*r0^12*m^6 + \\
 & 974*I1^5*fd0*r0^6*m^3 + 345*I1^4*fd0*r0^8*m^4 + 1107*I1^6*fd0*r0^4*m^2 - \\
 & 5062*r0^6*m^3*fd0^3*I1^5 - 5400*r0^4*m^2*fd0^3*I1^6 - 2412*r0^6*m^3*fd0^2*I1^5 - \\
 & 2305*r0^8*m^4*fd0^2*I1^4 - 1011*r0^4*m^2*fd0^2*I1^6 + 2414*r0^10*m^5*fd0^4*I1^3 - \\
 & 210*r0^10*m^5*fd0^3*I1^3 + 589*r0^12*m^6*fd0^4*I1^2 + 2112*I1^7*fd0^4*r0^2*m + \\
 & 340*m^3*r0^6*I1^5 + 96*m^2*r0^2*I1^7 + 280*m^4*r0^8*I1^4 + 5661*r0^8*m^4*fd0^4*I1^4 + \\
 & 5764*r0^4*m^2*fd0^4*I1^6 + 7672*r0^6*m^3*fd0^4*I1^5 - 2181*r0^8*m^4*fd0^3*I1^4 - \\
 & 12*r0^14*m^7*fd0^2*I1 + 4*r0^16*m^8*fd0^3 - 75*r0^12*m^6*fd0*I1^2 - 18*I1*fd0*r0^14*m^7 + \\
 & fd0^2*r0^16*m^8 + 36*I1^2*r0^12*m^6 + 4*m^7*r0^14*I1 - m^8*r0^16*fd0 + 80*I1^7*fd0^2*m*r0^2 \\
 & - 2720*I1^7*fd0^3*m*r0^2 + 136*I1^3*r0^10*m^5 + 128*fd0^2*I1^8 + 128*I1^8*fd0 - \\
 & 512*I1^8*fd0^3 + 256*I1^8*fd0^4))^(1/2)*I1^2)^(2/3) + 16*i^3^(1/2)*r0^6*m^3*fd0*I1 - 4*i^3^(1/2)*I1^2 \\
 & *r0^4*m^2 - 8*i^3^(1/2)*I1^3*m^2*r0^2 - 124*i^3^(1/2)*r0^4*m^2*fd0^2*I1^2 - 132*i^3^(1/2)*I1^3*fd0^2*r0^2*m \\
 & + 84*i^3^(1/2)*I1^2*fd0*r0^4*m^2 + 116*i^3^(1/2)*I1^3*fd0*m*r0^2 - 124*r0^4*m^2*fd0^2*I1^2))^(1/2)
 \end{aligned}$$

$52*m^5*r0^10*I1^3*fd0 - 221*m^6*r0^12*I1^2*fd0^2 + 16*I1^8 + 600*I1^7*fd0*m*r0^2 +$
 $244*m^2*r0^4*I1^6 - 1064*I1^3*fd0^2*r0^10*m^5 + 143*I1^2*fd0^3*r0^12*m^6 +$
 $974*I1^5*fd0*r0^6*m^3 + 345*I1^4*fd0*r0^8*m^4 + 1107*I1^6*fd0*r0^4*m^2 -$
 $5062*r0^6*m^3*fd0^3*I1^5 - 5400*r0^4*m^2*fd0^3*I1^6 - 2412*r0^6*m^3*fd0^2*I1^5 -$
 $2305*r0^8*m^4*fd0^2*I1^4 - 1011*r0^4*m^2*fd0^2*I1^6 + 2414*r0^10*m^5*fd0^4*I1^3 -$
 $210*r0^10*m^5*fd0^3*I1^3 + 589*r0^12*m^6*fd0^4*I1^2 + 2112*I1^7*fd0^4*r0^2*m +$
 $340*m^3*r0^6*I1^5 + 96*m^2*r0^2*I1^7 + 280*m^4*r0^8*I1^4 + 5661*r0^8*m^4*fd0^4*I1^4 +$
 $5764*r0^4*m^2*fd0^4*I1^6 + 7672*r0^6*m^3*fd0^4*I1^5 - 2181*r0^8*m^4*fd0^3*I1^4 -$
 $12*r0^14*m^7*fd0^2*I1 + 4*r0^16*m^8*fd0^3 - 75*r0^12*m^6*fd0*I1^2 - 18*I1*fd0*r0^14*m^7 +$
 $\phi d0^2*r0^16*m^8 + 36*I1^2*r0^12*m^6 + 4*m^7*r0^14*I1 - m^8*r0^16*fd0 + 80*I1^7*fd0^2*m*r0^2 -$
 $- 2720*I1^7*fd0^3*m*r0^2 + 136*I1^3*r0^10*m^5 + 128*fd0^2*I1^8 + 128*I1^8*fd0 -$
 $512*I1^8*fd0^3 + 256*I1^8*fd0^4))^(1/2)*I1^2)^(1/3)*3^(1/2)*(-(-8*r0^12*m^6*fd0^3 -$
 $24*I1^5*m^2*r0^2 - 8*I1^3*m^3*r0^6 - 24*I1^4*m^2*r0^4 - 8*I1^6 + 288*I1^6*fd0^2 - 288*I1^6*fd0 -$
 $348*I1^3*m^3*r0^6*fd0 + 1752*I1^3*r0^6*m^3*fd0^2 - 672*I1^2*r0^8*m^4*fd0^3 -$
 $1756*I1^3*r0^6*m^3*fd0^3 - 804*I1^4*fd0*r0^4*m^2 + 492*I1^2*r0^8*m^4*fd0^2 -$
 $60*I1^2*r0^8*m^4*fd0 + 1692*I1^5*fd0^2*r0^2*m - 804*I1^5*fd0*m*r0^2 +$
 $2712*I1^4*r0^4*m^2*fd0^2 - 936*I1^5*fd0^3*r0^2*m - 2124*I1^4*r0^4*m^2*fd0^3 +$
 $48*r0^10*m^5*fd0^2*I1 - 120*r0^10*m^5*fd0^3*I1 + 12*3^(1/2)*(-\phi d0*(\phi d0 -$
 $1)*(4*fd0^4*m^8*r0^16 + 46*m^7*r0^14*I1*fd0^3 + 76*r0^14*m^7*fd0^4*I1 -$
 $52*m^5*r0^10*I1^3*fd0 - 221*m^6*r0^12*I1^2*fd0^2 + 16*I1^8 + 600*I1^7*fd0*m*r0^2 +$
 $244*m^2*r0^4*I1^6 - 1064*I1^3*fd0^2*r0^10*m^5 + 143*I1^2*fd0^3*r0^12*m^6 +$
 $974*I1^5*fd0*r0^6*m^3 + 345*I1^4*fd0*r0^8*m^4 + 1107*I1^6*fd0*r0^4*m^2 -$
 $5062*r0^6*m^3*fd0^3*I1^5 - 5400*r0^4*m^2*fd0^3*I1^6 - 2412*r0^6*m^3*fd0^2*I1^5 -$
 $2305*r0^8*m^4*fd0^2*I1^4 - 1011*r0^4*m^2*fd0^2*I1^6 + 2414*r0^10*m^5*fd0^4*I1^3 -$
 $210*r0^10*m^5*fd0^3*I1^3 + 589*r0^12*m^6*fd0^4*I1^2 + 2112*I1^7*fd0^4*r0^2*m +$
 $340*m^3*r0^6*I1^5 + 96*m^2*r0^2*I1^7 + 280*m^4*r0^8*I1^4 + 5661*r0^8*m^4*fd0^4*I1^4 +$
 $5764*r0^4*m^2*fd0^4*I1^6 + 7672*r0^6*m^3*fd0^4*I1^5 - 2181*r0^8*m^4*fd0^3*I1^4 -$
 $12*r0^14*m^7*fd0^2*I1 + 4*r0^16*m^8*fd0^3 - 75*r0^12*m^6*fd0*I1^2 - 18*I1*fd0*r0^14*m^7 +$
 $\phi d0^2*r0^16*m^8 + 36*I1^2*r0^12*m^6 + 4*m^7*r0^14*I1 - m^8*r0^16*fd0 + 80*I1^7*fd0^2*m*r0^2 -$
 $- 2720*I1^7*fd0^3*m*r0^2 + 136*I1^3*r0^10*m^5 + 128*fd0^2*I1^8 + 128*I1^8*fd0 -$
 $512*I1^8*fd0^3 + 256*I1^8*fd0^4))^(1/2)*I1^2)^(1/3)*fd0*(i^3^(1/2)*(-8*r0^12*m^6*fd0^3 -$
 $24*I1^5*m^2*r0^2 - 8*I1^3*m^3*r0^6 - 24*I1^4*m^2*r0^4 - 8*I1^6 + 288*I1^6*fd0^2 - 288*I1^6*fd0 -$
 $348*I1^3*m^3*r0^6*fd0 + 1752*I1^3*r0^6*m^3*fd0^2 - 672*I1^2*r0^8*m^4*fd0^3 -$
 $1756*I1^3*r0^6*m^3*fd0^3 - 804*I1^4*fd0*r0^4*m^2 + 492*I1^2*r0^8*m^4*fd0^2 -$
 $60*I1^2*r0^8*m^4*fd0 + 1692*I1^5*fd0^2*r0^2*m - 804*I1^5*fd0*m*r0^2 +$
 $2712*I1^4*r0^4*m^2*fd0^2 - 936*I1^5*fd0^3*r0^2*m - 2124*I1^4*r0^4*m^2*fd0^3 +$
 $48*r0^10*m^5*fd0^2*I1 - 120*r0^10*m^5*fd0^3*I1 + 12*3^(1/2)*(-\phi d0*(\phi d0 -$
 $1)*(4*fd0^4*m^8*r0^16 + 46*m^7*r0^14*I1*fd0^3 + 76*r0^14*m^7*fd0^4*I1 -$
 $52*m^5*r0^10*I1^3*fd0 - 221*m^6*r0^12*I1^2*fd0^2 + 16*I1^8 + 600*I1^7*fd0*m*r0^2 +$
 $244*m^2*r0^4*I1^6 - 1064*I1^3*fd0^2*r0^10*m^5 + 143*I1^2*fd0^3*r0^12*m^6 +$
 $974*I1^5*fd0*r0^6*m^3 + 345*I1^4*fd0*r0^8*m^4 + 1107*I1^6*fd0*r0^4*m^2 -$
 $5062*r0^6*m^3*fd0^3*I1^5 - 5400*r0^4*m^2*fd0^3*I1^6 - 2412*r0^6*m^3*fd0^2*I1^5 -$
 $2305*r0^8*m^4*fd0^2*I1^4 - 1011*r0^4*m^2*fd0^2*I1^6 + 2414*r0^10*m^5*fd0^4*I1^3 -$
 $210*r0^10*m^5*fd0^3*I1^3 + 589*r0^12*m^6*fd0^4*I1^2 + 2112*I1^7*fd0^4*r0^2*m +$
 $340*m^3*r0^6*I1^5 + 96*m^2*r0^2*I1^7 + 280*m^4*r0^8*I1^4 + 5661*r0^8*m^4*fd0^4*I1^4 +$
 $5764*r0^4*m^2*fd0^4*I1^6 + 7672*r0^6*m^3*fd0^4*I1^5 - 2181*r0^8*m^4*fd0^3*I1^4 -$
 $12*r0^14*m^7*fd0^2*I1 + 4*r0^16*m^8*fd0^3 - 75*r0^12*m^6*fd0*I1^2 - 18*I1*fd0*r0^14*m^7 +$

$\phi d0^2 * r0^16 * m^8 + 36 * I1^2 * r0^12 * m^6 + 4 * m^7 * r0^14 * I1 - m^8 * r0^16 * \phi d0 + 80 * I1^7 * \phi d0^2 * m * r0^2$
 $- 2720 * I1^7 * \phi d0^3 * m * r0^2 + 136 * I1^3 * r0^10 * m^5 + 128 * \phi d0^2 * I1^8 + 128 * I1^8 * \phi d0 -$
 $512 * I1^8 * \phi d0^3 + 256 * I1^8 * \phi d0^4))^{(1/2)} * I1^2)^{(2/3)} - 4 * I1^3 * (1/2) * r0^8 * m^4 * \phi d0^2 +$
 $40 * r0^6 * m^3 * \phi d0^2 * I1 - 16 * m^3 * r0^6 * I1 * \phi d0 - 116 * I1^3 * \phi d0 * m * r0^2 + 132 * I1^3 * \phi d0^2 * r0^2 * m +$
 $8 * m * r0^2 * I1^3 + 4 * m^2 * r0^4 * I1^2 + 4 * r0^8 * m^4 * \phi d0^2 - 84 * I1^2 * \phi d0 * r0^4 * m^2 - 48 * I1^4 * \phi d0 + 4 * ($
 $- 8 * r0^12 * m^6 * \phi d0^3 - 24 * I1^5 * m * r0^2 - 8 * I1^3 * m^3 * r0^6 - 24 * I1^4 * m^2 * r0^4 - 8 * I1^6 +$
 $288 * I1^6 * \phi d0^2 - 288 * I1^6 * \phi d0 - 348 * I1^3 * m^3 * r0^6 * \phi d0 + 1752 * I1^3 * r0^6 * m^3 * \phi d0^2 -$
 $672 * I1^2 * r0^8 * m^4 * \phi d0^3 - 1756 * I1^3 * r0^6 * m^3 * \phi d0^3 - 804 * I1^4 * \phi d0 * r0^4 * m^2 +$
 $492 * I1^2 * r0^8 * m^4 * \phi d0^2 - 60 * I1^2 * r0^8 * m^4 * \phi d0 + 1692 * I1^5 * \phi d0^2 * r0^2 * m -$
 $804 * I1^5 * \phi d0 * m * r0^2 + 2712 * I1^4 * r0^4 * m^2 * \phi d0^2 - 936 * I1^5 * \phi d0^3 * r0^2 * m -$
 $2124 * I1^4 * r0^4 * m^2 * \phi d0^3 + 48 * r0^10 * m^5 * \phi d0^2 * I1 - 120 * r0^10 * m^5 * \phi d0^3 * I1 + 12 * 3^{(1/2)} * (-$
 $\phi d0 * (\phi d0 - 1) * (4 * \phi d0^4 * m^8 * r0^16 + 46 * m^7 * r0^14 * I1 * \phi d0^3 + 76 * r0^14 * m^7 * \phi d0^4 * I1 -$
 $52 * m^5 * r0^10 * I1^3 * \phi d0 - 221 * m^6 * r0^12 * I1^2 * \phi d0^2 + 16 * I1^8 + 600 * I1^7 * \phi d0 * m * r0^2 +$
 $244 * m^2 * r0^4 * I1^6 - 1064 * I1^3 * \phi d0^2 * r0^10 * m^5 + 143 * I1^2 * \phi d0^3 * r0^12 * m^6 +$
 $974 * I1^5 * \phi d0 * r0^6 * m^3 + 345 * I1^4 * \phi d0 * r0^8 * m^4 + 1107 * I1^6 * \phi d0 * r0^4 * m^2 -$
 $5062 * r0^6 * m^3 * \phi d0^3 * I1^5 - 5400 * r0^4 * m^2 * \phi d0^3 * I1^6 - 2412 * r0^6 * m^3 * \phi d0^2 * I1^5 -$
 $2305 * r0^8 * m^4 * \phi d0^2 * I1^4 - 1011 * r0^4 * m^2 * \phi d0^2 * I1^6 + 2414 * r0^10 * m^5 * \phi d0^4 * I1^3 -$
 $210 * r0^10 * m^5 * \phi d0^3 * I1^3 + 589 * r0^12 * m^6 * \phi d0^4 * I1^2 + 2112 * I1^7 * \phi d0^4 * r0^2 * m +$
 $340 * m^3 * r0^6 * I1^5 + 96 * m^2 * r0^2 * I1^7 + 280 * m^4 * r0^8 * I1^4 + 5661 * r0^8 * m^4 * \phi d0^4 * I1^4 +$
 $5764 * r0^4 * m^2 * \phi d0^4 * I1^6 + 7672 * r0^6 * m^3 * \phi d0^4 * I1^5 - 2181 * r0^8 * m^4 * \phi d0^3 * I1^4 -$
 $12 * r0^14 * m^7 * \phi d0^2 * I1 + 4 * r0^16 * m^8 * \phi d0^3 - 75 * r0^12 * m^6 * \phi d0 * I1^2 - 18 * I1 * \phi d0 * r0^14 * m^7 +$
 $\phi d0^2 * r0^16 * m^8 + 36 * I1^2 * r0^12 * m^6 + 4 * m^7 * r0^14 * I1 - m^8 * r0^16 * \phi d0 + 80 * I1^7 * \phi d0^2 * m * r0^2$
 $- 2720 * I1^7 * \phi d0^3 * m * r0^2 + 136 * I1^3 * r0^10 * m^5 + 128 * \phi d0^2 * I1^8 + 128 * I1^8 * \phi d0 -$
 $512 * I1^8 * \phi d0^3 + 256 * I1^8 * \phi d0^4))^{(1/2)} * I1^2)^{(1/3)} * r0^4 * m^2 * \phi d0 - 8 * (- 8 * r0^12 * m^6 * \phi d0^3 -$
 $24 * I1^5 * m * r0^2 - 8 * I1^3 * m^3 * r0^6 - 24 * I1^4 * m^2 * r0^4 - 8 * I1^6 + 288 * I1^6 * \phi d0^2 - 288 * I1^6 * \phi d0 -$
 $348 * I1^3 * m^3 * r0^6 * \phi d0 + 1752 * I1^3 * r0^6 * m^3 * \phi d0^2 - 672 * I1^2 * r0^8 * m^4 * \phi d0^3 -$
 $1756 * I1^3 * r0^6 * m^3 * \phi d0^3 - 804 * I1^4 * \phi d0 * r0^4 * m^2 + 492 * I1^2 * r0^8 * m^4 * \phi d0^2 -$
 $60 * I1^2 * r0^8 * m^4 * \phi d0 + 1692 * I1^5 * \phi d0^2 * r0^2 * m - 804 * I1^5 * \phi d0 * m * r0^2 +$
 $2712 * I1^4 * r0^4 * m^2 * \phi d0^2 - 936 * I1^5 * \phi d0^3 * r0^2 * m - 2124 * I1^4 * r0^4 * m^2 * \phi d0^3 +$
 $48 * r0^10 * m^5 * \phi d0^2 * I1 - 120 * r0^10 * m^5 * \phi d0^3 * I1 + 12 * 3^{(1/2)} * (- \phi d0 * (\phi d0 -$
 $1) * (4 * \phi d0^4 * m^8 * r0^16 + 46 * m^7 * r0^14 * I1 * \phi d0^3 + 76 * r0^14 * m^7 * \phi d0^4 * I1 -$
 $52 * m^5 * r0^10 * I1^3 * \phi d0 - 221 * m^6 * r0^12 * I1^2 * \phi d0^2 + 16 * I1^8 + 600 * I1^7 * \phi d0 * m * r0^2 +$
 $244 * m^2 * r0^4 * I1^6 - 1064 * I1^3 * \phi d0^2 * r0^10 * m^5 + 143 * I1^2 * \phi d0^3 * r0^12 * m^6 +$
 $974 * I1^5 * \phi d0 * r0^6 * m^3 + 345 * I1^4 * \phi d0 * r0^8 * m^4 + 1107 * I1^6 * \phi d0 * r0^4 * m^2 -$
 $5062 * r0^6 * m^3 * \phi d0^3 * I1^5 - 5400 * r0^4 * m^2 * \phi d0^3 * I1^6 - 2412 * r0^6 * m^3 * \phi d0^2 * I1^5 -$
 $2305 * r0^8 * m^4 * \phi d0^2 * I1^4 - 1011 * r0^4 * m^2 * \phi d0^2 * I1^6 + 2414 * r0^10 * m^5 * \phi d0^4 * I1^3 -$
 $210 * r0^10 * m^5 * \phi d0^3 * I1^3 + 589 * r0^12 * m^6 * \phi d0^4 * I1^2 + 2112 * I1^7 * \phi d0^4 * r0^2 * m +$
 $340 * m^3 * r0^6 * I1^5 + 96 * m^2 * r0^2 * I1^7 + 280 * m^4 * r0^8 * I1^4 + 5661 * r0^8 * m^4 * \phi d0^4 * I1^4 +$
 $5764 * r0^4 * m^2 * \phi d0^4 * I1^6 + 7672 * r0^6 * m^3 * \phi d0^4 * I1^5 - 2181 * r0^8 * m^4 * \phi d0^3 * I1^4 -$
 $12 * r0^14 * m^7 * \phi d0^2 * I1 + 4 * r0^16 * m^8 * \phi d0^3 - 75 * r0^12 * m^6 * \phi d0 * I1^2 - 18 * I1 * \phi d0 * r0^14 * m^7 +$
 $\phi d0^2 * r0^16 * m^8 + 36 * I1^2 * r0^12 * m^6 + 4 * m^7 * r0^14 * I1 - m^8 * r0^16 * \phi d0 + 80 * I1^7 * \phi d0^2 * m * r0^2$
 $- 2720 * I1^7 * \phi d0^3 * m * r0^2 + 136 * I1^3 * r0^10 * m^5 + 128 * \phi d0^2 * I1^8 + 128 * I1^8 * \phi d0 -$
 $512 * I1^8 * \phi d0^3 + 256 * I1^8 * \phi d0^4))^{(1/2)} * I1^2)^{(1/3)} * m * r0^2 * I1 + 4 * I1^4 + 24 * (-$
 $8 * r0^12 * m^6 * \phi d0^3 - 24 * I1^5 * m * r0^2 - 8 * I1^3 * m^3 * r0^6 - 24 * I1^4 * m^2 * r0^4 - 8 * I1^6 +$
 $288 * I1^6 * \phi d0^2 - 288 * I1^6 * \phi d0 - 348 * I1^3 * m^3 * r0^6 * \phi d0 + 1752 * I1^3 * r0^6 * m^3 * \phi d0^2 -$
 $672 * I1^2 * r0^8 * m^4 * \phi d0^3 - 1756 * I1^3 * r0^6 * m^3 * \phi d0^3 - 804 * I1^4 * \phi d0 * r0^4 * m^2 +$
 $492 * I1^2 * r0^8 * m^4 * \phi d0^2 - 60 * I1^2 * r0^8 * m^4 * \phi d0 + 1692 * I1^5 * \phi d0^2 * r0^2 * m -$

$804*I1^5*\phi d0*m*r0^2 + 2712*I1^4*r0^4*m^2*\phi d0^2 - 936*I1^5*\phi d0^3*r0^2*m -$
 $2124*I1^4*r0^4*m^2*\phi d0^3 + 48*r0^10*m^5*\phi d0^2*I1 - 120*r0^10*m^5*\phi d0^3*I1 + 12*3^{(1/2)}*(-\phi d0*(\phi d0 - 1)*(4*\phi d0^4*m^8*r0^16 + 46*m^7*r0^14*I1*\phi d0^3 + 76*r0^14*m^7*\phi d0^4*I1 -$
 $52*m^5*r0^10*I1^3*\phi d0 - 221*m^6*r0^12*I1^2*\phi d0^2 + 16*I1^8 + 600*I1^7*\phi d0*m*r0^2 +$
 $244*m^2*r0^4*I1^6 - 1064*I1^3*\phi d0^2*r0^10*m^5 + 143*I1^2*\phi d0^3*r0^12*m^6 +$
 $974*I1^5*\phi d0*r0^6*m^3 + 345*I1^4*\phi d0*r0^8*m^4 + 1107*I1^6*\phi d0*r0^4*m^2 -$
 $5062*r0^6*m^3*\phi d0^3*I1^5 - 5400*r0^4*m^2*\phi d0^3*I1^6 - 2412*r0^6*m^3*\phi d0^2*I1^5 -$
 $2305*r0^8*m^4*\phi d0^2*I1^4 - 1011*r0^4*m^2*\phi d0^2*I1^6 + 2414*r0^10*m^5*\phi d0^4*I1^3 -$
 $210*r0^10*m^5*\phi d0^3*I1^3 + 589*r0^12*m^6*\phi d0^4*I1^2 + 2112*I1^7*\phi d0^4*r0^2*m +$
 $340*m^3*r0^6*I1^5 + 96*m^2*r0^2*I1^7 + 280*m^4*r0^8*I1^4 + 5661*r0^8*m^4*\phi d0^4*I1^4 +$
 $5764*r0^4*m^2*\phi d0^4*I1^6 + 7672*r0^6*m^3*\phi d0^4*I1^5 - 2181*r0^8*m^4*\phi d0^3*I1^4 -$
 $12*r0^14*m^7*\phi d0^2*I1 + 4*r0^16*m^8*\phi d0^3 - 75*r0^12*m^6*\phi d0^2*I1^2 - 18*I1*\phi d0*r0^14*m^7 +$
 $\phi d0^2*r0^16*m^8 + 36*I1^2*r0^12*m^6 + 4*m^7*r0^14*I1 - m^8*r0^16*\phi d0 + 80*I1^7*\phi d0^2*m*r0^2 -$
 $- 2720*I1^7*\phi d0^3*m*r0^2 + 136*I1^3*r0^10*m^5 + 128*\phi d0^2*I1^8 + 128*I1^8*\phi d0 -$
 $512*I1^8*\phi d0^3 + 256*I1^8*\phi d0^4))^{(1/2)}*I1^2)^{(1/3)}*I1^2*\phi d0 + 48*I1^4*\phi d0^2 - 4*i^3^{(1/2)}*I1^4 -$
 $8*I1^2*(-8*r0^12*m^6*\phi d0^3 - 24*I1^5*m*r0^2 - 8*I1^3*m^3*r0^6 - 24*I1^4*m^2*r0^4 - 8*I1^6 +$
 $288*I1^6*\phi d0^2 - 288*I1^6*\phi d0 - 348*I1^3*m^3*r0^6*\phi d0 + 1752*I1^3*r0^6*m^3*\phi d0^2 -$
 $672*I1^2*r0^8*m^4*\phi d0^3 - 1756*I1^3*r0^6*m^3*\phi d0^3 - 804*I1^4*\phi d0*r0^4*m^2 +$
 $492*I1^2*r0^8*m^4*\phi d0^2 - 60*I1^2*r0^8*m^4*\phi d0 + 1692*I1^5*\phi d0^2*r0^2*m -$
 $804*I1^5*\phi d0*m*r0^2 + 2712*I1^4*r0^4*m^2*\phi d0^2 - 936*I1^5*\phi d0^3*r0^2*m -$
 $2124*I1^4*r0^4*m^2*\phi d0^3 + 48*r0^10*m^5*\phi d0^2*I1 - 120*r0^10*m^5*\phi d0^3*I1 + 12*3^{(1/2)}*(-\phi d0*(\phi d0 - 1)*(4*\phi d0^4*m^8*r0^16 + 46*m^7*r0^14*I1*\phi d0^3 + 76*r0^14*m^7*\phi d0^4*I1 -$
 $52*m^5*r0^10*I1^3*\phi d0 - 221*m^6*r0^12*I1^2*\phi d0^2 + 16*I1^8 + 600*I1^7*\phi d0*m*r0^2 +$
 $244*m^2*r0^4*I1^6 - 1064*I1^3*\phi d0^2*r0^10*m^5 + 143*I1^2*\phi d0^3*r0^12*m^6 +$
 $974*I1^5*\phi d0*r0^6*m^3 + 345*I1^4*\phi d0*r0^8*m^4 + 1107*I1^6*\phi d0*r0^4*m^2 -$
 $5062*r0^6*m^3*\phi d0^3*I1^5 - 5400*r0^4*m^2*\phi d0^3*I1^6 - 2412*r0^6*m^3*\phi d0^2*I1^5 -$
 $2305*r0^8*m^4*\phi d0^2*I1^4 - 1011*r0^4*m^2*\phi d0^2*I1^6 + 2414*r0^10*m^5*\phi d0^4*I1^3 -$
 $210*r0^10*m^5*\phi d0^3*I1^3 + 589*r0^12*m^6*\phi d0^4*I1^2 + 2112*I1^7*\phi d0^4*r0^2*m +$
 $340*m^3*r0^6*I1^5 + 96*m^2*r0^2*I1^7 + 280*m^4*r0^8*I1^4 + 5661*r0^8*m^4*\phi d0^4*I1^4 +$
 $5764*r0^4*m^2*\phi d0^4*I1^6 + 7672*r0^6*m^3*\phi d0^4*I1^5 - 2181*r0^8*m^4*\phi d0^3*I1^4 -$
 $12*r0^14*m^7*\phi d0^2*I1 + 4*r0^16*m^8*\phi d0^3 - 75*r0^12*m^6*\phi d0^2*I1^2 - 18*I1*\phi d0*r0^14*m^7 +$
 $\phi d0^2*r0^16*m^8 + 36*I1^2*r0^12*m^6 + 4*m^7*r0^14*I1 - m^8*r0^16*\phi d0 + 80*I1^7*\phi d0^2*m*r0^2 -$
 $- 2720*I1^7*\phi d0^3*m*r0^2 + 136*I1^3*r0^10*m^5 + 128*\phi d0^2*I1^8 + 128*I1^8*\phi d0 -$
 $512*I1^8*\phi d0^3 + 256*I1^8*\phi d0^4))^{(1/2)}*I1^2)^{(1/3)} + 20*(-8*r0^12*m^6*\phi d0^3 - 24*I1^5*m*r0^2 -$
 $8*I1^3*m^3*r0^6 - 24*I1^4*m^2*r0^4 - 8*I1^6 + 288*I1^6*\phi d0^2 - 288*I1^6*\phi d0 -$
 $348*I1^3*m^3*r0^6*\phi d0 + 1752*I1^3*r0^6*m^3*\phi d0^2 - 672*I1^2*r0^8*m^4*\phi d0^3 -$
 $1756*I1^3*r0^6*m^3*\phi d0^3 - 804*I1^4*\phi d0*r0^4*m^2 + 492*I1^2*r0^8*m^4*\phi d0^2 -$
 $60*I1^2*r0^8*m^4*\phi d0 + 1692*I1^5*\phi d0^2*r0^2*m - 804*I1^5*\phi d0*m*r0^2 +$
 $2712*I1^4*r0^4*m^2*\phi d0^2 - 936*I1^5*\phi d0^3*r0^2*m - 2124*I1^4*r0^4*m^2*\phi d0^3 +$
 $48*r0^10*m^5*\phi d0^2*I1 - 120*r0^10*m^5*\phi d0^3*I1 + 12*3^{(1/2)}*(-\phi d0*(\phi d0 -$
 $1)*(4*\phi d0^4*m^8*r0^16 + 46*m^7*r0^14*I1*\phi d0^3 + 76*r0^14*m^7*\phi d0^4*I1 -$
 $52*m^5*r0^10*I1^3*\phi d0 - 221*m^6*r0^12*I1^2*\phi d0^2 + 16*I1^8 + 600*I1^7*\phi d0*m*r0^2 +$
 $244*m^2*r0^4*I1^6 - 1064*I1^3*\phi d0^2*r0^10*m^5 + 143*I1^2*\phi d0^3*r0^12*m^6 +$
 $974*I1^5*\phi d0*r0^6*m^3 + 345*I1^4*\phi d0*r0^8*m^4 + 1107*I1^6*\phi d0*r0^4*m^2 -$
 $5062*r0^6*m^3*\phi d0^3*I1^5 - 5400*r0^4*m^2*\phi d0^3*I1^6 - 2412*r0^6*m^3*\phi d0^2*I1^5 -$
 $2305*r0^8*m^4*\phi d0^2*I1^4 - 1011*r0^4*m^2*\phi d0^2*I1^6 + 2414*r0^10*m^5*\phi d0^4*I1^3 -$
 $210*r0^10*m^5*\phi d0^3*I1^3 + 589*r0^12*m^6*\phi d0^4*I1^2 + 2112*I1^7*\phi d0^4*r0^2*m +$

$$\begin{aligned}
& 340*m^3*r0^6*I1^5 + 96*m*r0^2*I1^7 + 280*m^4*r0^8*I1^4 + 5661*r0^8*m^4*phi0^4*I1^4 + \\
& 5764*r0^4*m^2*phi0^4*I1^6 + 7672*r0^6*m^3*phi0^4*I1^5 - 2181*r0^8*m^4*phi0^3*I1^4 - \\
& 12*r0^14*m^7*phi0^2*I1 + 4*r0^16*m^8*phi0^3 - 75*r0^12*m^6*phi0*I1^2 - 18*I1*phi0*r0^14*m^7 + \\
& phi0^2*r0^16*m^8 + 36*I1^2*r0^12*m^6 + 4*m^7*r0^14*I1 - m^8*r0^16*phi0 + 80*I1^7*phi0^2*m*r0^2 \\
& - 2720*I1^7*phi0^3*m*r0^2 + 136*I1^3*r0^10*m^5 + 128*phi0^2*I1^8 + 128*I1^8*phi0 - \\
& 512*I1^8*phi0^3 + 256*I1^8*phi0^4))^(1/2)*I1^2)^(1/3)*r0^2*m*I1*phi0 - 40*i^3*(1/ \\
& 2)*r0^6*m^3*phi0^2*I1 + 48*i^3*(1/2)*I1^4*phi0 - 48*i^3*(1/2)*I1^4*phi0^2 + (-8*r0^12*m^6*phi0^3 - \\
& 24*I1^5*m^2*r0^2 - 8*I1^3*m^3*r0^6 - 24*I1^4*m^2*r0^4 - 8*I1^6 + 288*I1^6*phi0^2 - 288*I1^6*phi0 - \\
& 348*I1^3*m^3*r0^6*phi0 + 1752*I1^3*r0^6*m^3*phi0^2 - 672*I1^2*r0^8*m^4*phi0^3 - \\
& 1756*I1^3*r0^6*m^3*phi0^3 - 804*I1^4*phi0*r0^4*m^2 + 492*I1^2*r0^8*m^4*phi0^2 - \\
& 60*I1^2*r0^8*m^4*phi0 + 1692*I1^5*phi0^2*r0^2*m - 804*I1^5*phi0*m*r0^2 + \\
& 2712*I1^4*r0^4*m^2*phi0^2 - 936*I1^5*phi0^3*r0^2*m - 2124*I1^4*r0^4*m^2*phi0^3 + \\
& 48*r0^10*m^5*phi0^2*I1 - 120*r0^10*m^5*phi0^3*I1 + 12*3^(1/2)*(-phi0*(phi0 - \\
& 1)*(4*phi0^4*m^8*r0^16 + 46*m^7*r0^14*I1*phi0^3 + 76*r0^14*m^7*phi0^4*I1 - \\
& 52*m^5*r0^10*I1^3*phi0 - 221*m^6*r0^12*I1^2*phi0^2 + 16*I1^8 + 600*I1^7*phi0*m*r0^2 + \\
& 244*m^2*r0^4*I1^6 - 1064*I1^3*phi0^2*r0^10*m^5 + 143*I1^2*phi0^3*r0^12*m^6 + \\
& 974*I1^5*phi0*r0^6*m^3 + 345*I1^4*phi0*r0^8*m^4 + 1107*I1^6*phi0*r0^4*m^2 - \\
& 5062*r0^6*m^3*phi0^3*I1^5 - 5400*r0^4*m^2*phi0^3*I1^6 - 2412*r0^6*m^3*phi0^2*I1^5 - \\
& 2305*r0^8*m^4*phi0^2*I1^4 - 1011*r0^4*m^2*phi0^2*I1^6 + 2414*r0^10*m^5*phi0^4*I1^3 - \\
& 210*r0^10*m^5*phi0^3*I1^3 + 589*r0^12*m^6*phi0^4*I1^2 + 2112*I1^7*phi0^4*r0^2*m + \\
& 340*m^3*r0^6*I1^5 + 96*m*r0^2*I1^7 + 280*m^4*r0^8*I1^4 + 5661*r0^8*m^4*phi0^4*I1^4 + \\
& 5764*r0^4*m^2*phi0^4*I1^6 + 7672*r0^6*m^3*phi0^4*I1^5 - 2181*r0^8*m^4*phi0^3*I1^4 - \\
& 12*r0^14*m^7*phi0^2*I1 + 4*r0^16*m^8*phi0^3 - 75*r0^12*m^6*phi0*I1^2 - 18*I1*phi0*r0^14*m^7 + \\
& phi0^2*r0^16*m^8 + 36*I1^2*r0^12*m^6 + 4*m^7*r0^14*I1 - m^8*r0^16*phi0 + 80*I1^7*phi0^2*m*r0^2 \\
& - 2720*I1^7*phi0^3*m*r0^2 + 136*I1^3*r0^10*m^5 + 128*phi0^2*I1^8 + 128*I1^8*phi0 - \\
& 512*I1^8*phi0^3 + 256*I1^8*phi0^4))^(1/2)*I1^2)^(2/3) + 16*i^3*(1/2)*r0^6*m^3*phi0*I1 - 4*i^3*(1/ \\
& 2)*I1^2*r0^4*m^2 - 8*i^3*(1/2)*I1^3*m^2*r0^2 - 124*i^3*(1/2)*r0^4*m^2*phi0^2*I1^2 - 132*i^3*(1/ \\
& 2)*I1^3*phi0^2*r0^2*m + 84*i^3*(1/2)*I1^2*phi0*r0^4*m^2 + 116*i^3*(1/2)*I1^3*phi0*m*r0^2 + \\
& 124*r0^4*m^2*phi0^2*I1^2))^(1/2)
\end{aligned}$$

$$\lambda_{12} = -1/6/I1/(-8*r0^12*m^6*phi0^3 - 24*I1^5*m^2*r0^2 - 8*I1^3*m^3*r0^6 - 24*I1^4*m^2*r0^4 - \\
& 8*I1^6 + 288*I1^6*phi0^2 - 288*I1^6*phi0 - 348*I1^3*m^3*r0^6*phi0 + 1752*I1^3*r0^6*m^3*phi0^2 - \\
& 672*I1^2*r0^8*m^4*phi0^3 - 1756*I1^3*r0^6*m^3*phi0^3 - 804*I1^4*phi0*r0^4*m^2 + \\
& 492*I1^2*r0^8*m^4*phi0^2 - 60*I1^2*r0^8*m^4*phi0 + 1692*I1^5*phi0^2*r0^2*m - \\
& 804*I1^5*phi0*m*r0^2 + 2712*I1^4*r0^4*m^2*phi0^2 - 936*I1^5*phi0^3*r0^2*m - \\
& 2124*I1^4*r0^4*m^2*phi0^3 + 48*r0^10*m^5*phi0^2*I1 - 120*r0^10*m^5*phi0^3*I1 + 12*3^(1/2)*(- \\
& phi0*(phi0 - 1)*(4*phi0^4*m^8*r0^16 + 46*m^7*r0^14*I1*phi0^3 + 76*r0^14*m^7*phi0^4*I1 - \\
& 52*m^5*r0^10*I1^3*phi0 - 221*m^6*r0^12*I1^2*phi0^2 + 16*I1^8 + 600*I1^7*phi0*m*r0^2 + \\
& 244*m^2*r0^4*I1^6 - 1064*I1^3*phi0^2*r0^10*m^5 + 143*I1^2*phi0^3*r0^12*m^6 + \\
& 974*I1^5*phi0*r0^6*m^3 + 345*I1^4*phi0*r0^8*m^4 + 1107*I1^6*phi0*r0^4*m^2 - \\
& 5062*r0^6*m^3*phi0^3*I1^5 - 5400*r0^4*m^2*phi0^3*I1^6 - 2412*r0^6*m^3*phi0^2*I1^5 - \\
& 2305*r0^8*m^4*phi0^2*I1^4 - 1011*r0^4*m^2*phi0^2*I1^6 + 2414*r0^10*m^5*phi0^4*I1^3 - \\
& 210*r0^10*m^5*phi0^3*I1^3 + 589*r0^12*m^6*phi0^4*I1^2 + 2112*I1^7*phi0^4*r0^2*m + \\
& 340*m^3*r0^6*I1^5 + 96*m*r0^2*I1^7 + 280*m^4*r0^8*I1^4 + 5661*r0^8*m^4*phi0^4*I1^4 + \\
& 5764*r0^4*m^2*phi0^4*I1^6 + 7672*r0^6*m^3*phi0^4*I1^5 - 2181*r0^8*m^4*phi0^3*I1^4 - \\
& 12*r0^14*m^7*phi0^2*I1 + 4*r0^16*m^8*phi0^3 - 75*r0^12*m^6*phi0*I1^2 - 18*I1*phi0*r0^14*m^7 + \\
& phi0^2*r0^16*m^8 + 36*I1^2*r0^12*m^6 + 4*m^7*r0^14*I1 - m^8*r0^16*phi0 + 80*I1^7*phi0^2*m*r0^2$$

$- 2720*I1^7*\phi d0^3*m*r0^2 + 136*I1^3*r0^10*m^5 + 128*\phi d0^2*I1^8 + 128*I1^8*\phi d0 -$
 $512*I1^8*\phi d0^3 + 256*I1^8*\phi d0^4))^(1/2)*I1^2)^(1/3)*3^(1/2)*(-(-8*r0^12*m^6*\phi d0^3 -$
 $24*I1^5*m*r0^2 - 8*I1^3*m^3*r0^6 - 24*I1^4*m^2*r0^4 - 8*I1^6 + 288*I1^6*\phi d0^2 - 288*I1^6*\phi d0 -$
 $348*I1^3*m^3*r0^6*\phi d0 + 1752*I1^3*r0^6*m^3*\phi d0^2 - 672*I1^2*r0^8*m^4*\phi d0^3 -$
 $1756*I1^3*r0^6*m^3*\phi d0^3 - 804*I1^4*\phi d0*r0^4*m^2 + 492*I1^2*r0^8*m^4*\phi d0^2 -$
 $60*I1^2*r0^8*m^4*\phi d0 + 1692*I1^5*\phi d0^2*r0^2*m - 804*I1^5*\phi d0*m*r0^2 +$
 $2712*I1^4*r0^4*m^2*\phi d0^2 - 936*I1^5*\phi d0^3*r0^2*m - 2124*I1^4*r0^4*m^2*\phi d0^3 +$
 $48*r0^10*m^5*\phi d0^2*I1 - 120*r0^10*m^5*\phi d0^3*I1 + 12*3^(1/2)*(-\phi d0*(\phi d0 -$
 $1)*(4*\phi d0^4*m^8*r0^16 + 46*m^7*r0^14*I1*\phi d0^3 + 76*r0^14*m^7*\phi d0^4*I1 -$
 $52*m^5*r0^10*I1^3*\phi d0 - 221*m^6*r0^12*I1^2*\phi d0^2 + 16*I1^8 + 600*I1^7*\phi d0*m*r0^2 +$
 $244*m^2*r0^4*I1^6 - 1064*I1^3*\phi d0^2*r0^10*m^5 + 143*I1^2*\phi d0^3*r0^12*m^6 +$
 $974*I1^5*\phi d0*r0^6*m^3 + 345*I1^4*\phi d0*r0^8*m^4 + 1107*I1^6*\phi d0*r0^4*m^2 -$
 $5062*r0^6*m^3*\phi d0^3*I1^5 - 5400*r0^4*m^2*\phi d0^3*I1^6 - 2412*r0^6*m^3*\phi d0^2*I1^5 -$
 $2305*r0^8*m^4*\phi d0^2*I1^4 - 1011*r0^4*m^2*\phi d0^2*I1^6 + 2414*r0^10*m^5*\phi d0^4*I1^3 -$
 $210*r0^10*m^5*\phi d0^3*I1^3 + 589*r0^12*m^6*\phi d0^4*I1^2 + 2112*I1^7*\phi d0^4*r0^2*m +$
 $340*m^3*r0^6*I1^5 + 96*m^2*r0^2*I1^7 + 280*m^4*r0^8*I1^4 + 5661*r0^8*m^4*\phi d0^4*I1^4 +$
 $5764*r0^4*m^2*\phi d0^4*I1^6 + 7672*r0^6*m^3*\phi d0^4*I1^5 - 2181*r0^8*m^4*\phi d0^3*I1^4 -$
 $12*r0^14*m^7*\phi d0^2*I1 + 4*r0^16*m^8*\phi d0^3 - 75*r0^12*m^6*\phi d0^4*I1^2 - 18*I1*\phi d0*r0^14*m^7 +$
 $\phi d0^2*r0^16*m^8 + 36*I1^2*r0^12*m^6 + 4*m^7*r0^14*I1 - m^8*r0^16*\phi d0 + 80*I1^7*\phi d0^2*m*r0^2 -$
 $- 2720*I1^7*\phi d0^3*m*r0^2 + 136*I1^3*r0^10*m^5 + 128*\phi d0^2*I1^8 + 128*I1^8*\phi d0 -$
 $512*I1^8*\phi d0^3 + 256*I1^8*\phi d0^4))^(1/2)*I1^2)^(1/3)*\phi d0*(i^3^(1/2)*(-8*r0^12*m^6*\phi d0^3 -$
 $24*I1^5*m*r0^2 - 8*I1^3*m^3*r0^6 - 24*I1^4*m^2*r0^4 - 8*I1^6 + 288*I1^6*\phi d0^2 - 288*I1^6*\phi d0 -$
 $348*I1^3*m^3*r0^6*\phi d0 + 1752*I1^3*r0^6*m^3*\phi d0^2 - 672*I1^2*r0^8*m^4*\phi d0^3 -$
 $1756*I1^3*r0^6*m^3*\phi d0^3 - 804*I1^4*\phi d0*r0^4*m^2 + 492*I1^2*r0^8*m^4*\phi d0^2 -$
 $60*I1^2*r0^8*m^4*\phi d0 + 1692*I1^5*\phi d0^2*r0^2*m - 804*I1^5*\phi d0*m*r0^2 +$
 $2712*I1^4*r0^4*m^2*\phi d0^2 - 936*I1^5*\phi d0^3*r0^2*m - 2124*I1^4*r0^4*m^2*\phi d0^3 +$
 $48*r0^10*m^5*\phi d0^2*I1 - 120*r0^10*m^5*\phi d0^3*I1 + 12*3^(1/2)*(-\phi d0*(\phi d0 -$
 $1)*(4*\phi d0^4*m^8*r0^16 + 46*m^7*r0^14*I1*\phi d0^3 + 76*r0^14*m^7*\phi d0^4*I1 -$
 $52*m^5*r0^10*I1^3*\phi d0 - 221*m^6*r0^12*I1^2*\phi d0^2 + 16*I1^8 + 600*I1^7*\phi d0*m*r0^2 +$
 $244*m^2*r0^4*I1^6 - 1064*I1^3*\phi d0^2*r0^10*m^5 + 143*I1^2*\phi d0^3*r0^12*m^6 +$
 $974*I1^5*\phi d0*r0^6*m^3 + 345*I1^4*\phi d0*r0^8*m^4 + 1107*I1^6*\phi d0*r0^4*m^2 -$
 $5062*r0^6*m^3*\phi d0^3*I1^5 - 5400*r0^4*m^2*\phi d0^3*I1^6 - 2412*r0^6*m^3*\phi d0^2*I1^5 -$
 $2305*r0^8*m^4*\phi d0^2*I1^4 - 1011*r0^4*m^2*\phi d0^2*I1^6 + 2414*r0^10*m^5*\phi d0^4*I1^3 -$
 $210*r0^10*m^5*\phi d0^3*I1^3 + 589*r0^12*m^6*\phi d0^4*I1^2 + 2112*I1^7*\phi d0^4*r0^2*m +$
 $340*m^3*r0^6*I1^5 + 96*m^2*r0^2*I1^7 + 280*m^4*r0^8*I1^4 + 5661*r0^8*m^4*\phi d0^4*I1^4 +$
 $5764*r0^4*m^2*\phi d0^4*I1^6 + 7672*r0^6*m^3*\phi d0^4*I1^5 - 2181*r0^8*m^4*\phi d0^3*I1^4 -$
 $12*r0^14*m^7*\phi d0^2*I1 + 4*r0^16*m^8*\phi d0^3 - 75*r0^12*m^6*\phi d0^4*I1^2 - 18*I1*\phi d0*r0^14*m^7 +$
 $\phi d0^2*r0^16*m^8 + 36*I1^2*r0^12*m^6 + 4*m^7*r0^14*I1 - m^8*r0^16*\phi d0 + 80*I1^7*\phi d0^2*m*r0^2 -$
 $- 2720*I1^7*\phi d0^3*m*r0^2 + 136*I1^3*r0^10*m^5 + 128*\phi d0^2*I1^8 + 128*I1^8*\phi d0 -$
 $512*I1^8*\phi d0^3 + 256*I1^8*\phi d0^4))^(1/2)*I1^2)^(2/3) - 4*i^3^(1/2)*r0^8*m^4*\phi d0^2 +$
 $40*r0^6*m^3*\phi d0^2*I1 - 16*m^3*r0^6*I1*\phi d0 - 116*I1^3*\phi d0*m*r0^2 + 132*I1^3*\phi d0^2*r0^2*m +$
 $8*m^2*I1^3 + 4*m^2*r0^4*I1^2 + 4*r0^8*m^4*\phi d0^2 - 84*I1^2*\phi d0*r0^4*m^2 - 48*I1^4*\phi d0 + 4*($
 $- 8*r0^12*m^6*\phi d0^3 - 24*I1^5*m*r0^2 - 8*I1^3*m^3*r0^6 - 24*I1^4*m^2*r0^4 - 8*I1^6 +$
 $288*I1^6*\phi d0^2 - 288*I1^6*\phi d0 - 348*I1^3*m^3*r0^6*\phi d0 + 1752*I1^3*r0^6*m^3*\phi d0^2 -$
 $672*I1^2*r0^8*m^4*\phi d0^3 - 1756*I1^3*r0^6*m^3*\phi d0^3 - 804*I1^4*\phi d0*r0^4*m^2 +$
 $492*I1^2*r0^8*m^4*\phi d0^2 - 60*I1^2*r0^8*m^4*\phi d0 + 1692*I1^5*\phi d0^2*r0^2*m -$
 $804*I1^5*\phi d0*m*r0^2 + 2712*I1^4*r0^4*m^2*\phi d0^2 - 936*I1^5*\phi d0^3*r0^2*m -$

$2124*I1^4*r0^4*m^2*fd0^3 + 48*r0^10*m^5*fd0^2*I1 - 120*r0^10*m^5*fd0^3*I1 + 12*3^{(1/2)}*(-\phi d0*(\phi d0 - 1)*(4*\phi d0^4*m^8*r0^16 + 46*m^7*r0^14*I1*\phi d0^3 + 76*r0^14*m^7*\phi d0^4*I1 - 52*m^5*r0^10*I1^3*\phi d0 - 221*m^6*r0^12*I1^2*\phi d0^2 + 16*I1^8 + 600*I1^7*\phi d0*m*r0^2 + 244*m^2*r0^4*I1^6 - 1064*I1^3*\phi d0^2*r0^10*m^5 + 143*I1^2*\phi d0^3*r0^12*m^6 + 974*I1^5*\phi d0*r0^6*m^3 + 345*I1^4*\phi d0*r0^8*m^4 + 1107*I1^6*\phi d0*r0^4*m^2 - 5062*r0^6*m^3*\phi d0^3*I1^5 - 5400*r0^4*m^2*\phi d0^3*I1^6 - 2412*r0^6*m^3*\phi d0^2*I1^5 - 2305*r0^8*m^4*\phi d0^2*I1^4 - 1011*r0^4*m^2*\phi d0^2*I1^6 + 2414*r0^10*m^5*\phi d0^4*I1^3 - 210*r0^10*m^5*\phi d0^3*I1^3 + 589*r0^12*m^6*\phi d0^4*I1^2 + 2112*I1^7*\phi d0^4*r0^2*m + 340*m^3*r0^6*I1^5 + 96*m^2*r0^2*I1^7 + 280*m^4*r0^8*I1^4 + 5661*r0^8*m^4*\phi d0^4*I1^4 + 5764*r0^4*m^2*\phi d0^4*I1^6 + 7672*r0^6*m^3*\phi d0^4*I1^5 - 2181*r0^8*m^4*\phi d0^3*I1^4 - 12*r0^14*m^7*\phi d0^2*I1 + 4*r0^16*m^8*\phi d0^3 - 75*r0^12*m^6*\phi d0^4*I1^2 - 18*I1*\phi d0*r0^14*m^7 + \phi d0^2*r0^16*m^8 + 36*I1^2*r0^12*m^6 + 4*m^7*r0^14*I1 - m^8*r0^16*\phi d0 + 80*I1^7*\phi d0^2*m*r0^2 - 2720*I1^7*\phi d0^3*m*r0^2 + 136*I1^3*r0^10*m^5 + 128*\phi d0^2*I1^8 + 128*I1^8*\phi d0 - 512*I1^8*\phi d0^3 + 256*I1^8*\phi d0^4))^{(1/2)}*I1^2)^{(1/3)}*r0^4*m^2*\phi d0 - 8*(-8*r0^12*m^6*\phi d0^3 - 24*I1^5*m*r0^2 - 8*I1^3*m^3*r0^6 - 24*I1^4*m^2*r0^4 - 8*I1^6 + 288*I1^6*\phi d0^2 - 288*I1^6*\phi d0 - 348*I1^3*m^3*r0^6*\phi d0 + 1752*I1^3*r0^6*m^3*\phi d0^2 - 672*I1^2*r0^8*m^4*\phi d0^3 - 1756*I1^3*r0^6*m^3*\phi d0^3 - 804*I1^4*\phi d0*r0^4*m^2 + 492*I1^2*r0^8*m^4*\phi d0^2 - 60*I1^2*r0^8*m^4*\phi d0 + 1692*I1^5*\phi d0^2*r0^2*m - 804*I1^5*\phi d0*m*r0^2 + 2712*I1^4*r0^4*m^2*\phi d0^2 - 936*I1^5*\phi d0^3*r0^2*m - 2124*I1^4*r0^4*m^2*\phi d0^3 + 48*r0^10*m^5*fd0^2*I1 + 12*3^{(1/2)}*(-\phi d0*(\phi d0 - 1)*(4*\phi d0^4*m^8*r0^16 + 46*m^7*r0^14*I1*\phi d0^3 + 76*r0^14*m^7*\phi d0^4*I1 - 52*m^5*r0^10*I1^3*\phi d0 - 221*m^6*r0^12*I1^2*\phi d0^2 + 16*I1^8 + 600*I1^7*\phi d0*m*r0^2 + 244*m^2*r0^4*I1^6 - 1064*I1^3*\phi d0^2*r0^10*m^5 + 143*I1^2*\phi d0^3*r0^12*m^6 + 974*I1^5*\phi d0*r0^6*m^3 + 345*I1^4*\phi d0*r0^8*m^4 + 1107*I1^6*\phi d0*r0^4*m^2 - 5062*r0^6*m^3*\phi d0^3*I1^5 - 5400*r0^4*m^2*\phi d0^3*I1^6 - 2412*r0^6*m^3*\phi d0^2*I1^5 - 2305*r0^8*m^4*\phi d0^2*I1^4 - 1011*r0^4*m^2*\phi d0^2*I1^6 + 2414*r0^10*m^5*\phi d0^4*I1^3 - 210*r0^10*m^5*\phi d0^3*I1^3 + 589*r0^12*m^6*\phi d0^4*I1^2 + 2112*I1^7*\phi d0^4*r0^2*m + 340*m^3*r0^6*I1^5 + 96*m^2*r0^2*I1^7 + 280*m^4*r0^8*I1^4 + 5661*r0^8*m^4*\phi d0^4*I1^4 + 5764*r0^4*m^2*\phi d0^4*I1^6 + 7672*r0^6*m^3*\phi d0^4*I1^5 - 2181*r0^8*m^4*\phi d0^3*I1^4 - 12*r0^14*m^7*\phi d0^2*I1 + 4*r0^16*m^8*\phi d0^3 - 75*r0^12*m^6*\phi d0^4*I1^2 - 18*I1*\phi d0*r0^14*m^7 + \phi d0^2*r0^16*m^8 + 36*I1^2*r0^12*m^6 + 4*m^7*r0^14*I1 - m^8*r0^16*\phi d0 + 80*I1^7*\phi d0^2*m*r0^2 - 2720*I1^7*\phi d0^3*m*r0^2 + 136*I1^3*r0^10*m^5 + 128*\phi d0^2*I1^8 + 128*I1^8*\phi d0 - 512*I1^8*\phi d0^3 + 256*I1^8*\phi d0^4))^{(1/2)}*I1^2)^{(1/3)}*m*r0^2*I1 + 4*I1^4 + 24*(-8*r0^12*m^6*\phi d0^3 - 24*I1^5*m*r0^2 - 8*I1^3*m^3*r0^6 - 24*I1^4*m^2*r0^4 - 8*I1^6 + 288*I1^6*\phi d0^2 - 288*I1^6*\phi d0 - 348*I1^3*m^3*r0^6*\phi d0 + 1752*I1^3*r0^6*m^3*\phi d0^2 - 672*I1^2*r0^8*m^4*\phi d0^3 - 1756*I1^3*r0^6*m^3*\phi d0^3 - 804*I1^4*\phi d0*r0^4*m^2 + 492*I1^2*r0^8*m^4*\phi d0^2 - 60*I1^2*r0^8*m^4*\phi d0 + 1692*I1^5*\phi d0^2*r0^2*m - 804*I1^5*\phi d0*m*r0^2 + 2712*I1^4*r0^4*m^2*\phi d0^2 - 936*I1^5*\phi d0^3*r0^2*m - 2124*I1^4*r0^4*m^2*\phi d0^3 + 48*r0^10*m^5*fd0^2*I1 - 120*r0^10*m^5*fd0^3*I1 + 12*3^{(1/2)}*(-\phi d0*(\phi d0 - 1)*(4*\phi d0^4*m^8*r0^16 + 46*m^7*r0^14*I1*\phi d0^3 + 76*r0^14*m^7*\phi d0^4*I1 - 52*m^5*r0^10*I1^3*\phi d0 - 221*m^6*r0^12*I1^2*\phi d0^2 + 16*I1^8 + 600*I1^7*\phi d0*m*r0^2 + 244*m^2*r0^4*I1^6 - 1064*I1^3*\phi d0^2*r0^10*m^5 + 143*I1^2*\phi d0^3*r0^12*m^6 + 974*I1^5*\phi d0*r0^6*m^3 + 345*I1^4*\phi d0*r0^8*m^4 + 1107*I1^6*\phi d0*r0^4*m^2 - 5062*r0^6*m^3*\phi d0^3*I1^5 - 5400*r0^4*m^2*\phi d0^3*I1^6 - 2412*r0^6*m^3*\phi d0^2*I1^5 - 2305*r0^8*m^4*\phi d0^2*I1^4 - 1011*r0^4*m^2*\phi d0^2*I1^6 + 2414*r0^10*m^5*\phi d0^4*I1^3 - 210*r0^10*m^5*\phi d0^3*I1^3 + 589*r0^12*m^6*\phi d0^4*I1^2 + 2112*I1^7*\phi d0^4*r0^2*m + 340*m^3*r0^6*I1^5 + 96*m^2*r0^2*I1^7 + 280*m^4*r0^8*I1^4 + 5661*r0^8*m^4*\phi d0^4*I1^4 +$

$$\begin{aligned}
& 5764 * r0^4 * m^2 * \phi d0^4 * I1^6 + 7672 * r0^6 * m^3 * \phi d0^4 * I1^5 - 2181 * r0^8 * m^4 * \phi d0^3 * I1^4 - \\
& 12 * r0^14 * m^7 * \phi d0^2 * I1 + 4 * r0^16 * m^8 * \phi d0^3 - 75 * r0^12 * m^6 * \phi d0^1 * I1^2 - 18 * I1^1 * \phi d0 * r0^14 * m^7 + \\
& \phi d0^2 * r0^16 * m^8 + 36 * I1^2 * r0^12 * m^6 + 4 * m^7 * r0^14 * I1 - m^8 * r0^16 * \phi d0 + 80 * I1^7 * \phi d0^2 * m * r0^2 \\
& - 2720 * I1^7 * \phi d0^3 * m * r0^2 + 136 * I1^3 * r0^10 * m^5 + 128 * \phi d0^2 * I1^8 + 128 * I1^8 * \phi d0 - \\
& 512 * I1^8 * \phi d0^3 + 256 * I1^8 * \phi d0^4)^(1/2) * I1^2)^(1/3) * I1^2 * \phi d0 + 48 * I1^4 * \phi d0^2 - 4 * i^3 * 3^(1/2) * I1^4 - \\
& 8 * I1^2 * (-8 * r0^12 * m^6 * \phi d0^3 - 24 * I1^5 * m * r0^2 - 8 * I1^3 * m^3 * r0^6 - 24 * I1^4 * m^2 * r0^4 - 8 * I1^6 + \\
& 288 * I1^6 * \phi d0^2 - 288 * I1^6 * \phi d0 - 348 * I1^3 * m^3 * r0^6 * \phi d0 + 1752 * I1^3 * r0^6 * m^3 * \phi d0^2 - \\
& 672 * I1^2 * r0^8 * m^4 * \phi d0^3 - 1756 * I1^3 * r0^6 * m^3 * \phi d0^3 - 804 * I1^4 * \phi d0 * r0^4 * m^2 + \\
& 492 * I1^2 * r0^8 * m^4 * \phi d0^2 - 60 * I1^2 * r0^8 * m^4 * \phi d0 + 1692 * I1^5 * \phi d0^2 * r0^2 * m - \\
& 804 * I1^5 * \phi d0 * m * r0^2 + 2712 * I1^4 * r0^4 * m^2 * \phi d0^2 - 936 * I1^5 * \phi d0^3 * r0^2 * m - \\
& 2124 * I1^4 * r0^4 * m^2 * \phi d0^3 + 48 * r0^10 * m^5 * \phi d0^2 * I1 - 120 * r0^10 * m^5 * \phi d0^3 * I1 + 12 * 3^(1/2) * (- \\
& \phi d0 * (\phi d0 - 1) * (4 * \phi d0^4 * m^8 * r0^16 + 46 * m^7 * r0^14 * I1 * \phi d0^3 + 76 * r0^14 * m^7 * \phi d0^4 * I1 - \\
& 52 * m^5 * r0^10 * I1^3 * \phi d0 - 221 * m^6 * r0^12 * I1^2 * \phi d0^2 + 16 * I1^8 + 600 * I1^7 * \phi d0 * m * r0^2 + \\
& 244 * m^2 * r0^4 * I1^6 - 1064 * I1^3 * \phi d0^2 * r0^10 * m^5 + 143 * I1^2 * \phi d0^3 * r0^12 * m^6 + \\
& 974 * I1^5 * \phi d0 * r0^6 * m^3 + 345 * I1^4 * \phi d0 * r0^8 * m^4 + 1107 * I1^6 * \phi d0 * r0^4 * m^2 - \\
& 5062 * r0^6 * m^3 * \phi d0^3 * I1^5 - 5400 * r0^4 * m^2 * \phi d0^3 * I1^6 - 2412 * r0^6 * m^3 * \phi d0^2 * I1^5 - \\
& 2305 * r0^8 * m^4 * \phi d0^2 * I1^4 - 1011 * r0^4 * m^2 * \phi d0^2 * I1^6 + 2414 * r0^10 * m^5 * \phi d0^4 * I1^3 - \\
& 210 * r0^10 * m^5 * \phi d0^3 * I1^3 + 589 * r0^12 * m^6 * \phi d0^4 * I1^2 + 2112 * I1^7 * \phi d0^4 * r0^2 * m + \\
& 340 * m^3 * r0^6 * I1^5 + 96 * m * r0^2 * I1^7 + 280 * m^4 * r0^8 * I1^4 + 5661 * r0^8 * m^4 * \phi d0^4 * I1^4 + \\
& 5764 * r0^4 * m^2 * \phi d0^4 * I1^6 + 7672 * r0^6 * m^3 * \phi d0^4 * I1^5 - 2181 * r0^8 * m^4 * \phi d0^3 * I1^4 - \\
& 12 * r0^14 * m^7 * \phi d0^2 * I1 + 4 * r0^16 * m^8 * \phi d0^3 - 75 * r0^12 * m^6 * \phi d0^1 * I1^2 - 18 * I1^1 * \phi d0 * r0^14 * m^7 + \\
& \phi d0^2 * r0^16 * m^8 + 36 * I1^2 * r0^12 * m^6 + 4 * m^7 * r0^14 * I1 - m^8 * r0^16 * \phi d0 + 80 * I1^7 * \phi d0^2 * m * r0^2 \\
& - 2720 * I1^7 * \phi d0^3 * m * r0^2 + 136 * I1^3 * r0^10 * m^5 + 128 * \phi d0^2 * I1^8 + 128 * I1^8 * \phi d0 - \\
& 512 * I1^8 * \phi d0^3 + 256 * I1^8 * \phi d0^4)^(1/2) * I1^2)^(1/3) + 20 * (-8 * r0^12 * m^6 * \phi d0^3 - 24 * I1^5 * m * r0^2 - \\
& 8 * I1^3 * m^3 * r0^6 - 24 * I1^4 * m^2 * r0^4 - 8 * I1^6 + 28 * I1^6 * \phi d0^2 - 288 * I1^6 * \phi d0 - \\
& 348 * I1^3 * m^3 * r0^6 * \phi d0 + 1752 * I1^3 * r0^6 * m^3 * \phi d0^2 - 672 * I1^2 * r0^8 * m^4 * \phi d0^3 - \\
& 1756 * I1^3 * r0^6 * m^3 * \phi d0^3 - 804 * I1^4 * \phi d0 * r0^4 * m^2 + 492 * I1^2 * r0^8 * m^4 * \phi d0^2 - \\
& 60 * I1^2 * r0^8 * m^4 * \phi d0 + 1692 * I1^5 * \phi d0^2 * r0^2 * m - 804 * I1^5 * \phi d0 * m * r0^2 + \\
& 2712 * I1^4 * r0^4 * m^2 * \phi d0^2 - 936 * I1^5 * \phi d0^3 * r0^2 * m - 2124 * I1^4 * r0^4 * m^2 * \phi d0^3 + \\
& 48 * r0^10 * m^5 * \phi d0^2 * I1 - 120 * r0^10 * m^5 * \phi d0^3 * I1 + 12 * 3^(1/2) * (- \phi d0 * (\phi d0 - \\
& 1) * (4 * \phi d0^4 * m^8 * r0^16 + 46 * m^7 * r0^14 * I1 * \phi d0^3 + 76 * r0^14 * m^7 * \phi d0^4 * I1 - \\
& 52 * m^5 * r0^10 * I1^3 * \phi d0 - 221 * m^6 * r0^12 * I1^2 * \phi d0^2 + 16 * I1^8 + 600 * I1^7 * \phi d0 * m * r0^2 + \\
& 244 * m^2 * r0^4 * I1^6 - 1064 * I1^3 * \phi d0^2 * r0^10 * m^5 + 143 * I1^2 * \phi d0^3 * r0^12 * m^6 + \\
& 974 * I1^5 * \phi d0 * r0^6 * m^3 + 345 * I1^4 * \phi d0 * r0^8 * m^4 + 1107 * I1^6 * \phi d0 * r0^4 * m^2 - \\
& 5062 * r0^6 * m^3 * \phi d0^3 * I1^5 - 5400 * r0^4 * m^2 * \phi d0^3 * I1^6 - 2412 * r0^6 * m^3 * \phi d0^2 * I1^5 - \\
& 2305 * r0^8 * m^4 * \phi d0^2 * I1^4 - 1011 * r0^4 * m^2 * \phi d0^2 * I1^6 + 2414 * r0^10 * m^5 * \phi d0^4 * I1^3 - \\
& 210 * r0^10 * m^5 * \phi d0^3 * I1^3 + 589 * r0^12 * m^6 * \phi d0^4 * I1^2 + 2112 * I1^7 * \phi d0^4 * r0^2 * m + \\
& 340 * m^3 * r0^6 * I1^5 + 96 * m * r0^2 * I1^7 + 280 * m^4 * r0^8 * I1^4 + 5661 * r0^8 * m^4 * \phi d0^4 * I1^4 + \\
& 5764 * r0^4 * m^2 * \phi d0^4 * I1^6 + 7672 * r0^6 * m^3 * \phi d0^4 * I1^5 - 2181 * r0^8 * m^4 * \phi d0^3 * I1^4 - \\
& 12 * r0^14 * m^7 * \phi d0^2 * I1 + 4 * r0^16 * m^8 * \phi d0^3 - 75 * r0^12 * m^6 * \phi d0^1 * I1^2 - 18 * I1^1 * \phi d0 * r0^14 * m^7 + \\
& \phi d0^2 * r0^16 * m^8 + 36 * I1^2 * r0^12 * m^6 + 4 * m^7 * r0^14 * I1 - m^8 * r0^16 * \phi d0 + 80 * I1^7 * \phi d0^2 * m * r0^2 \\
& - 2720 * I1^7 * \phi d0^3 * m * r0^2 + 136 * I1^3 * r0^10 * m^5 + 128 * \phi d0^2 * I1^8 + 128 * I1^8 * \phi d0 - \\
& 512 * I1^8 * \phi d0^3 + 256 * I1^8 * \phi d0^4)^(1/2) * I1^2)^(1/3) * r0^2 * m * I1^1 * \phi d0 - 40 * i^3 * 3^(1/2) * \\
& 2 * r0^6 * m^3 * \phi d0^2 * I1 + 48 * i^3 * 3^(1/2) * I1^4 * \phi d0 - 48 * i^3 * 3^(1/2) * I1^4 * \phi d0^2 + (-8 * r0^12 * m^6 * \phi d0^3 - \\
& 24 * I1^5 * m * r0^2 - 8 * I1^3 * m^3 * r0^6 - 24 * I1^4 * m^2 * r0^4 - 8 * I1^6 + 288 * I1^6 * \phi d0^2 - 288 * I1^6 * \phi d0 - \\
& 348 * I1^3 * m^3 * r0^6 * \phi d0 + 1752 * I1^3 * r0^6 * m^3 * \phi d0^2 - 672 * I1^2 * r0^8 * m^4 * \phi d0^3 - \\
& 1756 * I1^3 * r0^6 * m^3 * \phi d0^3 - 804 * I1^4 * \phi d0 * r0^4 * m^2 + 492 * I1^2 * r0^8 * m^4 * \phi d0^2 -
\end{aligned}$$

$$\begin{aligned}
& 60*I1^2*r0^8*m^4*phi0 + 1692*I1^5*phi0^2*r0^2*m - 804*I1^5*phi0*m*r0^2 + \\
& 2712*I1^4*r0^4*m^2*phi0^2 - 936*I1^5*phi0^3*r0^2*m - 2124*I1^4*r0^4*m^2*phi0^3 + \\
& 48*r0^10*m^5*phi0^2*I1 - 120*r0^10*m^5*phi0^3*I1 + 12*3^(1/2)*(-phi0*(phi0 - \\
& 1)*(4*phi0^4*m^8*r0^16 + 46*m^7*r0^14*I1*phi0^3 + 76*r0^14*m^7*phi0^4*I1 - \\
& 52*m^5*r0^10*I1^3*phi0 - 221*m^6*r0^12*I1^2*phi0^2 + 16*I1^8 + 600*I1^7*phi0*m*r0^2 + \\
& 244*m^2*r0^4*I1^6 - 1064*I1^3*phi0^2*r0^10*m^5 + 143*I1^2*phi0^3*r0^12*m^6 + \\
& 974*I1^5*phi0*r0^6*m^3 + 345*I1^4*phi0*r0^8*m^4 + 1107*I1^6*phi0*r0^4*m^2 - \\
& 5062*r0^6*m^3*phi0^3*I1^5 - 5400*r0^4*m^2*phi0^3*I1^6 - 2412*r0^6*m^3*phi0^2*I1^5 - \\
& 2305*r0^8*m^4*phi0^2*I1^4 - 1011*r0^4*m^2*phi0^2*I1^6 + 2414*r0^10*m^5*phi0^4*I1^3 - \\
& 210*r0^10*m^5*phi0^3*I1^3 + 589*r0^12*m^6*phi0^4*I1^2 + 2112*I1^7*phi0^4*r0^2*m + \\
& 340*m^3*r0^6*I1^5 + 96*m^2*r0^2*I1^7 + 280*m^4*r0^8*I1^4 + 5661*r0^8*m^4*phi0^4*I1^4 + \\
& 5764*r0^4*m^2*phi0^4*I1^6 + 7672*r0^6*m^3*phi0^4*I1^5 - 2181*r0^8*m^4*phi0^3*I1^4 - \\
& 12*r0^14*m^7*phi0^2*I1 + 4*r0^16*m^8*phi0^3 - 75*r0^12*m^6*phi0*I1^2 - 18*I1*phi0*r0^14*m^7 + \\
& phi0^2*r0^16*m^8 + 36*I1^2*r0^12*m^6 + 4*m^7*r0^14*I1 - m^8*r0^16*phi0 + 80*I1^7*phi0^2*m*r0^2 - \\
& 2720*I1^7*phi0^3*m*r0^2 + 136*I1^3*r0^10*m^5 + 128*phi0^2*I1^8 + 128*I1^8*phi0 - \\
& 512*I1^8*phi0^3 + 256*I1^8*phi0^4))^(1/2)*I1^2)^(2/3) + 16*i^3^(1/2)*r0^6*m^3*phi0*I1 - 4*i^3^(1/ \\
& 2)*I1^2*r0^4*m^2 - 8*i^3^(1/2)*I1^3*m^2*r0^2 - 124*i^3^(1/2)*r0^4*m^2*phi0^2*I1^2 - 132*i^3^(1/ \\
& 2)*I1^3*phi0^2*r0^2*m + 84*i^3^(1/2)*I1^2*phi0*r0^4*m^2 + 116*i^3^(1/2)*I1^3*phi0*m*r0^2 + \\
& 124*r0^4*m^2*phi0^2*I1^2))^(1/2)
\end{aligned}$$

$$\lambda_{13,14} = +/- i * r0 * phi0 * (m / (3 * I3A))^(1/2)$$

$$\lambda_{15,16} = +/- phi0 * ((- r0^2*m + (r0^4*m^2 + 20*I3A^2 + 4*r0^2*m*I3A)^(1/2)) / (2*I3A))^(1/2)$$

$$\lambda_{17,18} = +/- phi0 * ((- r0^2*m - (r0^4*m^2 + 20*I3A^2 + 4*r0^2*m*I3A)^(1/2)) / (2*I3A))^(1/2)$$

where I1 represents I1A + I1D, I3 represents I3A + I3D, and m represents mA + mC.

Appendix C

TWO-VEHICLE EMFF OPTIMAL GAINS

The optimal gains discussed on page 160 were calculated using the Matlab Control Toolbox and are shown here. As discussed in Section 6.5, gains were calculated for three scenarios: cheap, reasonable, and expensive control. The corresponding gains are K_{cheap} , $K_{\text{reasonable}}$, and $K_{\text{expensive}}$, as shown below.

K_Expendive = 1.0e + 008 *

Columns 1 through 10

-0.0002	0.0002	0.0000	0.0000	-0.0000	-0.0000	0.0000	-0.0000	-0.0000	-0.0709
0.0003	0.0012	-0.0000	-0.0000	0.0000	-0.0021	-0.0000	0.0000	-0.0004	0.0680
-0.0000	-0.0000	0.0044	0.0000	0.0000	-0.0000	0.0000	0.0000	-0.0000	-0.0000
-0.0002	0.0002	0.0000	0.0000	-0.0000	-0.0000	0.0000	-0.0000	-0.0000	-0.0709
0.0003	0.0012	-0.0000	-0.0000	0.0000	-0.0004	-0.0000	0.0000	-0.0021	0.0680
-0.0000	-0.0000	0.0044	0.0000	0.0000	-0.0000	0.0000	0.0000	-0.0000	-0.0000
0.0000	0.0000	-0.0000	-0.0000	0.0000	0.0000	-0.0000	-0.0000	0.0000	0.0000
-0.0000	-0.0000	0.0000	-0.0000	-0.0000	-0.0000	0.0000	0.0000	-0.0000	-0.0000
-0.0000	-0.0000	0.0000	0.0000	-0.0000	-0.0000	0.0000	-0.0000	0.0000	-0.0000
0.0000	0.0000	-0.0000	-0.0000	-0.0000	0.0000	-0.0000	0.0000	0.0000	0.0000
-0.0000	-0.0000	0.0000	0.0000	0.0000	-0.0000	-0.0000	-0.0000	-0.0000	-0.0000
-0.0000	-0.0000	0.0000	0.0000	-0.0000	0.0000	0.0000	-0.0000	-0.0000	-0.0000
-0.0000	-0.0000	0.0000	0.0000	-0.0000	0.0000	0.0000	-0.0000	-0.0000	-0.0000

Columns 11 through 18

-0.0853	0.0000	0.0000	-0.0000	-0.0000	0.0000	-0.0000	-0.0000
0.9295	-0.0000	-0.0000	0.0000	-0.0171	-0.0000	0.0000	0.0004
-0.0000	1.4074	-0.0000	0.0000	-0.0000	-0.0000	0.0000	-0.0000
-0.0853	0.0000	0.0000	-0.0000	-0.0000	0.0000	-0.0000	-0.0000
0.9295	-0.0000	-0.0000	0.0000	0.0004	-0.0000	0.0000	-0.0171

-0.0000 1.4074 -0.0000 0.0000 -0.0000 -0.0000 0.0000 -0.0000
0.0000 -0.0000 -0.0000 0.0000 0.0000 0.0000 -0.0000 0.0000
-0.0000 0.0000 0.0000 -0.0000 -0.0000 -0.0000 0.0000 -0.0000
-0.0000 0.0000 0.0000 -0.0000 -0.0000 0.0000 -0.0000 0.0000
0.0000 -0.0000 0.0000 -0.0000 0.0000 -0.0000 0.0000 0.0000
-0.0000 0.0000 -0.0000 0.0000 -0.0000 0.0000 -0.0000 -0.0000
-0.0000 0.0000 0.0000 -0.0000 0.0000 0.0000 -0.0000 -0.0000

K_Reasonable = 1.0e + 008 *

Columns 1 through 10

-0.0016	0.0007	0.0000	0.0000	0.0000	-0.0000	0.0000	0.0000	-0.0000	-0.2181
0.0009	0.0164	-0.0000	0.0000	-0.0000	-0.0224	-0.0000	-0.0000	-0.0038	0.0737
-0.0000	-0.0000	0.0471	0.0001	0.0005	-0.0000	0.0000	0.0002	0.0000	-0.0000
-0.0016	0.0007	0.0000	0.0000	0.0000	-0.0000	0.0000	0.0000	-0.0000	-0.2181
0.0009	0.0164	-0.0000	0.0000	-0.0000	-0.0038	-0.0000	-0.0000	-0.0224	0.0737
-0.0000	-0.0000	0.0471	0.0000	0.0002	-0.0000	0.0001	0.0005	0.0000	-0.0000
-0.0000	-0.0000	-0.0000	-0.0000	0.0000	-0.0000	-0.0000	-0.0000	-0.0000	-0.0000
0.0000	0.0000	0.0000	-0.0000	-0.0000	0.0000	0.0000	0.0000	0.0000	0.0000
-0.0000	-0.0000	0.0000	-0.0000	0.0000	-0.0000	0.0000	0.0000	0.0000	-0.0000
0.0000	-0.0000	-0.0000	-0.0000	-0.0000	0.0000	-0.0000	0.0000	-0.0000	0.0000
0.0000	-0.0000	0.0000	0.0000	0.0000	-0.0000	-0.0000	-0.0000	0.0000	0.0000
-0.0000	-0.0000	0.0000	-0.0000	0.0000	0.0000	0.0000	0.0000	-0.0000	-0.0000

Columns 11 through 18

-0.0881	0.0000	-0.0000	0.0000	-0.0000	0.0000	0.0000	0.0000	-0.0000
2.7782	-0.0000	0.0000	-0.0000	-0.0554	-0.0000	0.0000	0.0011	
-0.0000	4.6022	-0.0000	0.0001	-0.0000	-0.0000	0.0000	0.0000	-0.0000
-0.0881	0.0000	-0.0000	0.0000	-0.0000	0.0000	0.0000	0.0000	-0.0000
2.7782	-0.0000	0.0000	-0.0000	0.0011	-0.0000	0.0000	0.0000	-0.0554

-0.0000 4.6022 -0.0000 0.0000 -0.0000 -0.0000 0.0001 -0.0000
-0.0000 -0.0000 -0.0000 0.0000 -0.0000 0.0000 -0.0000 -0.0000
0.0000 0.0000 0.0000 -0.0000 0.0000 -0.0000 0.0000 0.0000
-0.0000 0.0000 -0.0000 0.0000 -0.0000 0.0000 -0.0000 0.0000
0.0000 -0.0000 0.0000 -0.0000 0.0000 -0.0000 0.0000 0.0000
-0.0000 0.0000 -0.0000 0.0000 -0.0000 0.0000 -0.0000 -0.0000
-0.0000 0.0000 -0.0000 0.0000 0.0000 0.0000 -0.0000 -0.0000

K_Cheap = 1.0e + 009 *

Columns 1 through 10

-0.0016	0.0002	0.0000	0.0000	0.0000	-0.0000	0.0000	-0.0000	-0.0000	-0.0689
0.0003	0.0168	-0.0000	-0.0000	-0.0000	-0.0225	-0.0000	0.0000	-0.0039	0.0075
-0.0000	-0.0000	0.0474	0.0000	0.0005	-0.0000	0.0000	0.0003	0.0000	-0.0000
-0.0016	0.0002	0.0000	0.0000	0.0000	-0.0000	0.0000	-0.0000	-0.0000	-0.0689
0.0003	0.0168	-0.0000	-0.0000	-0.0000	-0.0039	-0.0000	0.0000	-0.0225	0.0075
-0.0000	-0.0000	0.0474	0.0000	0.0003	-0.0000	0.0000	0.0005	0.0000	-0.0000
0.0000	0.0000	-0.0000	-0.0000	0.0000	-0.0000	-0.0000	-0.0000	0.0000	0.0000
0.0000	0.0000	0.0000	-0.0000	-0.0000	-0.0000	0.0000	0.0000	0.0000	0.0000
-0.0000	-0.0000	0.0000	0.0000	0.0000	-0.0000	0.0000	-0.0000	0.0000	-0.0000
0.0000	0.0000	-0.0000	-0.0000	-0.0000	0.0000	-0.0000	0.0000	0.0000	0.0000
-0.0000	-0.0000	0.0000	0.0000	0.0000	-0.0000	-0.0000	-0.0000	0.0000	-0.0000
-0.0000	-0.0000	0.0000	0.0000	0.0000	0.0000	0.0000	-0.0000	-0.0000	-0.0000

Columns 11 through 18

-0.0089	0.0000	0.0000	0.0000	-0.0000	0.0000	-0.0000	-0.0000
0.8708	-0.0000	-0.0000	-0.0000	-0.0176	-0.0000	0.0000	0.0003
-0.0000	1.4602	-0.0000	0.0000	-0.0000	-0.0000	0.0000	-0.0000
-0.0089	0.0000	0.0000	0.0000	-0.0000	0.0000	-0.0000	-0.0000
0.8708	-0.0000	-0.0000	-0.0000	0.0003	-0.0000	0.0000	-0.0176

-0.0000 1.4602 -0.0000 0.0000 -0.0000 -0.0000 0.0000 -0.0000
0.0000 -0.0000 -0.0000 0.0000 0.0000 0.0000 -0.0000 0.0000
0.0000 0.0000 0.0000 -0.0000 0.0000 -0.0000 0.0000 0.0000
-0.0000 0.0000 0.0000 0.0000 -0.0000 0.0000 -0.0000 0.0000
0.0000 -0.0000 0.0000 -0.0000 0.0000 -0.0000 0.0000 0.0000
-0.0000 0.0000 -0.0000 0.0000 -0.0000 0.0000 -0.0000 -0.0000
-0.0000 0.0000 0.0000 0.0000 0.0000 0.0000 -0.0000 -0.0000

Appendix D

EMFF CONTROL EXPERIMENTS

The control analysis in Chapter 6 demonstrates some interesting characteristics of a rotating formation flight array. In particular, a two-spacecraft array linearized about a steady-spin maneuver has two real open-loop poles, one positive and one negative, whose magnitudes are proportional to the array’s spin rate. Hence the rotating system is unstable, with one pole lying in the right-half complex plane.

In Chapter 7, numerical simulations were used to demonstrate closed-loop, stable control of such a system. However, without a multi-body testbed on which to perform experiments, it is difficult to validate this control on hardware. If, instead, we can demonstrate control on a simplified hardware system *with unstable dynamics similar to those of the rotating array*, we will gain confidence in our ability to use electromagnetic control for interferometric formation flight applications.

In Section D.1, we describe a simple airtrack system and show experimental results demonstrating closed-loop control of an unstable system using electromagnets. Then in Section D.2, we introduce a testbed, currently under development, that is more representative of a true formation flight system. Preliminary experimental results are presented, and further experiments are suggested for the future.

D.1 Linear Airtrack

We now present a linear airtrack that can be configured in either a *stable* or *unstable* geometry. In Section D.1.1, we first describe the airtrack, and in Section D.1.2, we discuss the dynamics and control of both the stable and unstable configurations. In Section D.1.3, we discuss the poles of the unstable airtrack system and compare them to the poles of an electromagnetic formation flight system. Finally, in Section D.1.4, we present experimental results that demonstrate closed-loop control using the airtrack system.

D.1.1 Airtrack Description

The airtrack, shown in Figure D.1, is a one-dimensional platform on which bodies are allowed to translate with only linear motion. The bodies are levitated by compressed air flowing through small holes in the track surface, and thus “float” on the nearly frictionless surface.

A permanent magnet is mounted on a “slider,” free to translate along the track. An electromagnet is fixed to the far end of the track, so that the permanent magnet translates relative to the fixed electromagnet. The electromagnet is composed of a copper wire wound several times around an iron core. By modulating the current running through the wire, we achieve a desired strength for the electromagnet’s magnetic field, as described in Chapter 5¹. The interaction of this magnetic field with that of the permanent magnet then causes forces to be applied to the two bodies. The direction and magnitude of the forces depend on the direction and magnitude of the current in the electromagnet, as well as the field characteristics of the permanent magnet. These forces may be used to attract or repel the free magnet relative to the fixed electromagnet, thus controlling the relative separation distance b between the two bodies. Notice that mounting a permanent magnet onto the

1. The iron core acts to “amplify” the magnetic field. This amplification is useful for generating sufficient magnetic field strengths on this testbed, since copper wire is used instead of superconducting wire, and the applied current is therefore limited.

slider, instead of an electromagnet, eliminates any wires that would be connected to the free body, thus avoiding corruption of the nearly frictionless dynamics.

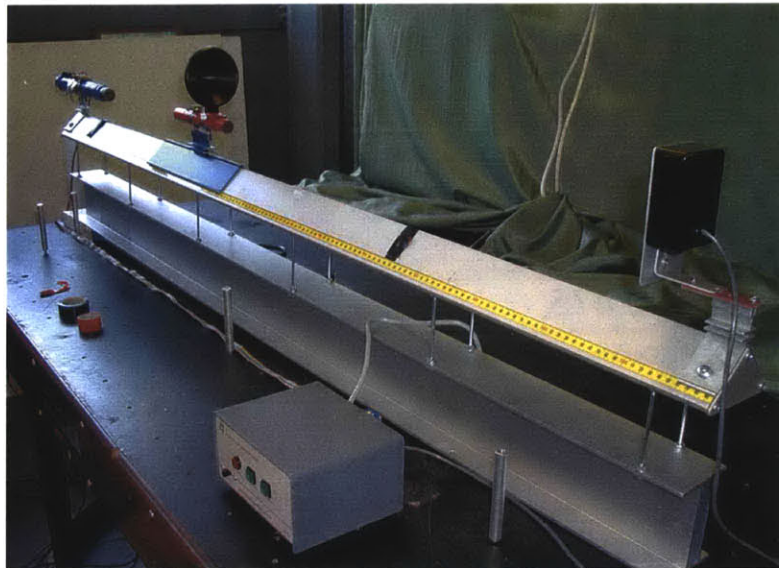


Figure D.1 Linear Airtrack Used to Demonstrate Simplified Electromagnetic Formation Control

Our goal is to implement feedback control of the relative separation distance between the fixed electromagnet and the free permanent magnet. Hence a sensory measurement of the distance between the two bodies is required. This is provided by an ultrasonic displacement sensor, shown fixed to the near end of the track in Figure D.1. The transceiver emits an ultrasonic signal, which reflects off a cone attached to the free magnet. The transceiver receives the reflected signal and calculates the distance at a 30 Hz update rate, based on the speed of sound and the time of flight. The separation distance between the two magnets is then computed by subtracting the measured distance from the length of the airtrack.

To implement feedback control, a real-time computer is used to process the sensor data, compute the required control, and output the control signal through an amplifier to the electromagnet. dSPACE hardware and software were used with a desktop computer for both data acquisition and real-time control. Figure D.2 shows a virtual control panel designed for this system. It allows the user to monitor variables such as the measured dis-

tance from the displacement sensor to the permanent magnet, the separation distance between the electromagnet and the permanent magnet, and both the raw and amplified feedback control signals. It also allows the user to tune the various control gains using virtual knobs or numeric inputs.

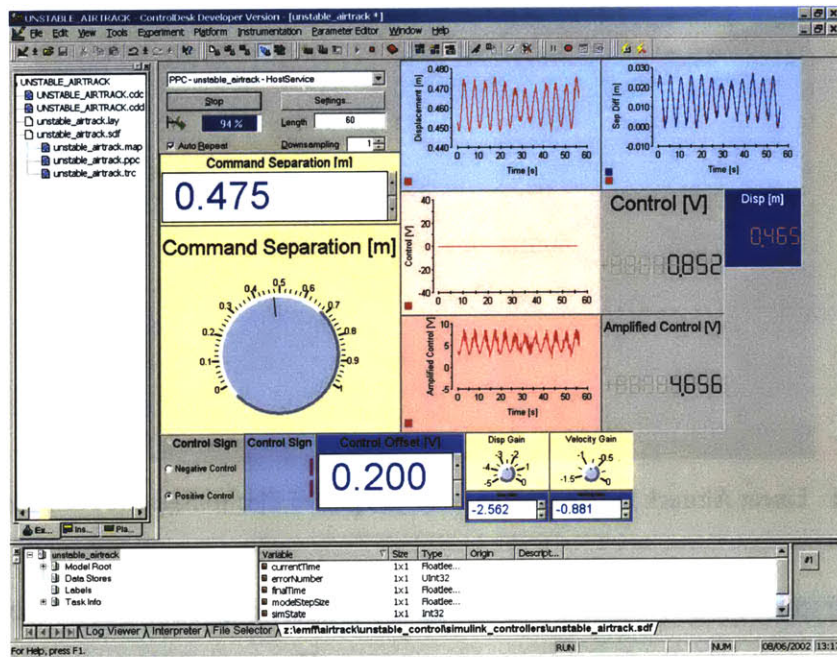


Figure D.2 dSPACE Virtual Control Panel Created for Airtrack System

D.1.2 Airtrack Dynamics and Control

In this section, we discuss the dynamics and control of two configurations of the airtrack: a stable configuration and an unstable configuration.

Stable Airtrack

A schematic of the stable airtrack configuration is shown in Figure D.3. The airtrack is inclined so that the free permanent magnet lies above the fixed electromagnet. (Figure D.3 is exaggerated; the actual inclination used in these experiments is roughly two degrees.) The free magnet tends to fall toward the fixed electromagnet because of the gravitational force acting on it. The magnets must then repel each other in order to main-

tain a fixed separation distance in the presence of the gravitational force and other disturbances. The goal for this configuration is to control the separation distance between the two magnets as precisely as possible, while rejecting disturbances to the system.

In Chapter 5, expressions were given for the forces generated between any two magnetic dipole moments. By reducing Equation 5.51 to represent this simplified system, we express the repulsive force between the two magnets as:

$$F_{EM} = \frac{c_0 \mu_p \mu}{x^4} \quad (D.1)$$

where μ_p is the dipole moment of the permanent magnet (a constant for a given permanent magnet), μ is the dipole moment of the electromagnet (defined by Equation 5.36, and opposite in direction to μ_p in order to generate a repulsive force), x is the separation distance between the two magnets, and c_0 is a constant:

$$c_0 = \frac{3\mu_0}{2\pi} \quad (D.2)$$

where $\mu_0 = 4\pi \cdot 10^{-7}$ T·m/A is the permeability of free space.

The gravitational force acting on the free magnet is:

$$F_g = mg \sin\theta \quad (D.3)$$

where m is the mass of the free magnet, and θ is the inclination angle of the airtrack.

Balancing the forces acting on the free magnet allows us to write the equation of motion for this system:

$$m\ddot{x} = F_{EM} - F_g = \frac{c_0 \mu_p \mu}{x^4} - mg \sin\theta \quad (D.4)$$

Assuming small perturbations from a nominal state, we linearize this equation about a nominal separation distance, x_0 , and a nominal steady-state electromagnetic dipole moment, μ_{avg} , so that:

$$x = x_0 + \delta x , \quad \frac{\delta x}{x_0} \ll 1 \quad (D.5)$$

$$\mu = \mu_{avg} + \delta\mu , \quad \frac{\delta\mu}{\mu_{avg}} \ll 1 \quad (D.6)$$

where δx and $\delta\mu$ are small perturbations from x_0 and μ_{avg} , respectively.

The equation of motion, Equation D.4, becomes:

$$m(\ddot{x}_0 + \delta\ddot{x}) = \frac{c_0\mu_p(\mu_{avg} + \delta\mu)}{(x_0 + \delta x)^4} - mg \sin\theta \quad (D.7)$$

where $\dot{x}_0 = 0$ because x_0 is a constant.

Solving the steady portion of this equation ($\delta\ddot{x} = 0$, $\delta x = 0$, $\delta\mu = 0$) gives the steady-state control required to counteract the gravitational force when no perturbations exist:

$$\mu_{avg} = \frac{mg \sin\theta x_0^4}{c_0\mu_p} \quad (D.8)$$

Hence for a given permanent magnet (with a specified mass and magnetic moment), a given airtrack inclination, and a given nominal separation distance, we can calculate the steady-state electromagnetic dipole moment needed to maintain the nominal separation distance in the presence of gravity when no external disturbances are applied.

Solving Equation D.8 for $mg \sin\theta$ and substituting into Equation D.7 yields:

$$m(\ddot{x}_0 + \delta\ddot{x}) = \frac{c_0\mu_p(\mu_{avg} + \delta\mu)}{(x_0 + \delta x)^4} - \frac{c_0\mu_p\mu_{avg}}{x_0^4} \quad (D.9)$$

Neglecting terms of order greater than one, we express the linearized equation of motion as:

$$\ddot{\delta x} + \frac{4c_0\mu_p\mu_{avg}}{mx_0^5}\delta x = \frac{c_0\mu_p}{mx_0^4}\delta\mu \quad (\text{D.10})$$

which has poles at $\pm j\sqrt{4c_0\mu_p\mu_{avg}/mx_0^5}$. These poles are plotted in Figure D.4 for the mass and geometric properties of this airtrack system. Both poles lie on the imaginary

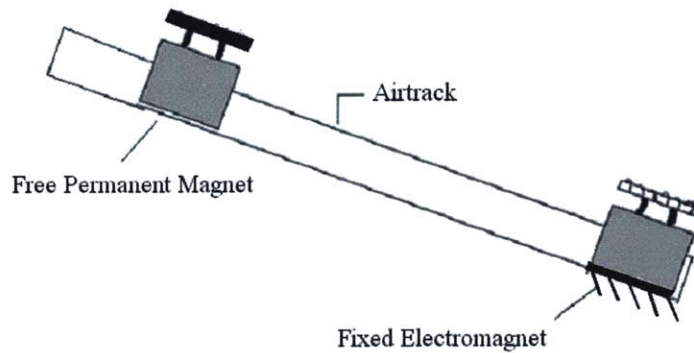


Figure D.3 Schematic of the Stable Airtrack Configuration

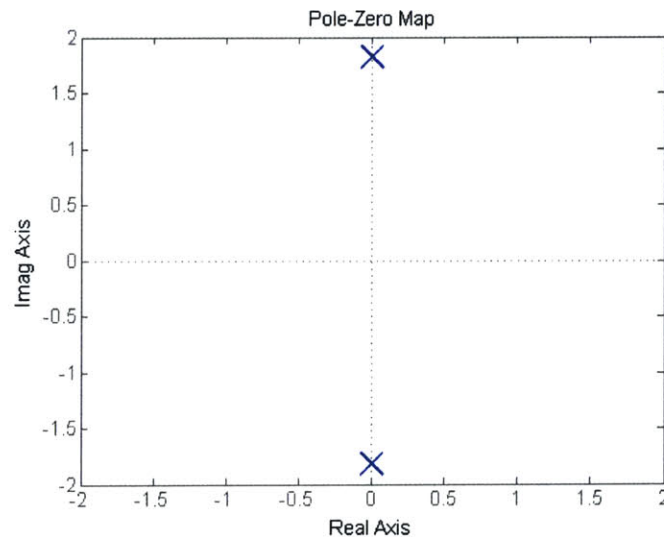


Figure D.4 Stable Airtrack Pole-Zero Map

axis, so that this “stable” system appears to be marginally stable. In reality, the small amount of friction on the airtrack will bring the poles slightly into the left-half complex plane.

Using the method described in Section 6.5, we find the optimal control gain matrix for this stable airtrack system to be:

$$K = \begin{bmatrix} \frac{-4\mu_{avg}}{x_0} + \sqrt{\frac{\lambda}{\rho} + \left(\frac{4\mu_{avg}}{x_0}\right)^2} & \sqrt{\frac{-8\mu_{avg}mx_0^3}{c_0\mu_p} - 2\sqrt{\frac{\lambda m^2 x_0^8}{\rho c_0^2 \mu_p^2} - \frac{4\mu_{avg}m^3 x_0^{11}}{c_0^3 \mu_p^3}}} \end{bmatrix} \quad (\text{D.11})$$

where the two components represent the displacement and velocity gains, respectively, λ is the penalty on the displacement (δx), ρ is the penalty on the control ($\delta\mu$), and the ratio λ/ρ is specified by the control designer.

Unstable Airtrack

A schematic of the unstable airtrack configuration is shown in Figure D.5. In this case, the track is inclined in the opposite manner from the stable configuration; the fixed magnet now lies above the free magnet, so that the free magnet tends to fall *away* from the fixed magnet because of the gravitational force acting on it. The magnets must then *attract* each other in order to maintain a fixed separation distance while counteracting the gravitational force and other disturbances.

We now derive the equation of motion for the unstable airtrack configuration. The attractive electromagnetic force between the two magnets is:

$$F_{EM} = \frac{c_0 \mu_p \mu}{x^4} \quad (\text{D.12})$$

while the gravitational force acting on the free magnet is:

$$F_g = mg \sin\theta \quad (\text{D.13})$$

Balancing the forces and applying the same perturbation as in the stable airtrack analysis, we find the perturbed equation of motion for this system:

$$m(\ddot{x}_0 + \delta\ddot{x}) = mg\sin\theta - \frac{c_0\mu_p(\mu_{avg} + \delta\mu)}{(x_0 + \delta x)^4} \quad (\text{D.14})$$

Solving the steady portion of this equation gives the steady-state control required to counteract the gravitational force when no perturbations exist:

$$\mu_{avg} = \frac{mg\sin\theta x_0^4}{c_0\mu_p} \quad (\text{D.15})$$

Notice that this steady-state magnetic dipole moment has the same magnitude as that in the stable configuration. However, in the stable configuration, the electromagnetic dipole moment is opposite in sign to the permanent magnet's dipole moment, so that the magnets repel one another. In this unstable case, the electromagnetic dipole moment has the same sign as the permanent magnet's dipole moment, so that the magnets attract one another.

Neglecting higher order terms, and substituting Equation D.15 for $mg\sin\theta$, the perturbation equation reduces to:

$$\delta\ddot{x} - \frac{4c_0\mu_p\mu_{avg}\delta x}{mx_0^5} = -\frac{c_0\mu_p\delta\mu}{mx_0^4} \quad (\text{D.16})$$

which has poles at $\pm\sqrt{4c_0\mu_p\mu_{avg}/mx_0^5}$. These poles are plotted in Figure D.6 for the mass and geometric properties of this airtrack system. Notice that this unstable system's poles have the same magnitudes as the stable airtrack's poles, but the two poles now lie on the *real* axis, instead of the imaginary axis. Because one pole lies in the right-half complex plane, we know that these dynamics are unstable.

Using the method described in Section 6.5, we find the optimal control gain matrix for this unstable airtrack system to be:

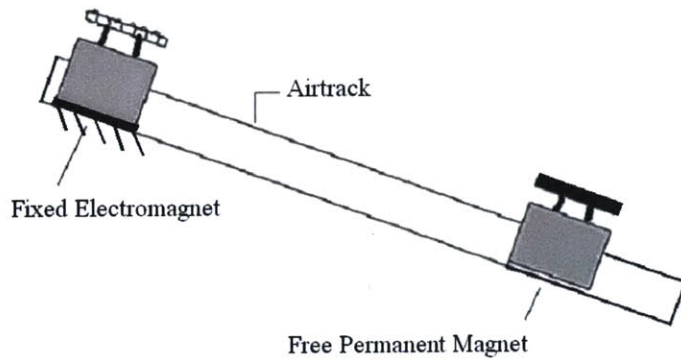


Figure D.5 Schematic of the Unstable Airtrack Configuration

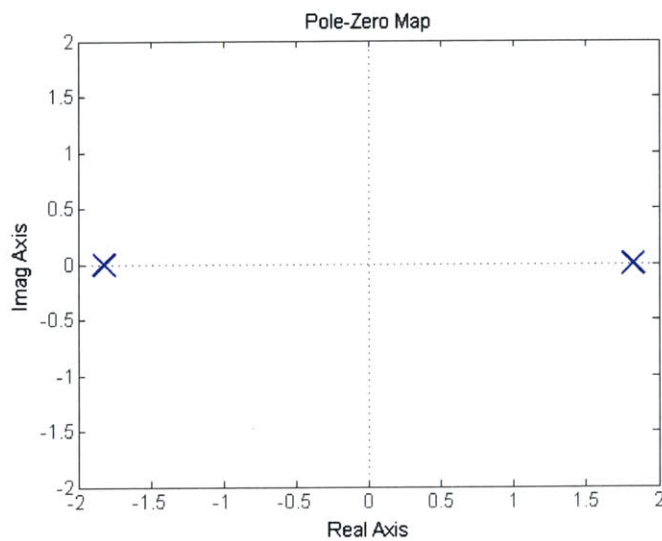


Figure D.6 Unstable Airtrack Pole-Zero Map

$$K = \left[\frac{-4\mu_{avg}}{x_0} + \sqrt{\frac{\lambda}{\rho} + \left(\frac{4\mu_{avg}}{x_0}\right)^2} \quad \sqrt{\frac{8\mu_{avg}mx_0^3}{c_0\mu_p} + 2\sqrt{\frac{\lambda m^2x_0^8}{\rho c_0^2\mu_p^2} + \frac{4\mu_{avg}m^3x_0^{11}}{c_0^3\mu_p^3}}} \right] \quad (\text{D.17})$$

where the two components represent the displacement and velocity gains, respectively, λ is the penalty on the displacement (δx), ρ is the penalty on the control ($\delta\mu$), and the ratio λ/ρ is specified by the control designer.

D.1.3 Discussion of System Poles

It is important to note that the dynamics of the unstable airtrack system are similar to those of a two-spacecraft array spinning at a constant rate within a plane. Just as the unstable pole of a spinning array was found in Section 6.3.1 to move out along the positive-real axis as the array’s spin-rate increases, the unstable pole of this airtrack configuration moves out along the positive-real axis as the inclination angle of the airtrack increases. Conversely, as the array’s spin-rate approaches zero, and as the inclination angle of the airtrack approaches zero, the unstable poles approach the origin.

In addition to having similar unstable pole structures, the two systems exhibit similar *physical behavior*. In both systems, the eigenmode corresponding to the unstable eigenvalue represents a divergence of the dynamics. For the airtrack system, the attractive force between the two magnets maintains the relative separation distance in the presence of gravity. However, if the attractive force is slightly too weak, the “sliding” magnet tends to fall away from the fixed magnet, but if it is slightly too strong, the sliding magnet tends to accelerate toward the fixed magnet. For the formation flying system, the attractive force between the two magnets maintains the centripetal acceleration necessary for the system to spin at a given radius. However, if the force is slightly too weak, the magnets will quickly “fall” away from one another, and if the force is slightly too strong, the magnets will accelerate toward each other. Hence we recognize very similar physics between the two systems, consistent with the mathematical similarity of their dynamics.

Because the unstable dynamics of these two systems are so similar, implementing closed-loop control of the unstable airtrack system using an electromagnetic actuator will prove encouraging in our effort to control a rotating formation flight array with a similar set of actuators. This is a very useful demonstration in the absence of a full-degree-of-freedom electromagnetic formation flight testbed.

D.1.4 Airtrack Experimental Results

Stable Airtrack

The poles of the stable airtrack system were deduced from the measured impulse response of the system. Very light damping due to slight friction from the airtrack surface was neglected, so that the system poles lie approximately on the imaginary axis, at $\pm 1.82j$, as shown in Figure D.4. Substituting these measured values in place of the analytical poles above, and specifying a control penalty four times that of the displacement penalty ($\lambda/\rho = 1/4$), yields the optimal gain matrix for the stable airtrack configuration:

$$K = [11.74 \quad 4.33] \quad (\text{D.18})$$

where the two components represent the displacement and velocity gains, respectively.

The feedback controller was implemented on the airtrack using dSPACE hardware and software, as described in Section D.1.1. The resulting open- and closed-loop step responses are shown in Figure D.7, where the separation distance between the fixed and free magnets is plotted as a function of time. As expected, the open-loop response is very lightly damped, making the system slightly stable, instead of marginally stable. The closed-loop response shows an improvement on the open-loop behavior: the overshoot is reduced and the damping is greater, yielding a much smaller settling time than the open loop response. There is room for improvement, however, since the “steady-state” behavior is still quite noisy, with a ~5 cm (or ~10%) oscillation about the steady value. This has been attributed to a noisy displacement sensor, model error, and a saturated amplifier. Addressing these issues in the future will likely improve the closed-loop performance of this system.

Unstable Airtrack

Since one cannot measure the poles for the unstable airtrack configuration as easily as for the stable configuration (using a measurement of the open-loop impulse response), we use the stable configuration results to predict the unstable poles. Section D.1.2 demonstrated

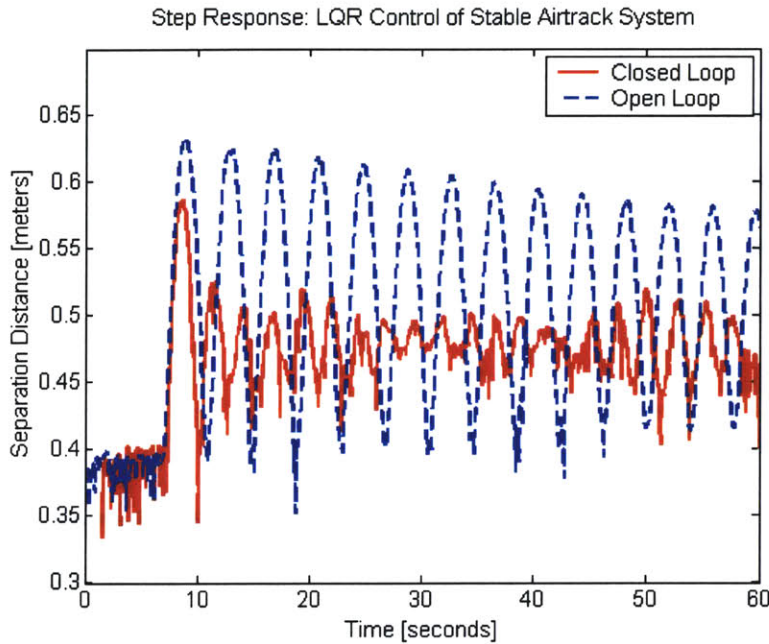


Figure D.7 Open- and Closed-Loop Step Responses of Stable Airtrack

that the unstable poles are of the same magnitude as the stable poles, but at positive and negative locations on the *real*, not the imaginary axis. Hence from the stable poles at $\pm 1.82j$, we assume the unstable poles lie at ± 1.82 , as shown in Figure D.6. Substituting these values in place of the analytical poles, and specifying a control penalty four times that of the displacement penalty ($\lambda/\rho = 1/4$), yields the optimal gain matrix for the unstable airtrack configuration:

$$K = -[2.56 \quad 0.88] \quad (\text{D.19})$$

where the two components represent the displacement and velocity gains, respectively.

The feedback controller was implemented on the airtrack, and the resulting open- and closed-loop responses are shown in Figure D.8, where the separation distance between the fixed and free magnets is plotted as a function of time.

Recall that in the stable airtrack configuration, a step response was used to gauge the control performance. In the unstable configuration, the open-loop response is divergent, so

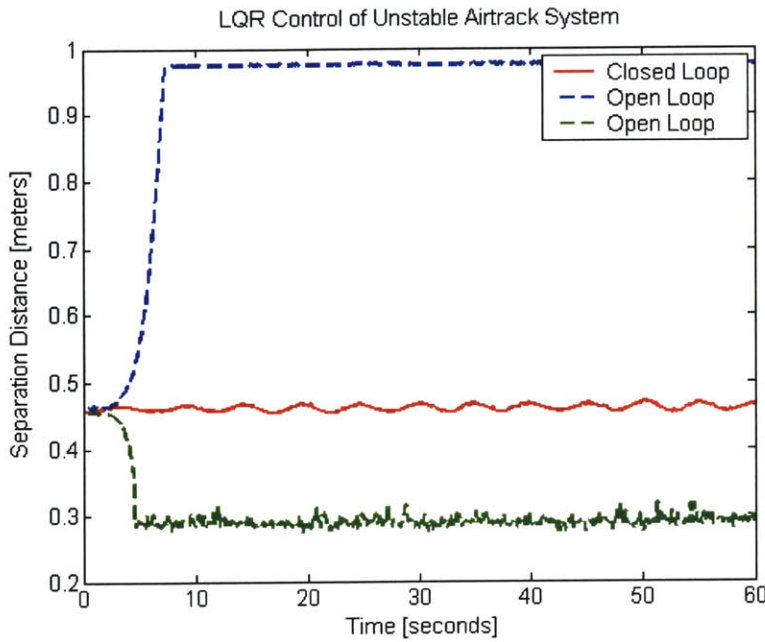


Figure D.8 Open- and Closed-Loop Responses of Unstable Airtrack.

rather than considering a step response, we consider the controller's ability to *reject disturbances and maintain a constant separation distance*. The closed-loop response performs fairly well; in addition to stabilizing the inherently unstable system, the controller maintains the oscillation to within ~ 2 cm of the steady-state displacement value, yielding even better performance than in the stable configuration. Also shown are two open-loop responses. In one case, the response diverges because the two magnets fall apart; in the other case, the two magnets come together. In both of these cases, the divergent magnet is stopped by barriers placed at the ends of the airtrack (visible in Figure D.1). Hence the response becomes constant once the free magnet reaches the barrier.

D.2 Planar Testbed

In the previous sections, we discussed an airtrack system that was used to demonstrate closed-loop control of a simplified system that is dynamically similar to an electromagnetic formation flight (EMFF) system. In the following sections, we discuss a higher-fidelity testbed that is more representative of an EMFF system.

In Section D.2.1, we first describe the testbed and provide references for additional information about the hardware. Then in Section D.2.2, we discuss the dynamics and control of the system. Since the testbed is still evolving and all the sensors are not yet fully functional, only preliminary experimental results are shown in Section D.2.3.¹ In Section D.2.4, suggestions are made for full-degree-of-freedom experiments that may be performed once all of the sensors are operational.

D.2.1 Testbed Description

The EMFF testbed consists of two vehicles that operate on a flat (planar) surface. The vehicles are allowed to translate relative to each other within the plane, and are also allowed to rotate inertially about axes perpendicular to the plane. This yields four system degrees of freedom: two relative separation components within the plane, and the inertial attitude angles of the two vehicles.²

One of the vehicles is depicted in Figure D.9. The two large torus-shaped devices are containers that house the electromagnetic coils. The coils are made of superconducting wire, which must be operated at temperatures under 110 Kelvin in order to superconduct [25]. The coils are thus bathed in liquid nitrogen (at 77 Kelvin), and the containers are necessary to house the coils and the liquid nitrogen bath. At the top is an additional container that stores a reserve of liquid nitrogen, since it boils off at a significant rate when the testbed is operated at ambient temperatures. In the center of the vehicle is a reaction wheel whose spin axis aligns with the rotation axis of the vehicle (and is perpendicular to the plane of the testbed). Finally, the entire vehicle is supported by a gas carriage system, which is used to levitate the vehicle so that it floats nearly frictionlessly on the flat surface.

-
1. Specifically, the metrology subsystem that measures the relative separations between vehicles is not yet operational, so only attitude control of an individual vehicle was achievable.
 2. Notice that we are not concerned with, and cannot control, the inertial position of the array's center of mass. We are concerned only with the relative separation components (Δx and Δy) between the vehicles, or equivalently, with the relative separation distance and the inertial clock angle of the line-of-sight between the vehicles.

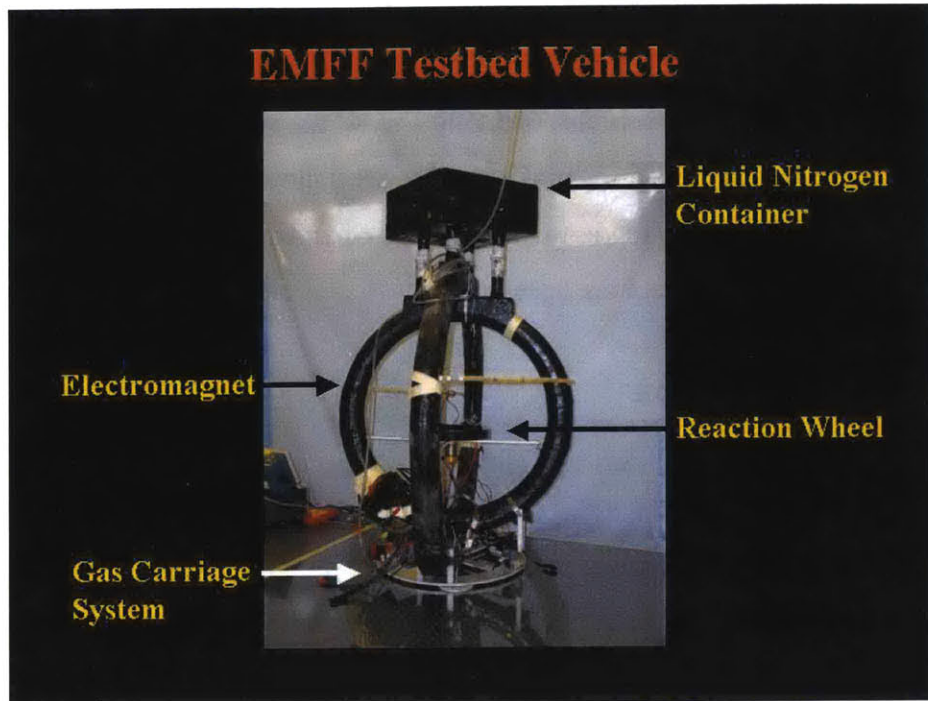


Figure D.9 EMFF Testbed Vehicle

The second vehicle is nearly identical to this one. Further information about all of the subsystems of each vehicle, including the electronics, metrology, power, structures, and other subsystems, can be found in reference [32]. As the entire testbed continues to evolve, this reference may eventually become outdated and will be replaced with more current documentation.

D.2.2 Testbed Dynamics and Control

It is simple to see that this system is a constrained (simplified) version of the two-spacecraft system discussed in Chapter 6. Specifically, we modify the linearized equations of motion in Chapter 6 by removing the following five degrees of freedom: two attitude rotations of each vehicle (about axes within the array's plane of operation), as well as motion of the array outside of the nominal plane of operation ("tipping" of the array about axes within this plane). Clearly the system then reduces to the four degrees of freedom described in Section D.2.1.

Following the same control design techniques presented in Section 6.5, we can find the optimal control gain matrix and implement it to form a feedback controller. However, because the sensors on the testbed are not yet fully functional -- specifically, the metrology system that provides relative separation information is not yet operational -- we cannot implement full-state feedback for this system. Since the onboard gyroscopes are functional, it has been possible to feed back only attitude information for each vehicle. Therefore, preliminary results demonstrating closed-loop attitude control of a single vehicle are presented in the following section. In Section D.2.4, we will propose further experiments that may be performed once the metrology system is operational.

D.2.3 Testbed Preliminary Experimental Results

To demonstrate attitude control of a single vehicle, a command signal was generated to specify the desired attitude of the vehicle as a function of time, with respect to an inertial reference. The command signal is shown in Figure D.10 (the darkest line), and is a series of steps in time. The vehicle is first commanded to rest at 0 degrees for 5 seconds, then to slew to -45 degrees and remain at rest for 15 seconds, then to slew again to -90 degrees and remain at rest for 15 seconds, and then to slew back to -45 degrees, and so forth.

The experimental results, plotted by integrating the gyroscope data, are plotted along with the command signal in Figure D.10. Results are plotted for several control designs, all generated using the optimal control design technique described in Chapter 6, with various penalties assigned to the state and control values. All of the experimental data track the command signal fairly well, although some perform better than others with reduced overshoot and increased damping.

D.2.4 Testbed Proposed Experiments

Once the metrology system is operational, and full-state feedback is possible for this planar testbed, the following experiments are suggested to demonstrate the EMFF concept:

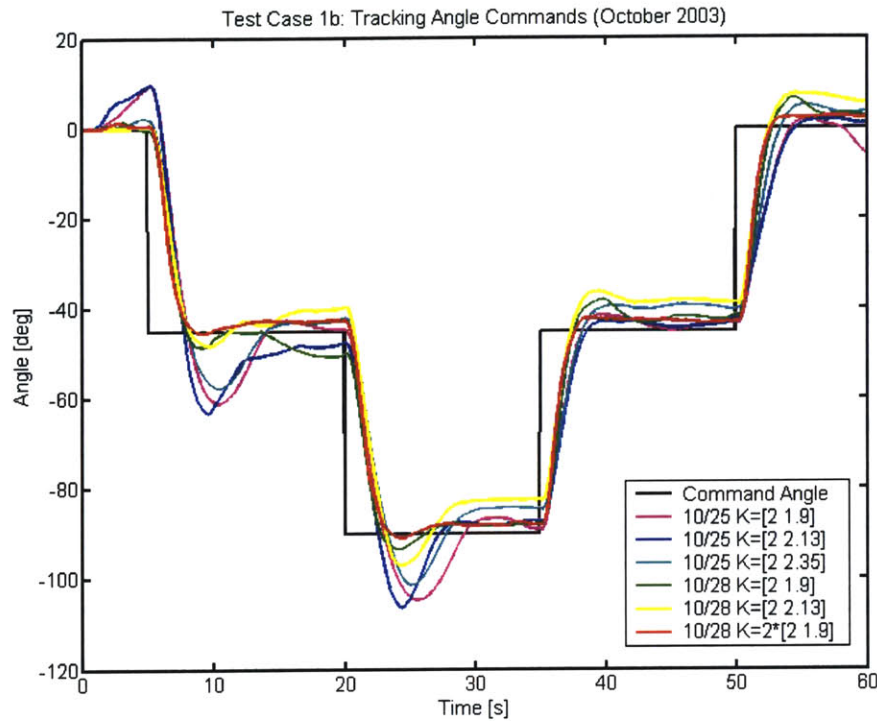


Figure D.10 Angle-Tracking Results Using One Vehicle on the Planar Testbed

- disturbance rejection in both the relative separation and inertial attitude degrees of freedom.
- tracking of a command profile in the relative separation degrees of freedom, while rejecting disturbances to the attitudes.
- tracking of a command profile in both the relative separation and attitude degrees of freedom. For example, “spin up” the array of two vehicles from rest into a steady-state spin maneuver, as described in Section 6.2.1. The transient dynamics of such a maneuver are discussed briefly in Appendix E.

D.3 Summary

Two hardware systems have been presented in this appendix: a linear airtrack and a planar testbed. Both systems are useful in demonstrating, via hardware, the feasibility of the EMFF concept. The airtrack is a simple system whose dynamics are similar to a very simplified set of EMFF dynamics. Encouraging results were presented using the airtrack, including the closed-loop stabilization of an unstable system using an electromagnetic

actuator and linear optimal control. The planar testbed, however, is a more complex system, but one that is more representative of a true EMFF system. Preliminary attitude-control experiments were presented, along with suggestions for future experiments that may be performed once the metrology subsystem is fully operational.

Appendix E

EMFF SPIN-UP DYNAMICS

One proposed architecture for NASA’s forthcoming Terrestrial Planet Finder (TPF) is a separated-spacecraft interferometer, where several collectors and one combiner are each flown on separate spacecraft, and the spacecraft are flown in formation. As described several times throughout this thesis, the scientific observation mode for such an interferometer will be for all of the spacecraft in the array to spin at a steady rate about an axis positioned at the array’s centerpoint and directed toward the target star. In this appendix, we discuss the “spin-up” of such a system, or the transient dynamics required to transform the array from a static one (at rest) to a steadily spinning one.

It was discovered by Miller, Sedwick, et. al. [39] that the loads needed to spin up an array from a static state to a steady spin may all be generated using electromagnets and reaction wheels. For instance, if the two spacecraft in a two-vehicle array are arranged such that their electromagnetic dipoles are initially perpendicular to each other, as shown in Figure E.1, then the loads generated on the static array are:

- a “shearing” force on each vehicle (depicted by the straight, light-colored arrows in Figure E.1) that acts perpendicular to the line-of-sight between the vehicles. This force is caused entirely by the electromagnetic interaction between the vehicles. Notice that no component of force is applied in the direction parallel to the line of sight when the electromagnetic dipoles are aligned as shown in Figure E.1. Also note that the forces applied to the two vehicles are equal in magnitude but opposite in direction.

- a torque on each vehicle that is generated by the interaction of the magnetic fields of the vehicles. These torques are shown as the curved, light-colored arrows in Figure E.1. The torques act in the same direction, but the torque on the right-hand vehicle in Figure E.1 has twice the magnitude as that on the left-hand vehicle.

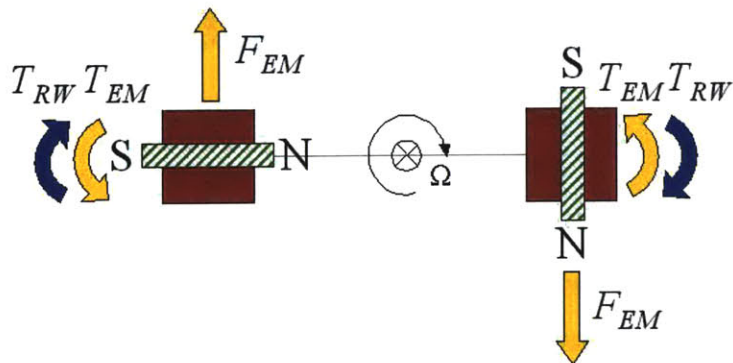


Figure E.1 Two Spacecraft Spinning Up About the Array Centerpoint

The forces are useful in that they provide the angular acceleration necessary to spin up the array about its centerpoint. The torques, however, are not necessarily useful. In fact, in order to maintain the shearing force between the vehicles, we must maintain their electromagnetic dipoles in a perpendicular configuration. This may be performed in one of two ways: by magnetically steering the dipoles to remain perpendicular, while allowing the attitude of the vehicle to react to the electromagnetic torques, or alternatively, by using the reaction wheels to provide counter-torques to the electromagnetic torques, thus steering the vehicles so that their attitudes remain fixed with respect to the line-of-sight between the vehicles. Hence the third load on the vehicles in the system is:

- reaction wheel motor torques, used to counteract the electromagnetic torques and to maintain the desired attitude of each vehicle during the spin-up maneuver. These torques are depicted by the curved, dark-colored arrows in Figure E.1.

As the array is accelerated to the desired angular velocity, the reaction wheels are used to gradually torque the vehicles so that their dipoles align with each other (and with the line-of-sight between the vehicles). (Alternatively, the dipoles may be magnetically steered so

that they eventually align.) The array then continues to spin at a steady rate, with the aligned electromagnetic dipoles maintaining the centripetal acceleration of the vehicles.

With the loads in Figure E.1, it is simple to see that the left-hand spacecraft will translate “upward” and the right-hand spacecraft will translate “downward.” In other words, the array will accelerate in a clockwise fashion, with its acceleration vector oriented into the spin-plane of the array, pointing away from the reader. If one of the dipoles were oriented in the opposite direction, the angular acceleration would also be in the opposite (counter-clockwise) direction.

Figure E.2 depicts the right-hand vehicle translated slightly in each direction. If the orientation of the dipole remains unchanged, the shear force varies as the vehicle translates away from the original line-of-sight between the vehicles. The shear force can be characterized in three separate regions, depicted in Figure E.2:

1. If the right-hand electromagnet is near the original line-of-sight between the vehicles (the axis of the left-hand electromagnet), it will be repelled downward.
2. If it is well above the original line-of-sight, it will be repelled even further upward.
3. If it is well below the original line-of-sight, it will be attracted upward.

Notice that these shear forces (indicated by arrows) change direction twice as a function of the vertical translation of the right-hand electromagnet, indicating the existence of two equilibrium positions. The equilibrium position that lies above the centerline is unstable, since the electromagnet tends to move away from it. The equilibrium position that lies below the centerline is stable, since an electromagnet in its vicinity tends to remain there.

An equilateral triangle is formed by the two equilibrium positions and the center of the horizontal electromagnet, so that the equilibrium positions lie at ± 30 degrees about the horizontal electromagnet’s axis. During the spin-up maneuver, the horizontal electromagnet must be pointed such that its axis points toward the vertical electromagnet. The

required pointing accuracy is a fraction of the angle between equilibrium positions. One tenth of this range should be sufficient, yielding a pointing accuracy of ± 3 degrees.

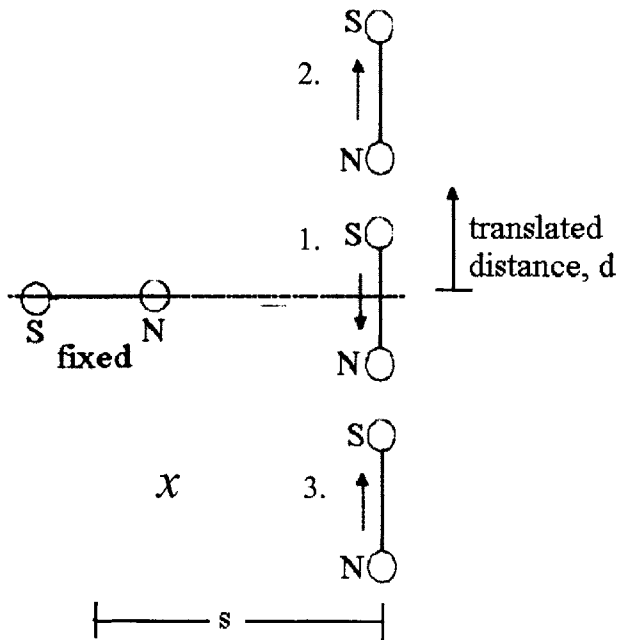


Figure E.2 Translation-Dependent Shear Force on Two Vehicles with Perpendicular Magnetic Dipoles

A phase-plane portrait of these equilibria is depicted in Figure E.3. Translation in the shear direction is plotted on the horizontal axis, while velocity in the shear direction is plotted on the vertical axis. The two equilibria are shown on the horizontal axis, at equal distances opposite each other from the “zero” position (± 1.5 meters). The location of the shearing magnet during spin-up corresponds to the origin. Notice that if the angle of the horizontal magnet remains fixed, and is not allowed to rotate to track the shearing magnet, the shearing magnet will accumulate sufficient velocity to pass through the stable equilibrium and not return. This further illustrates the complexity of the electromagnetic formation flight control problem.

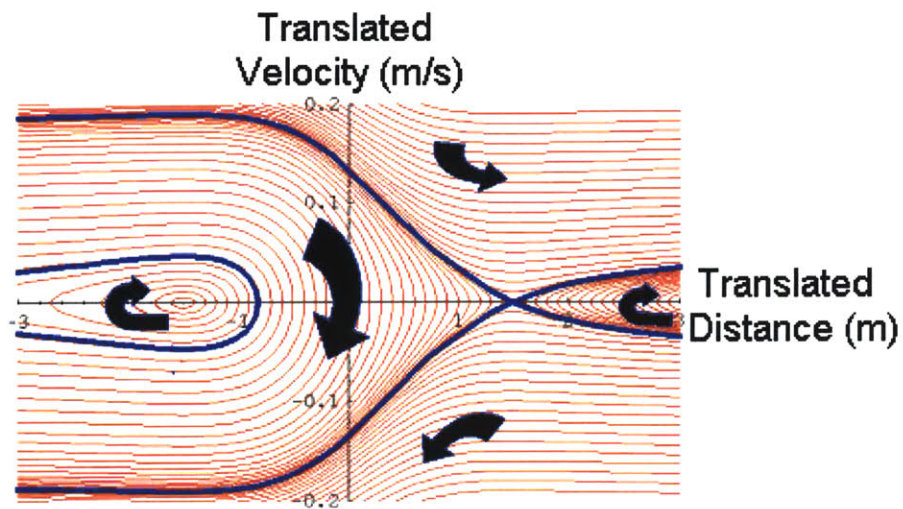


Figure E.3 Phase-Plane Portrait of the Perpendicular Magnet Geometry

